Title
Actin Filament Branching and Behavior under Mechanical Constraints

Author
Risca, Viviana Ioana

Publication Date
2012

Peer reviewed|Thesis/dissertation

Actin Filament Branching and Behavior under Mechanical Constraints

By

Viviana Ioana Risca

A dissertation submitted in partial satisfaction of the

requirements for the degree of

Doctor of Philosophy

in

Biophysics

in the

Graduate Division

of the

University of California, Berkeley

Committee in charge:

Professor Daniel A. Fletcher, Chair
Professor David G. Drubin
Professor Phillip Geissler
Professor Matthew Welch

Spring 2012

Abstract

Actin Filament Branching and Behavior under Mechanical Constraints

by

Viviana Ioana Risca

Doctor of Philosophy in Biophysics

University of California, Berkeley

Professor Daniel A. Fletcher, Chair

Mechanical cues affect a number of important biological processes in metazoan cells, such as migration, proliferation, and differentiation. Many of these processes are mediated by the cytoskeleton, an intracellular network of protein filaments that provides mechanical rigidity to the cell and drives cellular shape change. In particular, actin, a very highly conserved and abundant cytoskeletal protein, forms filaments that, when organized by a large and diverse group of actin-binding and regulatory proteins, self-assemble into dynamic and mechanically complex networks. The actin filament itself is polymorphic, with a structure and a set of mechanical properties that are modulated by the binding of regulatory proteins. Both the structure and the mechanical properties of actin filaments play an important role in determining the mechanical properties, architecture, and dynamics of the subcellular structure that result from self-assembly. We sought to investigate an important unanswered question: how do mechanical constraints help regulate the assembly of an actin network?

This dissertation focuses on branched actin networks, which play a key force-generating role in the formation of membrane protrusions, in endocytosis, and in several types of intracellular motility. These networks are nucleated by the Arp2/3 complex and display adaptive behavior in response to compressive forces. They consist of Y-shaped branches formed by a pre-existing filament, the Arp2/3 complex bound to its side, and a new actin filament nucleated by the Arp2/3 complex. To investigate how the architecture of these networks is shaped by mechanical constraints, such as compressive forces arising from the resistance of cellular membranes to deformation, we devised a methodology for mechanically constraining single actin filaments while new branches are nucleated from their sides by the Arp2/3 complex. Branch nucleation on individual filaments was imaged with two-color fluorescence microscopy using a protocol that distinguishes constrained mother filaments from freshly nucleated daughter filaments.

Combining this two-color assay with quantitative analysis of filament curvature, we show that filamentous actin serves in a mechanosensitive capacity itself, by biasing the location of actin branch nucleation in response to filament bending. We observed preferential branch formation by the Arp2/3 complex on the convex face of the curved filament. At radii of curvature of 1 μm, we observed approximately twice as many branches on the convex face as on the concave face.

In the cellular context, where actin filaments tend to make a ~35˚ angle with the normal to the membrane, this observation suggests that compressive forces that bend actin filament tips away from the membrane would result in an enhancement of branching nucleated on the membrane-facing convex face of each filament. This effect constitutes a novel mechanism by which branched actin networks may be oriented toward membranes, as observed in vivo. Furthermore, in the context of a limited branching zone near the membrane, which is expected from the known biochemistry of the process, orientation of new branches toward the membrane also leads to an increase in network density in response to force, which has been documented in experiments with motility of bacteria in cytoplasmic extract.

To explain the biased nucleation of branches on curved actin filaments, we propose a fluctuation gating model in which filament binding or branch nucleation by Arp2/3 occur only when a sufficiently large, transient, local curvature fluctuation causes a favorable conformational change in the filament. Using Monte Carlo simulations of a discretized worm-like chain model of the actin filament immobilized on a surface like the filaments in the constrained branching assay, we show that the fluctuation gating model can quantitatively account for our experimental data.

Expanding the scope of the simulations beyond the in vitro experiment, we hypothesize that the curvature fluctuations of filaments in the cell may be modulated by the architecture of the actin network to which they belong. To test this hypothesis, we computationally explore how three types of mechanical constraints – buckling or bending of a filament end by a hard wall, bundling of filaments by a crosslinking protein, and uniaxial tension applied to a single filament – affect local curvature fluctuations. We find that bending of simulated filaments by a hard wall can significantly alter curvature fluctuations, the magnitude of which can be approximately calculated by the simple geometry of filament bending at the barrier. On the other hand, crosslinking of simulated actin filaments with crosslinking elements of physiologically relevant stiffness has surprisingly little effect on the small-scale local curvature fluctuations. Similarly, enclosure of a simulated filament bundle in a tube does not significantly affect curvature of filaments on the nanometer scale. Tension, however, in the range of 100 pN, does have a marked effect on curvature fluctuations in our simulations, suggesting that any interactions of actin-binding proteins with actin filaments that depend on bending fluctuations may be modulated by tension. This has been observed in several recent experiments, suggesting that the effects of tension on the biochemical interactions regulating actin network assembly and disassembly warrant further study.

Overall, the results presented here demonstrate how filament curvature can alter the interaction of cytoskeletal filaments with regulatory proteins, suggesting that direct mechanotransduction by actin may serve as a general mechanism for organizing the cytoskeleton in response to force.

Table of contents

List of Figures and Tables

Units and Abbreviations

1,5-I-AEDANS: (N-(iodoacetyl- N'(5-sulfo-1-napthyl)))ethylenediamine

2-D: two-dimensional

3-D: three-dimensional

ABP: actin-binding protein

ADF: actin depolymerizing factor

ADP: adenosine monophosphate

AF: Alexa Fluor

AFM: atomic force microscopy

AMP-PNP: adenylyl-imidodiphosphate

ANCOVA: analysis of covariance

ANOVA: analysis of variance

Arp2: actin-related protein 2

Arp3: actin-related protein 3

ARPC1-ARPC5: actin-related protein complex proteins 1-5

ATP: adenosine triphosphate

BSA: bovine serum albumin

CA: C-terminal fragment including the connecting domain and acidic domain of Class I NPFs

cryo-EM: cryoelectron microscopy

DF: daughter filament

EDC: 1-ethyl-3-(3-dimethylaminopropyl)carbodiimide

EM: electron microscopy

F-actin: filamentous actin

FH2: formin homology 2

G-actin: globular actin

GTP: guanosine triphosphate

GUI: graphical user interface

HMM: heavy meromyosin

JMY: junction mediating and regulatory protein

k_B: Boltzmann's constant

m: meter
MF: mother filament
mg: milligram
min: minute
mm: millimeter
ms: millisecond
μL: microliter
μM: micromolar
μm: micrometer
μs: microsecond
N: Newton
N-WASP: neural Wiskott-Aldrich syndrome protein
NHS: N-hydroxysuccinimide
nM: nanomolar
nm: nanometer
NPF: nucleation-promoting factor
PEG: poly(ethylene glycol)
P_i: inorganic phosphate
PIPES: piperazine-N,N′-bis(2-ethanesulfonic acid)
PLL: poly(L-lysine)
pN: piconewton
ppk: pixels per knot (in spline fits)
r.m.s.: root mean square
s: second
SA: streptavidin
SD: standard deviation
SEM: standard error on the mean
TMR: tetramethylrhodamine
TPA: transient phosphorescence anisotropy
TRITC: tetramethylrhodamine isothiocyanate
TTCF: tangent-tangent correlation function
VASP: vasodilator-stimulated phosphoprotein

VCA: C-terminal fragment including the verprolin homology/WH2 domain, connecting domain, and acidic domain of Class I NPFs

WASP: Wiskott-Aldrich syndrome protein

WCA: see VCA

WH2: Wiskott-Aldrich syndrome protein homology 2

WLC: worm-like chain

Acknowledgments

I would like to thank my Ph.D. advisor, Professor Daniel Fletcher, for the opportunity to work in his lab, for years of patient support during the course of my research projects and for his support of my fellowship and job applications. Professor Fletcher suggested that I investigate the curvature dependence of Arp2/3 binding and was involved in interpreting the results of the project through all of its stages. I also thank Professor Fletcher for his extensive help and advice on the written and oral presentation of results, including his constructive comments on this dissertation, for his generous support of extracurricular and community outreach activities and for his ongoing efforts to foster creativity and create opportunities for learning and professional development in his lab.

Mr. Evan Wang has been my close collaborator in this work. He performed all Monte Carlo simulations described in this dissertation and continues the work begun by the investigation of the effect of curvature on actin branch nucleation. It has been a pleasure to work with him, and I thank him for his hard work and enthusiasm in our research collaboration. Professor Phillip Geissler has my sincere thanks for sharing his deep insights about the possible mechanisms underlying our experimental observations on many occasions, and working closely with us, while overseeing Mr. Wang's work, on actin curvature projects. I am also grateful for his excellent teaching, from which I benefited in Chemistry 220B.

I am grateful to the members of my thesis committee, Professors David Drubin, Phillip Geissler, and Matthew Welch, for the valuable and constructive feedback and the career advice they have given me, and for the time they took to meet with me throughout my Ph.D. I also appreciate the time that they took during a busy semester to review this dissertation. I am grateful to Professors Susan Marqusee and Sanjay Kumar, who, as members of my qualifying exam committee, helped steer me in a productive direction in the early stages of graduate school. Professor Marqusee has also been very kind to me throughout my Ph.D., has given me valuable advice about graduate school and beyond, and encouraged me to apply for the Soros Felowship for New Americans.

I have been lucky to work closely with brilliant, committed, and skilled labmates. I thank all the past and present members of the Fletcher Laboratory with whom I had the pleasure of working for their constant help, support, and insight. They have contributed to a positive and professional lab community.

I am grateful to Dr. Ovijit Chaudhuri for his insights and feedback, for many valuable converstations during our collaboration on the actin curvature project, for instrument training, and for critical reading of manuscripts. Dr. David Richmond was a pleasure to work with, on both simulations of bundled actin and on a few experiments on tropomyosin binding to actin using the TIRF microscope he assembled. I thank him for his collaboration and for his commitment to helping others in lab. Dr. Eva Schmid and Professor Jeanne Stachowiak have been unfailingly kind and supportive, and I am grateful for the time they have taken to help me and to share their expertise with me on countless occasions, including critical reading of a manuscript.

Dr. Peter Bieling has given me valuable technical and scientific advice on many occasions. I am indebted to him for taking the time to share his surface passivation methodology with me, to have many conversations about biochemistry, and for organizing the immensely helpful actin club, in which he, Mr. Scott Hansen, Mr. Evan Wang, and Dr. Julian Weichsel shared their knowledge and perspectives on actin and related topics. I also thank Dr. Weichsel for helpful conversations.

Professor Allen Liu, Dr. Ross Rounsevell and Professor Sapun Parekh helped train me, built the microscopes I used, and taught me basic biochemistry techniques, among the many things for which I am grateful to them. Professor Sander Pronk not only set up the lab computer network that I counted on for backing up and storing data, but also had several very useful conversations with me about actin filament physics and curvature measurement. I thank Professor Joshua Shaevitz for his supervision and encouragement during assembly of an optical trap during the beginning of my Ph.D. and for many helpful conversations. I thank Professor Wilbur Lam for help with statistics on many occasions. I am indebted to Mr. Neil Switz for countless fascinating and helpful conversations, for his safety advice, and for allowing me to participate in his outstanding microscopy boot camp.

Dr. Wendy Hansen, Dr. Martijn van Duijn and Dr. Michael Rosenbluth were very generous with their time and helped me with technical on many occasions during the early part of my Ph.D. I thank Dr. Alexis Crow for useful discussions. Mr. Arunan Skandarajah, Dr. Lina Nilsson, Ms. Win Pin Ng, Mr. Gautham Venugopalan and Mr. Kevin Webster were always there with helpful advice and performed the thankless but essential task of maintaining microscopes. In particular, I want to thank Dr. Nilsson and Mr. Venugopalan for being excellent bench-neighbors, and in particular Dr. Nilsson for her critical reading of one of my manuscripts. I thank Mr. Webster, Ms. Ng and Mr. Venugopalan in particular for their very helpful technique tutorials. I also thank Drs. Michael Vahey, Ben Ricca, Matthew Good, and Michael D'Ambrosio for their contributions to the lab and helpful conversations.

Ms. Stephanie Eistetter and Ms. Hyoungsook Ann have been invaluable in organizing the lab and both helping and training me in technical and administrative matters.

I have had the pleasure of working with two smart, hard-working, and enthusiastic high school students on summer projects. Ms. Jia Jun Chia worked with me during the early stages of experiments on curvature-biased branching by Arp2/3. Mr. Casey Drubin worked with me on analyzing tropomyosin binding data and exploring new methods for investigating the curvature sensitivity of ABP binding.

I thank Professors Rebecca Heald and George Oster for the opportunity to work for a research rotation period in their labs. I am also grateful to Professors Andrew Spakowitz, Michael Blower, and Petr Kalab, who took the time to supervise and help me during my rotations. Professor Heald has also kindly given me professional advice, and I am indebted to her for encouraging me to apply to the MBL Physiology Course and to pursue my career goals.

I would like to thank my collaborators on side projects: Professor Eva Nogales and Mr. Galo Garcia on a project studying yeast septins, Dr. Cesar Diaz-Celis on a project involving bacterial

tubulin, Professor Zach Cande and Dr. Alex Paredez on Giardia actin, and Professor Orion Weiner and Dr. Andrew Houk on the role of membrane tension in cell motility. Although not directly contributing to this dissertation, the work I did with them taught me many valuable skills that I applied to my primary research.

I am grateful to Dr. Orkun Akin, Professor Dyche Mullins, and Dr. Mark Dayel for the opportunity to work with them on symmetry breaking of actin networks. I learned a tremendous amount from watching Dr. Akin's approach to experimentation at the bench. I would also like to thank Prof. Mullins for his ongoing support.

I had the rare opportunity to participate in the Woods Hole MBL Physiology Course in 2007, and I would like to thank everyone who made that experience a great one, which taught me a tremendous amount about how to approach problems in cell biology and biochemistry. Many of the skills I leared at Woods Hole were applied directly to my dissertation work. I am grateful to my project teammates, Drs. Andreas Hilfinger, Karen Kasza, Elizabeth Villa, Alexandra Zidovska, and Professor Adam Cohen, as well as my Woods Hole TA, Dr. Aaron Groen, for their commitment to the projects and for many instructive conversations. I am indebted to Professors Dyche Mullins, Tim Mitchison, and Eric Wieschaus for sharing their knowledge, experience, and advice with me and for giving me the chance to work closely, at the bench, with world-class scientists in a truly unique environment. I also thank the many faculty members who gave tutorials, in particular, Professor Rob Phillips, and my Woods Hole classmates, including my Biophysics classmate, Dr. Rose Loughlin, whom I thank for many helpful discussions over the years.

I would like to thank the Berkeley Statistics Department consulting service for their statistics advice.

None of my work would have been possible without the Berkeley Biophysics Graduate Group, and the tireless work of Ms. Diane Sigman and Ms. Kate Chase. I would also like to thank Professor Ehud Isacoff for his advice during the beginning of graduate school. I also want to express my gratitude to my Biophysics program-mates for feedback at seminars and retreats and their eagerness to contribute to the program. In particular, I would like to thank Ms. Melania Strycharska and Dr. Phillip Elms for technical help.

I would like to thank Mr. Tom Eliaz for advice on programming and data management, helpful conversations, and critical reading of this manuscript.

I have been lucky to be supported by several fellowships and grant programs. I have been supported in part by a Berkeley Fellowship, the Paul and Daisy Soros Fellowship for New Americans, University of California Systemwide Biotechnology Research & Education Program GREAT Training Grant 2007-14, and a NSF Graduate Research Fellowship. Part of the work discussed in this dissertation was also supported by a NIH R01 grant to Professor Daniel Fletcher.

Chapter 1. Introduction and Background

The cytoskeleton

The diversity of cellular structures implies that an underlying framework must be creating and supporting cell shape, even in the absence of cell walls. As more has been revealed about the complexity of intracellular processes, involving directed motion, contractility, and local concentration of components by membrane-bound and non-membranous compartments, an organizing framework to direct the transport and localization of intracellular components has also emerged as a key element in our understanding of how cells function. The cytoskeleton performs both of these functions (Alberts et al., 2007).

Broadly, a cytoskeleton is defined as a network of protein filaments that endow a cell with mechanical stability, the ability to change shape, a system that spatially organizes other cellular components by providing tracks for motors or serving as a scaffold for the binding of non-motor molecules, or some combination of the above (Alberts et al., 2007). It has been shown to exist in all cell types, including prokaryotes (Wickstead & Gull, 2011).

The cytoskeleton of animal cells is composed of several classes of proteins that are highly conserved among eukaryotes, and in some cases, also exhibit significant homology to prokaryotic cytoskeletons (Wickstead & Gull, 2011). The two best understood cytoskeletal proteins are actin and tubulin, both of which are small globular proteins that bind adenosine triphosphate (ATP) and guanosine triphosphate (GTP), respectively. Tubulin exists as a constitutive dimer of alpha and beta tubulin, while actin exists as a monomer. These fundamental subunits assemble into long filaments, with a double-helical structure in the case of actin (termed filamentous actin or F-actin in the assembled form), and a hollow tube structure termed a microtubule, in the case of tubulin. They are polar and highly dynamic polymers. Both actin and tubulin interact with a very large number of actin-binding proteins (ABPs) and microtubule-associated proteins, respectively, which regulate their dynamics and organize them into subcellular structures with varied architectures (Akhmanova & Steinmetz, 2010; Alberts et al., 2007; Etienne-Manneville, 2010; McGough, 1998; Pollard & Cooper, 1986; Pollard & Cooper, 2009; Roll-Mecak & McNally, 2010). A third class consists of cytoskeletal filaments collectively termed intermediate filaments, but comprising many different proteins that are filamentous in nature as monomers, and assemble into larger rope-like, nonpolar filaments in a regulated, but not highly dynamic manner (Alberts et al., 2007). The fourth class is septins, a family of GTPases that assemble into stable heterooctameric (S. cerevisiae) or heterohexameric (mammals) rods, which then form higher-order nonpolar filaments and meshes (Caudron & Barral, 2009; McMurray & Thorner, 2009).

This dissertation will focus on the actin cytoskeleton of animal and yeast cells. It will take a biophysical approach, which is well suited for the study of the many mechanochemical processes that shape the cytoskeleton.

Central aim and overview of this work

The central aim of this dissertation is to explore how mechanical forces interact with the actin branch nucleation process to regulate the architecture and growth of the dendritic, or branched,

actin network. This question is addressed with a biophysical toolkit combining experiments, quantitative analysis, and simulations, and discussed in the larger context of mechanosensing and self-organization by the actin cytoskeleton.

Chapter 1 consists of background information that describes the state of the current understanding of actin biochemistry, actin nucleation by the actin-related protein 2/3 (Arp2/3) complex, the mechanical properties of actin filaments, and classical paradigms of molecular mechanosensing. Chapter 2 describes the development of a technique to immobilize actin filaments on surfaces for imaging, coupled with detection of fluorescently labeled protein or small molecule binding and measurement of the local curvature of actin filaments. Chapter 3 is a reproduction of a published paper describing an application of the technique outlined in Chapter 2 to study how actin filament curvature biases the direction of branch nucleation by the Arp2/3 complex, followed by the description of a coarse-grained model that quantitatively accounts for the experimental results by taking into account the spectrum of local curvature fluctuations of a partially immobilized actin filament. This chapter also discusses some of the implications of biased branching for the orientation of filaments in dendritic networks. Chapter 4 describes the results of a series of simulations that build on the coarse-grained filament model developed in Chapter 3 and explores how different types of constraints on actin filaments affect the distribution of local curvature fluctuations of the filament. Chapter 5 interprets the results described in the previous chapters in the broader cellular context, considering what the observation that filament curvature has a direct effect on the activity of an actin-binding protein means for the regulation of other actin binding proteins and for cellular mechanosensing in general.

Actin

The structure and sequence of eukaryotic actins are extremely well conserved, with less than 5% sequence variation among the actin genes found in animals and protozoa (Pollard & Cooper, 1986). It has been argued that this high degree of conservation is due to the large number and diversity of ABPs with which the actin filament has evolved to interact, but a building body of evidence points to an alternative explanation – namely, that the actin filament is highly tuned by evolution for cooperative and allosteric regulation of its dynamics and biochemical interactions by ABP binding (Galkin et al., 2012). For these reasons, the actin filament cannot be fully understood as a simple rod or fiber, or even as a linear assembly of block-like subunits. The details of actin structure, polymerization dynamics, and mechanical behavior, which we will discuss in the following sections, are essential to its function in the cell.

Actin structure

Actin is a ~42 kDa protein found as several isoforms in all eukaryotic cells and in many cases, is the most abundant protein in the cell (Figure 1) (Pollard & Borisy, 2003). Monomeric actin, termed G-actin because it is a globular protein, is approximately shaped like a rectangular prism with dimensions 5.5 x 5.5 x 3.5 nm (Figure 1A,B) (Dominguez & Holmes, 2011). It has four subdomains numbered according to their location along the polypeptide backbone: subdomains 1 (residues 1-32, 70-144, and 338-375), 2 (residues 33-69), 3 (residues 145-180 and 270-337) and 4 (residues 181-269) (Kabsch et al., 1990). Subdomains 1 and 2 form what is sometimes called

the small domain of actin, and subdomains 3 and 4 form the large domain (Kabsch et al., 1990). Between the two domains is a hinge region that connects subdomains 1 and 3 with a small cleft, and a large ATP-binding cleft between subdomains 2 and 4 (Figure 1) (Kabsch et al., 1990).

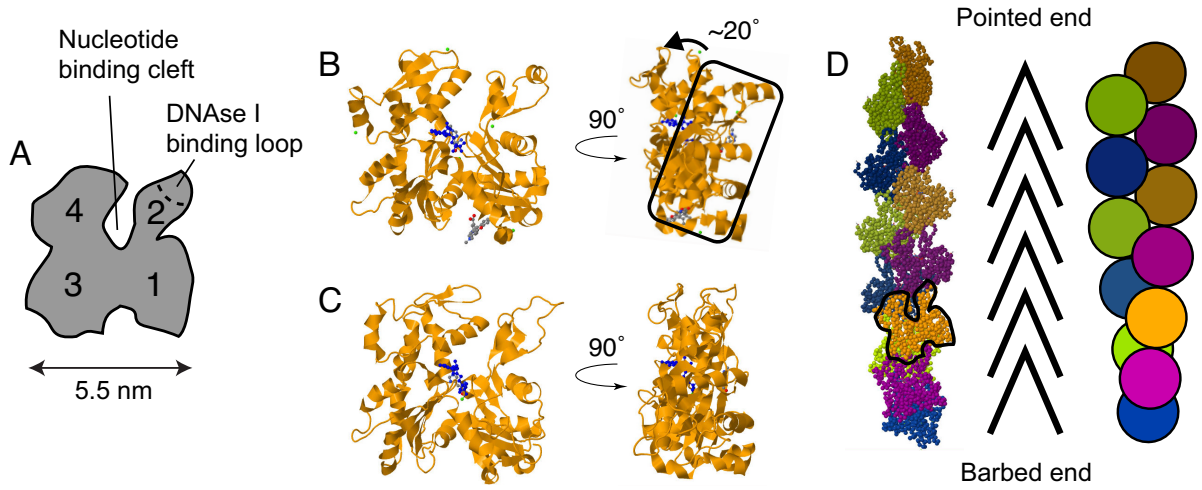

Figure 1. The structure of actin. (A) The G-actin monomer, with subdomains and the DNAse I binding loop in subdomain 2 labeled. The propeller twist present in G-actin can be thought of as a rotation around an axis running through subdomains 1 and 3, in the plane of the page, which pushes subdomain 2 into the page by ~20˚. (B) Ribbon diagram of the actin monomer in the ADP-G-actin state (upper; Image from the RCSB PDB (www.pdb.org) of PDB ID 1J6Z (Otterbein et al., 2001)). Actin is shown in orange, and ADP is shown in blue. The rotation of subdomains 1/2 (mostly due to changes in the conformation of subdomain 2) that transforms the monomer from its G-actin state to its F-actin state is indicated. (C) The actin monomer in the ADP-F-actin state (lower; PDB ID 2ZWH (Oda et al., 2009)). Note that the DNAse binding loop is extended, rather than helical as in B. Coloring is as in B. (D) A structure of the F-actin filament (left) shows how monomers assemble into a polar, double helical structure (PDB ID 3G37 (Murakami et al., 2010)). A single monomer is outlined in black. Cartoon representations of F-actin emphasize the barbed end and the pointed end (middle), or the two protofilaments (right).

Actin assembles into a filament with helical symmetry that can be described in two ways. It is a one-start, left-handed helix with a pitch of 5.9 nm and a twist per monomer of -166.6˚. Alternatively, it is a two-start, right-handed helix for which the two helices are termed protofilaments (although they do not form in isolation) with a pitch of 71.5 nm and a length between protofilament crossover points of 36 nm (Dominguez & Holmes, 2011).

The actin filament is structurally polar. One end is termed the “pointed end”, while the other is termed the “barbed end” (Figure 1C,D) (Pollard, 2007). This terminology results from the fact that the S1 fragment of myosin II binds F-actin in a stereospecific way, and actin decorated with myosin S1, used to study F-actin polarity in vivo, appears as a string of arrowheads pointing toward the pointed end (Figure 1D) (Holmes et al., 2003; Mooseker & Tilney, 1975).

Individual monomers inside the filament are oriented such that subdomains 1 and 3 lie toward the barbed end, and the smaller subdomains 2 and 4 lie toward the pointed end (Figure 1C) (Dominguez & Holmes, 2011; Pollard, 2007). A major difference in the conformation of the actin monomer between G-actin and F-actin is that the free G-actin monomer has a 20˚ propeller angle between subdomains 3/4 and subdomains 1/2, which can be described as a rotation of subdomains 1/2 around an axis that runs through the centers of mass of subdomains 1 and 3. Upon polymerization into F-actin, the monomer becomes nearly flat (Figure 1B) (Dominguez & Holmes, 2011). Lateral contacts holding the two protofilaments of F-actin together occur between a hydrophobic plug from subdomain 3 interacting with subdomain 2 of one monomer in the second protofilament, as well as between several residues in subdomain 4 interacting with subdomains 1 and 3 of the adjacent monomer in the second protofilament (Dominguez & Holmes, 2011; Fujii et al., 2010; Oda et al., 2009). This is possible because the protofilaments are staggered relative to each other by about 2.75 nm (Dominguez & Holmes, 2011). Within protofilaments, significant and stable longitudinal contacts between adjacent monomers are made through the one interface between subdomain 3 of one monomer and subdomain 4 of the next, and an adjacent interface between subdomain 2 of one monomer and the small cleft at the pointed end of the hinge region between subdomains 1 and 3 of the next (Figure 2) (Fujii et al., 2010; Oda et al., 2009). The former interface is relatively invariant and forms the core longitudinal interaction that holds the protofilament together, while the latter interface involving subdomain 2, which occurs at a larger distance from the medial axis of the filament, varies significantly between actin filaments in different states and is modulated by the binding of regulatory proteins, bound nucleotide of the actin, or bound cations (Galkin et al., 2012; Kim et al., 1995; Muhlrad et al., 2004; Muhlrad et al., 2006; Oda & Maeda, 2010; Oztug Durer et al., 2010; Reisler & Egelman, 2007).

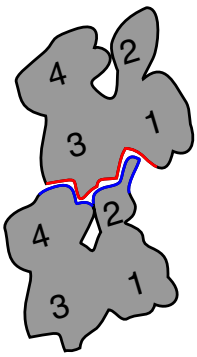

Figure 2. Longitudinal contacts between monomers in F-actin. Based on the Oda et al. F-actin structure (Oda et al., 2009). Details of the contacts are described in the text.

Biochemical properties of actin

Actin in the cell is highly dynamic, but the particular dynamics of any structure are highly regulated by ABPs, such that some actin filaments are selectively stabilized while others are quickly assembled and disassembled (Michelot & Drubin, 2011). In this section, we will discuss the dynamics of pure F-actin as measured in vitro, because such parameters are relevant to in vitro experiments involving actin polymerization in the presence of a limited set of ABPs, and because they serve as a baseline of actin functionality that is then modified by the action of ABPs in vivo.

The actin polymerization reaction is a simple binding equilibrium between a monomer and the end of a F-actin polymer (or a second monomer). The parameters associated with this reaction are explained in Figure 3, and their values under a variety of biochemical conditions are listed in Table 1.

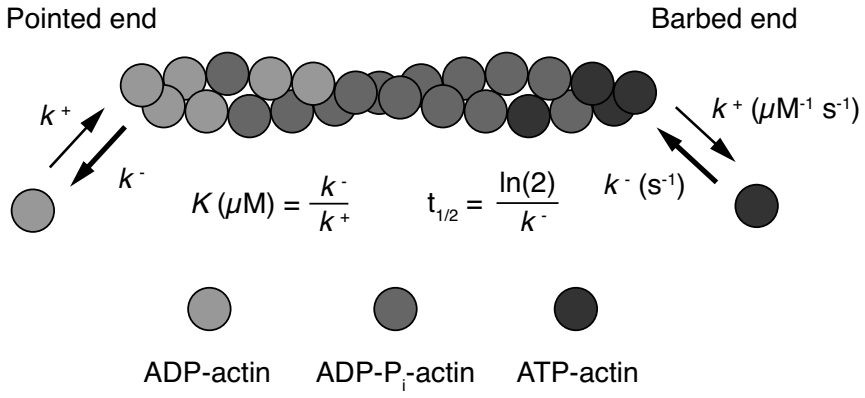

Figure 3: Actin assembly and disassembly. F-actin assembly is an equilibrium binding reaction between an actin monomer and the end of an actin filament. Actin assembly occurs with the second-order rate constant k^+, with units of $\mu M^{-1}s^{-1}$, while disassembly occurs with the first-order rate constant k^-, with units of s^{-1}. The ratio of these two rate constants is the dissociation constant for the equilibrium binding reaction, K, also called the critical concentration at the filament end in question. It has units of μM^{-1}. The critical concentration depends only on the state of the actin monomers (bound to ATP, ADP-P_i, or ADP), not on the end of the polymer at which binding happens. The rate constants, however, depend on both the end of the polymer and the nucleotide state of the monomers (Table 1). For the first-order rate constant, a half-time $t_{1/2}$ (also called a half-life in the context of radioactive decay) can be calculated. First-order kinetics also apply to the hydrolysis of ATP and release of phosphate from F-actin (Fujiwara et al., 2007). Here, the changing nucleotide state of monomers within an actin filament are shown as different shades of gray. The weight of the association/dissociation reaction arrows, with ATP-actin assembling at the barbed and ADP-actin disassembling at the pointed end, is one of treadmilling, which occurs when the overall actin monomer concentration is between the critical concentration of ATP-actin and the critical concentration of ADP-actin.

Actin polymerization requires the presence of cations, and although actin can polymerize in the absence of nucleotide (De La Cruz et al., 2000), ATP or ADP is necessary to maintain the stability of the protein buffer and hydrolysis of the bound nucleotide modulates the biochemical parameters of the polymerization reaction. The nature of the bound cations further modulates the interaction of actin with nucleotide as well as its polymerization kinetics (Blanchoin & Pollard, 2002; Carlier et al., 1986; Pollard & Borisy, 2003; Pollard & Cooper, 1986).

Table 1: Biochemical parameters for actin polymerization. After highly unfavorable spontaneous nucleation, actin polymerizes with different kinetics at the barbed and pointed ends. The rates of monomer association and dissociation also depend on the nucleotide state of the actin, which evolves from ATP-bound, via fast hydrolysis to ADP-P_i-bound, via somewhat slower phosphate release to ADP-bound.

Biochemical parameter	Value and units	Reference
K_d, G-actin monomer binding G-actin monomer or dimer (during nucleation)	~10^5 μM	(Pollard & Cooper, 1986)
k^+, Mg-ATP-actin, barbed end	11.6 $\mu M^{-1}s^{-1}$	(Fujiwara et al., 2007)
k^-, Mg-ATP-actin, barbed end	1.4 s^{-1}	(Fujiwara et al., 2007)
K, Mg-ATP-actin, barbed end	0.12 μM	(Fujiwara et al., 2007)
k^+, Mg-ATP-actin, pointed end	1.3 $\mu M^{-1}s^{-1}$	(Fujiwara et al., 2007)
k^-, Mg-ATP-actin, pointed end	0.8 s^{-1}	(Fujiwara et al., 2007)
K, Mg-ATP-actin, pointed end	By detailed balance, equal to K, Mg-ATP-actin, barbed end	(Fujiwara et al., 2007)
k^+, Mg-ADP-actin, barbed end	2.9 $\mu M^{-1}s^{-1}$	(Fujiwara et al., 2007)
k^-, Mg-ADP-actin, barbed end	5.4 s^{-1}	(Fujiwara et al., 2007)
K, Mg-ADP-actin, barbed end	1.8 μM	(Fujiwara et al., 2007)
k^+, Mg-ADP-actin, pointed end	0.09 $\mu M^{-1}s^{-1}$	(Fujiwara et al., 2007)
k^-, Mg-ADP-actin, pointed end	0.25 s^{-1}	(Fujiwara et al., 2007)
K, Mg-ADP-actin, pointed end	By detailed balance, equal to K, Mg-ADP-actin, barbed end	(Fujiwara et al., 2007)
First-order rate constant for ATP hydrolysis by Mg-ATP-F-actin	0.35 s^{-1} ($t_{1/2}$: 2 s) 0.30 s^{-1} ($t_{1/2}$: 2.3 s) 0.07 s^{-1} ($t_{1/2}$: 10 s)	(Pollard & Borisy, 2003) (Blanchoin & Pollard, 2002) (Pollard & Weeds, 1984)
First-order rate constant for ATP hydrolysis by Ca-ATP-F-actin	0.05 s^{-1} ($t_{1/2}$: 14 s) 0.02 s^{-1} ($t_{1/2}$: 35 s) 0.08 s^{-1} ($t_{1/2}$: 9 s)	(Blanchoin & Pollard, 2002) (Carlier et al., 1986) (Pollard & Weeds, 1984)
First-order rate constant for P_i release from Mg-F-actin interior	5.5 x 10^{-3} s^{-1} ($t_{1/2}$: 126 s) 2.0 x 10^{-3} s^{-1} ($t_{1/2}$: 350 s) 7 x 10^{-3} s^{-1} ($t_{1/2}$: 102 s) 2.0 x 10^{-3} s^{-1} ($t_{1/2}$: 350 s)	(Carlier et al., 1986) (Melki et al., 1996) (Jegou et al., 2011) (Pollard & Borisy, 2003)
First-order rate constant for P_i release from Ca-F-actin	1.4-2.5 x 10^{-3} s^{-1} ($t_{1/2}$: 277-500 s)	(Carlier et al., 1986)

Actin has binding sites for both monovalent cations and divalent cations (Carlier et al., 1986; Carlier et al., 1986). In the presence of at least 50-100 mM K^+ and several mM Mg^{2+} (Pollard, 1986), G-actin monomers assemble F-actin. Actin also polymerizes in the presence of Ca^{2+}, but with a slower nucleation rate (Carlier et al., 1986; Pollard & Cooper, 1986). There are also differences in the interaction with nucleotide. Actin binds ATP more tightly in the presence of Ca^{2+}, but hydrolyzes it more slowly (Carlier et al., 1986). For these reasons, actin is stored in pH 8 buffer containing Ca^{2+}, small amounts of ATP, and no monovalent salt, to stably maintain it in

the monomeric state. To initialize polymerization, the stock is diluted into pH 7 buffer containing EGTA to chelate the Ca^{2+}, Mg^{2+} to replace it, and 50-100 mM K+ (Zuchero, 2007). In vivo, the dominant species is Mg-ATP-actin (Pollard et al., 2000).

G-actin is a weak ATPase, but the conformational changes associated with polymerization into F-actin increase its ATPase activity by several orders of magnitude (Saunders & Voth, 2011). Hydrolysis of the bound ATP occurs with first-order kinetics with a half time of two seconds (Pollard & Borisy, 2003). The subsequent release of inorganic phosphate (P_i) is a slower process that also follows first-order kinetics with a half time of about 360 seconds, such that the barbed end side of an actin filament contains mostly ADP-P_i-F-actin, while the pointed end of the filament is composed of ADP-actin (Melki et al., 1996). If the concentration of monomeric actin available for polymerization at the barbed end leads to a rate of polymerization that exceeds the rate of ATP hydrolysis, there may also be a short ATP-F-actin cap at the barbed end of the filament, as likely occurs in vivo (Koestler et al., 2009; Korn et al., 1987; Vavylonis et al., 2005). Although phosphate can re-bind actin if present in large, unphysiological concentrations in the buffer, ATP hydrolysis is irreversible (Carlier & Pantaloni, 1988; Carlier et al., 1988).

Due to the structural asymmetry and different conformational changes between the barbed and pointed ends, the rate constant for monomer addition (and dissociation) is always faster for the barbed end than for the pointed end even if the bound nucleotide (ATP, ADP-P_i, or no nucleotide) is uniform throughout the filament (Pollard, 2007; Pollard & Cooper, 1986). However, in the case of uniform bound nucleotide, all monomers in the actin filament are identical, so there is no thermodynamic difference between monomer addition to the barbed end and monomer addition to the pointed end. Therefore, the equilibrium constant for monomer dissociation, called the critical concentration, is the same at the two ends of the filament (Howard, 2001).

The critical concentration has units of μM and can be expressed as the ratio of the monomer dissociation rate constant to the monomer association rate constant (Figure 3). This implies that if the barbed end has a faster monomer association rate constant than the pointed end but the same critical concentration, it must also have a faster monomer dissociation rate constant. For conditions under which all actin monomers are bound to the same nucleotide, as would be the case for the polymerization of ADP-G-actin, the filament then grows at both ends if the G-actin concentration exceeds the critical concentration, shrinks at both ends if the G-actin concentration is less than the critical concentration, and undergoes random fluctuations in length at both ends when the G-actin concentration equals the critical concentration.

Under conditions in which the polymerizable species is ATP-G-actin, which can undergo hydrolysis upon assembly into F-actin, the two ends of the resulting filament no longer have the same bound nucleotide. ATP-actin has a significantly lower critical concentration than ADP-actin, creating a range of G-actin concentrations between the critical concentrations for ATP- and ADP-actin, in which net assembly happens at the barbed end and net disassembly happens at the pointed end (Bugyi & Carlier, 2010; Fujiwara et al., 2007; Pollard, 2007). This situation is termed treadmilling (Pollard, 2007; Pollard & Borisy, 2003).

The nucleotide state of the actin filament is thought to serve as an internal clock that differentiates newly formed actin from older parts of the actin filament. It has important consequences for the interaction of F-actin with other actin-binding proteins (Sablin et al., 2002). For example, nucleotide state is a very strong modulator of the binding affinity of F-actin for the actin depolymerizing factor (ADF)/cofilin family of ABPs, described in the next section (Blanchoin & Pollard, 1999; Pollard et al., 2000). The importance of ATP hydrolysis by actin to cellular function is illustrated by the fact that approximately half of the ATP hydrolyzed by cultured neurons is due to actin turnover (Melki et al., 1996).

The regulation of actin disassembly by ABPs

The dissociation of ADP-actin from the pointed end of a filament has been shown to occur in vitro at a rate of 0.25 s^{-1} (Table 1), which translates to a rate of actin disassembly of 41 nm/min (Fujiwara et al., 2007). However, in vivo, tracking of actin speckles in dynamic actin structures at steady state has revealed actin treadmilling velocities consistent with treadmilling rates of 1000 nm/min or more (Iwasa & Mullins, 2007; Ponti et al., 2004; Watanabe & Mitchison, 2002). This mismatch highlights the important role played by ABPs that help to disassemble F-actin in vivo.

The most extensively studied family of actin disassembly proteins is the ADF/cofilin family, which also contains the Acanthamoeba protein actophorin (Bamburg & Bernstein, 2008). ADF/cofilin binds ADP-F-actin (but not ATP-F-actin or ADP-P_i-F-actin (Blanchoin & Pollard, 1999; Pollard et al., 2000)), accelerates the release of phosphate from ADP-Pi-F-actin (Blanchoin & Pollard, 1999; Suarez et al., 2011), accelerates debranching and Arp2/3 unbinding (Chan et al., 2009), severs filaments (Maciver, 1998; Maciver et al., 1991; McCullough et al., 2011; Pavlov et al., 2007), and also participates in depolymerizing filaments (Brieher et al., 2006; Carlier et al., 1999; Kueh et al., 2008). Cofilin binding induces a drastically overtwisted state in F-actin, as will be discussed in a later section (Galkin et al., 2011; McGough et al., 1997). This state has altered flexibility (Table 4) and is believed to play a role in cofilin's filament severing mechanism (McCullough et al., 2008; McCullough et al., 2011). Cofilin proteins have recently been shown to cooperate with other ABPs to more efficiently disassemble actin networks – coronin and Aip1 (Brieher et al., 2006; Kueh et al., 2008).

As yet another form of control on actin assembly and disassembly, ADF/cofilin proteins are antagonized by the action of certain isoforms of tropomyosin, which wrap around F-actin and prevent cofilin binding to selectively stabilize certain populations of filaments against both spontaneous and induced disassembly or severing (Bugyi & Carlier, 2010; Kuhn & Bamburg, 2008).

Actin nucleation

The assembly of actin monomers into filaments is, much like disassembly, controlled by ABPs in the cell (Pollard, 2007; Welch & Mullins, 2002). However, before discussing the details of how certain ABPs promote F-actin assembly, it is instructive to first consider the spontaneous initiation of assembly.

A solution of pure G-actin at a concentration that exceeds the critical concentration, in the presence of Mg^{2+} and K^{+} cations, will eventually polymerize into F-actin until the concentration of G-actin reaches the critical concentration of the barbed end and polymerization, once initiated, is fast. However, the initiation of polymerization is kinetically unfavorable because actin dimers are not stable, and often dissociate before they encounter a third monomer. The smallest oligomer that elongates as fast as longer polymers is an actin trimer (Cooper et al., 1983; Pollard, 1986; Sept & McCammon, 2001). Compared to actin filament elongation, initiation of new filaments, termed nucleation, is very slow. Once trimeric nuclei do form by chance, a process that proceeds faster at higher actin concentration, fast polymerization from barbed ends can proceed (Pollard, 1986; Pollard, 1986; Pollard & Cooper, 1986). This asymmetry between slow nucleation and fast elongation is a central feature of actin assembly, allowing the formation of actin-based structures to happen very quickly, but disfavoring unregulated polymerization (Campellone & Welch, 2010; Welch & Mullins, 2002). In vitro, it gives rise to a characteristic sigmoidal polymerization curve with a slow lag phase during which nucleation happens, followed by very fast polymerization until the monomer concentration drops to near the critical concentration (Pollard, 1983).

In vivo, the control of actin nucleation is enhanced by the fact that almost the entire cytoplasmic pool of monomeric actin is bound to profilin, a small protein that binds the barbed end side of G-actin, in the small cleft/hinge region between subdomains 1 and 3 (Dominguez & Holmes, 2011). Profilin-bound actin cannot associate to form nuclei, but can add to growing barbed ends at the same or a slightly lower rate than free G-actin (Pollard et al., 2000). The speed of actin polymerization is maintained because profilin quickly dissociates from the barbed end after the newly added monomer changes conformation from G-actin to F-actin (Pring et al., 1992). Profilin-actin is also competent for use by actin nucleators, which are the regulatory complexes that are responsible for creating actin filaments de novo in the cell, or can be captured by nucleation-promoting factors (NPFs) (Campellone & Welch, 2010).

Actin nucleators are a set of ABPs that bind several G-actin monomers, stabilizing oligomers, usually dimers or trimers, in a conformation that is primed for filament elongation, thus acting as catalysts for the normally filament nucleation process described above (Campellone & Welch, 2010). The first actin nucleator discovered is the Arp2/3 complex, which is described in the next section. Subsequently, a diverse and growing collection of actin nucleators have been discovered and characterized to varying degrees (Campellone & Welch, 2010; Dominguez, 2009; Firat-Karalar & Welch, 2011). For example, formins are an important class of relatively well-characterized nucleators that dimerize and nucleate straight actin filaments (Goode & Eck, 2007; Pollard, 2007). Their ring-like dimer of formin homology 2 (FH2) domains remains attached to the barbed end as subsequent actin monomers are added, producing forces in the range of ~1 pN (Kovar & Pollard, 2004). They have also been shown to rotate, tracking the helical path of the actin filament's protofilaments (Mizuno et al., 2011), but may slip under high torques (Kovar & Pollard, 2004). Several actin nucleators, such as Spire (Quinlan et al., 2005), JMY (Zuchero et al., 2009), and cordon-bleu, consist of tandem Wiskott-Aldrich syndrome protein homology 2 (WH2) domains, which bind individual actin monomers, connected by linkers (Campellone & Welch, 2010; Dominguez, 2009; Firat-Karalar & Welch, 2011). They stabilize longitudinal (intra-protofilament) or lateral (inter-protofilament) contacts between actin monomers to form a

nucleus. Different nucleators are involved in the formation of different actin structures. For example, formins participate in the formation of long, thin cellular protrusions called filopodia, which consist of a bundle of straight actin filaments surrounded by a membrane tube (Mellor, 2010; Yang & Svitkina, 2011). Formins also nucleate filaments for contractile bundles called stress fibers (Hotulainen & Lappalainen, 2006), and the contractile actin ring in cytokinesis (Goode & Eck, 2007). On the other hand, JMY and the Arp2/3 complex (described in detail below) are involved in the assembly of the lamellipodium (Firat-Karalar & Welch, 2011; Zuchero et al., 2009).

The Arp2/3 complex

Research over the last ten years has uncovered a multitude of actin nucleators (Campellone & Welch, 2010; Firat-Karalar & Welch, 2011), but the first one to be discovered and the best characterized is the Arp2/3 complex (Figure 4) (Machesky et al., 1994; Mullins et al., 1998; Welch et al., 1997). It is a seven-protein complex containing actin-related proteins (Arps) 2 and 3 and five accessory proteins named ARPC1-ARPC5 (or p40, p35, p21, p20, and p16 under older nomenclature) (Mullins & Pollard, 1999; Pollard, 2007). The nucleation mechanism is believed to rely on the large degree of homology between Arp2 and Arp3 and actin. In its active state, the Arp2/3 complex resembles a stabilized actin dimer (Goley & Welch, 2006; Rouiller et al., 2008). The addition of at least one actin monomer can create the trimer-like nucleus from which fast barbed end polymerization can occur (Goley & Welch, 2006; Pollard, 2007). There are three key elements that are necessary for full Arp2/3 complex activation: ATP binding, NPF binding, and binding to the side of a pre-existing actin filament (Goley & Welch, 2006; Pollard, 2007).

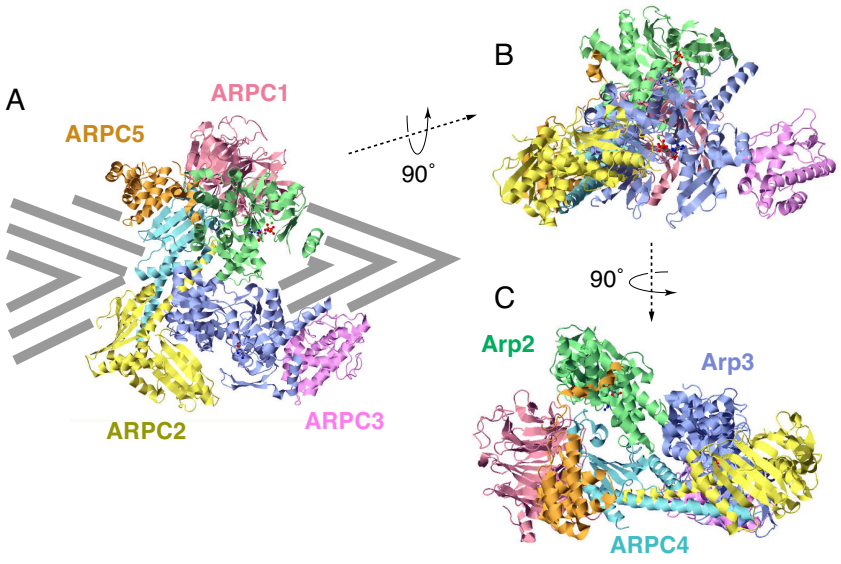

Figure 4. Structure of the inactive Arp2/3 complex. The subunits of the complex are labeled by color and proximity. (A) View of the face of the Arp2/3 complex that faces outward from the mother filament. The approximate location and polarity of the mother filament is indicated by gray arrowheads. (B) Side view of the complex. (C) View of the complex looking down the axis of the mother filament, toward the pointed end. Image from the RCSB PDB (www.pdb.org) of PDB ID 2P9I (Nolen & Pollard, 2007).

The mechanism of Arp2/3 complex activation is not fully understood, but many of the conditions and events that lead to activation have been discovered. In the inactive state of the Arp2/3 complex, Arp2 and Arp3 are positioned too far apart to mimic the conformation of monomers in the F-actin filament (Robinson et al., 2001). The complex is partially activated by the binding of ATP to Arp2 and Arp3 (discussed in more detail below), and of an NPF, a regulatory protein, to two sites on the Arp2/3 complex (Figure 5) (Goley et al., 2004; Goley & Welch, 2006; Padrick et al., 2011; Pollard, 2007; Ti et al., 2011). Many different NPFs participate in assembling actin structures, and each NPF is typically involved in only one or a few subcellular processes (Campellone & Welch, 2010). The most extensively studied family of NPFs, called Class I NPFs, are flexible molecules that contain several WH2 domains (often labeled W or V, for verprolin-homology), the central or connecting domain (labeled C), and the acidic domain (labeled A) (Campellone & Welch, 2010; Goley & Welch, 2006; Padrick & Rosen, 2010). Several examples of NPFs that fall into this class are the Wiskott-Aldrich Syndrome protein (WASP), which is involved in phagocytosis, N-WASP (called neural WASP, although it is not found exclusively in neurons), which is involved in endocytosis (Kaksonen et al., 2006), exocytosis and Golgi transport, and Scar/WAVE proteins, that are primarily responsible for activating the Arp2/3 complex in lamellipodial protrusions of spreading or migrating cells and are also involved in formation of the immunological synapse (Campellone & Welch, 2010; Goley & Welch, 2006). In all of these proteins, the C and A domains of the protein bind the Arp2/3 complex, while the WH2 domain binds an actin monomer that is probably delivered to the new barbed end for polymerization (Padrick & Rosen, 2010). Recent evidence shows that the Arp2/3 complex can bind two VCA domains simultaneously, suggesting that two NPF molecules and perhaps two actin monomers are involved in Arp2/3 activation (Figure 5, step 1) (Padrick et al., 2011; Padrick & Rosen, 2010; Ti et al., 2011).

Side-binding is necessary for branch nucleation to occur (Bailly et al., 2001), and it likely induces further conformational changes that bring Arp2 and Arp3 inside the Arp2/3 complex into position to form the pointed end of a new actin filament (Figure 5, steps 2a, 2b) (Goley et al., 2004; Pfaendtner et al., 2012; Rouiller et al., 2008). The relative roles that NPF binding and F-actin binding play in activating the Arp2/3 complex and nucleating branches are not clear because only the conformations of the inactive Arp2/3 complex and the final branch junction have been solved (Dalhaimer & Pollard, 2010; Nolen et al., 2004; Pfaendtner et al., 2012; Robinson et al., 2001; Rouiller et al., 2008). FRET-based experiments show that NPF binding in the presence of Mg-ATP on Arp2 and Arp3 leads to a conformational change in the complex (Goley et al., 2004), but this change is not sufficient for activation. Recent work revealing that the Arp2/3 complex can simultaneously bind the VCA domains of two NPF molecules also showed that one of the VCA binding sites lies on the face of the complex known to bind F-actin, suggesting that a particular sequence of VCA binding, unbinding, and filament binding may be necessary for actin branch nucleation (Padrick et al., 2011; Padrick & Rosen, 2010; Ti et al., 2011).

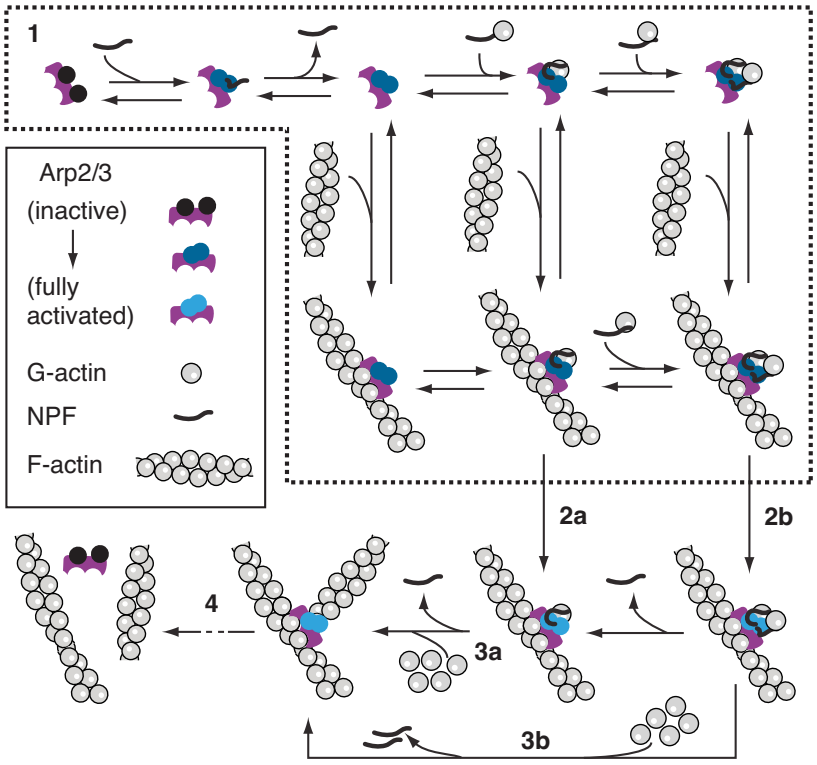

Figure 5. Arp2/3 branch nucleation occurs via a complex pathway (Beltzner & Pollard, 2008; Padrick et al., 2011; Pollard, 2007; Ti et al., 2011). (1) The Arp2/3 complex (violet and shades of blue), one or two molecules of nucleation-promoting factor (NPF, black curve), and one or two G-actin monomers (gray), assemble on a pre-existing F-actin "mother" filament (gray). Interaction with the NPF partially activates Arp2/3 (violet and dark blue). There are multiple possible pathways for assembly of this complex. (2a and 2b) The mother filament bound Arp2/3 is fully activated (violet and light blue) for nucleation of a new actin filament as a branch on the mother filament. (3a and 3b) This new filament then elongates, and the NPF dissociates soon after nucleation. (4) After several minutes, debranching occurs.

The second key element in Arp2/3 activation and branch nucleation is the binding of the Arp2/3 complex, probably together with bound NPF in the predominant pathway, to the side of a pre-existing actin filament (Bailly et al., 2001; Pollard, 2007; Rouiller et al., 2008). Once bound, the Arp2/3 complex nucleates the new actin filament, called the "daughter" filament, while remaining bound to the pre-existing "mother" filament. The resulting structure is a y-shaped branch, with a 70˚ angle between the mother and daughter filaments (Blanchoin et al., 2000; Mullins & Pollard, 1999), which in vitro, persists for several minutes (Mahaffy & Pollard, 2006). Through this activity, the Arp2/3 complex acts both as an actin nucleator and as a crosslinker, giving rise to dense and interconnected branched networks, also called dendritic networks (Pollard et al., 2000).

The branch nucleation process, in addition to moving Arp2 and Arp3 in the Arp2/3 complex closer to each other, also involves local changes in several monomers of the mother filament (Pfaendtner et al., 2012; Rouiller et al., 2008). The binding site of the Arp2/3 complex on the mother filament mostly tracks along one of the two protofilaments, including five monomers within both protofilaments and all subunits of the Arp2/3 complex, but most extensively involving contacts between ARPC1-4 and two monomers in the actin filament (Goley et al., 2010; Rouiller et al., 2008). A reconstruction of the branch from cryo-electron tomography and negative stain electron microscopy, combined with existing models of the actin filament, shows that a small kink in the mother filament's helix occurs at the branch site (Rouiller et al., 2008). The distortion causes the mother filament's two protofilaments to be subtly unwound at the branch site. Furthermore, the conformations of the two monomers making the most contacts with the Arp2/3 complex are altered, with their subdomains 2 released from making normal contacts with the adjacent monomer, and one of them adopting a G-actin like conformation while the other one is more severely distorted, its nucleotide binding cleft open. The branch structure is quite mechanically stable (Blanchoin et al., 2000), indicating that the disrupted contacts in the mother filament are stabilized by new contacts between F-actin and the Arp2/3 complex (Goley et al., 2010; Pfaendtner et al., 2012; Rouiller et al., 2008).

The kinetics of Arp2/3 nucleation have been studied extensively (Table 2) (Beltzner & Pollard, 2008), but questions remain because of the complex nature of a pathway involving many reacting species and the possibility that some steps, such as the binding and unbinding of the two activating NPFs, may have to happen in a particular sequence. What has been clearly established is that the binding of the Arp2/3 complex is slow relative to the binding of other proteins (Table 2), suggesting that it is far from being diffusion-limited (Beltzner & Pollard, 2008). This data supports the idea that the actin filament is not always in a state that can bind the Arp2/3 complex. In saturating conditions, it has also been well documented that there is a rate-limiting step that obeys first-order kinetics and is referred to simply as Arp2/3 activation (Table 2) (Pollard, 2007). This rate limiting step may involve a slow conformational change in the Arp2/3 complex, an NPF release step, or some combination of the two (Beltzner & Pollard, 2008; Padrick et al., 2011; Pollard, 2007; Ti et al., 2011).

Table 2. Biochemical parameters for branch nucleation. The reaction pathways of Arp2/3 branch nucleation, for which this table lists biochemical parameters, are described in Figure 5, above.

Parameter	Notes	Value	Reference
K_d, G-actin monomer binding G-actin monomer or dimer (spont. nucleation)	From kinetic modeling of pure actin polymerization	~10^5	(Pollard & Cooper, 1986)
K_d, Arp2/3 binding F-actin	Cosedimentation measurement	2	(Mullins et al., 1997)
K_d, Arp2/3 binding F-actin	Cosedimentation measurement	3-4	(Gournier et al., 2001)
K_d, Arp2/3 binding F-actin	*Sp.* Arp2/3, pyrene-labeled, binding isotherm	4.6	(Beltzner & Pollard, 2008)
K_d, Arp2/3 binding F-actin	*Sp.* Arp2/3, pyrene-labeled, k^-/k^+	6.7	
k^+, Arp2/3 association with F-actin	*Sp.* Arp2/3, pyrene-labeled	0.00015	
k^-, Arp2/3 dissociation from F-actin		0.001	
k^+, Arp2/3-$(VCA)_2$ association with F-actin	*Sp.* Arp2/3, pyrene-labeled, with 3 µM GST (dimerized) *Sp.* WASp VCA	0.00015	(Beltzner & Pollard, 2008)
k^-, Arp2/3-$(VCA)_2$ dissociation from F-actin		0.0034	
K_d, VCA binding Arp2/3	Rhodamine-labeled *Sp.* Wsp1 VCA	0.18	(Beltzner & Pollard, 2008)
K_d, VCA binding Arp2/3	Human WASP VCA, competition with labeled WASP VCA	0.9	(Marchand et al., 2001)
K_d, CA binding Arp2/3 high affinity site	*Sp.* Arp2/3 complex, isothermal titration calorimetry	0.13	(Ti et al., 2011)
K_d, CA binding Arp2/3 low affinity site		1.6	
K_d, CA binding Arp2/3 high affinity site	Bovine Arp2/3 complex, isothermal titration calorimetry	0.1	(Ti et al., 2011)
K_d, CA binding Arp2/3 low affinity site		10.1	
k^-, CA dissoc. from Arp2/3	*Sp.* Arp2/3 complex, rhodamine-labeled *Sp.* Wsp1 CA	28	(Ti et al., 2011)
k^-, CA dissoc. from Arp2/3-F-actin		22	
K_d, VCA-G-actin binding Arp2/3	Rhodamine-labeled *Sp.* Wsp1 VCA	0.1	(Beltzner & Pollard, 2008)
K_d, VCA binding G-actin	Human WASP VCA, competition with labeled WASP VCA, skeletal muscle actin	0.6	(Marchand et al., 2001)
K_d, VCA binding G-actin	Oregon green labeled skeletal muscle actin, rhodamine-labeled *Sp.* Wsp1 VCA	0.015	(Beltzner & Pollard, 2008)
k^+, VCA binding G-actin		29.3	
k^-, Arp2/3-VCA binding G-actin		0.44	
K_d, Arp2/3-VCA binding G-actin		0.029	
k^+, Arp2/3-VCA binding G-actin		15.2	
k^-, Arp2/3-VCA binding G-actin		0.44	
k^{act} activation rate (first order)	Simulation with other measured parameters	0.15	(Beltzner & Pollard, 2008)
Debranching rate, ADP-actin (s^{-1})	Microscopy of branches, estimated accounting for adhesion to cover slip surface	~0.2	(Mahaffy & Pollard, 2006)
Debranching rate, ADP-P_i-actin (s^{-1})		~0.04	

K_d: dissociation (dissoc.) equilibrium constant, has units of µM; Abbpreviation: spontaneous (spont.)
k^+: second-order rate constant for association, shown with units of $\mu M^{-1}\ s^{-1}$
k^-: first-order rate constant for dissociation, shown with units of s^{-1}
k^{act}: first-order rate constant for dissociation, shown with units of s^{-1}
Sp.: Schizozaccharomyces pombe

Like actin, Arp2 and Arp3 bind ATP. However, the role of ATP hydrolysis in regulating branch nucleation is less clear than it is in actin polymerization dynamics because the effects of hydrolysis of ATP bound to Arp2, Arp3, and the two actin filaments in the branch must be distinguished. ATP binding on Arp2 and Arp3 is necessary for branch nucleation (Dayel et al., 2001), enhances the affinity of NPFs for the Arp2/3 complex (Dayel et al., 2001; Goley et al., 2004; Kovar, 2006; Le Clainche et al., 2003) and induces a change in the conformation of the complex (Goley et al., 2004). However, the timing and necessity of ATP hydrolysis for branch nucleation and for subsequent branch dissociation, called "de-branching" (Figure 5, step 4), is not entirely resolved (Kovar, 2006). The results of in vitro pyrenyl-actin assembly assays with Acanthamoeba Arp2/3 using the nonhydrolyzable ATP analogue AMP-PNP indicated that ATP hydrolysis is necessary for branch nucleation, but that the binding of F-actin and NPF to the actin filament does not stimulate ATP hydrolysis (Dayel et al., 2001). Experiments with labeled azido-ATP crosslinked to bovine brain Arp3 or Arp2 and Arp3 indicated that hydrolysis occurs on Arp2 but not on Arp3 (Kovar, 2006; Le Clainche et al., 2003). ATP similarly crosslinked to Acanthamoeba actin corroborated the observation that hydrolysis occurs on Arp2 and showed that its timing coincides with branch nucleation (Dayel & Mullins, 2004; Kovar, 2006). In experiments that took an alternative approach with a S. cerevisiae hydrolysis-impaired Arp2 mutant, ATP hydrolysis by Arp2 was found to be unnecessary for branch nucleation, because the mutant's nucleation activity was normal despite its inability to hydrolyze ATP (Martin et al., 2006). This mutation and a similar mutation in Arp3 also caused defects in endocytic uptake in S. cerevisiae, which depends on branched actin nucleated by the Arp2/3 complex, suggesting that ATP hydrolysis on Arp3, although never directly observed, may also play a role in the in vivo function of Arp2/3 (Martin et al., 2006). The endocytic defect arose from a delay in branch dissociation, suggesting that ATP hydrolysis, while not being involved in branch nucleation, is necessary for efficient debranching (Martin et al., 2006), a fact that is difficult to reconcile with the timing of hydrolysis on Arp2 occurring concurrently or seconds after nucleation (Dayel & Mullins, 2004; Kovar, 2006).

There are similar controversies regarding the question of how branch nucleation and branch stability are regulated by ATP hydrolysis and phosphate release on the mother filament. This discussion will focus on the nucleotide state of the mother filament because the nucleotide state of the daughter filament has not been studied to the same extent. Early experiments investigating branch nucleation by the Arp2/3 complex showed a correlation between the lengths of the daughter filament and the barbed end side of the mother filament in y-branches (Pantaloni et al., 2000). This data suggested that the Arp2/3 complex binds to the barbed end of a growing mother filament to nucleate a branch. Conflicting evidence showed that new branches are nucleated from the sides of mother filaments (Blanchoin et al., 2000). The ensuing debate was resolved by the observation that branches are observed with much higher frequency on freshly polymerized sections of the mother filament near the barbed end, which at the time of nucleation, likely contain ATP-actin or ADP-P_i-actin (Ichetovkin et al., 2002).

Two models for this enhanced branching on new actin have been proposed. Under the first model, ATP-actin is a preferred substrate for nucleation, and branch stability is not modulated by nucleotide state (Ichetovkin et al., 2002). This model is based on evidence from microscopy of branches formed from pre-polymerized actin seeds bound to phalloidin, which inhibits phosphate

release and may also maintain some monomers in the ATP-bound state, AMP-PNP, to mimic ATP-actin, ADP-P_i-actin (obtained by incubating ADP-actin with 2 mM phosphate), and ADP-actin, which showed that more branches formed on AMP-PNP actin and phalloidin-stabilized actin than on any of the other types of mother filaments, and that ADP-P_i-actin behaves no differently from ADP-actin (Ichetovkin et al., 2002). The latter observation is probably due to a sub-saturating concentration of phosphate used in the experiment, resulting in mother filaments that remained mostly in the ADP state (Carlier & Pantaloni, 1988; Mahaffy & Pollard, 2006). Under the second model, nucleation by the Arp2/3 complex is independent of mother filament nucleotide state, but debranching occurs faster on ADP-actin than on ADP-P_i-actin or phalloidin-stabilized actin (Blanchoin et al., 2000; Mahaffy & Pollard, 2006). The second model is based on a comparison of branch nucleation rates in bulk solution as assayed by pyrenyl-actin polymerization, which showed that actin is nucleated at the same rate with and without saturating (25 mM) phosphate in solution, with microscopy-based assays of debranching which showed that the number of branches observed falls off with an approximately exponential dependence on time, but is stabilized by saturating phosphate (Mahaffy & Pollard, 2006). Although these two models are not directly compatible as stated, the differences in experimental conditions between the two studies, namely the fact that the experiments used to test the first model did not use saturating phosphate concentrations to create fully ADP-P_i-bound mother filaments, while the experiments used to test the second model did not measure branching on ATP-actin or one of its structural mimics, mean that it may be possible that their results do not contradict. ATP-actin may indeed be a more efficient substrate for branch nucleation, and the branches that are created would be more stable before the mother filament releases the cleaved phosphate, than after.

Dendritic actin networks

Under the currently accepted dendritic nucleation model, the activities of actin nucleation, polymerization, debranching and depolymerization described above combine to form a cycle that dynamically assembles a branched actin network at the leading edge of the lamellipodium of motile cells and quickly disassembles it toward the center of the cell (Insall & Machesky, 2009; Pollard et al., 2001; Pollard & Borisy, 2003). The lamellipodium is defined as the dense and highly dynamic section of flat cellular protrusions 1-4 μm from the leading edge (Burnette et al., 2011; Iwasa & Mullins, 2007; Ponti et al., 2004; Ridley, 2011). Behind the lamellipodium, and to some degree overlapping with it is the lamella, which contains a sparser and less dynamic population of actin filaments, but which adheres more strongly to the substrate and exhibits contractile activity (Burnette et al., 2011; Gardel et al., 2010; Ponti et al., 2004). Out of the lamellipodium emerge long, thin filopodia, which can be formed by filaments nucleated and protected from capping by formins, or by filaments nucleated by the Arp2/3 complex, which converge into a bundle and are protected from capping by post-nucleation binding of Ena/VASP proteins to their barbed ends (Mellor, 2010; Svitkina et al., 2003; Yang & Svitkina, 2011).

The lamellipodium has been the subject of intense study, and although the dendritic actin nucleation model as described applies most directly to lamellipodial actin dynamics, this model has relevance to many other cellular processes, such as endocytosis, phagocytosis, and intracellular motility, because Arp2/3 nucleation, albeit controlled by different NPFs, and

network disassembly are involved in all of those processes (Campellone & Welch, 2010; Goley & Welch, 2006; Kaksonen et al., 2006; Pollitt & Insall, 2009; Welch & Mullins, 2002).

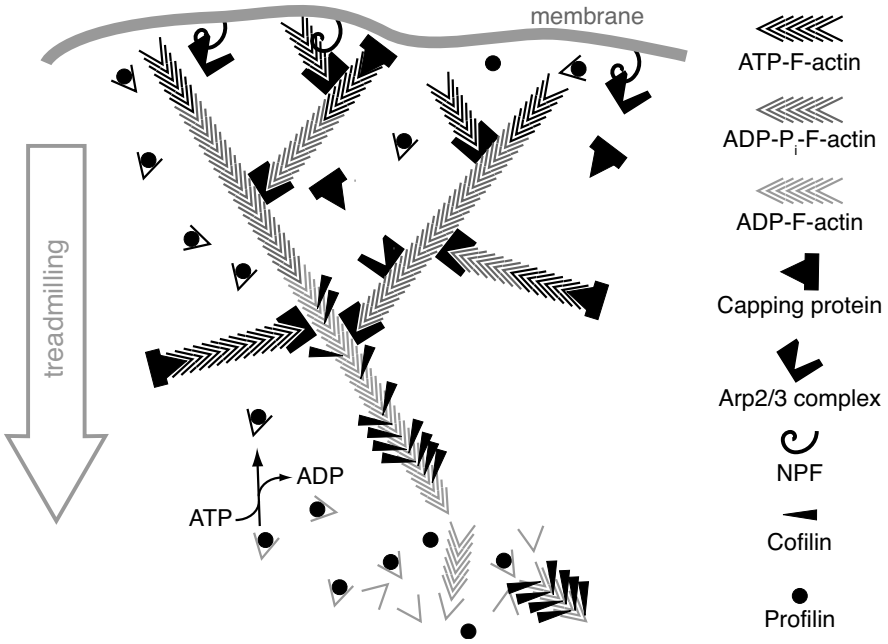

Figure 6. The dendritic nucleation model. The details of the model are described in the text, except the nucleotide exchange reaction shown in the lower left corner. Profilin catalyzes the exchange of ADP for ATP on G-actin.

Dendritic nucleation (Figure 6) (Pollard et al., 2000) is a model that helps to explain the important observation that actin networks are far more dynamic in vivo than actin filaments are in vitro (Fujiwara et al., 2007; Ponti et al., 2004; Watanabe & Mitchison, 2002). Besides the Arp2/3 complex, which speeds up actin nucleation, many other actin-binding proteins regulate other aspects of actin network assembly and disassembly. Their activities, characterized independently, form the basic elements of the dendritic nucleation model. The ADF/cofilin family of proteins accelerates disassembly as described above, and also accelerates debranching and Arp2/3 unbinding (Chan et al., 2009). Capping protein is a heterodimer that binds with nM affinity to the barbed end and dissociates with a half-life of 23 minutes (Cooper & Sept, 2008; Wear et al., 2003). Barbed end capping by capping protein limits filament length, which helps filaments in the network resist buckling (discussed below) (Howard, 2001; Mogilner & Oster, 1996; Pollard & Borisy, 2003), and funnels actin monomers from filament elongation to filament nucleation (Akin & Mullins, 2008; Carlier & Pantaloni, 1997). Its functions are essential to the formation of the lamellipodium (Mejillano et al., 2004). Profilin prevents monomeric actin from participating in spontaneous nucleation, but also accelerates the exchange of bound nucleotide on free monomers from ADP to ATP (Bugyi & Carlier, 2010).

The dendritic nucleation model also rests on the observation that branched actin networks grow near membranes, including the membrane at the leading edge of a cellular protrusion, and are oriented with barbed ends growing toward the membrane, forming an approximate angle of ± 35˚

with the overall direction of protrusion (Maly & Borisy, 2001; Pollard et al., 2000; Svitkina & Borisy, 1999; Verkhovsky et al., 2003). Although this angular distribution has been observed to change somewhat as a function of growth velocity (Koestler et al., 2008; Weichsel et al., 2012), it occurs with sufficient robustness to suggest a model of actin organization and dynamics in the lamellipodium that is highly consistent with the available biochemical data (Pollard et al., 2000; Pollard & Borisy, 2003). In this model, NPFs are activated at or near the leading edge (or otherwise protruding or propelled) membrane, consistent with what is known about the activation of NPFs by binding to membrane-bound regulatory proteins or lipids, such as the activation of N-WASP by the phospholipid $PI(4,5)P_2$ and the Rho family GTPase Cdc42 or the indirect activation and recruitment to the membrane of SCAR/WAVE by the GTPase Rac (Goley & Welch, 2006; Pollitt & Insall, 2009; Sukumvanich et al., 2004). This localized activation creates a narrow branching zone in close proximity to the leading edge where the Arp2/3 complex can bind active NPF and be activated in turn to nucleate new F-actin branches (Goley & Welch, 2006; Pollard, 2007).

As new filaments are created by the Arp2/3 complex, they grow with the addition of profilin-bound ATP-G-actin onto their barbed ends, and by growing, either push the membrane forward or, if the network is not sufficiently anchored, generate a force that pushes them back, leading to retrograde flow of the actin network (Mogilner & Oster, 1996; Mogilner & Oster, 2003; Ponti et al., 2004). Actin filaments keep growing until their barbed ends are bound by capping protein, which remains tightly bound for minutes, effectively stopping any monomer addition onto that barbed end (Wear et al., 2003). The combined action of the active Arp2/3 complex and capping protein, which, like Arp2/3, appears to bind actin close to the leading edge, although it does not require activation (Iwasa & Mullins, 2007; Pollard & Borisy, 2003), is a dense and branched network of actin filaments (Cameron et al., 2001; Svitkina & Borisy, 1999; Svitkina et al., 1997; Vinzenz et al., 2012). The importance of capping protein in shaping the architecture of the dendritic network is evident in depletion experiments, in which the lamellipodium effectively disappears, replaced by long, tangled bundles of actin filaments (Iwasa & Mullins, 2007).

The dynamic steady state of the lamellipodium, with most of its elements flowing toward the cell interior at a speed of 2.5 μm/min over approximately 1.4 μm, is maintained as the branched actin network nucleated at the leading edge is disassembled as it ages and moves toward the interior of the cell (Iwasa & Mullins, 2007; Pollard et al., 2001). As F-actin-bound ATP is very quickly hydrolyzed and phosphate is released, ADP-F-actin allows ADF/cofilin to bind (Bugyi & Carlier, 2010). Cofilin, together with more recently characterized disassembly factors such as coronin (Gandhi et al., 2009; Gandhi & Goode, 2008; Kueh et al., 2008; Lin et al., 2010), efficiently disassemble the dendritic network through a combination of accelerated phosphate release, accelerated debranching, severing, and overall filament destabilization (Chan et al., 2009; Kueh et al., 2008; McCullough et al., 2011; Suarez et al., 2011). Although F-actin may not have time to fully depolymerize, filament severing and the removal of Arp2/3 crosslinks releases small fragments that are free to diffuse away from the lamellipodium, eventually disassembling to rejoin the profilin-G-actin pool, where the nucleotide bound to the monomers can be replaced by ATP (Pollard et al., 2001; Pollard & Borisy, 2003). Thus, although the rate of individual filament treadmilling is relatively slow (Bugyi & Carlier, 2010), the network as a whole can be assembled and disassembled quickly.

One interesting feature of the dendritic actin networks in cells that is not entirely explained by the dendritic nucleation model is the high degree of orientation of filament barbed ends toward the membrane (Cameron et al., 2001; Svitkina & Borisy, 1999; Svitkina et al., 1997). It has been suggested that filaments growing toward the membrane may be prevented from being capped by steric interference between the membrane and the barbed end (Bear et al., 2002; Maly & Borisy, 2001), and that the side of the mother filament facing the membrane may be sterically favored for the binding of activated Arp2/3 complex that is tethered to the membrane via the NPF (Liu et al., 2010; Maly & Borisy, 2001; Svitkina & Borisy, 1999). Our work, described in Chapter 3 of this dissertation, has revealed a third mechanism that may contribute to the orientational order of the network (Risca et al., 2012). In this mechanism, force exerted by the membrane on filaments bends them, biasing branch nucleation to the convex side of bent filaments that faces the membrane.

Biophysical models of force generation by dendritic actin networks

The dendritic nucleation model and the decades of biochemistry and cell biology experiments that have contributed to it have been complemented by a series of biophysical models and biophysical experiments that have shed light on how dendritic actin networks produce the mechanical force that leads to protrusion of the plasma membrane or propulsion of other loads such as vesicles, bacteria, or beads (in reconstitution experiments).

The Brownian ratchet model explains how actin filament polymerization converts the free energy of monomer binding to the barbed end into a pushing force (Mogilner & Oster, 1996; Mogilner & Oster, 2003; Mogilner & Oster, 2003; Peskin et al., 1993). In the simplest case, the end of a filament abuts a fluctuating mechanical load, such as the cell membrane. Whenever the Brownian fluctuations of the load open a space large enough to fit a new monomer onto the end of the filament, a monomer diffuses in and increases the length of the filament, preventing the load's average position from returning to its previous value. The average position of the load is thus ratcheted forward, hence the name "Brownian ratchet". This model has been tested for bundles of straight actin filaments with an optical trapping experiment and shown to agree with the experimental results, within error (Footer et al., 2007). It has also been shown that load fluctuations can drive dendritic actin based motility (Shaevitz & Fletcher, 2007). The Brownian ratchet model has been extended to incorporate more realistic filament and load geometries and mechanics, including the elasticity of filaments at an angle to the load and their fluctuations, which could also serve to create space for monomer insertion when the load does not fluctuate (Mogilner & Oster, 1996), and the force balance between filaments that push against the load and those that are tethered to the load, creating friction that opposes forward motion (Mogilner & Oster, 2003). The elastic Brownian ratchet model predicts that an angle 48˚, close to the observed ~35˚ angle of the filaments to the growth direction, is optimal for force generation (Mogilner & Oster, 1996). The tethered elastic Brownian ratchet model further predicts an increase in actin network velocity with increased network density, and at constant nucleation rate, that the density of the network increases with the load, but the number of pushing filaments is constant (Mogilner & Oster, 2003). The predicted force-velocity curve for dendritic actin networks under these Brownian ratchet models is biphasic and concave up, with the speed dropping off quickly for low opposing forces, then changing to a regime where the speed drops off more slowly until eventual stall (Mogilner & Oster, 2003). These predictions are consistent

with the results of experiments that measure actin network growth at low forces, using flexible pipettes (Marcy et al., 2004) and viscous drag (McGrath et al., 2003) to oppose actin network growth.

Other experiments using atomic force microscopy (AFM) have probed the force-velocity of actin networks at high forces, up to the point of network stall (Parekh et al., 2005; Prass et al., 2006). In both cases, the force-velocity exhibited a regime in which the velocity was force-independent before eventual stall. This observation is consistent with another model of actin network growth called the autocatalytic model, which, unlike the tethered elastic Brownian ratchet model, assumes that the number of pushing filaments can be increased in response to increasing loads. It relies on a membrane-adjacent zone in which new actin filaments are generated in proportion to the amount of actin in the zone. As the load increases and the growth velocity decreases, filaments spend more time in the branching zone, creating more new filaments and reducing the overall force per filament. At steady state, this process gives rise to a load-independent growth velocity as observed in the experiments. It is possible that the autocatalytic model and the tethered Brownian ratchet model are compatible, if the nucleation rate and the network architecture depend on the growth velocity, such that different force-velocity curves may apply to different network architectures or force regimes (Weichsel & Schwarz, 2010).

Much progress has been made in understanding the whole-network response of branched actin to changing mechanical loads, but many questions remain about the mechanisms by which protein-protein interactions and the mechanical properties of single filaments work together to give rise to the collective behavior of dendritic networks (Fletcher & Mullins, 2010). Additionally, there are also still many outstanding questions about the interplay between different types of cytoskeletal structures, some of which, like filopodia, the lamellar network, and stress fibers and actin arcs, connect to or emerge from dendritic actin networks (Burnette et al., 2011; Michelot & Drubin, 2011; Ridley, 2011).

Mechanics and variable structure of F-actin

The mechanical properties and detailed structure of individual actin filaments have been studied for decades (Hanson, 1967; Millman et al., 1967; Oosawa, 1980), and yet new discoveries about both are still being made, revealing the details of the plastic, highly regulated, and functionally important structure of F-actin and its interaction with ABPs (Fujii et al., 2010; Galkin et al., 2012; Galkin et al., 2010; Kueh & Mitchison, 2009; Oda & Maeda, 2010; Reisler & Egelman, 2007).

Physical properties of the actin filament

Not surprisingly for a major component of muscle fibers, stress fibers, and other contractile and structural elements of the cell, actin is very stiff under stretching, with a spring constant 43.7 pN/nm (Kojima et al., 1994) or 34.5 pN/nm (Liu & Pollack, 2002) for phalloidin-Mg-F-actin, and 65.3 pN/nm for the same type of actin further stabilized by tropomyosin (Kojima et al., 1994). It also has a very large tensile strength, 600 pN, which decreases to about 320 pN if a 10 μm phalloidin-Mg-F-actin filament is twisted by 90˚ in either direction (Tsuda et al., 1996). Actin is much more fragile when subjected to strong bending forces, as examined by pulling on a

filament that has been tied into a knot. The filament broke at a force of only ~0.9 pN when the radius of curvature reached 180 nm (Arai et al., 1999).

The bending rigidity of F-actin puts it into a class of polymers termed semiflexible filaments, which lies between flexible polymers (MacKintosh et al., 1995), for which bending rigidity is largely immaterial, leaving polymer shape to be driven by the maximization of entropy toward a collapsed globule, and rigid rods, for which bending fluctuations are negligible and bending rigidity determines the mostly straight, rod-like shape of the polymer in the absence of non-thermal forces (Doi & Edwards, 1988; Howard, 2001). Although there are many models that have been used to describe polymers, the one most often and successfully applied to semiflexible polymers is the worm-like chain (WLC) model. This model treats the polymer as a continuous deformable rod with a given bending rigidity *EI*. This rigidity is stated as the product of *E*, the Young's modulus of the material constituting the rod, and *I*, the rod's moment of inertia, and has units of N m^2 (Howard, 2001). The rigidity determines the WLC polymer's bending energy, E_{bending}:

$$E_{bending} = \frac{EI}{2}\int_0^L \left(\frac{d\theta}{ds} - \frac{d\theta_0}{ds}\right)^2 ds \qquad \text{Equation 1}$$

where $\theta(s)$ is the tangent angle to the polymer curve as a function of arc length s, and $\theta_0(s)$ denotes the same parameter for the polymer's relaxed shape in the absence of any thermal fluctuations (Gittes et al., 1993). Another way to express $d\theta/ds$, the change in angle over the change in arc length, is as the curvature of the filament, κ. Effectively, the bending energy of a WLC is spring-like, where the spring extension parameter is the curvature and the spring constant is the bending rigidity *EI*.

Another intuitively useful measure of a WLC's bending rigidity is L_p, the persistence length, which describes the characteristic length over which the polymer "forgets" its initial direction because of random thermal fluctuations that bend the filament. To define it, we consider the tangent angle at some initial point on the polymer, and the tangent angle at a distance *s* away along the polymer. For a WLC, the average cosine of the difference of these two angles decays exponentially over a characteristic distance of L_p:

$$\left\langle \cos\left[\theta(s) - \theta(0)\right]\right\rangle = \exp\left(-\frac{s}{2L_p}\right) \qquad \text{Equation 2}$$

in two dimensions (where the curve has a single tangent angle) or

$$\left\langle \cos\left[\Delta\theta_{3D}(s)\right]\right\rangle = \exp\left(-\frac{s}{L_p}\right) \qquad \text{Equation 3}$$

in three dimensions, where the polymer has two degrees of freedom for fluctuations of the tangent angle, so the de-correlation of the total difference in angle occurs over a shorter distance (Howard, 2001). The relationship between L_p and *EI* is:

$$EI = k_B T L_p, \qquad \text{Equation 4}$$

where k_B is Boltzmann's constant and T is the ambient temperature (Gittes et al., 1993; Howard, 2001).

The concept of the persistence length allows us to more precisely define the three classes of polymers described above. Flexible polymers have a total contour length L that is much greater than their persistence length ($L >> L_p$), semiflexible polymers have a contour length on the order of their L_p ($L \sim L_p$), and rigid polymers have a contour length much smaller than their L_p ($L << L_p$). Therefore, the same polymer can move from one class to another simply by changing in length. A related concept, the Kuhn length, which defines the length of polymer that can be treated as a segment whose overall tangent angle is independent from that of the adjacent segment, is equal to $2L_p$ (Howard, 2001). Such a segment is the building model of the freely jointed chain model, which gives good results in modeling flexible polymers.

The persistence length of F-actin is on the order of 10 μm (Table 3), which is comparable to the contour lengths of actin filaments inside the cell (Alberts et al., 2007). As illustrated in Table 3, there is no single persistence length of F-actin. It depends markedly on the nucleotide state (with BeF_3^--ADP-F-actin used as a mimic of the ADP-P_i-F-actin state), with ADP-P_i-F-actin and phalloidin-ADP-F-actin being approximately twice as stiff as ADP-F-actin (Isambert et al., 1995). The larger stiffness of freshly polymerized F-actin may contribute to the ability of dendritic actin networks near the load to resist compression. It may also be functionally important that ABPs modify the persistence length of ADP-F-actin: the stabilizing ABP tropomyosin doubles it (Isambert et al., 1995), while the severing ABP cofilin reduces it by a factor of ~5 (Table 4) (McCullough et al., 2008). It has also been reported that the flexibility of F-actin, as measured by Forster resonance energy transfer (FRET), can be increased by the formin homology 2 (FH2) domain dimer of a formin (a different type of actin nucleator) bound to the barbed end, but it is not yet clear whether the observed flexibility is due to changes in bending rigidity, torsional rigidity (discussed below), or other changes in F-actin conformation (Bugyi et al., 2006).

The persistence length, and to an even larger degree, the contour length of actin filaments, together determine the filaments' ability to resist and support compressive mechanical loads, such as those from membrane tension or external forces acting on dendritic actin networks. For an actin filament that is rigidly coupled at its base into a large network, has an end that is normal to the load and is free to translate and rotate, and feels a purely axial force (Figure F0240), the force at which it buckles $F_{buckling}$ (Howard, 2001) is:

$$F_{buckling} = \frac{\pi^2}{4}\frac{EI}{L^2} = \frac{\pi^2}{4}\frac{k_B T L_p}{L^2}. \qquad \text{Equation 5}$$

Table 3: Bending rigidity of F-actin varies as a function of the filament's nucleotide state and stabilization by the drug phalloidin.

Biochemical condition	**Msrmt. method**	**Bending rigidity (x 10^{-26} N m^2)**	**Bending persistence length (μm)**	**Reference**
Rabbit skeletal muscle Ca-ADP-F-actin labeled with TMR on lysines.	A	(4.1-4.5)	10-11	(Isambert et al., 1995)
Rabbit skeletal muscle Mg-ADP-F-actin labeled with TMR on lysines.	A	(4)	9	(Isambert et al., 1995)
Rabbit skeletal muscle Mg-ADP-BeF_3^--F-actin labeled with TMR on lysines.	A	(5.3-5.5)	13-13.5	(Isambert et al., 1995)
Rabbit skeletal muscle Mg-ADP-P_i-F-actin labeled with TMR on lysines.	A	(4.3-4.5)	10.5-11	(Isambert et al., 1995)
Rabbit skeletal muscle Ca-F-actin stabilized with TMR-phalloidin.	B	5.8 ± 0.1	(14)	(Yasuda et al., 1996)
Rabbit skeletal muscle Ca-F-actin labeled with TMR on lysines stabilized with phalloidin.	A	(6.4-6.8)	15.5-16.5	(Isambert et al., 1995)
Rabbit skeletal muscle Mg-F-actin stabilized with TMR-phalloidin.	C	7.29 ± 0.44	17.7 ± 1.1	(Gittes et al., 1993)
Chicken skeletal muscle Mg-F-actin stabilized with TMR-phalloidin.	B	(6.9)	16.7± 0.2	(Ott et al., 1993)
Rabbit skeletal muscle Mg-F-actin stabilized with TMR-phalloidin.	A	(7.0)	17	(Isambert et al., 1995)
Rabbit skeletal muscle Mg-ADP-F-actin labeled with TMR on lysines and stabilized with phalloidin.	A	(7.6-7.8)	18.5-19	(Isambert et al., 1995)
Rabbit skeletal muscle Mg-F-actin stabilized with TMR-phalloidin.	B	6.2 ± 0.1	(15)	(Yasuda et al., 1996)
Chicken skeletal muscle Mg-F-actin stabilized with TRITC-phalloidin.	D	~1.5	(3.6)	(Dupuis et al., 1997)
Rabbit skeletal muscle Mg-F-actin stabilized with TMR-phalloidin.	D (knot)	5.5 ± 0.2	(13.4)	(Arai et al., 1999)
Rabbit skeletal muscle Mg-F-actin stabilized with TMR-phalloidin.	E	(3.6)	8.75	(Liu & Pollack, 2002)
Rabbit skeletal muscle Mg-F-actin stabilized with Alexa 488-phalloidin, or Alexa 488 – labeled actin stabilized with unlabeled phalloidin.	F	(7.0)	17.8 ± 2.0	(Brangwynne et al., 2007)
Rabbit skeletal muscle biotin-Mg-ADP-F-actin stabilized with TMR-phalloidin.	D	7.1± 0.8	17 ± 2	(van Mameren et al., 2009)

Values in parentheses are calculated using Equation 4.

Measurement (msrmt.) methods:

A: Microscopy and calculation of cosine correlation length and average transverse fluctuations.

B: Microscopy and fit to cosine correlation function.

C: Microscopy and Fourier mode analysis.

D: Filament bending in two-beam optical trap.

E: Filament stretching by microfabricated cantilevers.

F: Microscopy, polynomial fit with Gaussian profile refinement, and Fourier mode analysis.

Table 4: Bending rigidity of F-actin decorated with ABPs is modulated by structural changes in the filament that occur upon ABP binding.

Biochemical condition	**Msrmt. method**	**Bending rigidity (x 10^{-26} N m^2)**	**Bending L_p (μm)**	**Reference**
Rabbit skeletal muscle Mg-ADP-F-actin labeled with TMR on lysines.	A	(4)	9	(Isambert et al., 1995)
Rhodamine-labeled rabbit skeletal muscle and unlabeled chicken skeletal muscle Mg-ADP-F-actin.	B	(3.7)	9.1 ± 0.5	(Greenberg et al., 2008)
Rabbit skeletal muscle Mg-ADP-F-actin labeled with Alexa 488 on lysines.	C	(4.0)	9.8 ± 0.1	(McCullough et al., 2008)
Rabbit skeletal muscle Mg-ADP-F-actin stabilized and labeled with rhodamine-phalloidin.	D	6.5	(15.8)	(Yanagida et al., 1984)
Rabbit skeletal muscle Mg-ADP-F-actin	E	(2.9)	7.1	(Sharma et al., 2011)
Rabbit skeletal muscle Mg-ADP-F-actin labeled with TMR on lysines. Decorated with skeletal muscle tropomyosin.	A	(8.8)	21.5	(Isambert et al., 1995)
Rhodamine-labeled rabbit skeletal muscle and unlabeled chicken skeletal muscle Mg-ADP-F-actin. Decorated with skeletal muscle tropomyosin.	B	(7.4)	18 ± 1	(Greenberg et al., 2008)
Rhodamine-labeled rabbit skeletal muscle and unlabeled chicken skeletal muscle Mg-ADP-F-actin. Decorated with smooth muscle tropomyosin.	B	(5.5)	13.5 ± 2	(Greenberg et al., 2008)
Rhodamine-labeled rabbit skeletal muscle and unlabeled chicken skeletal muscle Mg-ADP-F-actin. Decorated with caldesmon fragment H32K.	B	(6.2)	15 ± 2	(Greenberg et al., 2008)
Rhodamine-labeled rabbit skeletal muscle and unlabeled chicken skeletal muscle Mg-ADP-F-actin. Decorated with smooth muscle tropomyosin and caldesmon fragment H32K.	B	(6.6)	16 ± 1	(Greenberg et al., 2008)
Rabbit skeletal muscle Mg-ADP-F-actin labeled with Alexa 488 on lysines. Decorated with human nonmuscle cofilin.	C	(9.0)	2.20 ± 0.03	(McCullough et al., 2008)
Rabbit skeletal muscle Mg-ADP-F-actin stabilized and labeled with rhodamine-phalloidin. Decorated with rabbit skeletal muscle HMM.	D	4.9	(11.9)	(Yanagida et al., 1984)
Rabbit skeletal muscle Mg-ADP-F-actin decorated with mouse drebrin A.	E	(4.5)	10.9	(Sharma et al., 2011)

Values in parentheses were calculated using Equation 4.
Measurement (msrmt.) methods:
A: Microscopy and calculation of cosine correlation length and average transverse fluctuations.
B: Microscopy and Fourier mode analysis.
C: Microscopy and fit to cosine correlation function.
D: Microscopy and fit to average end-to-end length.
E: AFM

The resistance of actin filaments under bending (non-axial) forces $F_{bending}$ is even more sensitive to filament contour length, scaling as the inverse third power of L, for small filament deformations (Howard, 2001):

$$F_{bending} = \frac{3EI}{L^3} y = \frac{3k_B T L_p}{L^3} y, \qquad \text{Equation 6}$$

where y is the deflection of the filament tip in the direction perpendicular to the filament's initial axis. These physical properties explain one of the reasons why capping protein is important in producing dendritic actin networks that can effectively exert force and withstand compression (Akin & Mullins, 2008; Mejillano et al., 2004). By limiting the lengths of unreinforced filament segments below ~1μm (Svitkina & Borisy, 1999; Vinzenz et al., 2012), it creates a network of stiffer mechanical elements.

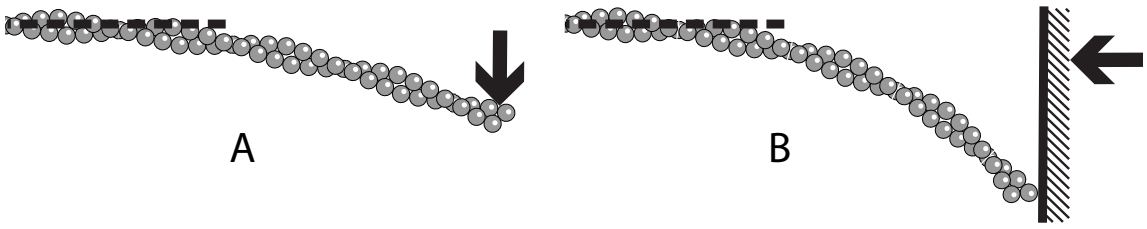

Figure 7. Forces on actin filaments impinging on a load. (A) Bending, (B) buckling. The filament shown is ~200 nm long and drawn to scale. Dark arrows indicate the direction of the applied force, while dashed lines indicate constraints. Both filaments are constrained against translation and rotation at the left end, while the right end is free to rotate and translate.

For actin filaments in the semiflexible regime, with contour lengths of several μm, the WLC response to large (higher than thermal) forces is highly asymmetric. Under compressive forces, filaments may resist buckling, but the longer they are, the smaller is the force under which they yield. Once buckled, the filaments exert a reaction force equal to the buckling force, but their end-to-end length is rapidly decreased. Therefore, semiflexible actin filaments are generally quite soft under compression, with the degree of compliance increasing steeply with filament length. On the other hand, under tension, semiflexible polymers exhibit entropic elasticity under small forces, and a very stiff enthalpic elastic response under high forces at which the filament's end-to-end length approaches its contour length (Bustamante et al., 1994; Gardel et al., 2008; Smith et al., 1992; Storm et al., 2005). Entropic elasticity occurs because a stretched filament can adopt fewer conformational states than a filament that is free to fluctuate, leading to an increase in the free energy of the system that manifests as a resistance to extension, which scales with the filament length. Under both compression and tension, longer filaments are more compliant for small forces, but regardless of the filament length, the WLC polymer exhibits much lower

compliance under tension than under compression for large forces (Gardel et al., 2008; Howard, 2001).

The bending of F-actin that is induced by thermal motion is transient, and the time scale of relaxation of filament bends depends on the filament's persistence length and contour length, on the viscosity of the surrounding medium, and on the wave vector of the fluctuation being considered. Large wave vector fluctuations have short wavelengths and decay quickly, while small wave vector fluctuations have long wavelengths, and decay much more slowly. It has been shown that for actin filaments fluctuating in buffer, a Fourier decomposition of the filament shape is a reasonable approximation, to within 10-15% of the (more complicated) normal mode decomposition (Brangwynne et al., 2007). The exponential relaxation time for the amplitude correlation of the *n*-th order Fourier mode, $\cos\left(n\pi s/L\right)$ can be approximated by:

$$\tau \approx \frac{\gamma}{EIq_*^4} \qquad \text{Equation 7}$$

where $q_* = \left(n+1/2\right)\pi/L$ and γ is the drag coefficient for the actin filament. The measured relaxation time for 8-15 μm long F-actin filaments ranges from ~10 s for q_* = 0.4 μm^{-1} and ~ 0.03 s for q_* = 1.5 μm^{-1} (Brangwynne et al., 2007).

Besides the two bending degrees of freedom in three dimensions (or the one degree in two dimensions), the actin filament is also free to twist due to Brownian motion. Its torsional rigidity, *C*, is analogous to the bending rigidity, but the extension parameter is the torsion angle per unit length rather than the curvature. The energy required to twist a filament of length *L* through a total angle ϕ is:

$$E_{twisting} = \frac{C\phi^2}{2L}. \qquad \text{Equation 8}$$

By the equipartition theorem, a relationship between the variance of the torsional angle per unit length and the torsional rigidity can be obtained (Tsuda et al., 1996):

$$\frac{C\left\langle\phi^2\right\rangle}{2L} = \frac{k_B T}{2} \qquad \text{Equation 9}$$

$$C = \frac{k_B TL}{\left\langle\phi^2\right\rangle}. \qquad \text{Equation 10}$$

Table 5: Torsional rigidity of F-actin is difficult to measure and the subject of controversy, because different techniques give results that differ by an order of magnitude. (Values in parentheses are calculated using Equation 11.)

Condition	**Measurement method**	**Torsional rigidity ($\times 10^{-26}$ N m^2)**	**R.M.S. angular disorder (°)**	**Reference**
Mg-F-actin	EM of isolated filaments, with negative stain.	(0.036)	~10	(Egelman et al., 1982)
Mg^{2+} paracrystals of scallop ADP-F-actin.	EM of angle-layered aggregates, with negative stain.	(0.1)	6	(Egelman et al., 1983)
Based on (Bremer et al., 1991)	EM of isolated filaments, with negative stain.	(0.15-0.10)	5-6	(Egelman & DeRosier, 1992)
Rabbit skeletal muscle Mg-F-actin stabilized with TMR-phalloidin.	Rotational fluctuations of end of a filament under < 1 pN of tension. Slope of variance w.r.t. filament length, equipartition thm. Sampling interval 0.2-1.0 s.	8.0 ± 1.2	(0.68)	(Tsuda et al., 1996)
Rabbit skeletal muscle Mg-F-actin stabilized with TMR-phalloidin.	Calculation from bending rigidity, assuming F-actin is a homogeneous cylinder.	5.8	(0.79)	(Kojima et al., 1994; Tsuda et al., 1996)
Based on (Kojima et al., 1994)	Normal mode analysis based on the atomic structure of F-actin.	2.6 – 3.6	(1.2-1.0)	(ben-Avraham & Tirion, 1995)
Rabbit skeletal muscle Ca-F-actin stabilized with TMR-phalloidin.	Rotational fluctuations of a filament attached to two beads, equipartition thm. Sampling interval 33 ms. Tension in filament estimated at 0.2-1.8 pN.	8.5 ± 1.3	(0.65)	(Yasuda et al., 1996)
Rabbit skeletal muscle Mg-F-actin stabilized with TMR-phalloidin.		2.8 ± 0.3	(1.1)	(Yasuda et al., 1996)
Rabbit skeletal muscle Mg-F-actin stabilized with TMR-phalloidin.	Rotational fluctuations of the tail of an actin filament imaged with bead aggregates.	3	(1)	(Suzuki et al., 1996)
Eosin-labeled Mg-F-actin in solution.	Transient phosphorescence anisotropy decay.	0.2	(4)	(Yoshimura et al., 1984)
Erythrosin-labeled Ca-F-actin in solution.	Transient phosphorescence anisotropy decay.	0.14	(5.1)	(Prochniewicz et al., 1996)
Erythrosin-labeled Ca-F-actin stabilized with phalloidin in solution.	Transient phosphorescence anisotropy decay.	0.077	(6.9)	(Prochniewicz et al., 1996)
Erythrosin-labeled Ca-ADP-F-actin in solution.	Transient phosphorescence anisotropy decay.	0.23 ± 0.1	(4.0)	(Prochniewicz et al., 2005)
Erythrosin-labeled Mg-ADP-F-actin in solution. Decorated with human cofilin.	Transient phosphorescence anisotropy decay.	0.013 ± 0.006	(16.8)	(Prochniewicz et al., 2005)
Phalloidin-Mg-ADP-F-actin labeled with 1,5-I-AEDANS and tetramethylrhodamine.	Total internal reflection polarization microscopy	0.2	(4.27)	(Forkey et al., 2005)

The torsional rigidity has been measured by direct manipulation and by transient phosphorescence anisotropy (TPA) decay (Table 5). TPA is a measurement that consists of illuminating actin labeled with a phosphorescent probe, such as erythrosin, with a vertically polarized laser pulse, and measuring the vertically and horizontally polarized phosphorescence signals over the course of microseconds (Ludescher & Thomas, 1988; Prochniewicz et al., 1996). As the labeled actin filament moves in solution, the angle of the erythrosin dipole changes from its orientation at the time of the laser pulse. At short times, the difference between the horizontally and vertically polarized emission signals, called the phosphorescence anisotropy, remains large because most of the erythrosin molecules retain their orientation. At longer times, this anisotropy signal decays exponentially due to wobbling motions of the erythrosin and internal motions of actin monomer, torsion of the actin filament, rotation of the filament around its axis, bending fluctuations of the filament, and end-to-end tumbling of the filament in solution. These processes are listed in approximate order of their time scale. Rotational and torsional motions occur on the order of microseconds, and generally appear in the TPA signal, causing its decay to take on the form of a sum of two to three exponentials. Bending and tumbling motions are too slow to be measured by this technique, on the scale of milliseconds or more (Prochniewicz et al., 1996). The TPA signal is thus interpreted as reporting on the torsional fluctuations of the actin filament, and the multiple exponential decay is fit with a model based on a segmented cylindrical rod, whose segments are frictionally and elastically coupled (Prochniewicz et al., 1996).

A related parameter, δ, called the angular disorder, which is the root mean square fluctuation in the angle between adjacent monomers in the one-start, left-handed helix, has been measured by electron microscopy (Table 5). In electron microscopy experiments, images of individual fixed and negatively stained actin filaments, or actin filaments in Mg^{2+} paracrystals can be analyzed to extract the variance in the angle of twist per monomer, either by measuring the distribution of spacings between cross-over points of the two protofilaments, or by taking the Fourier transform of segments of filament (Egelman & DeRosier, 1992; Egelman et al., 1982; Egelman et al., 1983). If the angular disorder, is the result of torsional fluctuations, then the angular disorder is equivalent to the square root of the variance of the torsional angle for a length of filament equivalent to the h, the rise per actin monomer (Yasuda et al., 1996):

$$\delta^2 = \frac{k_B T h}{C}. \qquad \text{Equation 11}$$

However, the discrepancy in values apparent in Table 5 suggests that different measurement methods may be probing different aspects of F-actin torsional flexibility. The torsional rigidity measured by mechanical methods is generally larger by an order of magnitude than the torsional rigidity measured by fluorescence methods or EM. In addition, phalloidin reduces the angular disorder observable by EM (Bremer et al., 1991), suggesting an increase in torsional flexibility if δ^2 and $<\phi^2>$ are equivalent quantities, but surprisingly, the addition of phalloidin appears to reduce the torsional flexibility of F-actin as measured by TPA decay (Prochniewicz et al., 1996). The discrepancy may be due to the fact that electron microscopy gives a static picture of a distribution of twist, which may arise from fluctuations or from a collection of stable states (Orlova & Egelman, 2000), TPA decay is a dynamic measurement in which the exact nature of

the motions being observed are only inferred (Prochniewicz et al., 1996), and fluctuations measured by mechanical measurements may be low-pass filtered by drag on the large beads used to manipulate F-actin (Forkey et al., 2005).

The time scales of torsional relaxation for F-actin have been measured by phosphorescence anisotropy decay to be on the order of 100 μs (Prochniewicz et al., 1996). As with the angular disorder, there is also disagreement in this parameter with EM data which suggests a relaxation time for the angular disorder of ~1 minute or more, suggesting that anisotropy decay may be due to other motions of the actin monomer besides filament twisting (Orlova & Egelman, 2000). The normal modes for torsion have been worked out by Greene (Greene, 1985).

Like bending rigidity, the torsional rigidity of F-actin is also regulated by the binding of ABPs and phalloidin (Table 5). Phalloidin reduces the torsional rigidity by a factor of ~2, while cofilin reduces the torsional rigidity by a factor of ~17. Decoration with the S1 fragment of myosin has been reported to increase filament torsional rigidity as measured by TPA (Prochniewicz & Thomas, 1997).

The angular disorder was also measured in the presence of tropomyosin, troponin, the S1 filament of myosin, which decorates F-actin, and on filaments frayed from the acrosomal bundle of Limulus sperm by incubation with high salt. Although tropomyosin and troponin had no effect on the angular disorder of actin, filaments decorated with myosin S1 and those frayed from the acrosomal bundle, possibly still partially decorated with some scruin, were highly ordered (Stokes & DeRosier, 1987).

The helical structure of F-actin suggests that, like other helical polymers, its bending and torsional fluctuations may be coupled to some degree. Intuitively, a double helix under tension, which reduces bending fluctuations, should unwind. This is the case for DNA, another biologically important double helical polymer, but only at very high tension (Gore et al., 2006). Surprisingly, the measured bend-twist coupling of DNA at moderate tension is negative, meaning that for a range of forces, the DNA double helix overwinds when pulled (Gore et al., 2006; Lionnet et al., 2006). These data indicate that although bend-twist coupling appears to be a simple matter of geometry, the structure and mechanical properties of the polymer in question can lead to surprising behavior.

The bend-twist coupling of F-actin has only been measured directly in one experiment. Using an optical trap, Hayakawa et al. showed a decrease of ~50% in the torsional fluctuations of an actin filament upon the application of ~5 pN of tension, but this effect was not studied systematically or further quantified (Hayakawa et al., 2011). Molecular dynamics simulations have been used to study twist-stretch coupling in short lengths of F-actin. They showed a change in actin structure under tensions of 200 pN and yielded a coupling modulus of 7.6×10^{-11} N (Matsushita et al., 2012; Matsushita et al., 2011). A positive value of the coupling constant, such as this one, indicates an unwinding of the helix upon stretching. A coarse-grained model based on the helical arrangement of the centroids of actin monomers in the F-actin filament has been constructed, but not yet tested against experiments (Yamaoka & Adachi, 2010). Another theoretical model based on the shape of F-actin has also been proposed, and used to predict a persistence length for bend-twist coupling of 0.15 – 0.4 μm (Yamaoka & Adachi, 2010).

Structural polymorphism in the actin filament

In previous sections of this chapter, we have discussed the structure of F-actin as if it were a single entity for the sake of simplicity (Holmes et al., 1990; Oda et al., 2009). However, there is ample evidence showing that F-actin adopts a multiplicity of states (Galkin et al., 2010), and that the frequency with which each state in the ensemble is observed is modulated by slow rearrangements of random fluctuations in the helical filament lattice (Egelman et al., 1982; Galkin et al., 2010; Kueh & Mitchison, 2009), actin-binding proteins (Galkin et al., 2001), and physical constraints (Orlova & Egelman, 2000). The existence of such polymorphism is highly relevant to any investigation of the regulatory role of force on actin behavior, because different structural states of F-actin may have different mechanical properties, with the measured parameters of actin (Tables 1-5) only reflecting an average over the polymorphic ensemble. Furthermore, mechanical inputs may modulate interconversion between states or favor particular states over others.

The first detailed model of F-actin was the "Holmes structure", deduced from X-ray fiber diffraction in the early 1990s (Holmes et al., 1990). In this structure, the angle between consecutive monomers in the one-start helix is 166˚ and the distance between crossovers of the two-start helix is 36 nm. The major contacts are within protofilaments (along the two-start helix) and include contacts between the DNAse I binding loop (residues 41-50) of subdomain 2 and subdomain 3 of the next monomer, as well as between the hydrophobic loop (residues 266-269) of monomers in one protofilament and the hydrophobic pocket formed by parts of subdomains 2 and 3 of monomers in the other protofilament. Subsequent refinements of this model have reduced the radius of gyration of the filament, shown that the propeller twist between subdomains 1/2 and 3/4 present in G-actin flattens as monomers incorporate into F-actin, and also shown that the DNAse I binding loop adopts an open loop conformation that docks into the small cleft in the hinge region between subdomains 1 and 3 of the next monomer (Holmes et al., 2003; Oda & Maeda, 2010). A further refined structure was obtained with very high resolution from filaments that were selected to be particularly ordered, and arrived at broadly the same conclusions, but because of the preparation method, observed a much lower angular disorder in monomer position within the filament (Fujii et al., 2010; Galkin et al., 2012).

There is an abundance of evidence from structural biology showing deviations from this canonical structure. The root mean square (r.m.s.) angular disorder of F-actin has been measured to be 6˚ or 10˚, depending on the data set measured (Egelman et al., 1982). This level of disorder suggests that monomers within the actin filament can twist through several degrees in order to accommodate packing into a hexagonal lattice, which the canonical actin filament symmetry does not support, but which is observable in some actin bundles (Egelman et al., 1982).

Several distinct states of F-actin have been characterized. EM of frozen hydrated F-actin in the absence of actin-binding proteins or stabilizing factors such as phalloidin exhibited a variety of structural states that could be characterized in detail by a helical averaging method that treats short sections of filaments, containing about 17 monomers, as single particles (Galkin et al., 2010). One state, occupied in 24% of analyzed actin segments was tilted relative to canonical F-actin (described in the actin section above) (Oda et al., 2009), with subdomain 2 making strong contacts with subdomain 3 of the next monomer, and the contacts between subdomain 4 and

subdomain 3 relatively weakened as subdomain 4 is tilted further from the radius of the filament (illustrated in Figure 8). In this state, the nucleotide cleft of the monomers is open.

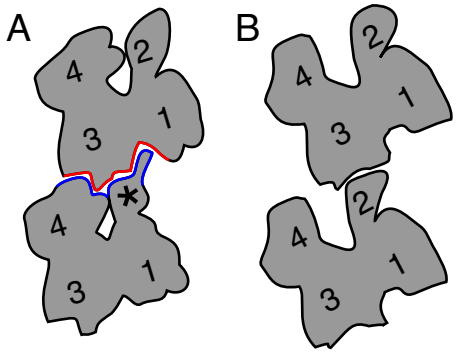

Figure 8. Structural states of F-actin. (A) The canonical state. (B) Tilted state. Other states of F-actin differ from the canonical state mainly in the conformation of subdomain 2 (indicated with an asterisk).

The other 76% of actin segments largely occupy the canonical state, with the exception of changes in the structure of and contacts made by subdomain 2, which, in unstabilized F-actin, adopts five different conformations (Galkin et al., 2010). One of those conformations is completely disordered (such that subdomain 2 does not appear in EM reconstructions). Together, this evidence suggests that the contacts made by subdomain 2 are not essential for the stability of the actin filament as a whole, but they are important in modulating the properties of F-actin in its interactions with other proteins (Galkin et al., 2010). Galkin et al. predict that a disordered state of subdomain 2 would reduce the torsional and flexural rigidity of the filament (Galkin et al., 2010), which is confirmed in the case of cofilin-bound actin (discussed below) (Galkin et al., 2011; McCullough et al., 2008; Prochniewicz et al., 2005).

The state of subdomain 2 has indeed been shown to correlate with changes in filament flexibility. Experiments with different nucleotide states and with a mutant that mimics the ADP-BeF_3^- state show that the nucleotide binding cleft of actin begins in an open state, and closes upon Pi release, changing the longitudinal contacts made by subdomain 2 (Belmont et al., 1999). This structural change correlates with the different persistence lengths of ADP-P_i- and ADP-F-actin (Table 1). Proteolysis data also showed a strong difference in the accessibility of subdomain 2 in ADP-bound and ATP-bound-like states of actin, which correlate with filament stiffness (Muhlrad et al., 1994).

A change in F-actin structure with clear functional implications is the overtwisting of the double helix, which can also be expressed as an increase in the azimuthal rotation angle between adjacent monomers in the one-start helix from -166.6˚ to -162˚, induced by the binding of the severing protein ADF/cofilin (Galkin et al., 2011). Although this dramatic change in the twist of the actin helix has been known for some time (McGough et al., 1997), the detailed changes in F-actin structure that occur upon cofilin binding have only recently been elucidated (Galkin et al., 2011). Monomers within F-actin, which normally have a flat conformation, are forced by cofilin into a propeller twist that undoes the flattening that occurs in the G-actin to F-actin transition (Oda et al., 2009), and causes subdomains 1/2 to adopt an extreme 30% propeller twist with respect to subdomains 3/4 (Galkin et al., 2011). This twisted state of the monomer and the fact that subdomain 2 is made disordered disrupts normal longitudinal contacts between subdomain 2

of one monomer and subdomains 1/3 of the next monomer in the protofilament, and because of a steric clash under the normal helical state of F-actin, also causes the helix to undergo the ~5° overtwisting that is a hallmark of the cofilin-bound state (Galkin et al., 2011; McGough et al., 1997). Longitudinal contacts between subdomains 3 and 4 are left intact (Galkin et al., 2011). These changes in F-actin are more extreme than the ensemble of six commonly observed structural modes present in pure F-actin, in the absence of ABPs (Galkin et al., 2010), but the disorder in subdomain 2 and the disruption of its longitudinal contacts is similar to spontaneously adopted conformations of F-actin, explaining why earlier literature based on lower-resolution structures suggested that cofilin simply stabilizes a preexisting state of F-actin (Galkin et al., 2003). The changes in contacts are also consistent with a significant weakening of the filament observed in measurements of the persistence length (McCullough et al., 2008) and with a severing model that rests on the mechanical stress induced by thermal fluctuations at boundaries between F-actin segments in the overtwisted state and in the standard state (McCullough et al., 2011).

A more extreme example of the plasticity of F-actin is in a reconstruction of the straight Limulus sperm acrosomal bundle, which is crystalline in form due to very tight crosslinking by the ABP scruin (Schmid et al., 2004). The helical symmetry of F-actin does not pack into a crystal lattice, so filaments are distorted in order to pack into the acrosomal bundle. Within the repeating filament unit in the crystal lattice, the deviation from the Holmes structure is as much as 10.4° under-twist and 23.6° over-twist while maintaining filament integrity. This structure is also unique because the two protofilaments adopt asymmetric conformations. The acrosomal bundle switches between a coiled, Ca^{2+}-free form, to a straight form in the presence of Ca^{2+}, which is the state studied by EM. It is believed that the rigid coupling of the actin filaments makes the bundle very stiff, while a very large amount of elastic energy is stored in the distortion of actin filaments while they are in the coiled bundle (Shin et al., 2007).

Cooperative structural transitions

An important feature of F-actin's plasticity is the cooperative propagation of a certain structural state between monomers. Galkin et al. used 17-monomer blocks in an iterative averaging algorithm to refine F-actin structures (Galkin et al., 2010). The fact that such blocks of consistent conformation can be isolated and averaged implies that these structural states of actin are cooperatively propagated, although the length of the cooperative unit (not quantified in their work) is much smaller than the length of the average actin filament.

Other evidence for cooperativity in propagating the structural state of actin comes from TPA measurements from filaments in which a fraction of the monomers are perturbed by the binding of myosin S1 fragment, by binding of an antibody, or by cross-linking with 1-ethyl-3-(3-dimethylaminopropyl)carbodiimide (EDC) (Prochniewicz & Thomas, 1997). The change in phosphorescence anisotropy decay time as a function of the concentration of perturbed monomer suggests that the effects of each perturbation propagate to adjacent monomers, although the number of adjacent monomers is different for the different perturbations, with EDC-crosslinked monomers having the greatest effect (Prochniewicz & Thomas, 1997).

The binding of some ABPs to F-actin, such as cofilin, is cooperative (De La Cruz, 2005). Because adjacent cofilin molecules do not directly contact each other, the cooperativity is necessarily transmitted through cooperative changes in F-actin structure (Galkin et al., 2011). This is in contrast to the cooperativity of tropomyosin binding to F-actin, which results from direct head to tail interactions between tropomyosin molecules (Wang & Coluccio, 2010). The cooperativity cofilin binding mediated allosterically through F-actin helps to explain how cofilin can work at substoichiometric concentrations to accelerate the dissociation of Arp2/3 (Chan et al., 2009) and phosphate (Suarez et al., 2011) from F-actin. Muscle heavy meromyosin (HMM) (Orlova & Egelman, 1997), nonmuscle myosin V (Prochniewicz et al., 2010), also exhibit cooperative binding to F-actin and muscle myosin S1 fragment exhibits anti-cooperative binding to F-actin with itself (Prochniewicz et al., 2010) or with HMM (Prochniewicz et al., 1993). Even more dramatically, there is evidence that a single ABP bound to the barbed end can alter the structure of an actin filament (Bugyi et al., 2006; Prochniewicz et al., 1996), in one case making it more flexible and perhaps speeding up phosphate release (Bugyi et al., 2006).

The dynamics of inter-conversion between structural states of F-actin are difficult to study because there is not a clear one-to-one mapping between high time resolution dynamical information, such as that obtained from fluorescence or phosphorescence anisotropy decay, which probes microsecond time scales, and high spatial resolution structure data, which comes from EM. A clever experiment tested whether the observed angular disorder of F-actin results from a continuous variation in the azimuthal angle between subunits or from a mixture of several, more narrowly defined structural states (Orlova & Egelman, 2000). Filament ends emerging from a Mg^{2+} paracrystal that imposes a narrowly defined structural symmetry on F-actin, reducing its angular disorder, did not relax into a high-angular disorder state for tens of seconds after they were dissociated from the paracrystals by Mg^{2+} wash-out (Orlova & Egelman, 2000). Although for short distances, cooperative interactions could have propagated the low-angular variance state from the paracrystal, the propagation would have had to occur over distances of over 100 nm. It is possible that this is due to long-range cooperative interactions, which may be consistent with changes in filament structure caused by a barbed end bound ABP (Orlova & Egelman, 2000), but the evidence is not yet conclusive. A slow structural rearrangement is consistent with an apparent slow transition between structural states observable by EM and through the rate of depolymerization (Kueh et al., 2008; Kueh & Mitchison, 2009). However, the evidence does not yet paint a complete picture of the relationship between F-actin structure and dynamics. The structural polymorphism of F-actin and its functional consequences constitute an area of active study (Galkin et al., 2012; Galkin et al., 2010).

What forces act on F-actin?

The diversity of F-actin structures present in animal cells subjects different populations of filaments to very different forces and constraints, which may contribute to differentiating their structural states. Dendritic networks near the membrane feel compressive forces as a reaction to the protrusive force produced by polymerization of barbed ends, which may bend or buckle the free ends of the filaments (Keren et al., 2008). This force per filament can be estimated by dividing the membrane resistance, 50-500 pN/μm of leading edge (Mogilner & Edelstein-Keshet, 2002), by the number of barbed ends at the leading edge, 50-250 filaments/μm (Abraham et al.,

1999), to obtain an estimate of 0.2-10 pN/filament. This range of forces represents the Euler buckling force for 830 to 120 nm long filaments, respectively, assuming an actin persistence length of 13.5 μm (Isambert et al., 1995).

In the bulk of the dendritic network of the lamellipodium and in the lamella, the forces on individual filaments can be more complicated than simple compression. First, shear forces may result from the frictional coupling between the dendritic network undergoing retrograde flow over focal adhesions (Gardel et al., 2010; Hu et al., 2007). Some of this force is transformed into traction forces on the substrate, which can be measured (Kraning-Rush et al., 2012) and are on the order of nN (Balaban et al., 2001), but because traction force is also produced by the contraction of actomyosin bundles that couple directly into the adhesions, it is difficult to estimate the magnitude of the frictional force alone. The dendritic network is effectively a dense (Svitkina & Borisy, 1999; Vinzenz et al., 2012) and rigidly crosslinked (Blanchoin et al., 2000) actin network, with some possible additional bracing that arises from the truss-like nature of Y-branches nucleated by the Arp2/3 complex. If we draw a comparison with randomly crosslinked studied in vitro, it is known that shear stresses on actin networks not only bend filaments, as would be expected, but also put some filaments under tension (Gardel et al., 2008). The nonlinear entropic elasticity of such filaments under tension is believed to be responsible for the stress-stiffening of crosslinked actin networks under shear. Similar behavior is expected from crosslinked actin networks under compression (Chaudhuri et al., 2007). Lastly, actin filaments in crosslinked networks may also be under either tensile or contractile forces because of long length scale fluctuations of the network that cause transient, large forces on individual filaments, or because the dynamics of network assembly has created stress which cannot be immediately relieved by rearrangement, as has been observed in fascin-actin networks in vitro (Breitsprecher et al., 2011; Lieleg et al., 2011).

Compressive forces are also found in filopodia, where, after the initial membrane deformations involved in filopodium initiation, the membrane forms a tube for which the force required to extend its length is relatively constant, with an estimated value of 10-50 pN (Mogilner & Rubinstein, 2005). For filopodia that contain 10-30 filaments, the force per filament in this case would be 0.33-5 pN (Mogilner & Rubinstein, 2005). These filaments do not buckle because they are bundled by crosslinkers and braced by the surrounding membrane (Liu et al., 2008; Pronk et al., 2008). As is the case with dendritic (and randomly crosslinked) networks, the forces acting on the filaments in the filopodial bundle diversify as we trace the bundle toward the center of the cell. Filopodia, like dendritic networks, undergo treadmilling and have been shown to transition into contractile bundles in the lamella (Anderson et al., 2008; Nemethova et al., 2008), or are disassembled by the action of myosin in the lamella (Medeiros et al., 2006). In either case, the force actin on individual filaments must involve a tensile component, and in the case of myosin-induced bundle disassembly, probably also shear or bending, because in vitro bundle disassembly by myosin requires that the motors actively produce force and morphologically, appears as a tearing away of filaments from the bundles (Haviv et al., 2008). The role of tension in filopodia is underscored by the observation that neuronal filopodia exert traction forces on soft substrates in what is likely a mechanosensing mechanism (Chan & Odde, 2008).

The last major context in which actin filaments feel force is also the canonical one, the well-studied contractile actomyosin bundle which is found in muscles as the highly organized and

stable sarcomere (Au, 2004), but is also present in most cells as stress fibers (Gardel et al., 2010; Hotulainen & Lappalainen, 2006; Naumanen et al., 2008), graded polarity bundles (Cramer, 1999; Cramer et al., 1997; Mseka et al., 2009), actin arcs that exhibit some contractile ability (Burnette et al., 2011), and disorganized myosin minifilament arrays present in the lamella (Svitkina et al., 1997; Verkhovsky & Borisy, 1993; Verkhovsky et al., 1995). Tension can vary over a large range, but as we estimated in Chapter 4, tension on individual filaments in stress fibers can reach ~100 pN or more, if we assume that stress fibers are coupled to focal adhesions (Gardel et al., 2010), which exert several nN of isometric traction force on the substrate (Balaban et al., 2001; Deguchi et al., 2006; Sugita et al., 2011; Tan et al., 2003), and contain tens of actin filaments (Cramer et al., 1997; Mogilner & Rubinstein, 2005).

Although not as common as sources of linear force, there are also sources of torque in the cell. The most common and probably quite important context in which torque is exerted on F-actin is the tight bundling of actin filaments into hexagonal close packed lattices by several different crosslinkers. The standard F-actin helix is not compatible with six-fold symmetry, and thus must be twisted slightly to allow contacts to form with the six nearest neighbors (DeRosier & Tilney, 1982). In addition, the crosslinkers often must be deformed themselves (Volkmann et al., 2001). The build-up of torsional stress in F-actin and shear stress in the crosslinkers eventually balances the binding energy of crosslinkers, limiting the size to which bundles of a certain symmetry can grow (Claessens et al., 2008). A change in the average twist of F-actin is also evident in Mg^{2+}-induced paracrystals (Orlova & Egelman, 2000).

Lastly, torque on F-actin may also be exerted by ABPs in two ways. Formins, which nucleate actin filaments, remain attached to the barbed end as new monomers are added. It has been shown that formins rotate around the barbed end as new monomers are added (Mizuno et al., 2011). If rotation of the formin is restricted by its attachment to other proteins, some torque may be imparted to the actin filament. The binding of cofilin, which overtwists F-actin in patches where it has cooperatively bound, also creates torsional stress on neighboring sections of F-actin, which, if it cannot be relieved by filament rotation, can lead to filament severing (McCullough et al., 2011).

Molecular Mechanosensing

Mechanosensing has been defined by Janmey and Weitz as “the ability of a cell or tissue to detect the imposition of a force” (Janmey & Weitz, 2004). Here, “molecular mechanosensing” or “molecular mechanosensitivity” refer to the intracellular molecular mechanisms responsible for that ability to detect forces. A related term is mechanotransduction, the conversion of physical stimuli into intracellular biochemical signals such as phosphorylation events or protein-protein binding events (Vogel & Sheetz, 2006). It has been shown to occur in several cellular contexts. Cultured cells from various tissues can respond to physical cues like substrate stiffness (Discher et al., 2005; Discher et al., 2009; Janmey et al., 2009; Provenzano & Keely, 2011; Vogel & Sheetz, 2009), as has also been demonstrated for stem cells whose differentiation outcome is dictated by the stiffness of the substrate on which they are cultured (Engler et al., 2006). Cells involved in bone building and remodeling have been shown to exhibit changes in their differentiation and proliferation (Eyckmans et al., 2011), and endothelial cells that have evolved to respond to shear stresses from blood flow also respond to cyclical mechanical stresses applied

in vitro (Eyckmans et al., 2011; Shyy & Chien, 2002). Another form of mechanotransduction, called mechanosensation, converts mechanical signals not into biochemical signaling cascades but into voltage signals that lead to intracellular signaling or are passed on to other neurons in multicellular organisms (Garcia-Anoveros & Corey, 1997).

The filamentous elements of the cytoskeleton are currently understood to serve in an organizing role, as templates for assembly of other protein complexes or tracks for motor-based transport (F-actin, microtubules, septins, and intermediate filaments) and in a structural role, transmitting forces to mechanosensing molecules that change conformation in response to force (F-actin, microtubules, and intermediate filaments) (Hoffman et al., 2011; Janmey & Weitz, 2004). In addition to this focused mechanotransduction, a more distributed and structural kind of mechanosensing at the molecular scale has been shown to play a role in several processes, such as molecular motor function. A recent review provides an excellent overview of many mechanotransduction mechanisms, with a focus on dynamic processes, and should be consulted for examples in addition to those described below (Hoffman et al., 2011).

Transmission of force by the cytoskeleton

Cytoskeletal structures have evolved not only to withstand applied forces, but also to precisely transmit those forces where they may be appropriately sensed or dissipated, as function requires, in a controlled manner, and often while the structures themselves are undergoing dynamic turnover (DuFort et al., 2011).

One classic example is the bundles of actin filaments that make up the stereocilia of hair cells in the ear. Stereocilia are F-actin bundles containing the actin crosslinkers fimbrin and espin enveloped by a membrane that contains mechanically gated ion channels (Vollrath et al., 2007). The cilia have finely tuned lengths and are arranged in bundles in stereotypical V-shapes (Lin et al., 2005). Both the lengths of the actin bundles and their arrangement tune their mechanical properties such that they respond to specific frequencies of sound, and allow different hair cells to respond to a specific frequency band (Tilney et al., 1992). Mechanosensing occurs when the bundle of stereocilia is bent by an incoming sound wave, stretching proteins that link the tips of the stereocilia via attachments to mechanically gated ion channels, opening the ion channels and changing membrane potential in the process (Vollrath et al., 2007). All of this happens while the actin bundles undergo constant treadmilling (Schneider et al., 2002), and while myosins connected to the stereocilium tip links actively tune the stiffness of the bundle and tension on the tip links to adapt the sensory system to the incoming sound amplitudes (Cotton & Grant, 2004; Vollrath et al., 2007). The architecture of the actin bundles, including the spatial arrangement and length of F-actin filaments and the mechanical properties of their crosslinkers and accessory proteins, such as the tip linkers, are key to transmitting force to the ion channels that are the direct mechanosensing element.

Cell adhesion to the extracellular matrix is a second example of force transmission by the cytoskeleton. When given a microenvironment that contains fibronectin or fibronectin-like peptides, cells make focal adhesions via transmembrane integrin molecules that tightly bind fibronectin (Geiger et al., 2001). Focal adhesions are plaques composed of a complex system of proteins that anchors stress fibers, F-actin bundles that also contain some tropomyosins, alpha-

actinin, and nonmuscle myosin (Geiger et al., 2009). Myosin-based contractility in stress fibers generates isometric tension that is focused by those same stress fibers on focal adhesions and is necessary for full maturations of the focal adhesions (Choi et al., 2008). Focal adhesions are important to cells' ability to sense the stiffness of their substrates, and mechanosensing by focal adhesions is an area of active research (Ghassemi et al., 2012).

In addition to coupling to focal adhesions, stress fibers have also been shown to transmit force to mechanosensitive Ca^{2+} channels, by experiments in which microinjected, phalloidin-coated beads bound to stress fibers were manipulated with an optical trap while monitoring Ca^{2+} influx in endothelial cells (Hayakawa et al., 2008). Application of tension onto stress fibers led to localized Ca^{2+} influx near the point of stress fiber attachment to the cell cortex.

There are many other ways in which the cytoskeleton couples with other cellular components to transmit force, such as adherens junctions in multicellular organisms or F-actin bundles involved in movements of or within the cell nucleus of yeast cells and fibroblasts (Koszul et al., 2008; Luxton et al., 2010). Here, the last example we will touch on is force transmission by the lamellipodial dendritic network and the less branched lamellar actin network in migrating cells. The protrusive force generated by actin polymerization at the leading edge combined with network treadmilling as described by the dendritic nucleation model (Pollard & Borisy, 2003) lead to fast retrograde flow lamellipodial actin network away from the leading edge. On surfaces where adhesion can happen, the polymerization force is divided between generating retrograde flow and forward protrusion of the lamellipodium, as nascent, integrin-based adhesions to the substrate called focal complexes, form under the lamellipodium (Bershadsky et al., 2003; Giannone et al., 2007). These focal adhesions mature in the region behind the lamellipodium, called the lamella, that marks the site of massive actin disassembly, bundling of F-actin by myosin into actin arcs, and a slow-down of actin flow velocities (Geiger et al., 2009; Hu et al., 2007; Ponti et al., 2004). It is believed that in the lamella, the protrusive force of actin polymerization is integrated with actomyosin bundle contraction and with adhesion to the substrate, to generate the forward protrusion that is an essential element of cell motility (Burnette et al., 2011). A "clutch" mechanism has been proposed for focal adhesions, in which the coupling between the F-actin network and the adhesion to the extracellular matrix can slip to a variable degree, determining how much the front of the cell advances relative to the substrate (Geiger et al., 2009). The traction force transmitted to the focal adhesion regulates its maturation and contributes to the overall motility of the cell (Gardel et al., 2010), while the actomyosin cytoskeleton, including actin arcs which mature into stress fibers, forms a coherent network that maintains cell shape during motility (Cai et al., 2010).

The force sensors that lead to downstream signaling events in these and other mechanosensitive subcellular modules fall into several categories: proteins that unfold under tension, mechanosensitive membrane channels, molecular motors, and active polymers.

Force-induced unfolding to reveal cryptic sites or cryptic enzymatic activity

Focal adhesions are important centers for mechanotransduction because of their central role in sensing substrate rigidity and the important role that force plays in their assembly and turnover (Balaban et al., 2001; Gardel et al., 2008; Gardel et al., 2010; Riveline et al., 2001). A common

motif in focal adhesion signaling and protein recruitment is the unfolding of protein domains with relatively low mechanical stability to reveal cryptic binding sites for other proteins, or sites for posttranslational modifications such as phosphorylation (Sawada et al., 2006; Vogel & Sheetz, 2006).

Fibronectin is a classic example of tension-induced unfolding. It is a large, multi-domain protein that is globular in its soluble form and circulates in the plasma, but upon binding to integrins on the cell surface and being stretched by forces as low as ~5 pN, it unfolds to five times its size, exposing many binding sites for integrins, as well as for fibronectin multimerization (Geiger et al., 2001). It has been measured by FRET that, consistent with its role as a mechanosensor, fibronectin is elastic and tension must be maintained in order to keep it unfolded (Baneyx et al., 2002). In this manner, tension applied by the cell and transmitted through integrins locally unfolds bound fibronectin molecules, allowing them to associate into fibrils that become part of the extracellular matrix in a mechanosensitive manner, although technically this cannot be called mechanotransduction because it occurs on the outside of the cell (Geiger et al., 2001).

Another example, which is found on the intracellular side of focal adhesions is the binding of vinculin to talin, which is enhanced by tension on talin (Geiger et al., 2009). Talin binds both integrins and F-actin, and is one of the earliest proteins to incorporate into nascent focal complexes (Gardel et al., 2010). As the focal complexes mature into focal adhesions, a process that requires tension, vinculin becomes associated with the focal adhesions (Gardel et al., 2010; Geiger et al., 2009). It is known that the rod domain of talin contains as many as 11 binding sites for vinculin, and in vitro single molecule experiments in which the talin rod domain was unfolded with 12 pN of applied tension show that the number of vinculin head domains bound to talin increased approximately threefold under tension, suggesting that a similar mechanosensing mechanism may be involved in the force-dependent maturation of focal adhesions in vivo (Rio et al., 2009). In a slight variation on the same mechanism, the focal adhesion protein p130Cas was shown to expose tyrosine phosphorylation sites for the Src family of kinases upon in vitro mechanical stretching of the molecule (Sawada et al., 2006).

A recent study (Ehrlicher et al., 2011) showed that the association of another ABP, filamin, with two of its binding partners, is modulated by strain. Filamin plays an important role the mechanical integrity of cells, as shown by filamin A deficient cell lines that constitutively bleb and are immotile (Nakamura et al., 2011). It is generally found in the actin network that makes up the cell cortex, creating crosslinks between approximately orthogonal actin filaments, but it also binds several components of focal adhesions, such as integrins (Nakamura et al., 2011). By reconstituting an actin network crosslinked by filamin A in vitro, Ehrlicher and coworkers were able to shear the network and monitor the binding of FilGAP, a GTPase activating protein for the important Rho family GTPase Rac, and of the cytoplasmic domain of β7 integrin (Ehrlicher et al., 2011). In analogy to the talin/vinculin interaction (Rio et al., 2009), shear of the filamin at actin filament intersections opened a cryptic binding site for the integrin. However, in a unique bimodal mechanosensing mechanism, the relaxed state of the molecule, besides hiding the integrin binding site, also created a new binding site for FilGAP, which is composed of two elements that are too far apart in the strained conformation (Ehrlicher et al., 2011).

Mechanosensing by unfolding also appears to occur outside of focal adhesions. A shotgun labeling approach for all cysteines that are exposed only under mechanical stress was used on red blood cells, which were subjected to shear stress and mesenchymal stem cells, which were relaxed by inhibition of myosin with blebbistatin (Johnson et al., 2007). It identified stretch-exposed sites on spectrin in red blood cells, and on nonmuscle myosin IIA in stem cells, as well as a site on vimentin that appears to be accessible only in the depolymerized state of vimentin in relaxed cells (Johnson et al., 2007). In the sarcomere of striated muscle cells, a kinase domain in the spring-like titin molecule is only active when it is mechanically stretched, and has been shown to interact with the zinc finger protein nbr1 as part of a pathway that modulates gene expression in the muscle cell (Lange et al., 2005; Puchner et al., 2008).

Mechanosensitive membrane channels

Mechanosensitive membrane channels transduce increases in membrane tension into a change in the membrane potential by opening to allow the flow of cations across the membrane. They are involved in many sensory processes, as well as in regulating cell volume and osmotic balance (Hamill & Martinac, 2001). The best characterized such channel is the bacterial K^+ channel MscL, which only opens at extremely high membrane tensions as tension transmitted by the phospholipid head groups in the membrane pulls on the transmembrane helices making up the pore, causing them to rotate and open the central pore cavity (Vogel & Sheetz, 2006). The mechanisms by which animal cell mechanosensitive channels sense force are less understood, because they tend to open at much lower membrane tensions, and because membrane tension in animal cells is buffered by a large reservoir of membrane that is shaped by membrane-cytoskeleton interactions (Hamill & Martinac, 2001).

Two competing models of mechanosensitive channel gating have been proposed: opening in response to membrane tension changes which couple directly to the channel, or opening in response to tension on "tethering" elements, perhaps coupled to the cytoskeleton, which pull on the channel to open it (Hamill & Martinac, 2001). The tethering model is clearly an explanation for the mechanosensitivity of channels in the membrane of stereocilia, for which the "tip links" that apply forces to channels have been imaged by EM and identified as a cadherin and a protocadherin (Gillespie & Muller, 2009). As discussed above, there is also evidence from endothelial cells that tension in stress fibers opens Ca^{2+} channels. The application of 5.5 pN of tension directly to stress fibers caused a localized influx of Ca^{2+} in the vicinity of focal adhesions. From the resulting current, it was estimated that 5-8 channels were opened by the applied force. While this suggests that channel opening was mediated by attachment of the actin cytoskeleton to mechanosensitive channels, the details of the actin-channel link are unclear and it is possible that the coupling to the channel occurred through local changes in membrane tension(Hayakawa et al., 2008).

Nevertheless, there is also evidence for a direct effect of membrane tension on channel opening. In some mammalian K^+ channels, it has been shown that the effect of membrane tension on pore opening can be mimicked by membrane curvature induced by polyunsaturated fatty acids (Patel et al., 2001; Vogel & Sheetz, 2006). A component of the vertebrate mechanosensitive channel, TRPC1, has been reconstituted in liposomes, and displays mechanosensitive opening in response

to moderate membrane tensions at ~10% of the maximum applied pressure that ruptured the liposomes (Maroto et al., 2005).

Mechanosensing by molecular motors

Individual myosin motor domains undergo a mechanochemical cycle in which they (1) begin in an ATP-bound state, unbound to actin, (2) hydrolyze ATP, "cock" its lever arm and bind actin, (3) release phosphate and bind actin more tightly, (4) undergo a large conformational change called the power stroke, that moves a lever-arm to produce force, (5) release ADP with an additional, smaller, conformational change while remaining tightly bound, and (6) re-bind ATP and release from the actin filament (Spudich, 1994; Sweeney & Houdusse, 2010). Although this mechanochemical cycle is common to all myosins, there are many families of myosins that have evolved to perform distinct cellular functions, and have developed different geometries in which the myosin motor domains are coupled to each other. For example, myosins I are monomers, myosins II associate into minifilaments of tens of motors, and myosins V are dimers that can walk along actin filaments (Cruz & Ostap, 2004; O'Connell et al., 2007).

Two of the most important parameters that determine how motors function are their duty ratio, the relative amounts of time the motor spends bound and unbound to F-actin, and their response to force. Myosin motors undergo several conformational changes in which parts of the molecule must move with or against an applied force. The force can modulate the rate of several kinetic steps, such as ADP or phosphate release, thereby modulating the duty ratio and overall speed of the motor (Sweeney & Houdusse, 2010). Myosins are finely tuned to respond to the forces that are relevant to the biological processes in which they participate, with different rate-limiting steps under force and different levels of coordination between motor domains, as the following examples illustrate (Cruz & Ostap, 2004).

The myosin I family, which participates in many processes involving organelle transport and is often associated with cellular membranes, also contains myosin-Ic, which is believed to be the motor responsible for tuning the tension in tip links between stereocilia to adapt their response to changes in sound amplitude (Holt et al., 2002). In order to maintain such tension, myosin-1c must be able to remain attached to its substrate for large periods of time. It was recently shown that myosin I is extremely mechanosensitive (Laakso et al., 2008). Its power stroke occurs in two sub-steps, the second of which is coupled to ADP release. The kinetic rate of the conformational change associated with ADP release is very strongly modulated by force. This has important consequences for the duty rate of the motor, because it cannot detach from F-actin until after ADP has been released. Under an applied force as low as 2 pN, the detachment rate of myosin 1 decreases 75-fold, thus allowing it to maintain tension between stereocilia (Laakso et al., 2008).

Mechanosensitivity is also important for myosin V, which is a family of two-headed myosin motors that walk along actin filaments with one motors stepping over the other in a hand-over-hand motion (Purcell et al., 2005). In this case, their long-range transport function requires them not to maintain tension for long periods of time, but to coordinate the mechanochemical cycles of the two motor domains to maximize processive walking along F-actin tracks for long distances (Cruz & Ostap, 2004). Specifically, the myosin motor domain that has just taken a step must then remain locked in a state that strongly binds F-actin, to allow the rear motor domain time to swing

around it and search for a new binding site ahead of the first motor domain (Purcell et al., 2005). Because the rate-limiting step for myosin V is ADP release (Rief et al., 2000), it is the key step that must be regulated to prevent premature motor detachment. Force-based coordination of the two motor domains is possible because as the molecule walks, there is a large asymmetry in the forces felt by the leading motor domain and the trailing motor domain. Purcell et al. showed that ADP release is strongly modulated by the direction of force applied to the myosin V motor domain (Rief et al., 2000). Force pulling forward does not affect the ADP release rate except on the motor's first step, while force pulling backwards prevents ADP release. This result indicates that the tension felt by the leading head while the lagging head is still bound to actin prevents ADP release in the front head. Because the ADP-bound state is locked onto F-actin, the lead head remains attached while the lagging head detaches and swings around to find a new binding site. Once tension is relieved, the leading head is free to resume its mechanochemical cycle and eventually detach for the next step.

These two examples show that mechanosensing by myosin motors can be used both as a response to external stimuli, such as an increase in tension like that applied by sound vibrations to stereocilia bundles, and as an integral part of the functioning of a motor in which tension is used to coordinate different motor domains.

Mechanosensing by active polymers

Lastly, we can consider active polymerization, such as the growth of actin filaments by monomer addition to their barbed ends, as a mechanosensitive process. Filament polymerization against a load, which generates force by the Brownian ratchet model described in a previous section of this chapter, is modulated by the applied force, and given enough force, can be stalled, just as a motor is stalled, when the chemical energy, in this case of monomer binding, is equal to the work required to push the load the distance of a monomer width (Howard, 2001). The response of this process to applied forces is augmented in actin networks by generation of new filaments through autocatalytic branching by the Arp2/3 complex (Parekh et al., 2005), as well as by the mechanical response of the network, in which filaments may bend or buckle once a critical force is reached (Chaudhuri et al., 2007), as described above. These processes work together to generate the force-velocity behavior of actin networks, which can be thought of as a form of mechanosensing that adjusts the speed of protrusion and the density of the network in response to force. Polymer-based mechanosensing also occurs in the microtubule cytoskeleton, as shown by in vitro experiments in which centrosome- or bead-centered asters can center themselves in a cell-sized enclosure as a result of the pushing, stall, buckling, and catastrophic depolymerization of the microtubules that comprise them (Holy et al., 1997; Faivre-Moskalenko & Dogterom, 2002).

Conclusions

Explanations of actin's role in cellular function to a lay audience often begin with a description of G-actin as a simple building block that strings itself into polymers, which can then be organized into the scaffolding that helps give animal cells their shape. Although that is not an inaccurate description, the last 70 years of research on this humble protein have revealed that,

together with its hundreds of binding partners, actin constitutes a formidably complex and versatile Lego set (Pollard & Cooper, 2009).

Actin networks are highly dynamic, with high turnover rates that are the result of a combination of F-actin's intrinsic biochemical properties, including a built-in timer based on ATP hydrolysis and phosphate release, and the action of many actin-binding proteins, such as actin nucleators and severing proteins (Pollard, 2007). They generate forces by polymerization, and respond to forces in ways that are dependent on the lengths and stiffnesses of their constituent filaments (Fletcher & Mullins, 2010). These mechanical properties are regulated by ABPs, as is the structure of F-actin itself. ABPs can allosterically affect each other's binding by altering the structure of F-actin. However, even in the absence of ABPs, F-actin is polymorphic (Galkin et al., 2010).

An emerging question in the field has been whether this polymorphism can be modulated by force, as part of a mechanosensing mechanism that does not depend on the classical paradigm of specialized force sensing molecules. Actin filaments are subject to a wide variety of forces in their cellular context, making force sensitivity potentially relevant for their biological function (Hoffman et al., 2011). Recent evidence showing alterations of F-actin structure and ABP binding in response to force suggests that F-actin may indeed be mechanosensitive (Galkin et al., 2012). We sought to test this hypothesis in the context of a central pathway of actin assembly, the dendritic actin network, and to develop a generally applicable method for probing the mechanosensitivity of F-actin-ABP interactions.

References

Abraham VC, Krishnamurthi V, Taylor DL, Lanni F (1999) The actin-based nanomachine at the leading edge of migrating cells. *Biophys J* 77, 1721-1732.

Akhmanova A, Steinmetz MO (2010) Microtubule +TIPs at a glance.. *J Cell Sci* 123, 3415-3419.

Akin O, Mullins RD (2008) Capping protein increases the rate of actin-based motility by promoting filament nucleation by the Arp2/3 complex. *Cell* 133, 841-851.

Alberts B, Johnson A, Lewis J, Raff M, Roberts K, Walter P (2007) Molecular Biology of the Cell. Garland Science.

Anderson TW, Vaughan AN, Cramer LP (2008) Retrograde flow and myosin II activity within the leading cell edge deliver F-actin to the lamella to seed the formation of graded polarity actomyosin II filament bundles in migrating fibroblasts. *Mol Biol Cell* 19, 5006-5018.

Arai Y, Yasuda R, Akashi K, Harada Y, Miyata H, Kinosita K Jr, Itoh H (1999) Tying a molecular knot with optical tweezers. *Nature* 399, 446-448.

Au Y (2004) The muscle ultrastructure: a structural perspective of the sarcomere. *Cell Mol Life Sci* 61, 3016-3033.

Bailly M, Ichetovkin I, Grant W, Zebda N, Machesky LM, Segall JE, Condeelis J (2001) The F-actin side binding activity of the Arp2/3 complex is essential for actin nucleation and lamellipod extension. *Curr Biol* 11, 620-625.

Balaban NQ, Schwarz US, Riveline D, Goichberg P, Tzur G, Sabanay I, Mahalu D, Safran S, Bershadsky A, Addadi L, Geiger B (2001) Force and focal adhesion assembly: a close relationship studied using elastic micropatterned substrates. *Nat Cell Biol* 3, 466-472.

Bamburg JR, Bernstein BW (2008) ADF/cofilin. *Curr Biol* 18, R273-R275.

Baneyx G, Baugh L, Vogel V (2002) Fibronectin extension and unfolding within cell matrix fibrils controlled by cytoskeletal tension. *Proc Natl Acad Sci U S A* 99, 5139-5143.

Bear JE, Svitkina TM, Krause M, Schafer DA, Loureiro JJ, Strasser GA, Maly IV, Chaga OY, Cooper JA, Borisy GG, Gertler FB (2002) Antagonism between Ena/VASP proteins and actin filament capping regulates fibroblast motility. *Cell* 109, 509-521.

ben-Avraham D, Tirion MM (1995) Dynamic and elastic properties of F-actin: a normal-modes analysis. *Biophys J* 68, 1231-1245.

Belmont LD, Orlova A, Drubin DG, Egelman EH (1999) A change in actin conformation associated with filament instability after P_i release. *Proc Natl Acad Sci U S A* 96, 29-34.

Beltzner CC, Pollard TD (2008) Pathway of actin filament branch formation by Arp2/3 complex. *J Biol Chem* 283, 7135-7144.

Bershadsky AD, Balaban NQ, Geiger B (2003) Adhesion-dependent cell mechanosensitivity. *Annu Rev Cell Dev Biol* 19, 677-695.

Blanchoin L, Amann KJ, Higgs HN, Marchand JB, Kaiser DA, Pollard TD (2000) Direct observation of dendritic actin filament networks nucleated by Arp2/3 complex and WASP/Scar proteins. *Nature* 404, 1007-1011.

Blanchoin L, Pollard TD (2002) Hydrolysis of ATP by polymerized actin depends on the bound divalent cation but not profilin. *Biochemistry* 41, 597-602.

Blanchoin L, Pollard TD (1999) Mechanism of interaction of Acanthamoeba actophorin (ADF/Cofilin) with actin filaments. *J Biol Chem* 274, 15538-15546.

Brangwynne CP, Koenderink GH, Barry E, Dogic Z, MacKintosh FC, Weitz DA (2007) Bending Dynamics of Fluctuating Biopolymers Probed by Automated High-Resolution Filament Tracking. *Biophys J* 93, 346-359.

Breitsprecher D, Koestler SA, Chizhov I, Nemethova M, Mueller J, Goode BL, Small JV, Rottner K, Faix J (2011) Cofilin cooperates with fascin to disassemble filopodial actin filaments. *J Cell Sci* 124, 3305-3318.

Bremer A, Millonig RC, Sutterlin R, Engel A, Pollard TD, Aebi U (1991) The structural basis for the intrinsic disorder of the actin filament: the "lateral slipping" model. *J Cell Biol* 115, 689-703.

Brieher WM, Kueh HY, Ballif BA, Mitchison TJ (2006) Rapid actin monomer-insensitive depolymerization of Listeria actin comet tails by cofilin, coronin, and Aip1. *J Cell Biol* 175, 315-324.

Bugyi B, Carlier M (2010) Control of actin filament treadmilling in cell motility. *Annu Rev Biophys* 39, 449-470.

Bugyi B, Papp G, Hild G, Lorinczy D, Nevalainen EM, Lappalainen P, Somogyi B, Nyitrai M (2006) Formins regulate actin filament flexibility through long range allosteric interactions. *J Biol Chem* 281, 10727-10736.

Burnette DT, Manley S, Sengupta P, Sougrat R, Davidson MW, Kachar B, Lippincott-Schwartz J (2011) A role for actin arcs in the leading-edge advance of migrating cells. *Nat Cell Biol* 13, 371-382.

Bustamante C, Marko JF, Siggia ED, Smith S (1994) Entropic elasticity of lambda-phage DNA. *Science* 265, 1599-600.

Cai Y, Rossier O, Gauthier NC, Biais N, Fardin M, Zhang X, Miller LW, Ladoux B, Cornish VW, Sheetz MP (2010) Cytoskeletal coherence requires myosin-IIA contractility. *J Cell Sci* 123, 413-423.

Cameron LA, Svitkina TM, Vignjevic D, Theriot JA, Borisy GG (2001) Dendritic organization of actin comet tails. *Curr Biol* 11, 130-135.

Campellone KG, Welch MD (2010) A nucleator arms race: cellular control of actin assembly. *Nat Rev Mol Cell Biol* 11, 237-251.

Carlier MF, Pantaloni D (1988) Binding of phosphate to F-ADP-actin and role of F-ADP-Pi-actin in ATP-actin polymerization. *J Biol Chem* 263, 817-825.

Carlier MF, Pantaloni D (1997) Control of actin dynamics in cell motility. *J Mol Biol* 269, 459-467.

Carlier MF, Pantaloni D, Evans JA, Lambooy PK, Korn ED, Webb MR (1988) The hydrolysis of ATP that accompanies actin polymerization is essentially irreversible. *FEBS Lett* 235, 211-214.

Carlier MF, Pantaloni D, Korn ED (1986) The effects of Mg^{2+} at the high-affinity and low-affinity sites on the polymerization of actin and associated ATP hydrolysis. *J Biol Chem* 261, 10785-10792.

Carlier MF, Pantaloni D, Korn ED (1986) Fluorescence measurements of the binding of cations to high-affinity and low-affinity sites on ATP-G-actin. *J Biol Chem* 261, 10778-10784.

Carlier MF, Ressad F, Pantaloni D (1999) Control of actin dynamics in cell motility. Role of ADF/cofilin. *J Biol Chem* 274, 33827-33830.

Caudron F, Barral Y (2009) Septins and the lateral compartmentalization of eukaryotic membranes. *Dev Cell* 16, 493-506.

Chan C, Beltzner CC, Pollard TD (2009) Cofilin dissociates Arp2/3 complex and branches from actin filaments. *Curr Biol* 19, 537-545.

Chan CE, Odde DJ (2008) Traction dynamics of filopodia on compliant substrates. *Science* 322, 1687-1691.

Chaudhuri O, Parekh SH, Fletcher DA (2007) Reversible stress softening of actin networks. *Nature* 445, 295-298.

Choi CK, Vicente-Manzanares M, Zareno J, Whitmore LA, Mogilner A, Horwitz AR (2008) Actin and α-actinin orchestrate the assembly and maturation of nascent adhesions in a myosin II motor-independent manner. *Nat Cell Biol* 10, 1039-1050.

Claessens MMAE, Semmrich C, Ramos L, Bausch AR (2008) Helical twist controls the thickness of F-actin bundles. *Proc Natl Acad Sci U S A* 105, 8819-8822.

Cooper JA, Buhle EL, Walker SB, Tsong TY, Pollard TD (1983) Kinetic evidence for a monomer activation step in actin polymerization. *Biochemistry* 22, 2193-2202.

Cooper JA, Sept D (2008) New insights into mechanism and regulation of actin capping protein. *Int Rev Cell Mol Biol* 267, 183-206.

Cotton J, Grant W (2004) Computational models of hair cell bundle mechanics: II. Simplified bundle models. *Hear Res* 197, 105-111.

Cramer LP (1999) Organization and polarity of actin filament networks in cells: implications for the mechanism of myosin-based cell motility. *Biochem Soc Symp* 65, 173-205.

Cramer LP, Siebert M, Mitchison TJ (1997) Identification of novel graded polarity actin filament bundles in locomoting heart fibroblasts: implications for the generation of motile force. *J Cell Biol* 136, 1287-1305.

Dalhaimer P, Pollard TD (2010) Molecular dynamics simulations of Arp2/3 complex activation. *Biophys J* 99, 2568-2576.

Dayel MJ, Holleran EA, Mullins RD (2001) Arp2/3 complex requires hydrolyzable ATP for nucleation of new actin filaments. *Proc Natl Acad Sci U S A* 98, 14871-14876.

Dayel MJ, Mullins RD (2004) Activation of Arp2/3 complex: addition of the first subunit of the new filament by a WASP protein triggers rapid ATP hydrolysis on Arp2. *PLoS Biol* 2, E91.

De La Cruz EM (2005) Cofilin binding to muscle and non-muscle actin filaments: isoform-dependent cooperative interactions. *J Mol Biol* 346, 557-64.

De La Cruz EM, Mandinova A, Steinmetz MO, Stoffler D, Aebi U, Pollard TD (2000) Polymerization and structure of nucleotide-free actin filaments. *J Mol Biol* 295, 517-526.

De La Cruz EM, Ostap EM (2004) Relating biochemistry and function in the myosin superfamily. *Curr Opin Cell Biol* 16, 61-67.

DeRosier DJ, Tilney LG (1982) How actin filaments pack into bundles. *Cold Spring Harb Symp Quant Biol* 46 Pt 2, 525-540.

Deguchi S, Ohashi T, Sato M (2006) Tensile properties of single stress fibers isolated from cultured vascular smooth muscle cells. *J Biomech* 39, 2603-2610.

del Rio A, Perez-Jimenez R, Liu R, Roca-Cusachs P, Fernandez JM, Sheetz MP (2009) Stretching single talin rod molecules activates vinculin binding. *Science* 323, 638-641.

Discher DE, Janmey P, Wang Y (2005) Tissue cells feel and respond to the stiffness of their substrate. *Science* 310, 1139-1143.

Discher DE, Mooney DJ, Zandstra PW (2009) Growth factors, matrices, and forces combine and control stem cells. *Science* 324, 1673-1677.

Doi M, Edwards SF (1988) The Theory of Polymer Dynamics. International Series of Monographs on Physics. Clarendon Press.

Dominguez R (2009) Actin filament nucleation and elongation factors--structure-function relationships. *Crit Rev Biochem Mol Biol* 44, 351-366.

Dominguez R, Holmes KC (2011) Actin structure and function. *Annu Rev Biophys* 40, 169-186.

DuFort CC, Paszek MJ, Weaver VM (2011) Balancing forces: architectural control of mechanotransduction. *Nat Rev Mol Cell Biol* 12, 308-319.

Dupuis DE, Guilford WH, Wu J, Warshaw DM (1997) Actin filament mechanics in the laser trap. *J Muscle Res Cell Motil* 18, 17-30.

Egelman EH, DeRosier DJ (1992) Image analysis shows that variations in actin crossover spacings are random, not compensatory. *Biophys J* 63, 1299-1305.

Egelman EH, Francis N, DeRosier DJ (1982) F-actin is a helix with a random variable twist. *Nature* 298, 131-135.

Egelman EH, Francis N, DeRosier DJ (1983) Helical disorder and the filament structure of F-actin are elucidated by the angle-layered aggregate. *J Mol Biol* 166, 605-629.

Ehrlicher AJ, Nakamura F, Hartwig JH, Weitz DA, Stossel TP (2011) Mechanical strain in actin networks regulates FilGAP and integrin binding to filamin A. *Nature* 478, 260-263.

Engler AJ, Sen S, Sweeney HL, Discher DE (2006) Matrix elasticity directs stem cell lineage specification. *Cell* 126, 677-689.

Etienne-Manneville S (2010) From signaling pathways to microtubule dynamics: the key players. *Curr Opin Cell Biol* 22, 104-111.

Eyckmans J, Boudou T, Yu X, Chen CS (2011) A hitchhiker's guide to mechanobiology. *Dev Cell* 21, 35-47.

Faivre-Moskalenko C, Dogterom M (2002) Dynamics of microtubule asters in microfabricated chambers: The role of catastrophes. *Proc Natl Acad Sci U S A* 99, 16788-16793.

Firat-Karalar EN, Welch MD (2011) New mechanisms and functions of actin nucleation. *Curr Opin Cell Biol* 23, 4-13.

Fletcher DA, Mullins RD (2010) Cell mechanics and the cytoskeleton. *Nature* 463, 485-492.

Footer MJ, Kerssemakers JWJ, Theriot JA, Dogterom M (2007) Direct measurement of force generation by actin filament polymerization using an optical trap. *Proc Natl Acad Sci U S A* 104, 2181-2186.

Forkey JN, Quinlan ME, Goldman YE (2005) Measurement of single macromolecule orientation by total internal reflection fluorescence polarization microscopy. *Biophys J* 89, 1261-1271.

Fujii T, Iwane AH, Yanagida T, Namba K (2010) Direct visualization of secondary structures of F-actin by electron cryomicroscopy. *Nature* 467, 724-728.

Fujiwara I, Vavylonis D, Pollard TD (2007) Polymerization kinetics of ADP- and ADP-Pi-actin determined by fluorescence microscopy. *Proc Natl Acad Sci U S A* 104, 8827-8832.

Galkin VE, Orlova A, Egelman EH (2012) Actin filaments as tension sensors. *Curr Biol* 22, R96-R101.

Galkin VE, Orlova A, Kudryashov DS, Solodukhin A, Reisler E, Schröder GF, Egelman EH (2011) Remodeling of actin filaments by ADF/cofilin proteins. *Proc Natl Acad Sci U S A* 108, 20568-20572.

Galkin VE, Orlova A, Lukoyanova N, Wriggers W, Egelman EH (2001) Actin depolymerizing factor stabilizes an existing state of F-actin and can change the tilt of F-actin subunits. *J Cell Biol* 153, 75-86.

Galkin VE, Orlova A, Schroder GF, Egelman EH (2010) Structural polymorphism in F-actin. *Nat Struct Mol Biol* 17, 1318-1323.

Galkin VE, Orlova A, VanLoock MS, Shvetsov A, Reisler E, Egelman EH (2003) ADF/cofilin use an intrinsic mode of F-actin instability to disrupt actin filaments. *J Cell Biol* 163, 1057-1066.

Gandhi M, Achard V, Blanchoin L, Goode BL (2009) Coronin switches roles in actin disassembly depending on the nucleotide state of actin. *Mol Cell* 34, 364-74.

Gandhi M, Goode BL (2008) Coronin: the double-edged sword of actin dynamics. *Subcell Biochem* 48, 72-87.

Garcia-Anoveros J, Corey DP (1997) The molecules of mechanosensation. *Annu Rev Neurosci* 20, 567-594.

Gardel ML, Kasza KE, Brangwynne CP, Liu J, Weitz DA (2008) Chapter 19: Mechanical response of cytoskeletal networks. *Methods Cell Biol* 89, 487-519.

Gardel ML, Sabass B, Ji L, Danuser G, Schwarz US, Waterman CM (2008) Traction stress in focal adhesions correlates biphasically with actin retrograde flow speed. *J Cell Biol* 183, 999-1005.

Gardel ML, Schneider IC, Aratyn-Schaus Y, Waterman CM (2010) Mechanical integration of actin and adhesion dynamics in cell migration. *Annu Rev Cell Dev Biol* 26, 315-333.

Geiger B, Bershadsky A, Pankov R, Yamada KM (2001) Transmembrane crosstalk between the extracellular matrix and the cytoskeleton. *Nat Rev Mol Cell Biol* 2, 793-805.

Geiger B, Spatz JP, Bershadsky AD (2009) Environmental sensing through focal adhesions. *Nat Rev Mol Cell Biol* 10, 21-33.

Ghassemi S, Meacci G, Liu S, Gondarenko AA, Mathur A, Roca-Cusachs P, Sheetz MP, Hone J (2012) Cells test substrate rigidity by local contractions on submicrometer pillars. *Proc Natl Acad Sci U S A* 109, 5328-5333.

Giannone G, Dubin-Thaler BJ, Rossier O, Cai Y, Chaga O, Jiang G, Beaver W, Döbereiner H, Freund Y, Borisy G, Sheetz MP (2007) Lamellipodial actin mechanically links myosin activity with adhesion-site formation. *Cell* 128, 561-575.

Gillespie PG, Muller U (2009) Mechanotransduction by hair cells: models, molecules, and mechanisms. *Cell* 139, 33-44.

Gittes F, Mickey B, Nettleton J, Howard J (1993) Flexural rigidity of microtubules and actin filaments measured from thermal fluctuations in shape. *J Cell Biol* 120, 923-934.

Goley ED, Rammohan A, Znameroski EA, Firat-Karalar EN, Sept D, Welch MD (2010) An actin-filament-binding interface on the Arp2/3 complex is critical for nucleation and branch stability. *Proc Natl Acad Sci U S A* 107, 8159-8164.

Goley ED, Rodenbusch SE, Martin AC, Welch MD (2004) Critical conformational changes in the Arp2/3 complex are induced by nucleotide and nucleation promoting factor. *Mol Cell* 16, 269-279.

Goley ED, Welch MD (2006) The ARP2/3 complex: an actin nucleator comes of age. *Nat Rev Mol Cell Biol* 7, 713-726.

Goode BL, Eck MJ (2007) Mechanism and function of formins in the control of actin assembly. *Annu Rev Biochem* 76, 593-627.

Gore J, Bryant Z, Nöllmann M, Le MU, Cozzarelli NR, Bustamante C (2006) DNA overwinds when stretched. *Nature* 442, 836-839.

Gournier H, Goley ED, Niederstrasser H, Trinh T, Welch MD (2001) Reconstitution of human Arp2/3 complex reveals critical roles of individual subunits in complex structure and activity. *Mol Cell* 8, 1041-1052.

Greenberg MJ, Wang CA, Lehman W, Moore JR (2008) Modulation of actin mechanics by caldesmon and tropomyosin. *Cell Motil Cytoskeleton* 65, 156-164.

Greene PR (1985) Thermal torsion of F-actin. *J Theor Biol* 117, 489-492.

Hamill OP, Martinac B (2001) Molecular Basis of Mechanotransduction in Living Cells. *Physiol Rev* 81, 685-740.

Hanson J (1967) Axial Period of Actin Filaments. *Nature* 213, 353-356.

Haviv L, Gillo D, Backouche F, Bernheim-Groswasser A (2008) A cytoskeletal demolition worker: myosin II acts as an actin depolymerization agent. *J Mol Biol* 375, 325-330.

Hayakawa K, Tatsumi H, Sokabe M (2011) Actin filaments function as a tension sensor by tension-dependent binding of cofilin to the filament. *J Cell Biol* 195, 721-727.

Hayakawa K, Tatsumi H, Sokabe M (2008) Actin stress fibers transmit and focus force to activate mechanosensitive channels. *J Cell Sci* 121, 496-503.

Hoffman BD, Grashoff C, Schwartz MA (2011) Dynamic molecular processes mediate cellular mechanotransduction. *Nature* 475, 316-323.

Holmes KC, Angert I, Kull FJ, Jahn W, Schröder RR (2003) Electron cryo-microscopy shows how strong binding of myosin to actin releases nucleotide. *Nature* 425, 423-427.

Holmes KC, Popp D, Gebhard W, Kabsch W (1990) Atomic model of the actin filament. *Nature* 347, 44-49.

Holt JR, Gillespie SKH, Provance DW, Shah K, Shokat KM, Corey DP, Mercer JA, Gillespie PG (2002) A chemical-genetic strategy implicates myosin-1c in adaptation by hair cells. *Cell* 108, 371-381.

Holy TE, Dogterom M, Yurke B, Leibler S (1997) Assembly and positioning of microtubule asters in microfabricated chambers. *Proc Natl Acad Sci U S A* 94, 6228-6231.

Hotulainen P, Lappalainen P (2006) Stress fibers are generated by two distinct actin assembly mechanisms in motile cells. *J Cell Biol* 173, 383-94.

Howard J (2001) Mechanics of motor proteins and the cytoskeleton. Sunderland, Mass.: Sinauer Associates, Inc.

Hu K, Ji L, Applegate KT, Danuser G, Waterman-Storer CM (2007) Differential transmission of actin motion within focal adhesions. *Science* 315, 111-115.

Ichetovkin I, Grant W, Condeelis J (2002) Cofilin produces newly polymerized actin filaments that are preferred for dendritic nucleation by the Arp2/3 complex. *Curr Biol* 12, 79-84.

Insall RH, Machesky LM (2009) Actin dynamics at the leading edge: from simple machinery to complex networks. *Dev Cell* 17, 310-322.

Isambert H, Venier P, Maggs AC, Fattoum A, Kassab R, Pantaloni D, Carlier MF (1995) Flexibility of actin filaments derived from thermal fluctuations. Effect of bound nucleotide, phalloidin, and muscle regulatory proteins. *J Biol Chem* 270, 11437-11444.

Iwasa JH, Mullins RD (2007) Spatial and Temporal Relationships between Actin-Filament Nucleation, Capping, and Disassembly. *Curr Biol* 17, 395 - 406.

Janmey PA, Weitz DA (2004) Dealing with mechanics: mechanisms of force transduction in cells. *Trends Biochem Sci* 29, 364-370.

Janmey PA, Winer JP, Murray ME, Wen Q (2009) The hard life of soft cells. *Cell Motil Cytoskeleton* 66, 597-605.

Jegou A, Niedermayer T, Orban J, Didry D, Lipowsky R, Carlier M, Romet-Lemonne G (2011) Individual Actin Filaments in a Microfluidic Flow Reveal the Mechanism of ATP Hydrolysis and Give Insight Into the Properties of Profilin. *PLoS Biol* 9, e1001161.

Johnson CP, Tang H, Carag C, Speicher DW, Discher DE (2007) Forced unfolding of proteins within cells. *Science* 317, 663-666.

Kabsch W, Mannherz HG, Suck D, Pai EF, Holmes KC (1990) Atomic structure of the actin:DNase I complex. *Nature* 347, 37-44.

Kaksonen M, Toret CP, Drubin DG (2006) Harnessing actin dynamics for clathrin-mediated endocytosis. *Nat Rev Mol Cell Biol* 7, 404-414.

Keren K, Pincus Z, Allen GM, Barnhart EL, Marriott G, Mogilner A, Theriot JA (2008) Mechanism of shape determination in motile cells. *Nature* 453, 475-480.

Kim E, Motoki M, Seguro K, Muhlrad A, Reisler E (1995) Conformational changes in subdomain 2 of G-actin: fluorescence probing by dansyl ethylenediamine attached to Gln-41. *Biophys J* 69, 2024-2032.

Koestler SA, Auinger S, Vinzenz M, Rottner K, Small JV (2008) Differentially oriented populations of actin filaments generated in lamellipodia collaborate in pushing and pausing at the cell front. *Nat Cell Biol* 10, 306-313.

Koestler SA, Rottner K, Lai F, Block J, Vinzenz M, Small JV (2009) F- and G-actin concentrations in lamellipodia of moving cells. *PLoS One* 4, e4810.

Kojima H, Ishijima A, Yanagida T (1994) Direct measurement of stiffness of single actin filaments with and without tropomyosin by in vitro nanomanipulation. *Proc Natl Acad Sci U S A* 91, 12962-12966.

Korn E, Carlier M, Pantaloni D (1987) Actin polymerization and ATP hydrolysis. *Science* 238, 638-644.

Koszul R, Kim KP, Prentiss M, Kleckner N, Kameoka S (2008) Meiotic chromosomes move by linkage to dynamic actin cables with transduction of force through the nuclear envelope. *Cell* 133, 1188-1201.

Kovar DR (2006) Arp2/3 ATP hydrolysis: to branch or to debranch? *Nat Cell Biol* 8, 783-785.

Kovar DR, Pollard TD (2004) Insertional assembly of actin filament barbed ends in association with formins produces piconewton forces. *Proc Natl Acad Sci U S A* 101, 14725-14730.

Kraning-Rush CM, Carey SP, Califano JP, Reinhart-King CA (2012) Quantifying traction stresses in adherent cells. *Methods Cell Biol* 110, 139-178.

Kueh HY, Brieher WM, Mitchison TJ (2008) Dynamic stabilization of actin filaments. *Proc Natl Acad Sci U S A* 105, 16531-16536.

Kueh HY, Charras GT, Mitchison TJ, Brieher WM (2008) Actin disassembly by cofilin, coronin, and Aip1 occurs in bursts and is inhibited by barbed-end cappers. *J Cell Biol* 182, 341-353.

Kueh HY, Mitchison TJ (2009) Structural plasticity in actin and tubulin polymer dynamics. *Science* 325, 960-963.

Kuhn TB, Bamburg JR (2008) Tropomyosin and ADF/cofilin as collaborators and competitors. *Adv Exp Med Biol* 644, 232-249.

Laakso JM, Lewis JH, Shuman H, Ostap EM (2008) Myosin I can act as a molecular force sensor. *Science* 321, 133-136.

Lange S, Xiang F, Yakovenko A, Vihola A, Hackman P, Rostkova E, Kristensen J, Brandmeier B, Franzen G, Hedberg B, Gunnarsson LG, Hughes SM, Marchand S, Sejersen T, Richard I, Edstrom L, Ehler E, Udd B, Gautel M (2005) The Kinase Domain of Titin Controls Muscle Gene Expression and Protein Turnover. *Science* 308, 1599-1603.

Le Clainche C, Pantaloni D, Carlier M (2003) ATP hydrolysis on actin-related protein 2/3 complex causes debranching of dendritic actin arrays. *Proc Natl Acad Sci U S A* 100, 6337-6342.

Lieleg O, Kayser J, Brambilla G, Cipelletti L, Bausch AR (2011) Slow dynamics and internal stress relaxation in bundled cytoskeletal networks. *Nat Mater* 10, 236-242.

Lin HW, Schneider ME, Kachar B (2005) When size matters: the dynamic regulation of stereocilia lengths. *Curr Opin Cell Biol* 17, 55-61.

Lin M, Galletta BJ, Sept D, Cooper JA (2010) Overlapping and distinct functions for cofilin, coronin and Aip1 in actin dynamics in vivo. *J Cell Sci* 123, 1329-1342.

Lionnet T, Joubaud S, Lavery R, Bensimon D, Croquette V (2006) Wringing Out DNA. *Phys. Rev. Lett.* 96, 178102.

Liu AP, Richmond DL, Maibaum L, Pronk S, Geissler PL, Fletcher DA (2008) Membrane-induced bundling of actin filaments. *Nat Phys* 4, 789-793.

Liu B, Kim T, Wang Y (2010) Live cell imaging of mechanotransduction. *J R Soc Interface* 7 Suppl 3, S365-S375.

Liu X, Pollack GH (2002) Mechanics of F-actin characterized with microfabricated cantilevers. *Biophys J* 83, 2705-2715.

Ludescher RD, Thomas DD (1988) Microsecond rotational dynamics of phosphorescent-labeled muscle cross-bridges. *Biochemistry* 27, 3343-3351.

Luxton GWG, Gomes ER, Folker ES, Vintinner E, Gundersen GG (2010) Linear arrays of nuclear envelope proteins harness retrograde actin flow for nuclear movement. *Science* 329, 956-959.

MacKintosh F, Kas J, Janmey P (1995) Elasticity of semiflexible biopolymer networks.. *Phys Rev Lett* 75, 4425-4428.

Machesky LM, Atkinson SJ, Ampe C, Vandekerckhove J, Pollard TD (1994) Purification of a cortical complex containing two unconventional actins from Acanthamoeba by affinity chromatography on profilin-agarose. *J Cell Biol* 127, 107-115.

Maciver SK (1998) How ADF/cofilin depolymerizes actin filaments. *Curr Opin Cell Biol* 10, 140-144.

Maciver SK, Zot HG, Pollard TD (1991) Characterization of actin filament severing by actophorin from Acanthamoeba castellanii. *J Cell Biol* 115, 1611-1620.

Mahaffy RE, Pollard TD (2006) Kinetics of the formation and dissociation of actin filament branches mediated by Arp2/3 complex. *Biophys J* 91, 3519-3528.

Maly IV, Borisy GG (2001) Self-organization of a propulsive actin network as an evolutionary process. *Proc Natl Acad Sci U S A* 98, 11324-11329.

Marcy Y, Prost J, Carlier M, Sykes C (2004) Forces generated during actin-based propulsion: a direct measurement by micromanipulation. *Proc Natl Acad Sci U S A* 101, 5992-5997.

Maroto R, Raso A, Wood TG, Kurosky A, Martinac B, Hamill OP (2005) TRPC1 forms the stretch-activated cation channel in vertebrate cells. *Nat Cell Biol* 7, 179-185.

Martin AC, Welch MD, Drubin DG (2006) Arp2/3 ATP hydrolysis-catalysed branch dissociation is critical for endocytic force generation. *Nat Cell Biol* 8, 826-833.

Matsushita S, Inoue Y, Adachi T (2012) Quantitative analysis of extension-torsion coupling of actin filaments. *Biochem Biophys Res Commun* 420, 710-713.

Matsushita S, Inoue Y, Hojo M, Sokabe M, Adachi T (2011) Effect of tensile force on the mechanical behavior of actin filaments. *J Biomech* 44, 1776-1781.

McCullough BR, Blanchoin L, Martiel J, De la Cruz EM (2008) Cofilin increases the bending flexibility of actin filaments: implications for severing and cell mechanics. *J Mol Biol* 381, 550-558.

McCullough BR, Grintsevich EE, Chen CK, Kang H, Hutchison AL, Henn A, Cao W, Suarez C, Martiel J, Blanchoin L, Reisler E, De La Cruz EM (2011) Cofilin-linked changes in actin filament flexibility promote severing. *Biophys J* 101, 151-159.

McGough A (1998) F-actin-binding proteins. *Curr Opin Struct Biol* 8, 166-176.

McGough A, Pope B, Chiu W, Weeds A (1997) Cofilin changes the twist of F-actin: implications for actin filament dynamics and cellular function. *J Cell Biol* 138, 771-781.

McGrath JL, Eungdamrong NJ, Fisher CI, Peng F, Mahadevan L, Mitchison TJ, Kuo SC (2003) The force-velocity relationship for the actin-based motility of *Listeria monocytogenes*. *Curr Biol* 13, 329-332.

McMurray MA, Thorner J (2009) Septins: molecular partitioning and the generation of cellular asymmetry. *Cell Div* 4, 18.

Medeiros NA, Burnette DT, Forscher P (2006) Myosin II functions in actin-bundle turnover in neuronal growth cones. *Nat Cell Biol* 8, 215-226.

Mejillano MR, Kojima S, Applewhite DA, Gertler FB, Svitkina TM, Borisy GG (2004) Lamellipodial versus filopodial mode of the actin nanomachinery: pivotal role of the filament barbed end. *Cell* 118, 363-373.

Melki R, Fievez S, Carlier MF (1996) Continuous monitoring of P_i release following nucleotide hydrolysis in actin or tubulin assembly using 2-amino-6-mercapto-7-methylpurine ribonucleoside and purine-nucleoside phosphorylase as an enzyme-linked assay. *Biochemistry* 35, 12038-12045.

Mellor H (2010) The role of formins in filopodia formation. *Biochim Biophys Acta* 1803, 191-200.

Michelot A, Drubin DG (2011) Building distinct actin filament networks in a common cytoplasm. *Curr Biol* 21, R560-R569.

Millman BM, Elliott GF, Lowy J (1967) Axial Period of Actin Filaments: X-ray Diffraction Studies. *Nature* 213, 356-358.

Mizuno H, Higashida C, Yuan Y, Ishizaki T, Narumiya S, Watanabe N (2011) Rotational movement of the formin mDia1 along the double helical strand of an actin filament.. *Science* 331, 80--83.

Mogilner A, Edelstein-Keshet L (2002) Regulation of actin dynamics in rapidly moving cells: a quantitative analysis. *Biophys J* 83, 1237-1258.

Mogilner A, Oster G (1996) Cell motility driven by actin polymerization. *Biophys J* 71, 3030-3045.

Mogilner A, Oster G (2003) Force generation by actin polymerization II: the elastic ratchet and tethered filaments. *Biophys J* 84, 1591-1605.

Mogilner A, Oster G (2003) Polymer motors: pushing out the front and pulling up the back. *Curr Biol* 13, R721-R733.

Mogilner A, Rubinstein B (2005) The Physics of Filopodial Protrusion. *Biophys J* 89, 782-795.

Mooseker MS, Tilney LG (1975) Organization of an actin filament-membrane complex. Filament polarity and membrane attachment in the microvilli of intestinal epithelial cells. *J Cell Biol* 67, 725-743.

Mseka T, Coughlin M, Cramer LP (2009) Graded actin filament polarity is the organization of oriented actomyosin II filament bundles required for fibroblast polarization. *Cell Motil Cytoskeleton* 66, 743-753.

Muhlrad A, Cheung P, Phan BC, Miller C, Reisler E (1994) Dynamic properties of actin. Structural changes induced by beryllium fluoride. *J Biol Chem* 269, 11852-11858.

Muhlrad A, Kudryashov D, Michael Peyser Y, Bobkov AA, Almo SC, Reisler E (2004) Cofilin induced conformational changes in F-actin expose subdomain 2 to proteolysis. *J Mol Biol* 342, 1559-1567.

Muhlrad A, Ringel I, Pavlov D, Peyser YM, Reisler E (2006) Antagonistic effects of cofilin, beryllium fluoride complex, and phalloidin on subdomain 2 and nucleotide-binding cleft in F-actin. *Biophys J* 91, 4490-4499.

Mullins RD, Stafford WF, Pollard TD (1997) Structure, subunit topology, and actin-binding activity of the Arp2/3 complex from Acanthamoeba. *J Cell Biol* 136, 331-343.

Mullins RD, Heuser JA, Pollard TD (1998) The interaction of Arp2/3 complex with actin: nucleation, high affinity pointed end capping, and formation of branching networks of filaments. *Proc Natl Acad Sci U S A* 95, 6181-6186.

Mullins RD, Pollard TD (1999) Structure and function of the Arp2/3 complex. *Curr Opin Struct Biol* 9, 244-249.

Murakami K, Yasunaga T, Noguchi TQP, Gomibuchi Y, Ngo KX, Uyeda TQP, Wakabayashi T (2010) Structural basis for actin assembly, activation of ATP hydrolysis, and delayed phosphate release. *Cell* 143, 275-287.

Nakamura F, Stossel TP, Hartwig JH (2011) The filamins: organizers of cell structure and function.. *Cell Adh Migr* 5, 160-169.

Naumanen P, Lappalainen P, Hotulainen P (2008) Mechanisms of actin stress fibre assembly. *J Microsc* 231, 446-454.

Nemethova M, Auinger S, Small JV (2008) Building the actin cytoskeleton: filopodia contribute to the construction of contractile bundles in the lamella. *J Cell Biol* 180, 1233-1244.

Nolen BJ, Littlefield RS, Pollard TD (2004) Crystal structures of actin-related protein 2/3 complex with bound ATP or ADP. *Proc Natl Acad Sci U S A* 101, 15627-15632.

Nolen BJ, Pollard TD (2007) Insights into the influence of nucleotides on actin family proteins from seven structures of Arp2/3 complex. *Mol Cell* 26, 449-457.

O'Connell CB, Tyska MJ, Mooseker MS (2007) Myosin at work: Motor adaptations for a variety of cellular functions. *Biochim Biophys Acta - Mol Cell Res* 1773, 615-630.

Oda T, Iwasa M, Aihara T, Maeda Y, Narita A (2009) The nature of the globular- to fibrous-actin transition. *Nature* 457, 441-445.

Oda T, Maeda Y (2010) Multiple Conformations of F-actin. *Structure* 18, 761-767.

Oosawa F (1980) The flexibility of F-actin. *Biophys Chem* 11, 443-446.

Orlova A, Egelman EH (2000) F-Actin Retains a Memory of Angular Order. *Biophys J* 78, 2180 - 2185.

Orlova A, Egelman EH (1997) Cooperative rigor binding of myosin to actin is a function of F-actin structure. *J Mol Biol* 265, 469-474.

Ott A, Magnasco M, Simon A, Libchaber A (1993) Measurement of the persistence length of polymerized actin using fluorescence microscopy. *Phys Rev E Stat Phys Plasmas Fluids Relat Interdiscip Topics* 48, R1642-R1645.

Otterbein LR, Graceffa P, Dominguez R (2001) The crystal structure of uncomplexed actin in the ADP state. *Science* 293, 708-711.

Oztug Durer ZA, Diraviyam K, Sept D, Kudryashov DS, Reisler E (2010) F-actin structure destabilization and DNase I binding loop: fluctuations mutational cross-linking and electron microscopy analysis of loop states and effects on F-actin. *J Mol Biol* 395, 544-557.

Padrick SB, Doolittle LK, Brautigam CA, King DS, Rosen MK (2011) Arp2/3 complex is bound and activated by two WASP proteins. *Proc Natl Acad Sci U S A* 108, E472-E479.

Padrick SB, Rosen MK (2010) Physical mechanisms of signal integration by WASP family proteins. *Annu Rev Biochem* 79, 707-735.

Pantaloni D, Boujemaa R, Didry D, Gounon P, Carlier M (2000) The Arp2/3 complex branches filament barbed ends: functional antagonism with capping proteins. *Nat Cell Biol* 2, 385-391.

Parekh SH, Chaudhuri O, Theriot JA, Fletcher DA (2005) Loading history determines the velocity of actin-network growth. *Nat Cell Biol* 7, 1219-1223.

Patel AJ, Lazdunski M, Honoré E (2001) Lipid and mechano-gated 2P domain K($^{+}$) channels. *Curr Opin Cell Biol* 13, 422-428.

Pavlov D, Muhlrad A, Cooper J, Wear M, Reisler E (2007) Actin filament severing by cofilin. *J Mol Biol* 365, 1350-1358.

Peskin CS, Odell GM, Oster GF (1993) Cellular motions and thermal fluctuations: the Brownian ratchet. *Biophysical Journal* 65, 316-324.

Pfaendtner J, Volkmann N, Hanein D, Dalhaimer P, Pollard TD, Voth GA (2012) Key Structural Features of the Actin Filament Arp2/3 Complex Branch Junction Revealed by Molecular Simulation. *Journal of Molecular Biology* 416, 148-161.

Pollard TD (2007) Regulation of actin filament assembly by Arp2/3 complex and formins. *Annu Rev Biophys Biomol Struct* 36, 451-477.

Pollard TD (1986) Assembly and dynamics of the actin filament system in nonmuscle cells. *J Cell Biochem* 31, 87-95.

Pollard TD (1986) Rate constants for the reactions of ATP- and ADP-actin with the ends of actin filaments. *J Cell Biol* 103, 2747-2754.

Pollard TD (1983) Measurement of rate constants for actin filament elongation in solution.. *Anal Biochem* 134, 406-412.

Pollard TD, Blanchoin L, Mullins RD (2000) Molecular mechanisms controlling actin filament dynamics in nonmuscle cells. *Annu Rev Biophys Biomol Struct* 29, 545-576.

Pollard TD, Blanchoin L, Mullins RD (2001) Actin dynamics. *J Cell Sci* 114, 3-4.

Pollard TD, Borisy GG (2003) Cellular motility driven by assembly and disassembly of actin filaments. *Cell* 112, 453-465.

Pollard TD, Cooper JA (1986) Actin and actin-binding proteins. A critical evaluation of mechanisms and functions. *Annu Rev Biochem* 55, 987-1035.

Pollard TD, Cooper JA (2009) Actin, a central player in cell shape and movement. *Science* 326, 1208-1212.

Pollard TD, Weeds AG (1984) The rate constant for ATP hydrolysis by polymerized actin. *FEBS Lett* 170, 94-98.

Pollitt AY, Insall RH (2009) WASP and SCAR/WAVE proteins: the drivers of actin assembly. *J Cell Sci* 122, 2575-2578.

Ponti A, Machacek M, Gupton SL, Waterman-Storer CM, Danuser G (2004) Two distinct actin networks drive the protrusion of migrating cells. *Science* 305, 1782-1786.

Prass M, Jacobson K, Mogilner A, Radmacher M (2006) Direct measurement of the lamellipodial protrusive force in a migrating cell. *J Cell Biol* 174, 767-772.

Pring M, Weber A, Bubb MR (1992) Profilin-actin complexes directly elongate actin filaments at the barbed end. *Biochemistry* 31, 1827-1836.

Prochniewicz E, Chin HF, Henn A, Hannemann DE, Olivares AO, Thomas DD, De La Cruz EM (2010) Myosin isoform determines the conformational dynamics and cooperativity of actin filaments in the strongly bound actomyosin complex. *J Mol Biol* 396, 501-509.

Prochniewicz E, Janson N, Thomas DD, De la Cruz EM (2005) Cofilin increases the torsional flexibility and dynamics of actin filaments. *J Mol Biol* 353, 990-1000.

Prochniewicz E, Katayama E, Yanagida T, Thomas DD (1993) Cooperativity in F-actin: chemical modifications of actin monomers affect the functional interactions of myosin with unmodified monomers in the same actin filament. *Biophys J* 65, 113-123.

Prochniewicz E, Thomas DD (1997) Perturbations of functional interactions with myosin induce long-range allosteric and cooperative structural changes in actin. *Biochemistry* 36, 12845-12853.

Prochniewicz E, Zhang Q, Howard EC, Thomas DD (1996) Microsecond rotational dynamics of actin: spectroscopic detection and theoretical simulation. *J Mol Biol* 255, 446-457.

Prochniewicz E, Zhang Q, Janmey PA, Thomas DD (1996) Cooperativity in F-actin: binding of gelsolin at the barbed end affects structure and dynamics of the whole filament. *J Mol Biol* 260, 756-766.

Pronk S, Geissler PL, Fletcher DA (2008) Limits of filopodium stability. *Phys Rev Lett* 100, 258102.

Provenzano PP, Keely PJ (2011) Mechanical signaling through the cytoskeleton regulates cell proliferation by coordinated focal adhesion and Rho GTPase signaling. *J Cell Sci* 124, 1195-1205.

Puchner EM, Alexandrovich A, Kho AL, Hensen U, Schafer LV, Brandmeier B, Grater F, Grubmuller H, Gaub HE, Gautel M (2008) Mechanoenzymatics of titin kinase. *Proceedings of the National Academy of Sciences* 105, 13385-13390.

Purcell TJ, Sweeney HL, Spudich JA (2005) A force-dependent state controls the coordination of processive myosin V. *Proc Natl Acad Sci U S A* 102, 13873-13878.

Quinlan ME, Heuser JE, Kerkhoff E, Mullins RD (2005) Drosophila Spire is an actin nucleation factor. *Nature* 433, 382-388.

Reisler E, Egelman EH (2007) Actin structure and function: what we still do not understand. *J Biol Chem* 282, 36133-36137.

Ridley AJ (2011) Life at the leading edge. *Cell* 145, 1012-1022.

Rief M, Rock RS, Mehta AD, Mooseker MS, Cheney RE, Spudich JA (2000) Myosin-V stepping kinetics: a molecular model for processivity. *Proc Natl Acad Sci U S A* 97, 9482-9486.

Risca VI, Wang EB, Chaudhuri O, Chia JJ, Geissler PL, Fletcher DA (2012) Actin filament curvature biases branching direction. *Proc Natl Acad Sci U S A* 109, 2913-2918.

Riveline D, Zamir E, Balaban NQ, Schwarz US, Ishizaki T, Narumiya S, Kam Z, Geiger B, Bershadsky AD (2001) Focal contacts as mechanosensors: externally applied local mechanical force induces growth of focal contacts by an mDia1-dependent and ROCK-independent mechanism. *J Cell Biol* 153, 1175-1186.

Robinson RC, Turbedsky K, Kaiser DA, Marchand JB, Higgs HN, Choe S, Pollard TD (2001) Crystal structure of Arp2/3 complex. *Science* 294, 1679-1684.

Roll-Mecak A, McNally FJ (2010) Microtubule-severing enzymes. *Curr Opin Cell Biol* 22, 96-103.

Rouiller I, Xu X, Amann KJ, Egile C, Nickell S, Nicastro D, Li R, Pollard TD, Volkmann N, Hanein D (2008) The structural basis of actin filament branching by the Arp2/3 complex. *J Cell Biol* 180, 887-895.

Sablin EP, Dawson JF, VanLoock MS, Spudich JA, Egelman EH, Fletterick RJ (2002) How does ATP hydrolysis control actin's associations? *Proc Natl Acad Sci U S A* 99, 10945-10947.

Saunders MG, Voth GA (2011) Water molecules in the nucleotide binding cleft of actin: effects on subunit conformation and implications for ATP hydrolysis. *J Mol Biol* 413, 279-291.

Sawada Y, Tamada M, Dubin-Thaler BJ, Cherniavskaya O, Sakai R, Tanaka S, Sheetz MP (2006) Force sensing by mechanical extension of the Src family kinase substrate p130Cas. *Cell* 127, 1015-1026.

Schmid MF, Sherman MB, Matsudaira P, Chiu W (2004) Structure of the acrosomal bundle. *Nature* 431, 104-107.

Schneider ME, Belyantseva IA, Azevedo RB, Kachar B (2002) Rapid renewal of auditory hair bundles. *Nature* 418, 837-838.

Sept D, McCammon JA (2001) Thermodynamics and kinetics of actin filament nucleation. *Biophys J* 81, 667-674.

Shaevitz JW, Fletcher DA (2007) Load fluctuations drive actin network growth. *Proc Natl Acad Sci U S A* 104, 15688-15692.

Sharma S, Grintsevich EE, Phillips ML, Reisler E, Gimzewski JK (2011) Atomic force microscopy reveals drebrin induced remodeling of f-actin with subnanometer resolution. *Nano Lett* 11, 825-827.

Shin JH, Tam BK, Brau RR, Lang MJ, Mahadevan L, Matsudaira P (2007) Force of an actin spring. *Biophys J* 92, 3729-3733.

Shyy JY, Chien S (2002) Role of Integrins in Endothelial Mechanosensing of Shear Stress. *Circulation Research* 91, 769-775.

Smith SB, Finzi L, Bustamante C (1992) Direct mechanical measurements of the elasticity of single DNA molecules by using magnetic beads. *Science* 258, 1122-1126.

Spudich JA (1994) How molecular motors work. *Nature* 372, 515-518.

Stokes DL, DeRosier DJ (1987) The variable twist of actin and its modulation by actin-binding proteins. *J Cell Biol* 104, 1005-1017.

Storm C, Pastore JJ, MacKintosh FC, Lubensky TC, Janmey PA (2005) Nonlinear elasticity in biological gels. *Nature* 435, 191-194.

Suarez C, Roland J, Boujemaa-Paterski R, Kang H, McCullough BR, Reymann A, Guérin C, Martiel J, De la Cruz EM, Blanchoin L (2011) Cofilin tunes the nucleotide state of actin filaments and severs at bare and decorated segment boundaries. *Curr Biol* 21, 862-868.

Sugita S, Adachi T, Ueki Y, Sato M (2011) A novel method for measuring tension generated in stress fibers by applying external forces. *Biophys J* 101, 53-60.

Sukumvanich P, DesMarais V, Sarmiento CV, Wang Y, Ichetovkin I, Mouneimne G, Almo S, Condeelis J (2004) Cellular localization of activated N-WASP using a conformation-sensitive antibody. *Cell Motil Cytoskeleton* 59, 141-152.

Suzuki N, Miyata H, Ishiwata S, Kinosita KJ (1996) Preparation of bead-tailed actin filaments: estimation of the torque produced by the sliding force in an in vitro motility assay. *Biophys J* 70, 401-408.

Svitkina TM, Borisy GG (1999) Arp2/3 complex and actin depolymerizing factor/cofilin in dendritic organization and treadmilling of actin filament array in lamellipodia. *J Cell Biol* 145, 1009-1026.

Svitkina TM, Borisy GG (1999) Progress in protrusion: the tell-tale scar. *Trends Biochem Sci* 24, 432-436.

Svitkina TM, Bulanova EA, Chaga OY, Vignjevic DM, Kojima S, Vasiliev JM, Borisy GG (2003) Mechanism of filopodia initiation by reorganization of a dendritic network. *J Cell Biol* 160, 409-421.

Svitkina TM, Verkhovsky AB, McQuade KM, Borisy GG (1997) Analysis of the actin-myosin II system in fish epidermal keratocytes: mechanism of cell body translocation. *J Cell Biol* 139, 397-415.

Sweeney HL, Houdusse A (2010) Structural and Functional Insights into the Myosin Motor Mechanism. *Annu Rev Biophys* 39, 539-557.

Tan JL, Tien J, Pirone DM, Gray DS, Bhadriraju K, Chen CS (2003) Cells lying on a bed of microneedles: an approach to isolate mechanical force. *Proc Natl Acad Sci U S A* 100, 1484-1489.

Ti S, Jurgenson CT, Nolen BJ, Pollard TD (2011) Structural and biochemical characterization of two binding sites for nucleation-promoting factor WASp-VCA on Arp2/3 complex. *Proc Natl Acad Sci U S A* 108, E463-E471.

Tilney LG, Tilney MS, DeRosier DJ (1992) Actin filaments, stereocilia, and hair cells: how cells count and measure. *Annu Rev Cell Biol* 8, 257-274.

Tsuda Y, Yasutake H, Ishijima A, Yanagida T (1996) Torsional rigidity of single actin filaments and actin-actin bond breaking force under torsion measured directly by in vitro micromanipulation. *Proc Natl Acad Sci U S A* 93, 12937-12942.

van Mameren J, Vermeulen KC, Gittes F, Schmidt CF (2009) Leveraging single protein polymers to measure flexural rigidity. *J Phys Chem B* 113, 3837-3844.

Vavylonis D, Yang Q, O'Shaughnessy B (2005) Actin polymerization kinetics, cap structure, and fluctuations. *Proc Natl Acad Sci U S A* 102, 8543-8548.

Verkhovsky AB, Borisy GG (1993) Non-sarcomeric mode of myosin II organization in the fibroblast lamellum. *J Cell Biol* 123, 637-652.

Verkhovsky AB, Chaga OY, Schaub S, Svitkina TM, Meister J, Borisy GG (2003) Orientational order of the lamellipodial actin network as demonstrated in living motile cells. *Mol Biol Cell* 14, 4667-4675.

Verkhovsky AB, Svitkina TM, Borisy GG (1995) Myosin II filament assemblies in the active lamella of fibroblasts: their morphogenesis and role in the formation of actin filament bundles. *J Cell Biol* 131, 989-1002.

Vinzenz M, Nemethova M, Schur F, Mueller J, Narita A, Urban E, Winkler C, Schmeiser C, Koestler SA, Rottner K, Resch GP, Maeda Y, Small JV (2012) Actin branching in the initiation and maintenance of lamellipodia. *J Cell Sci,* Advance Online Publication, March 19, 2012, doi:10.1242/jcs.107623.

Vogel V, Sheetz M (2006) Local force and geometry sensing regulate cell functions. *Nat Rev Mol Cell Biol* 7, 265-275.

Vogel V, Sheetz MP (2009) Cell fate regulation by coupling mechanical cycles to biochemical signaling pathways. *Curr Opin Cell Biol* 21, 38-46.

Volkmann N, DeRosier D, Matsudaira P, Hanein D (2001) An atomic model of actin filaments cross-linked by fimbrin and its implications for bundle assembly and function. *J Cell Biol* 153, 947-956.

Vollrath MA, Kwan KY, Corey DP (2007) The micromachinery of mechanotransduction in hair cells. *Annu Rev Neurosci* 30, 339-365.

Wang CA, Coluccio LM (2010) New insights into the regulation of the actin cytoskeleton by tropomyosin. *Int Rev Cell Mol Biol* 281, 91-128.

Watanabe N, Mitchison TJ (2002) Single-molecule speckle analysis of actin filament turnover in lamellipodia. *Science* 295, 1083-1086.

Wear MA, Yamashita A, Kim K, Maéda Y, Cooper JA (2003) How capping protein binds the barbed end of the actin filament. *Curr Biol* 13, 1531-1537.

Weichsel J, Schwarz US (2010) Two competing orientation patterns explain experimentally observed anomalies in growing actin networks. *Proc Natl Acad Sci U S A* 107, 6304-6309.

Weichsel J, Urban E, Small J, Schwarz U (2012) Reconstructing the orientation distribution of actin filaments in the lamellipodium of migrating keratocytes from electron microscopy tomography data.. *Cytometry A*, Advance Online Publication, April 12, 2012, 10.1002/cyto.a.22050.

Welch MD, Iwamatsu A, Mitchison TJ (1997) Actin polymerization is induced by Arp2/3 protein complex at the surface of Listeria monocytogenes. *Nature* 385, 265-269.

Welch MD, Mullins RD (2002) Cellular control of actin nucleation. *Annu Rev Cell Dev Biol* 18, 247-288.

Wickstead B, Gull K (2011) The evolution of the cytoskeleton. *J Cell Biol* 194, 513-525.

Yamaoka H, Adachi T (2010) Coupling between axial stretch and bending/twisting deformation of actin filaments caused by a mismatched centroid from the center axis. *International Journal of Mechanical Sciences* 52, 329-333.

Yanagida T, Nakase M, Nishiyama K, Oosawa F (1984) Direct observation of motion of single F-actin filaments in the presence of myosin. *Nature* 307, 58-60.

Yang C, Svitkina T (2011) Filopodia initiation: focus on the Arp2/3 complex and formins.. *Cell Adh Migr* 5, 402-408.

Yasuda R, Miyata H, Kinosita KJ (1996) Direct measurement of the torsional rigidity of single actin filaments. *J Mol Biol* 263, 227-236.

Yoshimura H, Nishio T, Mihashi K, Kinosita KJ, Ikegami A (1984) Torsional motion of eosin-labeled F-actin as detected in the time-resolved anisotropy decay of the probe in the sub-millisecond time range. *J Mol Biol* 179, 453-467.

Zuchero JB (2007) In vitro actin assembly assays and purification from Acanthamoeba. *Methods Mol Biol* 370, 213-26.

Zuchero JB, Coutts AS, Quinlan ME, Thangue NBL, Mullins RD (2009) P53-cofactor JMY is a multifunctional actin nucleation factor. *Nat Cell Biol* 11, 451-459.

Chapter 2. A Fluorescence Microscopy Assay for Imposing and Measuring Curvature of Actin Filaments

The work described in this chapter was done with help from Ms. Jia Jun Chia (on Arp2/3), Professor Gerard Marriott and Dr. David Richmond (on tropomyosin). It has not been previously published elsewhere, but served as preliminary work for the published work described in Chapter 3.

Introduction

The structural and motile roles played by actin networks involve mechanical loads from elasticity of surrounding cytoskeletal networks, membrane tension or rigidity, myosin motors, forces exerted by neighboring cells, and extracellular obstacles (DuFort et al., 2011; Eyckmans et al., 2011; Fletcher & Mullins, 2010). The broad range of geometries adopted by actin networks also pose geometric constraints on actin filaments that may be important in regulating their behavior and their ability to support forces, such as is the case in actin bundles (Bathe et al., 2008; Schmid et al., 2004; Vignjevic et al., 2006). A key challenge in cell biology research is to understand how such forces and mechanical constraints regulate the structure and dynamics of the actin cytoskeleton.

This challenge has been addressed by the development of techniques that can control the mechanical inputs and visualize or otherwise detect the changing morphology or dynamics of the actin structure under investigation. Many indirect means, such as biochemical perturbation by myosin inhibition and actin depolymerization (Ponti et al., 2004), genetic approaches that alter or inhibit ABP function (Iwasa & Mullins, 2007; Leyman et al., 2009), or changes in membrane area by the addition of detergents (Raucher & Sheetz, 2000), have been used, but the information that can be gained from such experiments is often only on the whole-cell scale, and can be complicated by unwanted changes in network organization or biochemical interactions that accompany such perturbations. Force has been applied more directly, to detect differential binding of ABPs and other regulatory proteins to actin networks under tension (Ehrlicher et al., 2011; Galkin et al., 2012; Hayakawa et al., 2011; Uyeda et al., 2011) or to measure the force-velocity curve as a growing actin network is stalled by opposing force and to probe its mechanical properties (Gerbal et al., 2000; Heinemann et al., 2011; Marcy et al., 2004; McGrath et al., 2003; Parekh et al., 2005; Prass et al., 2006; Wiesner et al., 2003). Lastly, several different kinds of microrheology have probed the mechanical properties of actin networks in vivo and in vitro, showing that actin networks can take on a surprising range of stiffnesses, which are respond to external stress or contractile elements of the network (Chaudhuri et al., 2007; Stricker et al., 2010). Such experiments have characterized the mechanical and force response properties of many actin structures as a whole. Although many open questions remain on the cellular and subcellular scale, the success of these types of experiments in revealing the complex behavior of actin structures, in terms of both material properties and dynamics, has underscored the necessity to understand how the individual building blocks, from single filaments to simple interacting units of filaments and ABPs, respond to forces and geometric constraints.

Tremendous progress in understanding the mechanochemistry of myosin motors has been made with optical trap based experiments in which force can be applied to stall or unbind the motor, while the stepping of the motors is simultaneously tracked (Finer et al., 1994; Spudich, 2011). Experiments with other actin-binding proteins or with single actin filaments have generally combined a force probe with fluorescence imaging, or used fluorescence imaging to quantify thermal fluctuations. The unbinding of the actin crosslinking proteins α-actinin and filamin, as well as the Arp2/3-NPF complex, from the side of actin filaments, has been measured with optical traps, using fluorescence microscopy to visualize the crosslinked actin filaments before they are pulled (Ferrer et al., 2008; Fujiwara et al., 2002). The mechanical properties of actin, as

described in the previous chapter, have been measured with fluorescence microscopy used to observe either thermally driven fluctuations, or to monitor the filament's state as a force probe such as a microneedle or optical trap is used to apply force to the filament or constrain its shape (Arai et al., 1999; Gittes et al., 1993; Isambert et al., 1995; Kojima et al., 1994; Ott et al., 1993; Tsuda et al., 1996; Yanagida et al., 1984). More recently, fluorescence microscopy has been used more directly to measure the tension-dependent fluorescence of a molecule covalently linked to monomers in an actin filament that was stretched by an optical trap (Shimozawa & Ishiwata, 2009).

The set of biochemical events that give rise to dendritic actin networks, namely F-actin binding and branch nucleation by the Arp2/3 complex, is challenging to study for several reasons. In vivo and in realistic reconstituted systems, dendritic actin networks as nucleated near membranes or NPF-coated surfaces are extremely dense (Cameron et al., 2001; Svitkina & Borisy, 1999; Svitkina et al., 1997; Vinzenz et al., 2012), eluding the ability of even super-resolution light microscopy techniques to resolve individual filaments (Xu et al., 2012). Electron microscopy (EM) studies have studied paracrystal-induced geometric constraints (Egelman et al., 1983; Mooseker & Tilney, 1975; Orlova & Egelman, 2000), bundling-induced constraints or compared different regions of a cell that are at different stages of the protrusion-retraction cycle (Koestler et al., 2008), but dynamics cannot be captured by EM, and filament shape can only be expected to be preserved in cryo-EM (Schmid et al., 2004). Lastly, dendritic actin networks near membranes, where most active nucleation takes place, are largely under compression due to membrane tension and bending rigidity (Raucher & Sheetz, 2000; Raucher & Sheetz, 1999). Because of the semiflexible nature of actin filaments (Howard, 2001), application of compressive forces involves filament bending and buckling, which is only practically compatible with imaging of branch nucleation if the bent or buckled filament can be constrained to a two-dimensional plane.

Assay criteria

We sought to devise an assay that would permit us to constrain actin filaments in bent conformations, while also allowing us to image branches nucleated by the Arp2/3 complex. Such an assay must satisfy the following criteria:

(1) actin filaments must be fluorescently labeled;

(2) actin filaments must lie on a horizontal plane to allow high-resolution fluorescence microscopy;

(3) actin filaments (and their branches) must be at low enough density to allow the shapes and locations of individual filaments to be resolved;

(4) it must be possible to know the shape or stress state of the mother filaments at the time of branching, which implies that either the filaments are constrained during branch nucleation, or that branch nucleation is observed in real time;

(5) mother filaments which are under constraint, and daughter filaments, which are not under constraints, must be somehow differentiated; and

(6) it must be possible to observe sufficient branching events to allow a thorough statistical analysis of branch nucleation as a function of the local stress or strain on the mother filament.

Actin filament labeling and immobilization

We were inspired by other studies that have imaged fluorescently labeled actin filaments on surfaces, as part of the myosin motility assay, to characterize the products of actin assembly assays, and to directly observe actin and ABP kinetics with TIRF microscopy. Generally, these assays fall into two categories: (a) those that use real-time imaging of filament polymerization and ABP binding or function (such as branching by Arp2/3 or severing by cofilin) and (b) those that image filaments after polymerization or ABP binding has occurred. We chose to pursue the second general strategy primarily because it allows us to image and analyze a much larger number of actin filaments and therefore to detect much more subtle effects of actin filament bending, thus satisfying criterion (6), above. In addition, we did not have reliable access to a TIRF microscope at the time when the Arp2/3 experiments were performed, and the signal to noise ratio from confocal imaging of actin filament growth is too low to precisely measure filament shape (Ichetovkin et al., 2002).

In particular, we drew on the work of Blanchoin et al. and Amann et al., who employed a two-color fluorescent labeling strategy that differentiates new actin growth from pre-polymerized mother filaments, and satisfies criteria (1,2,3,5, and 6) above. They allowed branch nucleation with in the presence of green fluorescent phalloidin to occur from mother filaments saturated with red fluorescent phalloidin in solution, and deposited the resulting branch filaments on a surface for imaging (Amann & Pollard, 2001; Blanchoin et al., 2000).

Our work is similar to that of Ichetovkin et al., who aimed to control the nucleotide state of the mother filaments separately from the nucleotide state of the freshly polymerized actin, and used a similar two-color fluorescent labeling strategy combining biotinylated mother filaments polymerized in the presence of green fluorescent phalloidin with red fluorescent labeled G-actin present during branch nucleation (Ichetovkin et al., 2002). Rather than allowing branching to occur in solution, they pre-immobilized mother filaments on glass surfaces using anti-biotin antibodies. However, they did not analyze the impact of mother filament bending on branch nucleation.

To fully satisfy the criteria for measuring the effect of physical constraints on branch nucleation, and in particular, criterion (4), we sought a filament immobilization strategy that would create very stable and specific links between the glass surface and the mother filaments. The streptavidin-biotin interaction is specific and is one of the strongest known noncovalent interactions, with a dissociation half-life of 290,000 s (80 hours) (Piran & Riordan, 1990), and the ability to withstand forces up to ~300 pN (Wong et al., 1999). This very stable interaction allowed us to immobilize mother filaments in an essentially irreversible manner. Filaments did not exhibit fluctuations in shape once immobilized on the surface (Figure 9). The amount of biotinylated actin included in the mother filaments, 10% in most experiments, was tuned to minimize unbound filament segments (which are not under a clearly measurable constraint) that were detected by fluorescence microscopy because they are freely thermally fluctuating, while also keeping the total fraction of biotinylated actin monomers as low as possible, to minimize

any artifacts in APB binding or filament dynamics that may occur from the chemical modification of monomers. It has been shown that labeled actin monomers polymerize with different kinetics than unlabeled actin (Amann & Pollard, 2001), and therefore there may be other subtle differences between labeled monomer conformation and unlabeled monomer conformation in F-actin.

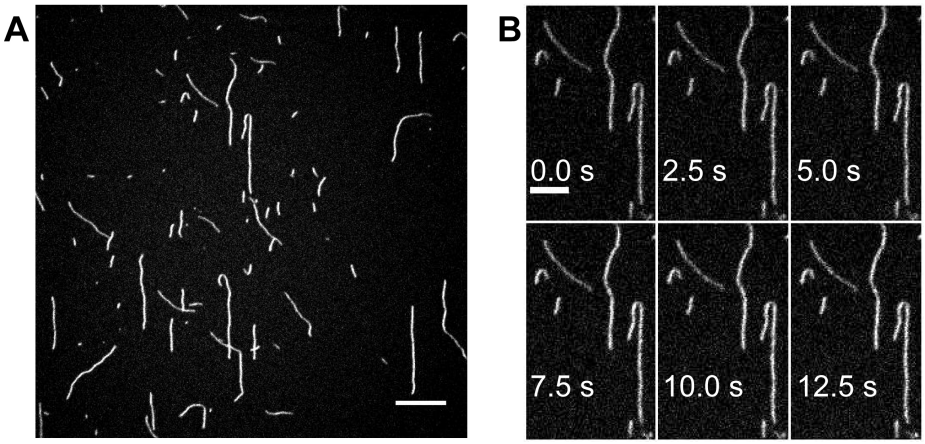

Figure 9: Actin immobilization on a surface. (A) Biotinylated (10%) F-actin stabilized and labeled by TRITC-phalloidin was immobilized on a surface coated with biotinylated BSA and streptavidin. Bar: 10 µm. (B) The shape of the immobilized filaments was robust to thermal fluctuations. Images represent a subset of the larger image shown in A. Bar: 5 µm.

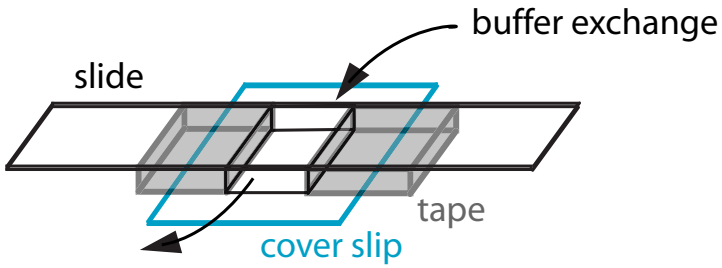

Figure 10: Flow channel assembly. The flow channel was assembled from a glass slide, a # 1.5 cover slip, and two pieces of 3M Scotch permanent double sided tape. The slides were cleaned with detergent, while the cover slip was cleaned or etched (with KOH/ETOH, acid solution, or oxygen plasma; see Materials and Methods) before assembly of the chamber. Cleaned cover slips were used immediately to assemble a chamber, < 1 min for plasma-cleaned glass, or stored submerged in water or ethanol before being dried and used immediately. Assembled chambers were quickly filled with the first surface coating solution. During incubation, flow channels were stored in a closed box with a platform that allowed water to be placed under, but not in contact with, the flow channel, to prevent evaporation.

Mother filaments were polymerized from a mixture of unlabeled and biotinylated G-actin and incubated with red fluorescent phalloidin, which stabilized and fluorescently labeled them. A more biologically relevant version of this protocol without phalloidin pre-stabilization of mother filaments is described in the following chapter. Because filaments had to be immobilized before branching could take place, we performed these experiments in flow channels constructed from a slide, a cover slip, and double-stick tape which was used to create a ~6 mm x 0.08 mm channel with a volume of ~14 μL (Figure 10). The glass surface of the channel was coated with streptavidin (described in detail below), before pre-polymerized mother filaments were diluted, flowed in, incubated, and washed, by flowing through 5-10 channel volumes of buffer to remove unbound filaments.

Because different parts of the filament bind the surface at different times, we found that we were able to use flow of the mother filament containing solution and of the wash buffer to exert some control over the shape of the immobilized filaments. By flowing 3-4 volumes of mother filament solution through the channel in one direction, and reversing the direction of the flow for an equal volume, long filaments were entrained by the reversed flow as they bound to the surface, creating tight hairpin turns with radii of curvature as small as 500 nm (Figure 9, Figure 11). Flow rates were not precisely controlled, because buffer was flown through the channel by pipetting fluid in one end and wicking the other end with filter paper, quickly rotating the filter paper to a dry section to maximize the wicking rate. The fast flow rate used to create hairpin filaments was ~4.4 μL/s. Higher flow rates are achievable by using vacuum suction, but were not employed in most cases because the channel was occasionally emptied of fluid by the vacuum, rendering the surface unusable. The creation of hairpin turns was most efficient for long filaments on the order of 20 μm or more that form in the presence of equimolar phalloidin, probably by annealing (Sept et al., 1999). Although this is a promising technique for investigating the effects of very high curvature, we found that it was not amenable to analysis that requires averaging over a large number of filament segments, because the highly curved hairpin turn segments were rare compared to the long lengths of relatively straight filament that flanked the hairpin turns (Figure 9).

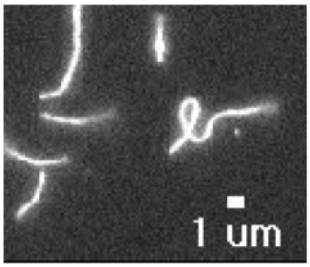

Figure 11. Example of a highly curved immobilized mother filament.

By reducing the speed of the flow through the channel to ~1.8 μL/s by wicking fluid at the exit of the channel with a narrower corner of filter paper that was not turned often, we achieved a smoother curvature distribution in which hairpin turns occurred much less often, but filaments also were only weakly or not at all aligned with the flow, and thus were bound to the streptavidin

surface with a broad range of curvatures that arise from a combination of fluid flow and thermal bending fluctuations.

Glass surface passivation

To study branching from the constrained filaments prepared as described above, we flowed a branching mix, containing unlabeled Arp2/3 complex and NPF (VCA from N-WASP) and unlabeled G-actin. After the branching reaction was allowed to occur for 2 minutes, the branching mix was washed out with a buffer containing fluorescently labeled phalloidin to stabilize and label the new daughter filaments a different color than the mother filaments. The concentration of Arp2/3 complex and G-actin, as well as the branching time, were optimized to limit both the density of branches and the length of daughter filaments. When branching was allowed to proceed for too long (e.g. more than 1 minute with 2 μM G-actin in the branching mix), newly polymerized daughter filaments tended to serve as the preferred substrate for further branching, presumably because they contained a higher proportion of ATP-F-actin or ADP-P_i-F-actin than the mother filaments. This process gave rise to small dendritic "bushes" rather than individual branches, making the exact location and direction of the original branches nucleated from the mother filament difficult to measure (Figure 12).

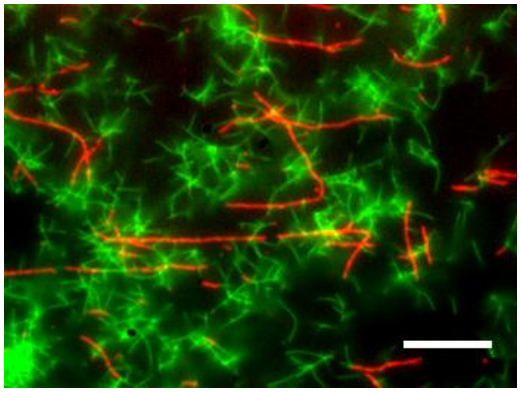

Figure 12. Overgrown daughter filaments. Biotinylated BSA surface. 10% biotinylated mother filaments were polymerized with equimolar rhodamine phalloidin at 5 μM and diluted to 50 nM in F-buffer. After excess mother filaments were washed out, the sample was incubated with branching mix: 1 mM ATP, 2 mg/mL BSA, 100 nM N-WASP VCA, 100 nM Arp2/3, 2 μM G-actin, and incubated 5 min. The branching mix was replaced with F-buffer containing 2 μM Alexa Fluor 488 phalloidin, incubated 2 min., and replaced with F-buffer. This sample was imaged with wide-field epi-fluorescence imaging and a 1000 ms exposure. Bar: 10 μm.

To ensure reproducible results, we optimized blocking conditions such that all glass surfaces were sufficiently blocked to minimize nonspecific binding of branching mix proteins (Arp2/3 complex, NPF, and G-actin) to the glass. Blocking against nonspecific actin binding was also very important to prevent newly polymerized daughter filaments from binding to the surface,

such that the observed branch direction was a true representation of the location of Arp2/3 binding on the filament. With unconstrained branches, we could be confident that (a) filaments labeled in the color representing newly polymerized actin appearing to grow from a mother filament were anchored via the Arp2/3 complex, and (b) the direction of growth of a short branch is an indicator of where on the mother filament the Arp2/3 complex bound, because at lengths of less than 1 μm, actin filaments are quite stiff.

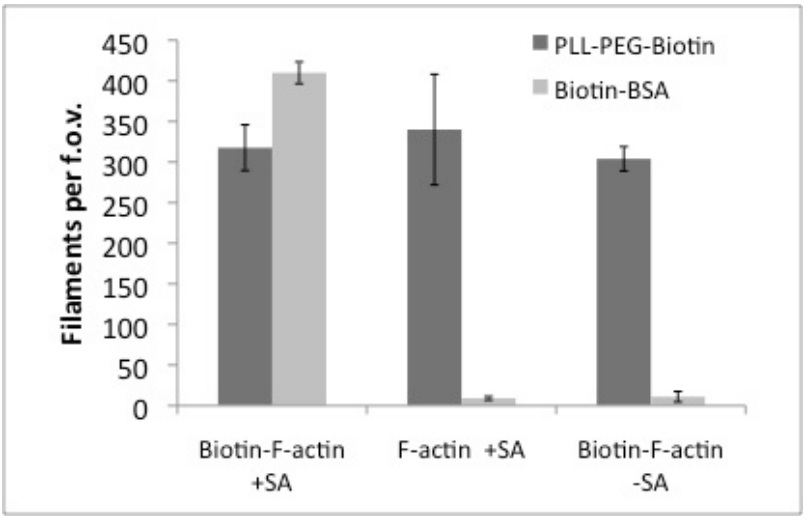

Figure 13. Comparison of nonspecific binding of F-actin to surfaces passivated with BSA and PLL-PEG. SA: streptavidin. Actin filaments containing 25% biotinylated monomers were stabilized by TRITC-phalloidin and sheared by brief sonication prior to incubation on surface for 15 minutes to ensure a more uniform distribution of filament lengths.

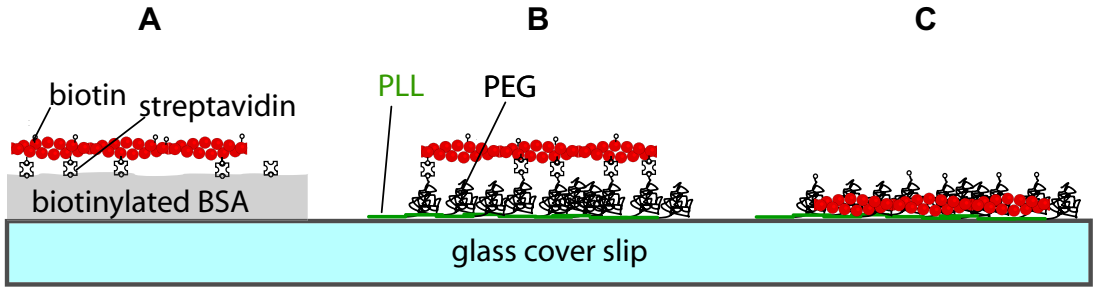

Figure 14. Surface coating methods. (A) Biotinylated BSA was nonspecifically bound to a glass surface, and incubated with streptavidin to create a surface that immobilizes biotinylated F-actin. (B) Poly(L-lysine)-PEG (PLL-PEG) copolymer was bound to the glass, then used as in (A). (C) F-actin bound the PLL-PEG surface even in the absence of streptavidin, probably because of electrostatic attraction to the positively charged PLL underlayer.

To block the glass surface and create a layer to which we could subsequently bind the streptavidin that would anchor biotinylated mother filaments, we first tried a poly(L-lysine)-polyethylene glycol (PLL-PEG) copolymer, which is biotinylated on 20% of PEG chains (Figure 14). In buffer, this copolymer self-assembles on clean glass to form an under layer of PLL that is electrostatically bound to the glass, and a lightly biotinylated outer layer of PEG, which is generally an excellent blocking agent for most proteins. We found that in the relatively low ionic strength of the 50 mM KCl reaction buffer (in order to be consistent with many other studies on dendritic nucleation), the PEG layer was not sufficient to shield the negatively charged actin filaments (Angelini et al., 2003) from the highly positively charged PLL under layer. The mother filaments bound to the passivated surface under control conditions, when the filaments were not biotinylated, or streptavidin was omitted from the experiment (Figure 13). Furthermore, the PLL under layer occasionally cause actin filaments to become bundled with each other, or sometimes with themselves, forming rings (Figure 15). This polycation-induced bundling and ring formation of F-actin and has been characterized by Tang et al., with Mg^{2+} as the polycation (Tang et al., 2001).

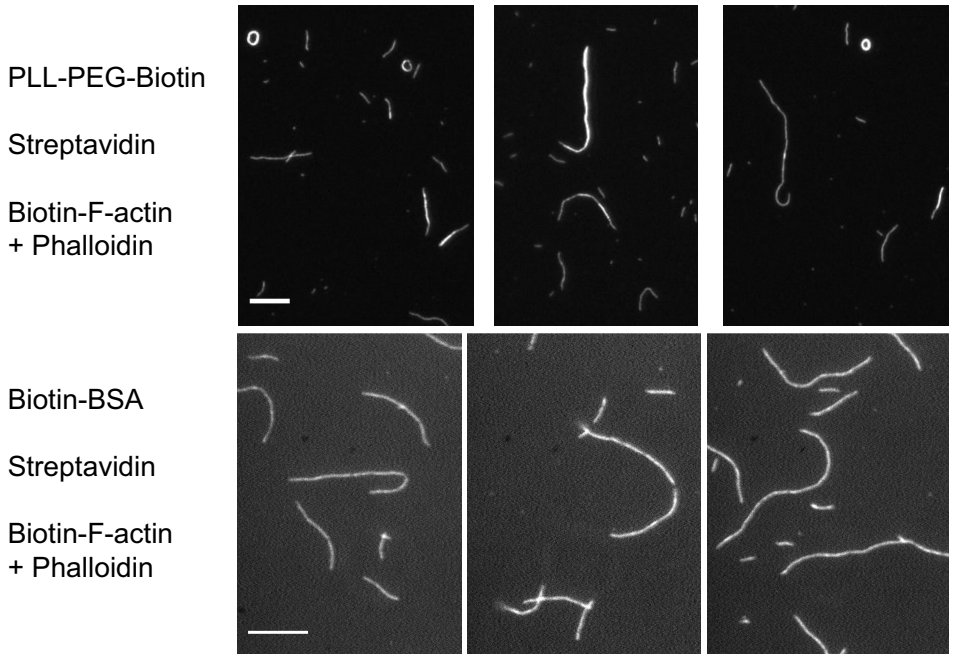

Figure 15. Bundling of F-actin on PLL-PEG surfaces. 10 μM F-actin was polymerized with equimolar rhodamine-phalloidin, then diluted in F-buffer (see Materials and Methods) to 13 nM. F-actin was flowed onto the surface, then washed with 50-100 μL F-buffer in the opposite direction. Upper images: F-actin on a PLL-PEG surface prepared by sonicating the glass cover slip in isopropanol, plasma-cleaning, incubation with 1 mg/mL PLL-PEG in PBS for 30 min., and washing with F-buffer. Lower images: F-actin on a biotin-BSA surface prepared by KOH/EtOH cleaning, incubation for 2 hours with 10 mg/mL biotin-BSA, washing with 100 μL PEM-80 and 100 μL Tris-B, incubation with 0.2 mg/mL streptavidin in Tris-B, and washing with 100 μL Tris-B and 100 μL F-buffer. Scale bars: 5 μm.

Biotinylated bovine serum albumin (BSA) is a more robust blocking agent for actin filaments, while simultaneously serving as a base layer onto which streptavidin could be specifically bound (Figure 14). This result is consistent with the overall negative charge of BSA at neutral pH, which should be less likely to nonspecifically bind the negatively charged actin filaments in low ionic strength buffer and at relatively low concentrations of divalent cation (Mg^{2+}, in these experiments). To facilitate biotinylated BSA adsorption to the glass, the cover slip and slide were first washed and plasma-cleaned to remove adsorbed organic material by oxidation or etched with a saturated EtOH/KOH solution. A 1-3 hour incubation at 4˚C with a high concentration of BSA (10 mg/mL) was used to fully saturate the cover slip surface with biotinylated BSA, and was more effective at blocking than short (15 min) incubations. BSA (≥98% pure) was also included at 1-2 mg/mL in solution during the branching reaction to enhance blocking. Biotinylated BSA proved quite effective for our experiments. However, it is not the only effective passivation strategy. Effective passivation methods using PEG covalently linked to the glass surface have also been developed and published (Bieling et al., 2010). We primarily employed biotinylated BSA, but do discuss a preliminary experiment with such a method below.

Preliminary applications of the surface-immobilized actin filament assay

Branch nucleation by the Arp2/3 complex

The branching assay described above was used to study how mother filament curvature affects branching direction. In preliminary experiments, daughter filaments growing from sections of mother filaments with radii of curvature of less than 1.5 μm were chosen by using ImageJ to draw osculating circles to the curve of the mother filament at the base of each branch. The branches were then manually analyzed in terms of their direction – whether they grew toward the center of the osculating circle (on the concave side of the curved filament) or away from the center of the osculating circle (on the convex side of the mother filament). The results of this preliminary analysis indicated that there is a statistically significant bias toward the convex side of the filament for branches growing on high-curvature sections of mother filament (Figure 16 and Table 6).

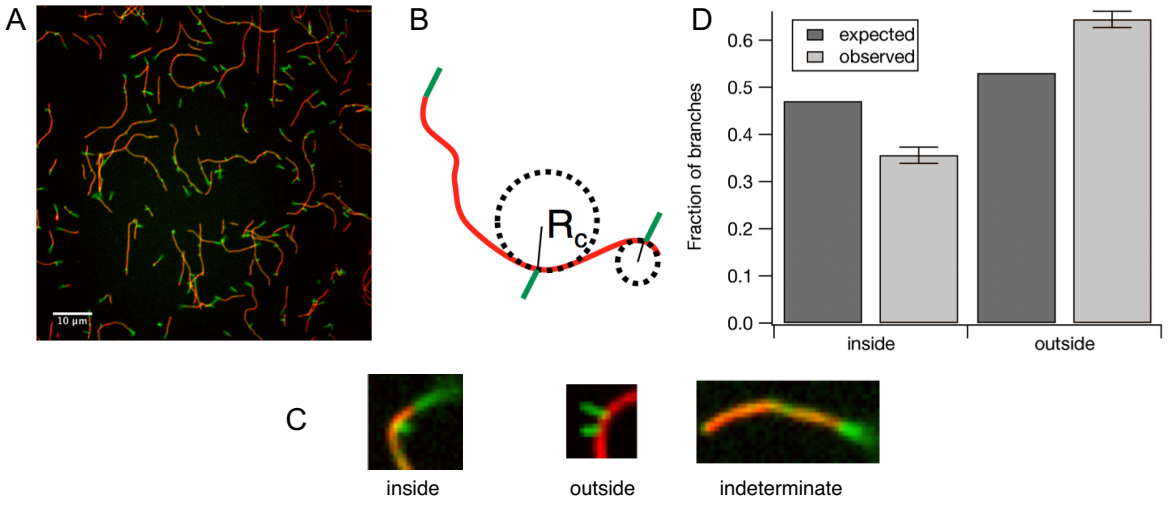

Figure 16. Manual analysis of Arp2/3 branch direction as a function of curvature reveals a significant bias toward branching outside the osculating circle. (A) Bar: 10 µm. (B) The osculating circle was drawn at the base of branches. The local curvature is the reciprocal of the radius of the osculating circle, also called the radius of curvature, R_c. (C) Branches were scored as lying inside the osculating circle, outside of it, or in an indeterminate direction. Indeterminate branches were discarded. (D) The expected fraction of branches lying inside or outside the osculating circle was calculated geometrically, assuming an osculating circle of average radius 1.125 µm and a branch measurement distance of 1 µm away from the branch point. Error bars: SEM from n = 5 independent experiments.

Table 6: χ^2 analysis of the effect of local curvature on branch direction.

	Left/ Outside	**Right/ Inside**	**Counted**
Straight ($R_c \geq 6$ µm)	69 *(66.5)*	64 *(66.5)*	133
Bent ($R_c \leq 1.5$ µm)	494 *(406.51)*	273 *(360.49)*	767
Totals	563 *(473.01)*	337 *(426.99)*	900

Counts in each cell are: observed *(expected)*. The expected proportions are based on the geometry of a 1 µm branch on a 1.25 µm radius osculating circle (an average value approximately representing the curvature distribution of the analyzed filaments. Data is pooled from 5 independent experiments, and data from curved filaments is also shown in Figure 16*D*. Straight filaments were analyzed as a control, with left and right defined with respect to the barbed end of the filament (marked by some green actin growth, (Figure 16*A-B*)) pointing up. The analysis showed that curvature has a significant effect on branch direction, with $p < 0.001$.

Tropomyosin

To test the applicability of this method to other actin-binding proteins, the same assay was used to observe the unbinding of fluorescently labeled cardiac muscle tropomyosin from actin filaments polymerized from 30% Alexa Fluor 488 labeled and 10% biotinylated actin monomers immobilized on a biotinylated BSA and streptavidin coated surface (Figure 17). We did not observe a qualitative preference for tropomyosin unbinding from different curvatures. We also implemented a published alternative protocol that uses biotinylated PEG covalently linked to the glass to passivate the surface and a combination of biotinylated and fluorescently (Alexa Fluor 488) labeled phalloidin to stabilize and link the F-actin filaments to the streptavidin-coated biotin-PEG surface (Bieling et al., 2010). As shown in Figure 18, the relatively fast (~24 min) half-life of phalloidin dissociation from F-actin did not immobilize the mother filaments as well as biotin-labeled monomers did (De La Cruz & Pollard, 1994).

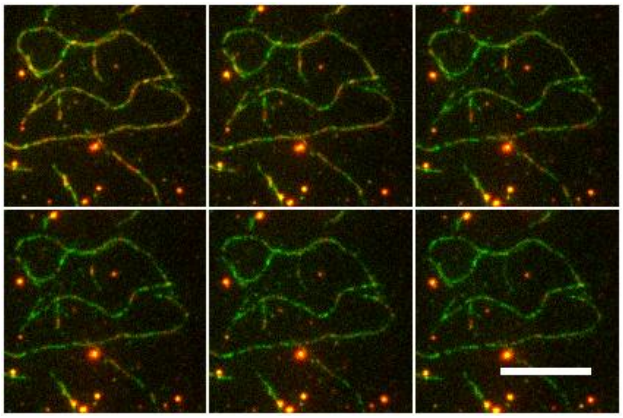

Figure 17. Tropomyosin unbinding from F-actin. Fluorescently labeled tropomyosin (red) decorated F-actin (green) polymerized from a mixture of 30% Alexa Fluor 488 and 10% biotinylated monomers on a biotinylated BSA/streptavidin surface. The sample was imaged using TIRF microscopy with successive frames 60 s apart, after excess tropomyosin-decorated filaments and unbound tropomyosin was washed out with F-buffer containing unlabeled phalloidin to stabilize actin filaments after unbinding of tropomyosin. Bar: 10 μm.

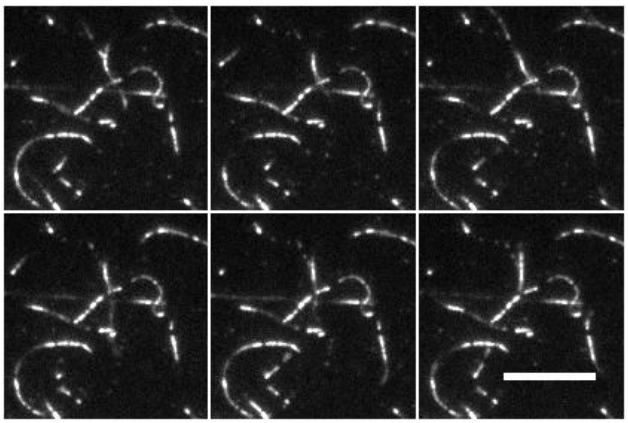

Figure 18. Fluorescently labeled tropomyosin bound to F-actin immobilized by biotin-phalloidin on a PLL-PEG-biotin/streptavidin surface. Successive frames are 3 s apart, imaged with TIRF microscopy. Buffer contained 100 nM fluorescently labeled tropomyosin and F-actin was initially undecorated. Images were acquired after ~15 min incubation with lower tropomyosin concentrations followed by buffer wash-out, and a 2 min incubation with 100 nM tropomyosin. Cooperative binding generated tropomyosin clusters on the F-actin which did not dissociate in the ~1 min wash-out steps. Lower concentrations of tropomyosin (50 nM, not shown), exhibited single fluorescent binding events, fewer clusters, and possibly single-molecule binding events, although in this experiment, single-step bleaching was not confirmed. Bar: 10 μm.

Automated analysis of mother filament images

To more carefully quantify the preliminary result indicating that branching by the Arp2/3 complex occurs with greater frequency on the convex side of curved filaments, we sought to develop a strategy for automatically detecting, tracing, and analyzing large numbers of mother filaments. By measuring the curvature of mother filaments at branch points as well as over the lengths of filaments, we sought to quantify the relative branching rate and branching direction at the range of curvatures adopted by the surface-immobilized F-actin.

The surface preparation methods described above were essential in generating fluorescence microscopy images that were suitable for quantitative analysis, because they allowed the filament density to be tuned to prevent filament bundling or nonspecific aggregation, and to ensure that filaments bound to the surface were sparse enough to minimize filament cross-over points. The flow channel's cover slip surface was raster-scanned manually to collect 30-120 images per channel, because small deviations from horizontal mounting of the slide resulted in imperfect focusing during automatic scanning. Manual focusing at each field of view was used to obtain filament images that were as sharp as possible. This was useful, but not essential, in analyzing fluorescent phalloidin-saturated mother filaments, because of their bright and smooth fluorescence signal, but it became very important in imaging mother filaments assembled from actin with a fraction fluorescently labeled monomers, because their fluorescence was weaker and slightly irregular over the length of the filament (see next chapter). Long exposures of 0.5-1

second were used to reduce noise in filament images and to ensure that if there were filament ends that had not bound to the streptavidin surface, their Brownian fluctuations would blur them in the final filament image and they would not pass threshold. The blurring effect was also useful in detecting the point where daughter filaments in branches attached to the mother filament, because their free end was more blurred by their Brownian fluctuations.

Image processing

Thresholding is a necessary first step in many image analysis strategies, to identify the "foreground" pixels that define interesting objects out of the "background" of uninteresting pixels by transforming a grayscale image into a binary image in which foreground pixels are white and background pixels are black. A variety of automatic threshold selection algorithms, all available as plugins in ImageJ, were tested on representative images of actin filaments. The Otsu method was the most robustly effective, especially for phalloidin-labeled filaments (Otsu, 1979). Mother filaments polymerized from fluorescently labeled G-actin have a less even fluorescence profile along their length, and the signal to noise in experiments involving unstabilized mother filaments was lower than in experiments with phalloidin-stabilized and labeled mother filaments. In some cases, threshold chosen by the Otsu method broke some filaments into puncta, and it was manually adjusted or the threshold was chosen by the Renyi Entropy method in ImageJ (Kapur et al., 1985) for groups of 5-10 images.

Filtering of the images was used to smooth single-pixel noise that created ragged filament outlines and led to spurs during filament image skeletonization (below). We tested Gaussian filtering and median filtering using masks with a radius of 1 pixel before thresholding, as well as median filtering of the thresholded binary images. Median filtering proved most effective in eliminating single-pixel noise, especially when used after thresholding, to smooth thresholded filament images before thinning, to prevent the formation of artifactual spurs.

Thresholded filament images were then skeletonized using the ImageJ skeletonization plugin to yield 8-connected single pixel wide digital curves. We verified that the results of this skeletonization algorithm agree with the medial axis transform of the filament shapes (Figure 19). The medial axis transform is a standard representation of an object's shape (Gonzalez et al., 2003), but it is not suitable to be directly used for our purposes because unlike the result of skeletonization, it does not necessarily maintain the continuity of the filament, and is not always a single pixel wide.

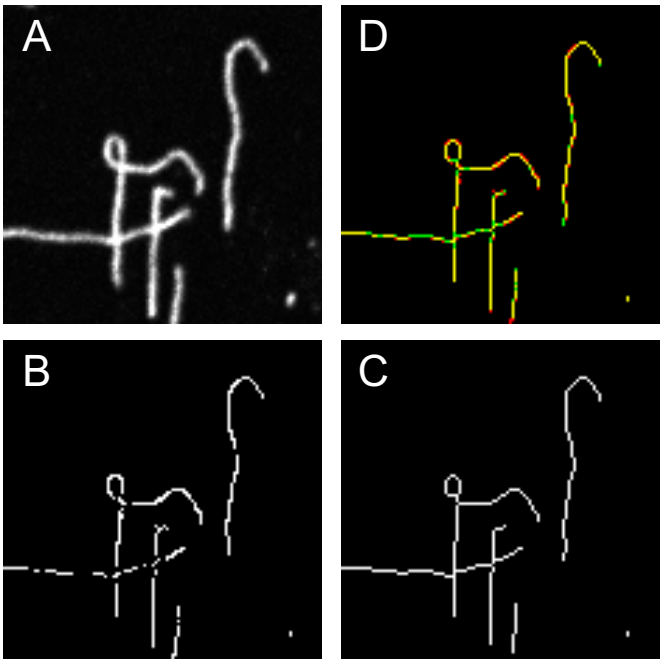

Figure 19. Skeletonization of filaments. (A) Original filament grayscale image. (B) Medial axis transform of the thresholded filament image (not shown). The medial axis transform was calculated using the BinaryThin Skeleton4 implementation written by G. Landini (Available online at: http://www.dentistry.bham.ac.uk/landinig/software/software.html). (C) Result of skeletonization of the thresholded filament image. (D) Merge of B (red) and C (green).

The single pixel wide digital curves produced by skeletonization of binary filament images are good representations of filament shape, but have two features that can cause problems in further analysis. The first is that the skeletonization process removes pixels from the outside of a binary object until only a single pixel skeleton is left. While most of the pixels are removed from the width of the curve, a few pixels are also removed from the ends, slightly shortening each object. This introduces a small error in the overall estimation of filament length, but this error is mitigated by the fact that filament images appear longer than the true filament because of convolution with the circular (in the *x*-*y* plane) point spread function of the microscope. Regardless of the exact size and magnitude of this small error, the exact length of filaments did not impact our analysis of branch location and direction on curved filaments, because we were primarily concerned with measuring the local curvature at branch points. In fact, the ends of filaments were excluded from analysis with both of the curvature estimation methods described below, to avoid end effects that distort curvature measurements with any method.

The second problem that we encountered in analyzing filament skeletons is that despite optimization of filament density, by chance, there would still be filaments that occasionally intersected. Tracing filaments or paths through intersections is a non-trivial problem, and had the potential of introducing systematic errors into our curvature analysis if filaments were traced through an intersection on the basis of, for example, minimum curvature. Rather than risk introducing such errors, we chose instead to break filament curves at intersections by removing

any pixel that had more than two nearest neighbors (Figure 20). The advantage of this strategy is that it does not introduce spurious high curvature values when two filaments cross, or when the skeletonization procedure occasionally produces a small spur in the filament curve. The disadvantage is that longer filaments are broken into shorter curves for the analysis. If the filament length distribution were a concern, this would be problematic, but in our analysis, it is not. Effectively, the breaking of filament curves at intersections creates new ends, such that more segments of filaments are discarded from the analysis. Because of the large number of filament images available for every experiment, discarding some data did not present a significant problem (Chapter 3).

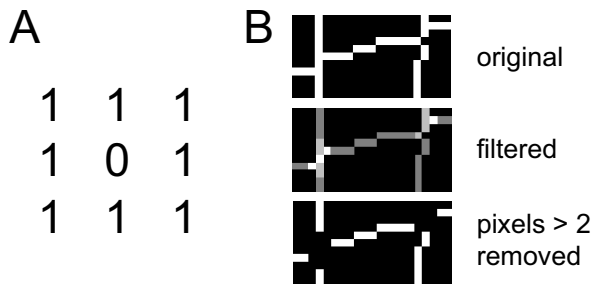

Figure 20. Removal of filament intersections. (A) The filter shown was used to label each pixel with the number of nonzero nearest neighbors in the binary filament skeleton image. (B) The original binary image was filtered, creating a grayscale image in which the value of each pixel represents the number of nearest neighbors of that pixel. The image was then thresholded to create a new binary skeleton image without intersections.

The skeleton images were further cleaned up by removing filament segments containing fewer than a threshold number of pixels, which would be too short to yield curvature measurements, as well as by clearing a border of two pixels around the edges of the image.

Curvature measurement

To measure the curvature distribution of the mother filaments and the curvature at branch points, we employed two different strategies. The first, which we term spline-based curvature measurement, globally fit piecewise polynomials to the shape of the digital curves. The second, which we term tangent angle based curvature measurement, determined curvature from the local change in tangent angle over reparameterized arc length increments, using smoothing with a linear Gaussian filter to remove high-curvature artifacts created by the discrete pixels of the filament image.

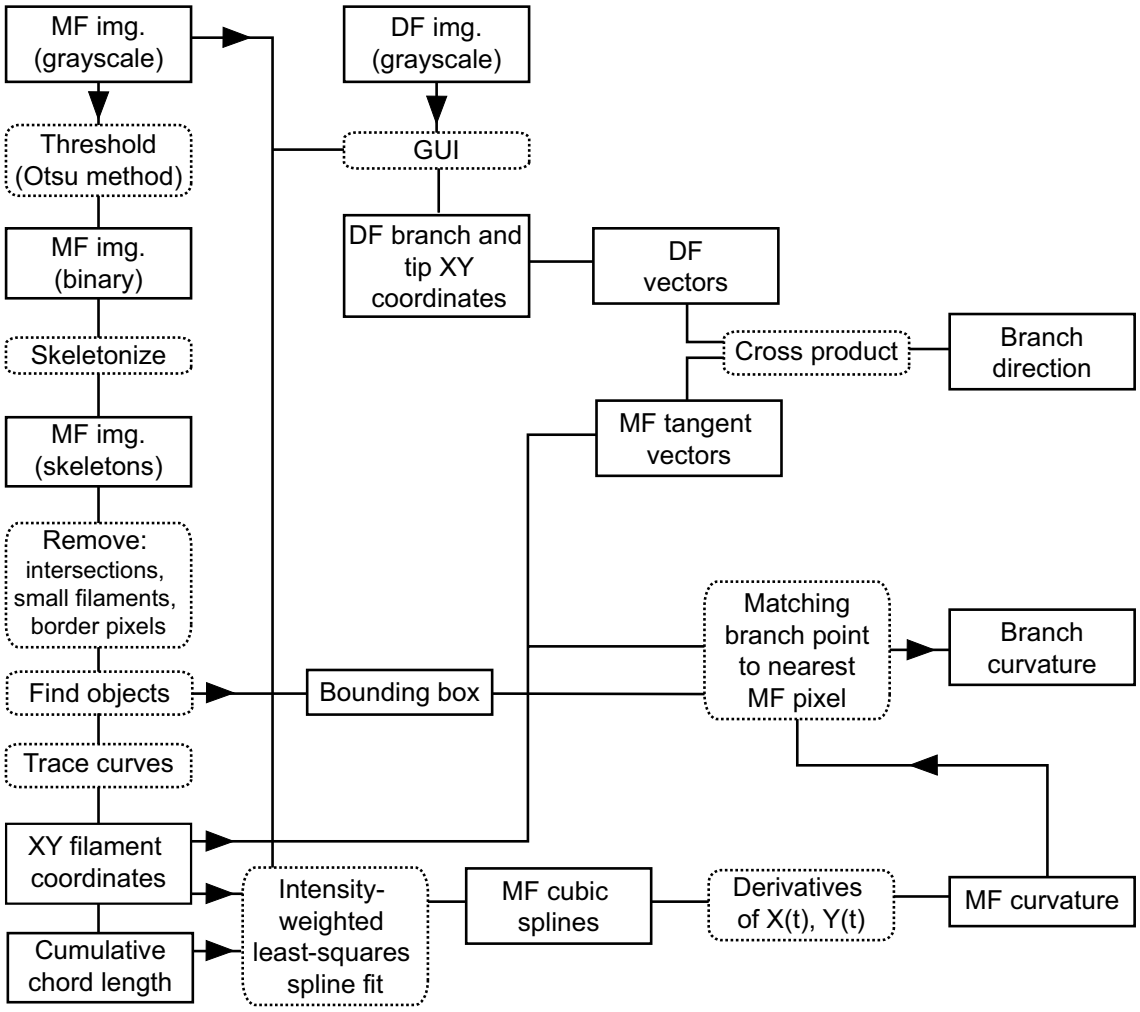

Figure 21. Flow chart of image analysis for spline-based curvature measurement. The procedure is described in the text. Abbreviations used in the chart are, MF: mother filament, DF: daughter filament, img.: image, GUI: graphical user interface.

Spline method

The spline-based curvature analysis procedure is outlined in Figure 21. Filament objects were identified using a label matrix and the bounding boxes and images of each object were stored for further analysis. Within each object image, the leftmost pixel was identified and used to trace the *x*,*y* coordinates of the other pixels in the object. For each pixel, the intensity of the original mother filament image was also recorded. The *x*,*y* path was parameterized in terms of chord length between consecutive pixels and used to interpolate the filament shape by fitting a cubic spline using a least-squares algorithm, with the original pixel intensities as weights. Skeleton pixels that in rare cases did not correspond to a high-intensity area of the original filament image were discounted in the fitting.

The splines were converted to piecewise polynomials so that their $X(t),Y(t)$ position, where t is the chord length parameterization variable, and derivatives could be calculated at any point along the filament curve. The curvature of the filament could then be measured at any point using Equation 12 (see Chapter 3). Tangent angles at any point along the filament skeleton were calculated as the tangent between adjacent pixel locations, and the bounding box of every filament object was used for coarse co-localization of points of interest with the filament, such as branch locations.

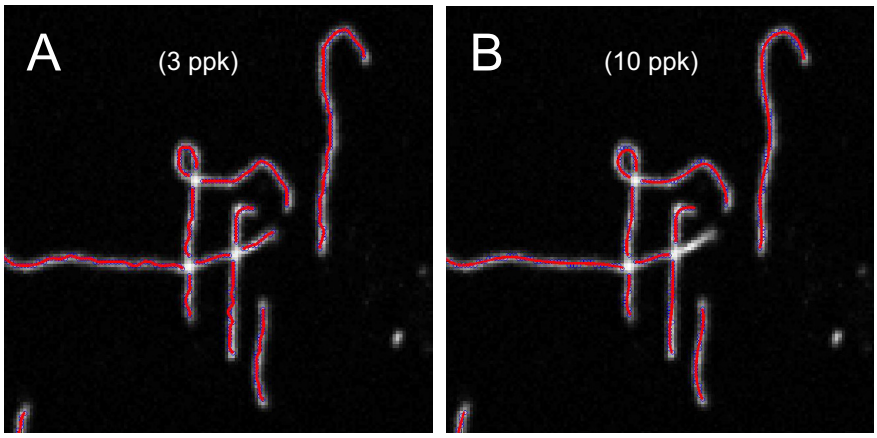

Figure 22. Cubic splines (red) fitted to filament skeletons (blue circles) overlaid on the original mother filament image (gray). (A) 3 ppk, (B) 10 ppk.

An important parameter in fitting splines was the spacing of polynomial pieces making up the spline, called knots (Figure 22). The larger the number of pixels between knots (here referred to as ppk, or pixels per knot), the more the spline smoothes over small variations in curvature, while the smaller the ppk, the more responsive the spline is to changes in curvature. When fitting splines to resolution-limited digital curves, the discrete nature of angles between adjacent pixels caused high-curvature artifacts. Model circles and hairpins with known curvatures were used to measure the accuracy of curvature estimation using splines with different ppk values (Figure 23). A value of 10 ppk was chosen as a compromise between avoiding pixilation effects and underestimating or distorting the true curvature. Any segments of filament with a length of less than 11 pixels were discarded in image pre-processing before fitting the splines.

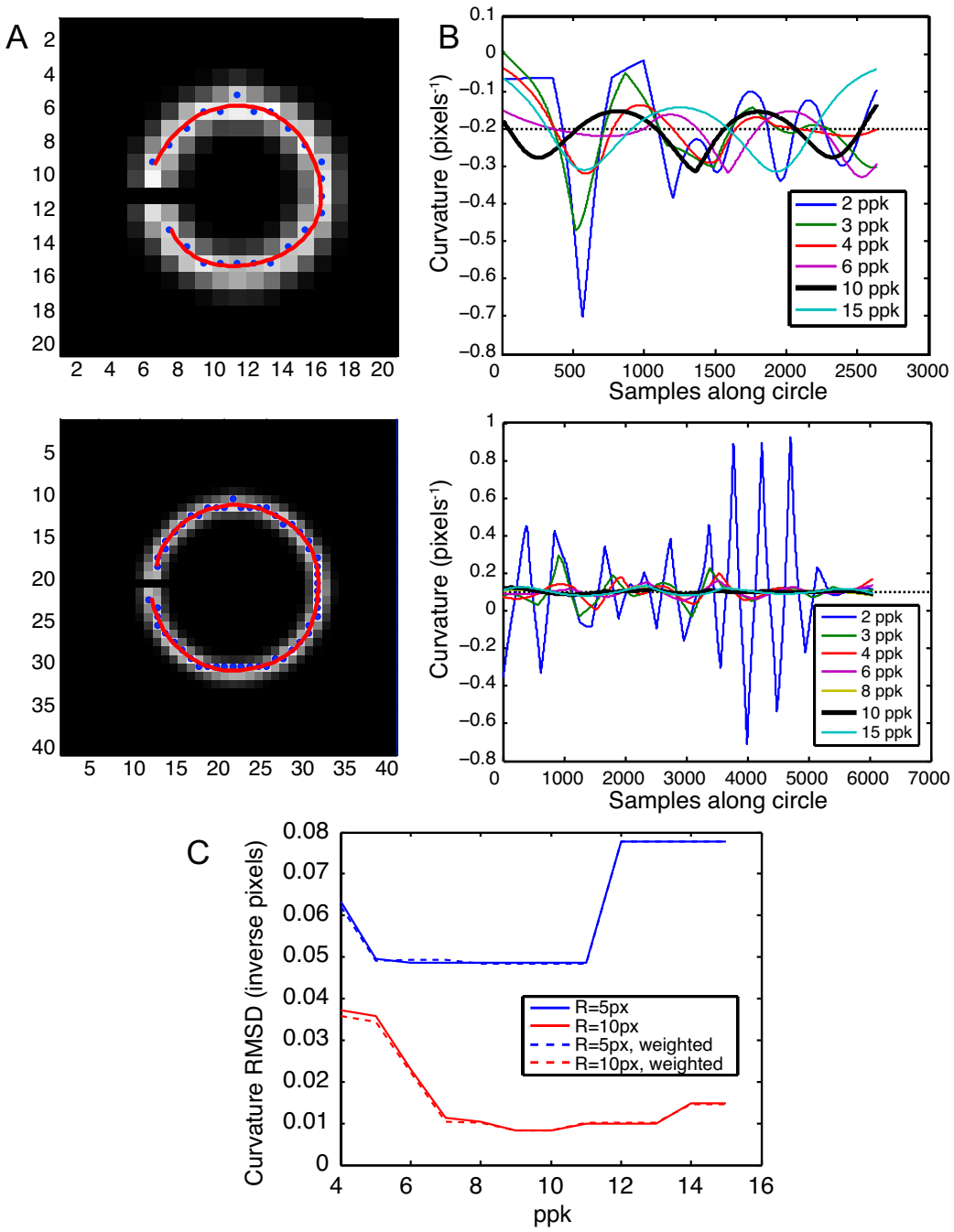

Figure 23. Curvature error analysis for the spline-based method. (A) Cubic splines (red) fit to test circles of 5 pixel (top) and 10 pixel (bottom) radii. Circles were blurred, then skeletonized. The original grayscale image and the skeleton (indicated by blue dots) were used to test the curvature measurement algorithm (Figure 21). (B) Measured curvature along the circle perimeter for different ppk values. The nominal curvature is shown as a dotted line. (C) Root mean square deviation of the measured curvature from the nominal curvature as a function of ppk. An inflated curvature can be seen for too-small ppk values for both curvatures because of pixilation artifacts.

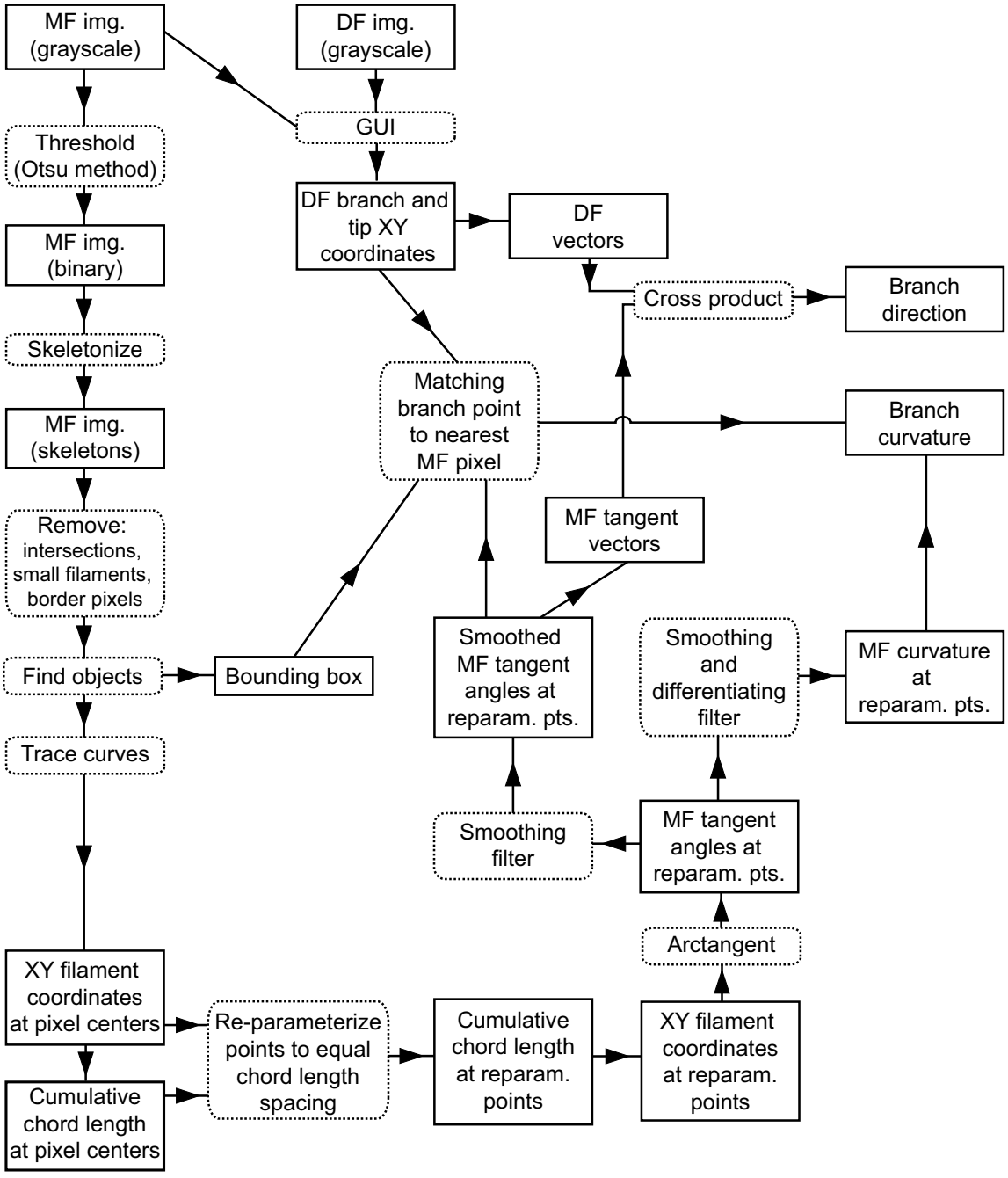

Figure 24. Flow chart of image analysis using the tangent angle method to measure curvature. Abbreviations used in the chart are MF: mother filament, DF: daughter filament, GUI: graphical user interface, reparam. pts.: reparameterized points, img.: image.

Tangent angle method

The tangent angle method algorithm is illustrated in Figure 24 and follows Method II described by Worring and Smeulders (Worring & Smeulders, 1993). Image skeletons were processed as for the spline method, producing x,y lists of pixel centers for each filament exceeding a minimum

length that depends on the curvature measurement parameters. The pixel lists were then parameterized in terms of chord length (as an approximation of arc length), and a new set of interpolated points, spaced by equal chord length intervals, were chosen to reparameterize the curve. This reparameterization is important because the distance between adjacent pixels on an 8-connected curve varies between 1 and 1.414 pixel units, and this difference in the chord length between different sets of pixels distorts a curvature measurement that relies on the change in tangent angles between adjacent pixels (Worring & Smeulders, 1993). Tangent angles of the vectors joining successive points in the filament skeleton were calculated from the arctangent of the difference in x and y coordinates, and the resulting lists of angles were processed to remove discontinuities at $-\pi$ and π. The tangent angle lists were then processed with a smoothing, differentiating filter based on a Gaussian kernel to calculate the list of curvature values along the filament skeleton (Figure 25) (Worring & Smeulders, 1993). The Gaussian width, *s*, and filter window half-width, *m*, were varied on test data with known curvature. The results of this analysis are shown in Figures 26 and 27. For further curvature estimation, *s* was set to 3 and *m* was set to 9, making the minimum filament size $2m + 1 = 19$ pixels. A Gaussian smoothing filter was used to obtain tangent angles used in determining the direction of branches relative to the mother filament curve, when analyzing Arp2/3 branching data (discussed in detail in Chapter 3).

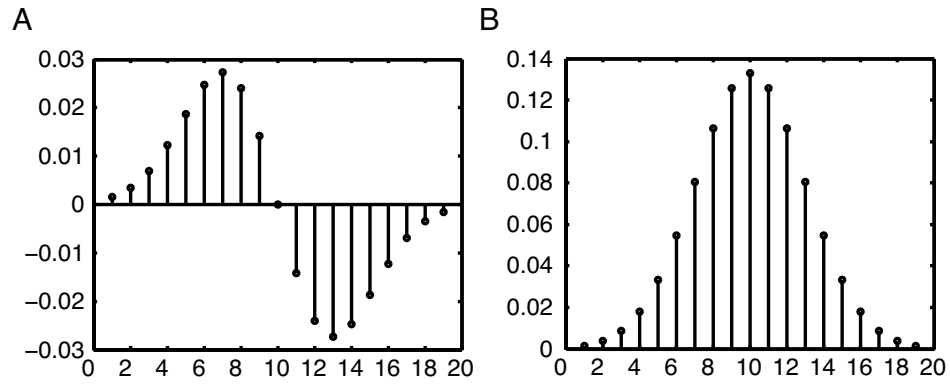

Figure 25. Gaussian filters used for smoothing. (A) Smoothing, differentiating filter used to calculate curvature and (B) smoothing filter used to calculate tangent angles. For both filters, the Gaussian width $s = 3$ and the filter window half-width $m = 9$, making the entire window size 19 pixels.

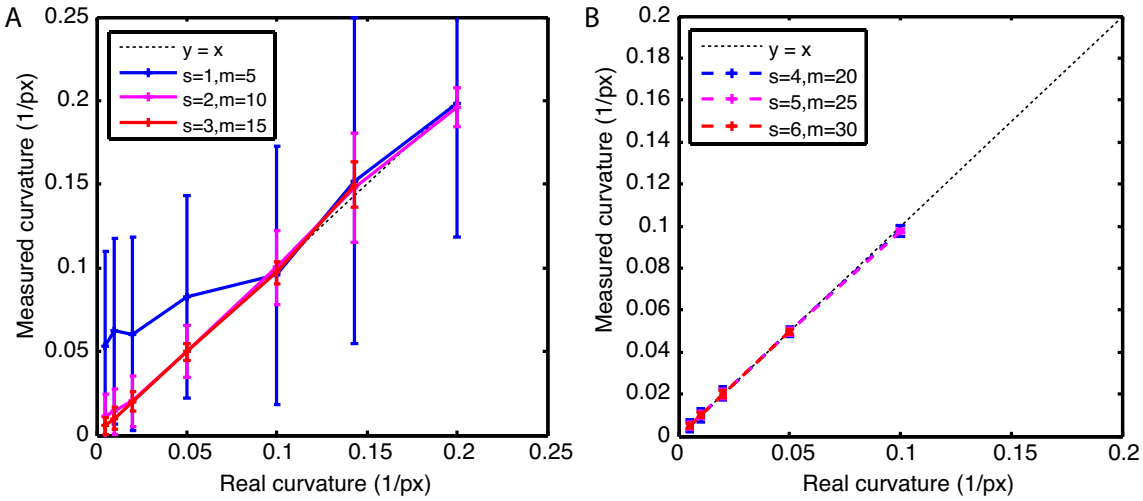

Figure 26. Curvature error analysis: variation of Gaussian kernel width. The filter width was varied from $s = 1$ to $s = 6$, with the filtering window width $m = 5s$. (A) $s = 1$ to 3, (B) $s = 4$ to 6. The curvature was calculated using the tangent angle method from an ensemble of circle skeletons of known curvature with one-pixel gaps at random locations along the circle. At larger curvatures, the filter window was larger than half the perimeter of the circle and the curvature could not be calculated. At small curvatures, a too-small value of s (blue curve) shows an artificially inflated curvature due to pixilation effects. A value of $s = 3$ was chosen as a compromise between smoothing over pixilation artifacts and filter window size. The same value of s was used for both the differentiating filter use to calculate curvature and for the smoothing filter used to calculate tangent angles to the filament skeleton. Bars: SD.

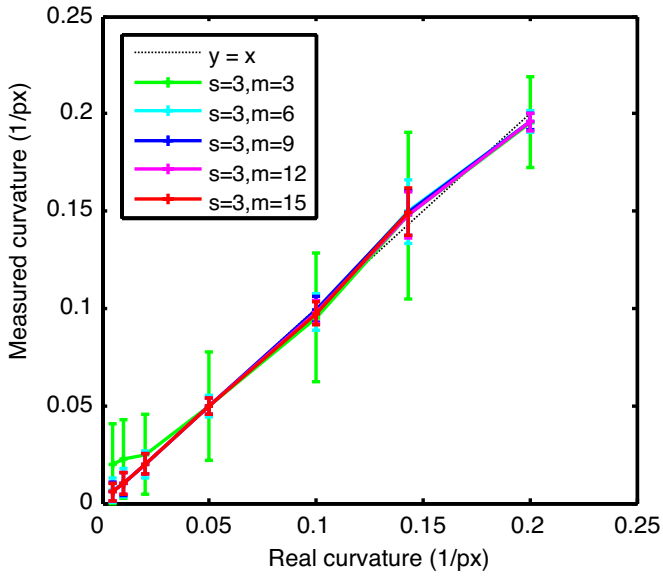

Figure 27. Curvature error analysis: variation of filter window half-width. The filter window half-width was varied from $m = s$ to $m = 15s$, with the filter width $s = 3$. The curvature was calculated using the tangent angle method from an ensemble of circle skeletons of known curvature with one-pixel gaps at random locations along the circle. A value of $m = 3s$ was chosen to maintain the shape of the filter kernel while minimizing window size, allowing curvature measurement on filament skeletons of >19 pixels. The curvature of filament skeletons at the 9 pixels closest to each end was ignored, because the end effects from applying a filter to the zeros padding the ends of the curve distorted those results. Bars: SD.

Conclusion

A surface passivation and attachment strategy was developed to image actin filaments immobilized on a glass surface in order to correlate local filament curvature with ABP binding or activity. This was demonstrated for branching by the Arp2/3 complex.

Actin branching experiments followed by a manual analysis of branch direction on coarsely measured curvature indicated that the Arp2/3 complex preferentially nucleates branches from the convex side of curved filaments. Experiments following up on this observation are described in Chapter 3.

In preparation for more detailed curvature measurements, an automated image analysis protocol was developed, using two different methods of measuring filament curvature. Error analysis using test data with known curvature indicates that the spline-based curvature measurement method with the chosen parameters has an error depending strongly on filament curvature that is 0.05 pixels^{-1} for curvatures of ~0.2 pixels^{-1}, and drops to ~0.01 pixels^{-1} for lower curvatures. The tangent angle-based curvature measurement has an error depending less strongly on curvature, which is ~0.01 pixels^{-1} for the curvatures measured. As discussed by Worring and Smeulders, and Bicek et al. (Bicek et al., 2007; Worring & Smeulders, 1993), another difference between the spline-based curvature measurement method and the tangent angle-based method is that the spline-based method involves a global fit to the digitized skeleton, and thus can be biased by end effects that are highly shape-dependent, while the tangent angle-based method is purely local, and thus is only dependent on features the size of the filtering window. Discarding a span of pixels the size of half the filtering window at each end helps to remove these end effects.

Outlook for the surface-immobilized filament assay

The methodology described in this chapter has the potential to be applicable to the study of other actin-binding proteins. To this end, there are several ways in which the method could be improved upon.

First, sub-pixel resolution in localizing the mother filament axis may allow enhanced curvature resolution that would improve the precision of the assay, allowing smaller curvature-induced effects in protein binding to be detected. The Gaussian fitting method described by Brangwynne et al. has been used to localize fluctuating filament outlines with a precision of ~20 nm (Brangwynne et al., 2007). Although it relies on fitting polynomials to the filament shape, which can introduce artifacts in the curvature, refinement based on Gaussian profiles of the filament image and the interpolation of the filament curve that allows sampling on a scale smaller than the pixel grid should result in an overall improvement in the accuracy of curvature measurement. That is because most errors in curvature measurement from digitized curves are inversely proportional to number of digitized samples available (Worring & Smeulders, 1993). Alternatively, a smaller gain in curvature resolution without fitting of the filament intensity profile or interpolation may be obtainable by increasing the magnification of the imaging system such that filament images are oversampled by the charge-coupled device. Although this would not improve the optical resolution of the images, having more pixels covering the same curve would allow for more efficient use of the available data, because the same number of pixels discarded at filament ends would represent a smaller real contour length. Higher sampling

density would also improve the overall curvature resolution, because the need to smooth over pixilation artifacts with a 19 pixel filtering window means that curvature resolution in current experiments was limited by magnification, rather than by optical resolution.

For actin-binding proteins (ABPs) other than the Arp2/3 complex, binding to F-actin may be the only read-out of activity available. Therefore, the assay must be compatible with single molecule imaging of labeled or genetically tagged ABPs. Although biotinylated BSA served as a good passivating agent for F-actin, preliminary experiments with tropomyosin (Chapter 2) suggest that a covalently linked surface treatment of biotinylated PEG (Bieling et al., 2010), which has been used in many single molecule imaging experiments with microtubule-associated proteins (Telley et al., 2011), would be an appropriate modification to the protocol described in Chapters 2 and 3. It may be possible to adjust the ratio of biotinylated and unbiotinylated PEG molecules in the surface coating to more precisely control the spacing between attachment points of the mother filaments to the surface, thus affecting their fluctuations. One possible strategy is to maintain a constant biotinylation ratio on filaments while the biotinylation ratio on the surface is altered. In such an assay, it may be possible to estimate the number and location of filament attachment points by using single molecule imaging of fluorescently labeled streptavidin at low surface biotinylation ratios, and to extrapolate the attachment density at higher biotin-PEG/PEG ratios based on either the amount of biotin on the surface or the relative fluorescence intensity of labeled streptavidin.

On the mother filament side, there is an important caveat for the biotinylation strategy. The connection between the biotin-streptavidin surface must be sufficiently long-lived and constraining that the shape of the mother filament is stable over either hundreds of milliseconds or minutes-to-hours, depending on the exact experiment. Even for experiments based on live imaging of ABP binding to mother filaments, when in theory, the spontaneous fluctuations of the filament could be recorded without the need for immobilization, signal to noise considerations dictate that the exposure probably has to be on the order of hundreds of milliseconds, in order to have the best possible curvature measurement accuracy. Therefore, a surface immobilization strategy that works on the time scale of many seconds to minutes is important. Biotinylated phalloidin may be a good choice in these cases, because its half life for unbinding is ~20 min, based on a measurement on rhodamine-phalloidin (De La Cruz & Pollard, 1994). For experiments in which live imaging is not feasible, mother filament shape must be stable over many minutes, and the use of biotinylated phalloidin is not advised. Actin monomers covalently labeled with biotin and incorporated into the mother filaments are the best-suited method of biotinylated the mother filaments for such an application. Lastly, because the extent to which actin filaments are buried in the PEG layer may create artifacts that mimic curvature dependence of ABP binding, controls with different molecular weight PEG chains should be performed.

Surface-based experiments that impose constraints will be useful for relatively high-throughput assays that can test whether particular ABPs are sensitive to bending of F-actin. They can serve to complement more versatile but low-throughput techniques such as manipulation of single filaments with micromanipulators (Tsuda et al., 1996), magnetic tweezers (Hayakawa et al., 2011) or optical traps (Arai et al., 1999; Ferrer et al., 2008; Hayakawa et al., 2011; Shimozawa & Ishiwata, 2009; Tsuda et al., 1996; Yasuda et al., 1996; Mameren et al., 2009), which can access the full range of forces and torques that actin filaments experience in vivo.

Materials and methods

Buffers and chemicals

F-Buffer: 50 mM KCl, 1 mM $MgCl_2$, 1 mM EGTA, 10 mM imidazole, 0.1 mM $CaCl_2$, 0.2 mM Tris-HCl, 0.02 mM ATP, 0.05 mM DTT, pH 7.0.

Tris-B: 10 mM Tris pH 8, 10 mM NaCl.

PEM-80: 80 mM PIPES pH 6.9, 1 mM EGTA, and 4 mM $MgCl_2$.

Calcium and magnesium free PBS was purchased from Cellgro, Mediatech, Inc.

PLL-PEG was purchased from Surface Solutions, AG, Dubendorf, Switzerland (PLL(20)-g[3.5]-PEG(2)/PEG(3.4)- biotin(20%)).

TRITC-phalloidin was purchased from Sigma, and Alexa Fluor 488-phalloidin was purchased from Invitrogen.

IC3 maleimide reactive dye was a gift from Dr. Gerard Marriott (UC Berkeley).

Proteins

Streptavidin (S4762), biotinylated BSA(A6043), and BSA (A0281) were purchased from Sigma. Although other biotinylated BSA grades are available, this product gave the best passivation for F-actin.

Actin was prepared from rabbit skeletal muscle acetone powder (Pelfreez, Inc.) according to the method of Spudich & Watt (Spudich & Watt, 1971) and labeled with biotin-maleimide (Pierce, Inc.) according to manufacturer instructions while in the monomeric state. Alexa Fluor 488 actin was labeled with Alexa Fluor 488 5-SDP ester (Invitrogen). Arp2/3 complex was purified from bovine brain as described (Egile et al., 1999). Rat N-WASP $(His)_6$-WCA, a gift from D. Wong and J. Taunton, was expressed in E. coli BL21 DE3 R2L and purified by affinity chromatography as described previously (Egile et al., 1999).

Porcine muscle tropomyosin was purchased from Sigma and labeled with IC3-PE-maleimide reactive dye (Dojindo Labs) as follows. 1 mg tropomyosin (Sigma T-2400) was dissolved in 500 mM KCl, 50 mM Tris-HCl pH 8.3 at 1 mg/mL. 7x molar excess of the labeling reagent (200 μM final concentration) was incubated with the tropomyosin solution for 1 hr. at room temperature. The reaction was stopped by purifying the tropomyosin from free dye using a PD-10 column (GE Healthcare).

Glass cleaning

KOH/EtOH cleaning: ethanol was saturated with potassium hydroxide while stirring. Glass cover slips were immersed in this solution while stirring, using a Teflon holder, for 15 minutes. The cover slips were then rinsed in three changes of distilled deionized water, and dried with filtered

compressed air. They were used the same day or stored in a closed container to protect from dust for less than a week.

Acid cleaning: cover slips were immersed in 1M HCl overnight at 60˚C, then sonicated in distilled deionized water three times for 30 minutes each time, then sonicated, 30 minutes at a time, in a series of 50%, 75%, and 95% ethanol solutions (with distilled deionized water making up the balance) and stored in 95% ethanol. Before use, cover slips were rinsed extensively with distilled deionized water and dried with a nitrogen stream. This procedure was most often effective when employed before plasma cleaning.

Plasma cleaning: cover slips in a metal rack were etched with an oxygen plasma of ~300-500 mTorr using a Plasmod plasma cleaner (March Instruments) for 30 seconds (most effective) to 3 minutes.

Imaging

Epi-fluorescence imaging was performed with a Nikon TE-2000 microscope using a 100x, 1.49 NA objective lens, a halogen arc lamp and a Qimaging Retiga SRV camera. Confocal imaging was performed using a Zeiss Axio Observer microscope with a 63x, 1.4 NA objective lens, 488 nm and 561 nm lasers, a Solamere spinning disk confocal unit, and a Photometrics Cascade II camera. TIRF imaging was performed using a Nikon Ti microscope using a 100x, 1.49 NA objective lens, 488 nm and 561 nm laser illumination (Coherent, Inc.), and a Photometrics Evolve camera.

References

Amann KJ, Pollard TD (2001) Direct real-time observation of actin filament branching mediated by Arp2/3 complex using total internal reflection fluorescence microscopy. *Proc Natl Acad Sci U S A* 98, 15009-15013.

Angelini TE, Liang H, Wriggers W, Wong GCL (2003) Like-charge attraction between polyelectrolytes induced by counterion charge density waves. *Proc Natl Acad Sci U S A* 100, 8634-8637.

Arai Y, Yasuda R, Akashi K, Harada Y, Miyata H, Kinosita K Jr, Itoh H (1999) Tying a molecular knot with optical tweezers. *Nature* 399, 446-448.

Bathe M, Heussinger C, Claessens MMAE, Bausch AR, Frey E (2008) Cytoskeletal bundle mechanics. *Biophys J* 94, 2955-2964.

Bicek AD, Tüzel E, Kroll DM, Odde DJ (2007) Analysis of microtubule curvature. *Methods Cell Biol* 83, 237-268.

Bieling P, Telley IA, Hentrich C, Piehler J, Surrey T (2010) Chapter 28 - Fluorescence Microscopy Assays on Chemically Functionalized Surfaces for Quantitative Imaging of Microtubule, Motor, and +TIP Dynamics. 95, 555 - 580.

Blanchoin L, Amann KJ, Higgs HN, Marchand JB, Kaiser DA, Pollard TD (2000) Direct observation of dendritic actin filament networks nucleated by Arp2/3 complex and WASP/Scar proteins. *Nature* 404, 1007-1011.

Brangwynne CP, Koenderink GH, Barry E, Dogic Z, MacKintosh FC, Weitz DA (2007) Bending Dynamics of Fluctuating Biopolymers Probed by Automated High-Resolution Filament Tracking. *Biophys J* 93, 346-359.

Cameron LA, Svitkina TM, Vignjevic D, Theriot JA, Borisy GG (2001) Dendritic organization of actin comet tails. *Curr Biol* 11, 130-135.

Chaudhuri O, Parekh SH, Fletcher DA (2007) Reversible stress softening of actin networks. *Nature* 445, 295-298.

De La Cruz EM, Pollard TD (1994) Transient kinetic analysis of rhodamine phalloidin binding to actin filaments. *Biochemistry* 33, 14387-14392.

DuFort CC, Paszek MJ, Weaver VM (2011) Balancing forces: architectural control of mechanotransduction. *Nat Rev Mol Cell Biol* 12, 308-319.

Egelman EH, Francis N, DeRosier DJ (1983) Helical disorder and the filament structure of F-actin are elucidated by the angle-layered aggregate. *J Mol Biol* 166, 605-629.

Egile C, Loisel TP, Laurent V, Li R, Pantaloni D, Sansonetti PJ, Carlier MF (1999) Activation of the CDC42 effector N-WASP by the *Shigella flexneri* IcsA protein promotes actin nucleation by Arp2/3 complex and bacterial actin-based motility. *J Cell Biol* 146, 1319-1332.

Ehrlicher AJ, Nakamura F, Hartwig JH, Weitz DA, Stossel TP (2011) Mechanical strain in actin networks regulates FilGAP and integrin binding to filamin A. *Nature* 478, 260-263.

Eyckmans J, Boudou T, Yu X, Chen CS (2011) A hitchhiker's guide to mechanobiology. *Dev Cell* 21, 35-47.

Ferrer JM, Lee H, Chen J, Pelz B, Nakamura F, Kamm RD, Lang MJ (2008) Measuring molecular rupture forces between single actin filaments and actin-binding proteins. *Proc Natl Acad Sci U S A* 105, 9221-9226.

Finer JT, Simmons RM, Spudich JA (1994) Single myosin molecule mechanics: piconewton forces and nanometre steps. *Nature* 368, 113-119.

Fletcher DA, Mullins RD (2010) Cell mechanics and the cytoskeleton. *Nature* 463, 485-492.

Fujiwara I, Suetsugu S, Uemura S, Takenawa T, Ishiwata S (2002) Visualization and force measurement of branching by Arp2/3 complex and N-WASP in actin filament. *Biochem Biophys Res Commun* 293, 1550-1555.

Galkin VE, Orlova A, Egelman EH (2012) Actin filaments as tension sensors. *Curr Biol* 22, R96-R101.

Gerbal F, Laurent V, Ott A, Carlier MF, Chaikin P, Prost J (2000) Measurement of the elasticity of the actin tail of Listeria monocytogenes. *Eur Biophys J* 29, 134-140.

Gittes F, Mickey B, Nettleton J, Howard J (1993) Flexural rigidity of microtubules and actin filaments measured from thermal fluctuations in shape. *J Cell Biol* 120, 923-934.

Gonzalez RC, Woods RE, Eddins SL (2003) Digital Image Processing Using MATLAB. Upper Saddle River, New Jersey: Prentice-Hall, Inc.

Hayakawa K, Tatsumi H, Sokabe M (2011) Actin filaments function as a tension sensor by tension-dependent binding of cofilin to the filament. *J Cell Biol* 195, 721-727.

Heinemann F, Doschke H, Radmacher M (2011) Keratocyte lamellipodial protrusion is characterized by a concave force-velocity relation. *Biophys J* 100, 1420-7.

Howard J (2001) Mechanics of motor proteins and the cytoskeleton. Sunderland, Mass.: Sinauer Associates, Inc.

Ichetovkin I, Grant W, Condeelis J (2002) Cofilin produces newly polymerized actin filaments that are preferred for dendritic nucleation by the Arp2/3 complex. *Curr Biol* 12, 79-84.

Isambert H, Venier P, Maggs AC, Fattoum A, Kassab R, Pantaloni D, Carlier MF (1995) Flexibility of actin filaments derived from thermal fluctuations. Effect of bound nucleotide, phalloidin, and muscle regulatory proteins. *J Biol Chem* 270, 11437-11444.

Iwasa JH, Mullins RD (2007) Spatial and Temporal Relationships between Actin-Filament Nucleation, Capping, and Disassembly. *Curr Biol* 17, 395 - 406.

Kapur JN, Sahoo PK, Wong AKC (1985) A new method for gray-level picture thresholding using the entropy of the histogram. *Computer Vision, Graphics, and Image Processing* 29, 273-285.

Koestler SA, Auinger S, Vinzenz M, Rottner K, Small JV (2008) Differentially oriented populations of actin filaments generated in lamellipodia collaborate in pushing and pausing at the cell front. *Nat Cell Biol* 10, 306-313.

Kojima H, Ishijima A, Yanagida T (1994) Direct measurement of stiffness of single actin filaments with and without tropomyosin by in vitro nanomanipulation. *Proc Natl Acad Sci U S A* 91, 12962-12966.

Leyman S, Sidani M, Ritsma L, Waterschoot D, Eddy R, Dewitte D, Debeir O, Decaestecker C, Vandekerckhove J, van Rheenen J, Ampe C, Condeelis J, Van Troys M (2009) Unbalancing the phosphatidylinositol-4,5-bisphosphate-cofilin interaction impairs cell steering. *Mol Biol Cell* 20, 4509-4523.

Marcy Y, Prost J, Carlier M, Sykes C (2004) Forces generated during actin-based propulsion: a direct measurement by micromanipulation. *Proc Natl Acad Sci U S A* 101, 5992-5997.

McGrath JL, Eungdamrong NJ, Fisher CI, Peng F, Mahadevan L, Mitchison TJ, Kuo SC (2003) The force-velocity relationship for the actin-based motility of Listeria monocytogenes. *Curr Biol* 13, 329-332.

Mooseker MS, Tilney LG (1975) Organization of an actin filament-membrane complex. Filament polarity and membrane attachment in the microvilli of intestinal epithelial cells. *J Cell Biol* 67, 725-743.

Orlova A, Egelman EH (2000) F-Actin Retains a Memory of Angular Order. *Biophys J* 78, 2180 - 2185.

Otsu N (1979) A Threshold Selection Method from Gray-Level Histograms. *Systems, Man and Cybernetics, IEEE Transact* 9, 62-66.

Ott A, Magnasco M, Simon A, Libchaber A (1993) Measurement of the persistence length of polymerized actin using fluorescence microscopy. *Phys Rev E Stat Phys Plasmas Fluids Relat Interdiscip Topics* 48, R1642-R1645.

Parekh SH, Chaudhuri O, Theriot JA, Fletcher DA (2005) Loading history determines the velocity of actin-network growth. *Nat Cell Biol* 7, 1219-1223.

Piran U, Riordan WJ (1990) Dissociation rate constant of the biotin-streptavidin complex. *J Immunol Methods* 133, 141-143.

Ponti A, Machacek M, Gupton SL, Waterman-Storer CM, Danuser G (2004) Two distinct actin networks drive the protrusion of migrating cells. *Science* 305, 1782-1786.

Prass M, Jacobson K, Mogilner A, Radmacher M (2006) Direct measurement of the lamellipodial protrusive force in a migrating cell. *J Cell Biol* 174, 767-772.

Raucher D, Sheetz MP (2000) Cell spreading and lamellipodial extension rate is regulated by membrane tension. *J Cell Biol* 148, 127-136.

Raucher D, Sheetz MP (1999) Characteristics of a membrane reservoir buffering membrane tension. *Biophys J* 77, 1992-2002.

Schmid MF, Sherman MB, Matsudaira P, Chiu W (2004) Structure of the acrosomal bundle. *Nature* 431, 104-107.

Sept D, Xu J, Pollard TD, McCammon JA (1999) Annealing accounts for the length of actin filaments formed by spontaneous polymerization. *Biophys J* 77, 2911-2919.

Shimozawa T, Ishiwata S (2009) Mechanical Distortion of Single Actin Filaments Induced by External Force: Detection by Fluorescence Imaging. *Biophys J* 96, 1036-1044.

Spudich JA (2011) Molecular motors: forty years of interdisciplinary research. *Mol Biol Cell* 22, 3936-3939.

Spudich JA, Watt S (1971) The regulation of rabbit skeletal muscle contraction. I. Biochemical studies of the interaction of the tropomyosin-troponin complex with actin and the proteolytic fragments of myosin. *J Biol Chem* 246, 4866-4871.

Stricker J, Falzone T, Gardel ML (2010) Mechanics of the F-actin cytoskeleton. *J Biomech* 43, 9-14.

Svitkina TM, Borisy GG (1999) Arp2/3 complex and actin depolymerizing factor/cofilin in dendritic organization and treadmilling of actin filament array in lamellipodia. *J Cell Biol* 145, 1009-1026.

Svitkina TM, Verkhovsky AB, McQuade KM, Borisy GG (1997) Analysis of the actin-myosin II system in fish epidermal keratocytes: mechanism of cell body translocation. *J Cell Biol* 139, 397-415.

Tang JX, Kas JA, Shah JV, Janmey PA (2001) Counterion-induced actin ring formation.. *Eur Biophys J* 30, 477-484.

Telley IA, Bieling P, Surrey T (2011) Reconstitution and quantification of dynamic microtubule end tracking in vitro using TIRF microscopy. *Methods Mol Biol* 777, 127-145.

Tsuda Y, Yasutake H, Ishijima A, Yanagida T (1996) Torsional rigidity of single actin filaments and actin-actin bond breaking force under torsion measured directly by in vitro micromanipulation.. *Proc Natl Acad Sci U S A* 93, 12937-12942.

Uyeda TQP, Iwadate Y, Umeki N, Nagasaki A, Yumura S (2011) Stretching actin filaments within cells enhances their affinity for the myosin II motor domain. *PLoS One* 6, e26200.

van Mameren J, Vermeulen KC, Gittes F, Schmidt CF (2009) Leveraging single protein polymers to measure flexural rigidity. *J Phys Chem B* 113, 3837-3844.

Vignjevic D, Kojima S, Aratyn Y, Danciu O, Svitkina T, Borisy GG (2006) Role of fascin in filopodial protrusion. *J Cell Biol* 174, 863-875.

Vinzenz M, Nemethova M, Schur F, Mueller J, Narita A, Urban E, Winkler C, Schmeiser C, Koestler SA, Rottner K, Resch GP, Maeda Y, Small JV (2012) Actin branching in the initiation and maintenance of lamellipodia. *J Cell Sci,* Advance Online Publication, March 19, 2012, doi:10.1242/jcs.107623.

Wiesner S, Helfer E, Didry D, Ducouret G, Lafuma F, Carlier M, Pantaloni D (2003) A biomimetic motility assay provides insight into the mechanism of actin-based motility. *J Cell Biol* 160, 387-398.

Wong J, Chilkoti A, Moy VT (1999) Direct force measurements of the streptavidin-biotin interaction. *Biomol Eng* 16, 45-55.

Worring M, Smeulders AWM (1993) Digital curvature estimation. *CVGIP: Image Underst* 58, 366-382.

Xu K, Babcock HP, Zhuang X (2012) Dual-objective STORM reveals three-dimensional filament organization in the actin cytoskeleton. *Nat Methods* 9, 185-188.

Yanagida T, Nakase M, Nishiyama K, Oosawa F (1984) Direct observation of motion of single F-actin filaments in the presence of myosin. *Nature* 307, 58-60.

Yasuda R, Miyata H, Kinosita KJ (1996) Direct measurement of the torsional rigidity of single actin filaments. *J Mol Biol* 263, 227-236.

Chapter 3. Actin Filament Curvature Biases Branching by the Arp2/3 Complex

The work described in this chapter is used with permission and was previously published as:

Risca VI, Wang EB, Chaudhuri O, Chia JJ, Geissler PL, Fletcher DA (2012) Actin filament curvature biases branching direction. *Proc Natl Acad Sci U S A* 109, 2913-2918.

Introduction

Mechanical forces from a metazoan cell's environment are transduced into biochemical signals during many biological processes, such as the differentiation, proliferation and migration of cells, to regulate processes ranging from cytoskeletal remodeling to gene expression (Farge, 2011). Mechanotransduction has been thought to occur primarily via specialized mechanosensing molecules, which stretch or unfold in response to applied forces (Hoffman et al., 2011; Vogel & Sheetz, 2006), while the filament networks that make up the bulk of the cytoskeleton have been studied primarily as materials, whose mechanical properties determine how they transmit or absorb forces (Fletcher & Mullins, 2010; Janmey & McCulloch, 2007). We asked whether filamentous actin (F-actin), a major part of the cytoskeleton, can act as a mechanosensor in its own right.

The actin cytoskeleton consists of an organized network of filaments that bear both tensile and compressive forces and largely determine the shape and rigidity of metazoan cells (Janmey & McCulloch, 2007). Growth of one specialized cytoskeletal structure, the branched actin network (Goley & Welch, 2006; Pollard & Borisy, 2003; Welch & Mullins, 2002), produces forces that act on cellular membranes to help them protrude or change shape (Giardini et al., 2003; Marcy et al., 2004; Parekh et al., 2005; Prass et al., 2006) and plays an important role in cell motility, the trafficking of cellular membranes including endocytosis, and the motility of intracellular pathogens (Firat-Karalar & Welch, 2011; Gouin et al., 2005). When this protrusive growth is opposed by resistance from the surrounding cytoskeleton or plasma membrane, the actin network compresses, and filaments in the network bend (Chaudhuri et al., 2007; Gardel et al., 2004; Kim et al., 2009; Lieleg et al., 2011). In vitro studies have shown that compressive forces applied to branched networks can not only reversibly deform them (Chaudhuri et al., 2007) but can also alter their density (Soo & Theriot, 2005) and growth velocity (Marcy et al., 2004; Parekh et al., 2005), suggesting that their architecture may respond actively to mechanical forces. While the binding of many actin binding proteins (ABPs) to the side of an actin filament has been characterized (McGough, 1998) and, in some cases, shown to depend on the filament's twist (De La Cruz, 2005; Galkin et al., 2001) or its bound nucleotide (Maciver et al., 1991; Okreglak & Drubin, 2007), the response of most F-actin-ABP interactions to filament bending is unknown (Fletcher & Mullins, 2010). The only such response that has been documented is an increased frequency of severing by actophorin or its homolog ADF/cofilin at highly curved sections of actin filaments (Maciver et al., 1991; McCullough et al., 2011).

Bending of F-actin is particularly relevant to its interaction with the Arp2/3 complex because of the complex's central regulatory and structural roles in the formation of branched actin networks (Goley & Welch, 2006). Upon activation by two molecules of nucleation-promoting factor (NPF) localized at or near a membrane, the Arp2/3 complex nucleates a new, 'daughter' filament from the side of a pre-existing 'mother' filament, forming a Y-shaped branch that serves as the basic structural unit of these networks (Fig. S1) (Padrick et al., 2011; Pollard, 2007; Ti et al., 2011). Importantly, the Arp2/3 binding site on F-actin spans three actin monomers along F-actin's long-pitch helix, suggesting that its binding may be affected by changes in both monomer conformation and inter-monomer distance induced by bending stresses (Rouiller et al., 2008).

The mechanism of Arp2/3 branch nucleation (Fig. 5) is understood to involve conformational changes in the Arp2/3 complex induced by the binding of NPFs (Beltzner & Pollard, 2008; Goley et al., 2004; Padrick et al., 2011; Pollard, 2007; Ti et al., 2011). Additional conformational changes in both the Arp2/3 complex and several monomers in the mother filament probably occur upon the binding of the ternary complex of NPFs, Arp2/3, and G-actin to the mother filament or during a subsequent activation step that is necessary to allow branch nucleation (Beltzner & Pollard, 2008; Pollard, 2007), because the bound NPFs appear to partially overlap the F-actin binding surface of the Arp2/3 complex (Xu et al., 2011). Once formed, the branch can then survive for minutes in vitro before dissociating (a process called "debranching") (Mahaffy & Pollard, 2006). The rate of debranching has been shown to depend on the nucleotide bound to the mother filament (ATP, ADP-P_i or ADP) (Mahaffy & Pollard, 2006), and on the presence of the actin stabilizing drug phalloidin (Blanchoin et al., 2000; Mahaffy & Pollard, 2008). Branch nucleation appears to happen most readily on actin in the ATP-bound state, (Ichetovkin et al., 2002), although it is not yet fully determined whether this is due to enhanced nucleation or stability against fast debranching. Experiments that used saturating amounts of phosphate to stabilize actin in the ADP-P_i-bound state showed a rate of barbed end creation similar to that on unstabilized actin (Mahaffy & Pollard, 2006). The regulation of both branch nucleation and branch stability by direct mechanical factors has not yet been studied. We asked whether filament bending by externally imposed geometric constraints plays a regulatory role at any point in this actin branch nucleation pathway.

Results and discussion

Surface-based branching assay reveals that actin filament curvature biases branching direction

To examine whether and how the bending of filaments affects their interaction with the Arp2/3 complex, we imaged branch nucleation from fluorescently labeled F-actin that was pre-immobilized on a surface before incubation with Arp2/3 complex, an NPF, and monomeric actin (G-actin) (Figure 28A-C). From the total of 403 images (Figure 28D) acquired in five independent experiments, we measured the distribution of curvature along the immobilized mother filaments (Figure 28E-H) (Worring & Smeulders, 1993). Curvature varied smoothly as observed by fluorescence microscopy and could be measured on filaments spanning at least 3 μm, with a spatial resolution of ~1.1 μm. We were able to infer the location of Arp2/3 complex binding on the mother filament, with a spatial resolution of ~500 nm, from the location and direction of the short and stiff actin branches it nucleated, which were imaged separately from mother filaments using a two-color fluorescent labeling strategy (Blanchoin et al., 2000; Ichetovkin et al., 2002). Filament curvature at branch points and the direction of branch growth (Figure 28C) determined the sign of the curvature value assigned to each branch. Branches on the convex side of the filament curve were assigned negative curvature, and branches on the concave side were assigned positive curvature.

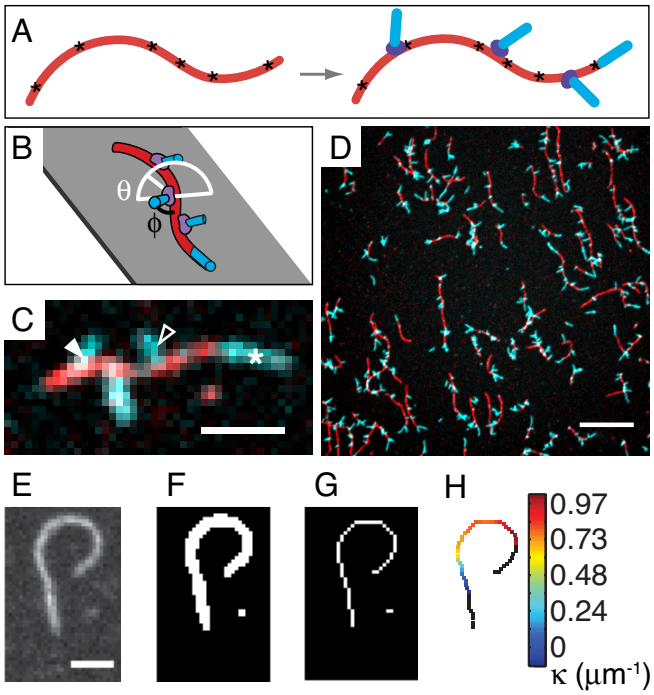

Figure 28. Branching from curved filaments was observed in vitro. (A) Mother filaments (red) immobilized via biotin-streptavidin tethers (asterisks) before nucleation of branches (cyan blue) by Arp2/3 complex (violet). (B) Actin branches grow at a branch angle $\varphi \sim 70°$ to the mother filament (black line) with an azimuthal angle θ from 0 to 180° (white line). (C) Fluorescence image of actin growth at mother filament ends (white asterisk) and on branches on concave (open arrowhead) and convex (filled arrowhead) sides of mother filament curves. (D) Sample field of view. (E-G) Filament image thresholded and skeletonized to an 8-connected digital curve. (H), Mother filament curvature measured with the tangent angle method. Scale bars: C, E, 2 μm; D, 10 μm.

Interestingly, we observed that branches were more likely to be found on the convex surface of a curved filament than on the concave surface. We compared the distribution of curvatures measured at equally spaced points 182 nm apart along a total of 27.4 mm of mother filaments where branches could have formed (Figure 29A), to the distribution of curvatures observed at 10,443 branch points, where branches actually formed (Figure 29B). If branch density were independent of mother filament curvature, the two distributions would be identical after normalization. Instead, we found that the distributions were different (Figure 29C and Table 7) and calculated their ratio, which we call the relative branch density (Figure 0302D).

The relative branch density increased with negative curvature, indicating that extensional strain on the Arp2/3-binding surface of F-actin makes branch nucleation more likely, while compressional strain makes it less likely (Figure 29D). We quantified the trend with a weighted least-squares linear fit to the relative branch density calculated from a subset of mother filament curvature samples selected randomly, one per filament to strictly satisfy the assumptions underlying linear regression. The weights were the number of samples of mother filament curvature in each curvature bin. The relative linear branch density decreased with a slope of -33% per μm^{-1} of curvature (95% C.I.: (-40%, -26%), $R^2 = 0.56$) (Figure 30A and Table 8). Thus, the probability of finding a branch on the convex side of a filament with a curvature of 1 μm^{-1} is 99% higher than finding it on the concave side. Linear regression against the full data set containing multiple curvature measurements from each mother filament yielded similar results (Table 8).

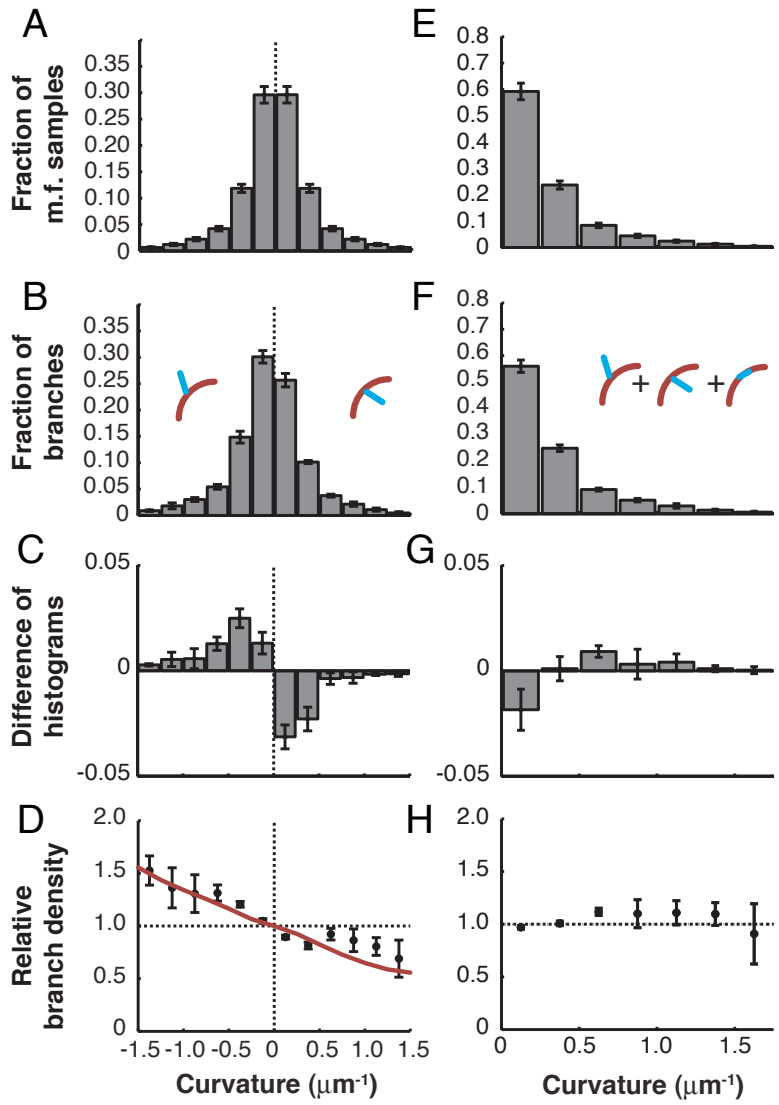

Figure 29. Filament curvature biases branching direction. (A) Mother filament curvature distribution and (B) the distribution of mother filament curvature at branch points measured with the tangent angle method. (C) The difference and (D) the ratio of the histograms in B and A. The latter is called the relative branch density. The red curve represents the best fit (by least-squares) by the fluctuation gating model with a 5 μm^{-1} threshold curvature. C,D,G, and H were normalized using a simulated control (see Materials and Methods). (E-H) The unsigned curvature distributions corresponding to (A-D). Error bars: SEM, n = 5 independent experiments.

To quantify the effect of filament bending on total linear branch density, we carried out the same analysis as above with unsigned branch curvatures (Figure 29E,F) and found that the likelihood of branching per unit length shows a weak dependence on curvature (Figure 29G,H and Figure 30B) with a slope of 13% per μm^{-1} (95% CI: (3.3%, 23%)). However, the linear fit does not describe the unsigned curvature data very well (Figure 30B, Table 8, $R^2 = 0.17$), and the size of the deviation from a flat curve is comparable to the size of systematic errors in digital curvature estimation (Figure 30). In addition, fitting the data with a higher-order polynomial did not significantly improve the fit ($p = 0.06$, ANOVA). We conclude that total linear branch density depends weakly on absolute curvature, and we focus on studying the predominant effect of mother filament curvature on branch direction.

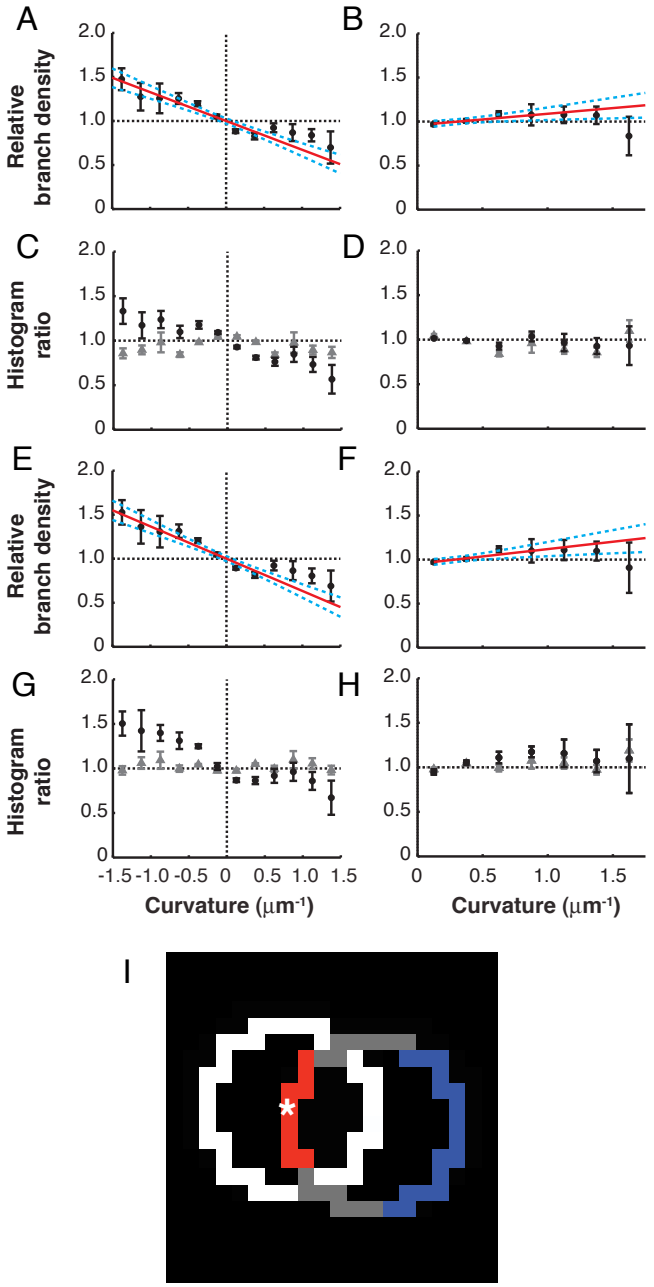

Figure 30. Quantification of the curvature dependence of branching. A subset of the data in Figure 29, with curvature estimated by the tangent angle method, was used to assemble histograms and relative branch density curves from uncorrelated curvature samples. The signed and unsigned mother filament curvature distribution was measured by sampling the curvature of mother filaments at only one randomly chosen point (away from the ends) on each filament. This sampling method was used to avoid correlations between curvature points collected at nearby locations on the same filament. Relative linear branch density is shown as a function of (A) signed and (B) unsigned curvature. These measurements of the linear branch density, based on independent samples, satisfy the assumptions of linear regression and were used to estimate the magnitude of the linear trends in branch density with curvature. The results of a weighted least squares regression on pooled data are shown as the line of means (red line) and the 95% confidence interval on the line of means (cyan, dashed lines) (Table 8). (C) and (D) show the raw histogram ratios used to calculate branch density (black circles) and the ratios calculated from randomly generated branches along the same set of mother filament curves, analyzed identically and used to correct the branch density data for systematic errors introduced by bias in the curvature estimation method (gray triangles). (E-H), similar plots describing the same set of experiments analyzed by making many curvature measurements on each filament. Data shown in panels E and F is identical to Figure 29D,H. (I) For a digitized circle with a radius of 5 pixels, a branch of length 5 pixels centered at * is schematically shown as a circle depicting possible locations of the branch tip, color coded as inside the circle (red), outside the circle (blue), or overlapping with the circle and having indeterminate direction. Note

that more branch tip locations external to the circle are possible when the branch length is comparable to the circle radius, introducing a curvature-dependent systematic error into our measurement. Such errors were compensated for by subtracting the simulated random branch density (gray triangles in C,D,G and H) from the real density (black circles in same plots). Error bars: SEM.

To confirm that the existence of a branching bias due to curvature was robust to the analysis method, we applied an alternative spline-based curvature estimation algorithm (Figure 31) (Bicek et al., 2007; Worring & Smeulders, 1993). The exact value of the slope depended on the curvature estimation method, but the observation of branch direction bias due to curvature (-14% per μm^{-1} of curvature, 95% C.I.: (-17%, -10%)) was unchanged (Table 8). We also checked how our estimate of bias in the direction of branching was affected by changes in image magnification and found only a weak effect (Figure 32, Table 9, $p = 0.076$).

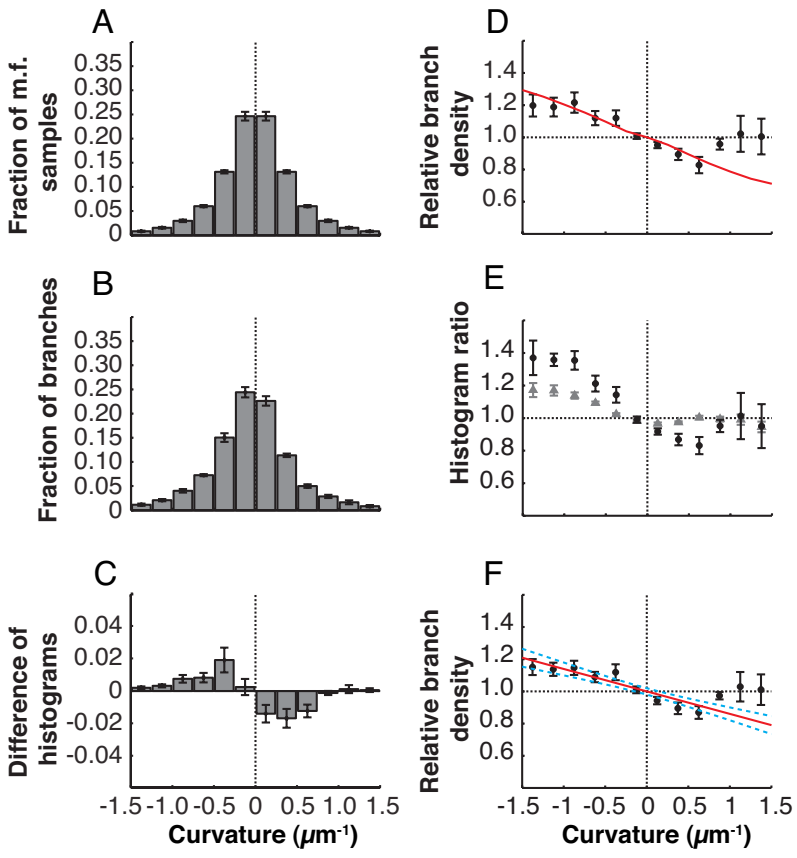

Figure 31. Branching bias induced by curvature is also seen with spline-based curvature analysis. Raw data is the same as analyzed in Fig. 2. (A) Mother filament curvature distribution. (B) Distribution of curvature at branch points. (C) Difference of histograms in A and B. (D) Relative branch density as a function of curvature (gray circles) and the least-squares best fit fluctuation gating model with a threshold curvature of 1 μm^{-1}. (E) Raw branch density (black circles) and control density calculated from random, simulated branches (gray triangles). The control curve was subtracted from the raw curve, experiment-by-experiment, to generate the final branch density curves averaged to generate D. (F) Subsampled data (with one curvature measurement per filament) shown with the best straight line fit (red, calculated by linear regression on the pooled data from 7 experiments) and 95% confidence interval on the line of means (cyan, dashed lines). The only difference between the data shown in D and F is the set of points at which mother filament curvature was measured to sample the overall curvature distribution. Branch data and the subsequent analysis steps, including the normalization step described in E, are identical between D and F. Error bars: SEM.

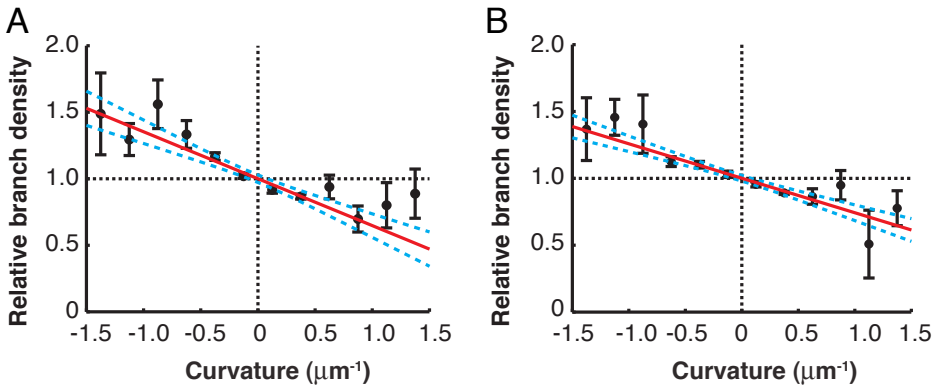

Figure 32. The effect of image magnification on the change in relative branch density with curvature. All data was analyzed with the tangent angle-based method as in Fig. 2D. (A) Relative branch density of NHS-labeled mother filaments with 25 mM phosphate at 165 nm/pixel, n = 6 independent experiments. (B) Relative branch density measured from a different set of images acquired at 103 nm/pixel under the same biochemical conditions, n = 5. Solid red lines: linear trend fit to pooled data by least squares, weighted by the number of mother filament samples in each bin. Dotted blue lines: 95% confidence interval for the best-fit line. Error bars: SEM.

As biochemical controls, we verified that our results do not depend on the mode of actin labeling (Figure 33A,C,E and Table 9, p = 0.69). We also tested whether stabilizing the mother filament in the ADP-P_i-bound state by adding 25 mM phosphate affected the observed branching bias and did not observe an effect (Figure 33C-E and Table 9) (p = 0.998), nor did we observe a significant change in slope due to phalloidin stabilization of F-actin (Figure 33A,B,E) (p = 0.10).

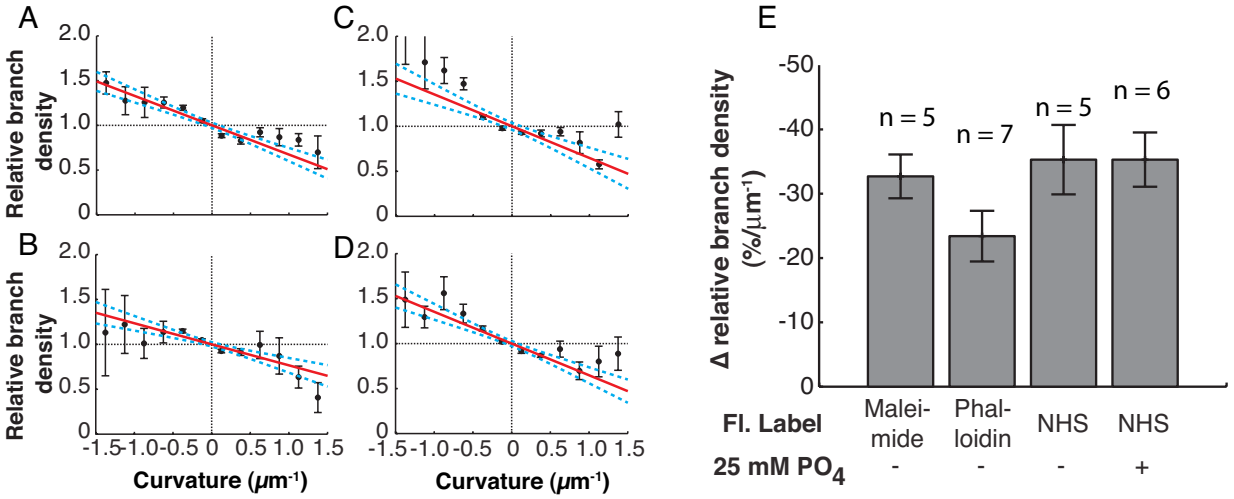

Figure 33. Relative branch density plots and linear slope for different biochemical conditions. (A) Mother filaments unstabilized by phalloidin during branching, labeled with 30% maleimide-AF546 and 10% maleimide-biotin in buffer KMEI (percentages refer to fraction of labeled monomers) (see Figure 29D) (n = 5). (B) Mother filaments labeled only with 10% maleimide-biotin and stabilized with rhodamine-phalloidin during branching (n = 7). (C) Unstabilized mother filaments labeled with 30% NHS-Cy3 and 10% NHS-biotin in buffer KMEI (n = 5). (D) NHS labeled mother filaments in buffer KMEI with 25 mM phosphate (n = 6). Red lines: best-fit linear slope (least-squares weighted by the number of mother filament samples in each bin). Dotted blue lines: 95% confidence interval on the slope. (E) The slope of the relative branch density (quantification of red lines from A-D) shown as a function of the mode of fluorescent labeling (AF-546-maleimide or NHS-Cy3) or actin stabilization (phalloidin, phosphate, or none). All error bars: SEM.

The observed bias in branch direction is not caused by debranching

Mother filament curvature may influence one or several of the steps in the branch nucleation pathway. Because we imaged the end products of this branching pathway, we could not address the effect of mother filament curvature on Arp2/3 binding separately from branch nucleation. To address the role of debranching, we incubated our standard samples, in which branching had occurred for 2 min, for an additional 33 min in the absence of Arp2/3 complex. We did not observe debranching during the additional incubation time (Figure 34A), even with a high concentration of blocking protein (2 mg/mL BSA) included in solution to prevent nonspecific adsorption of branches onto the cover slip surface. To quantify branch density and its dependence on curvature, we incubated different samples for either 50 s or 15 min before stabilization with phalloidin. In these experiments, the branch density decreased, but not to a statistically significant extent (Figure 34B), and there was not a statistically significant difference in the slope of the relative branch density as a function of curvature (Figure 34C, Table 9). These results indicate that mother filament curvature primarily acts on branch nucleation.

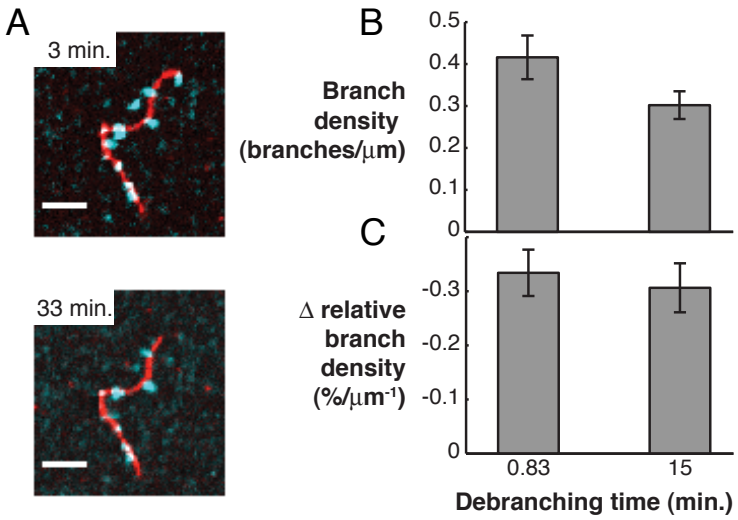

Figure 34. Branch stability does not affect the branching bias. (A) Actin branches (cyan blue) grown from unstabilized mother filaments (red) and incubated in buffer with unlabeled actin but without phalloidin stabilization for times shown exhibited little to no debranching when the same sample was imaged at the two time points. Bars, 5 μm. (B-C) To obtain enough images for curvature analysis, identical but separate samples were prepared with incubation times of 0.83 or 15 min. in KMEI buffer (Materials and Methods) with unlabeled actin before stabilization with phalloidin and imaging. (B) We found a decrease in overall branch density between short and long incubation samples, but it was not statistically significant, ($p = 0.12$, Welch's t test, $n = 4$). (C) There was no significant difference in the slope of relative branch density with respect to curvature (Table 9, $p = 0.66$). Error bars: SEM.

It is also possible that curvature acts on the stability of very short branches that were proposed by Mahaffy et al. to dissociate before microscopy-based methods can detect them (Mahaffy & Pollard, 2006). However, the lack of dependence on phosphate added at a concentration similar to that used by Mahaffy et al. suggests that curvature most likely acts on nucleation rather than dissociation. Overall, we do not exclude the possibility that curvature may affect fast de-branching that we do not detect, but we favor the interpretation that curvature primarily affects branch nucleation. Ichetovkin et al. observed an enhanced branch density on filaments stabilized in the ATP-bound state (Ichetovkin et al., 2002), suggesting that the presence of ATP may have an effect on the nucleation process and may also affect sensitivity to curvature. However in our experiments, freshly polymerized actin containing ATP was only present on filament ends, where curvature could not be accurately measured.

Monte Carlo simulations reveal the nanometer-scale curvature fluctuations of constrained filaments

Because the length scale relevant to Arp2/3 binding and branch nucleation is 5-10 nm, well below the length scale at which fluorescence microscopy can measure curvature and also below the micrometer length scale at which curvature can be externally imposed, we used Monte Carlo simulations of a discretized worm-like chain (WLC) polymer (Figure 35A,B) to assess the nanometer-scale implications of the micrometer-scale curvature. The validity of the WLC model to F-actin elasticity has been demonstrated for filament curvatures as high as 5 μm^{-1} (Arai et al., 1999). In our work, the WLC polymer, with the persistence length of actin (L_p = 9 μm) (Isambert et al., 1995), was pinned to a plane with imposed curvature, κ_0, mimicking the experiment (Figure 36A).

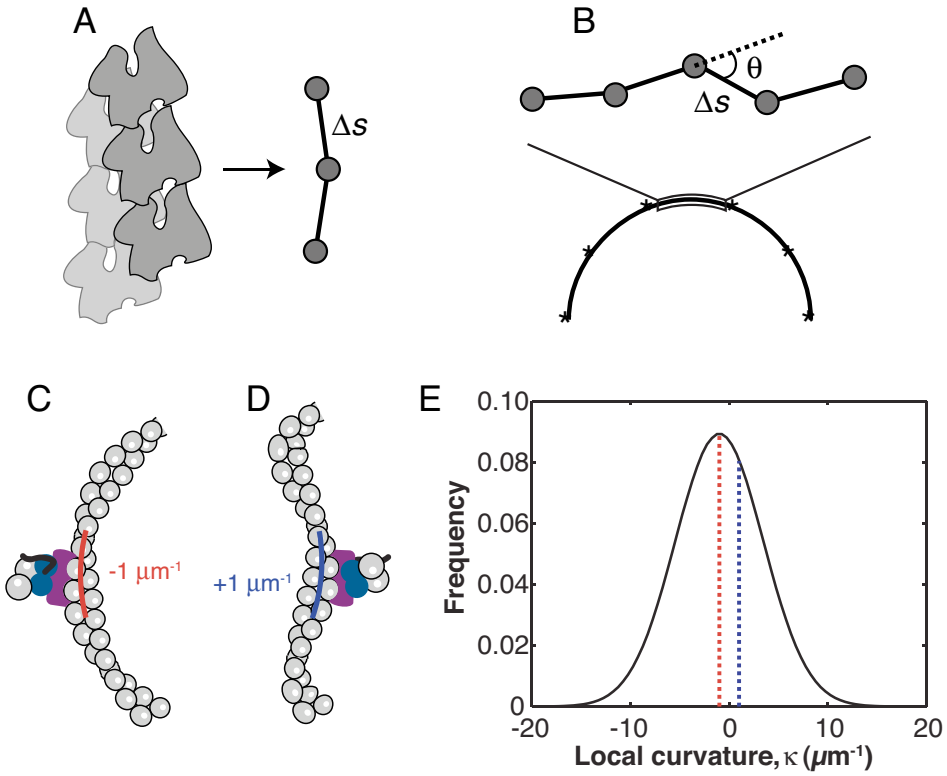

Figure 35. The actin filament was simulated as a discretized WLC polymer. (A) Each particle of the WLC polymer stands for two actin monomers, with Δs = 5.4 nm bonds between particles. (B) The WLC polymer was tethered to a path with a defined curvature at six particles (asterisks), and curvature was calculated (Equation 16), from the section between the middle two tethered particles, in order to avoid end effects. The likelihood of curvature inverting fluctuations is high because the curvature distribution is wide relative to changes in the mean, ruling out a simple equilibrium mechanism for the branching bias. (C) Schematic representation of the imposed curvature (shown by red arc) of a segment of an actin filament, which is concave to the right in this case. (D) A shape fluctuation of the filament can transiently give rise to the same local curvature, but with opposite concavity (blue arc). A state in which the NPF- and G-actin-bound Arp2/3 complex is bound to the left side of the filament in C has the same energy as the ternary complex bound to the right side of the filament in D, because the microscopic curvature is locally the same. Therefore, the total probability of the Arp2/3 complex being bound to the right or left side of the filament depends only on the relative likelihood of states C and D (E) Distribution of local curvatures on a simulated filament with imposed curvature κ_0 = -1 μm^{-1} (choosing the coordinate system arbitrarily). The average curvature does not fully describe the shape of the filament as encountered by the Arp2/3 complex. The likelihood of that location on the filament having the same local curvature as the imposed mean curvature (red line, state depicted in C) is only 10% larger than its likelihood having the curvature of opposite concavity, and hence opposite sign (blue line, state depicted in D). For comparison, the experimental results (Figure 29) showed 99% more branching on the convex side than on the concave side.

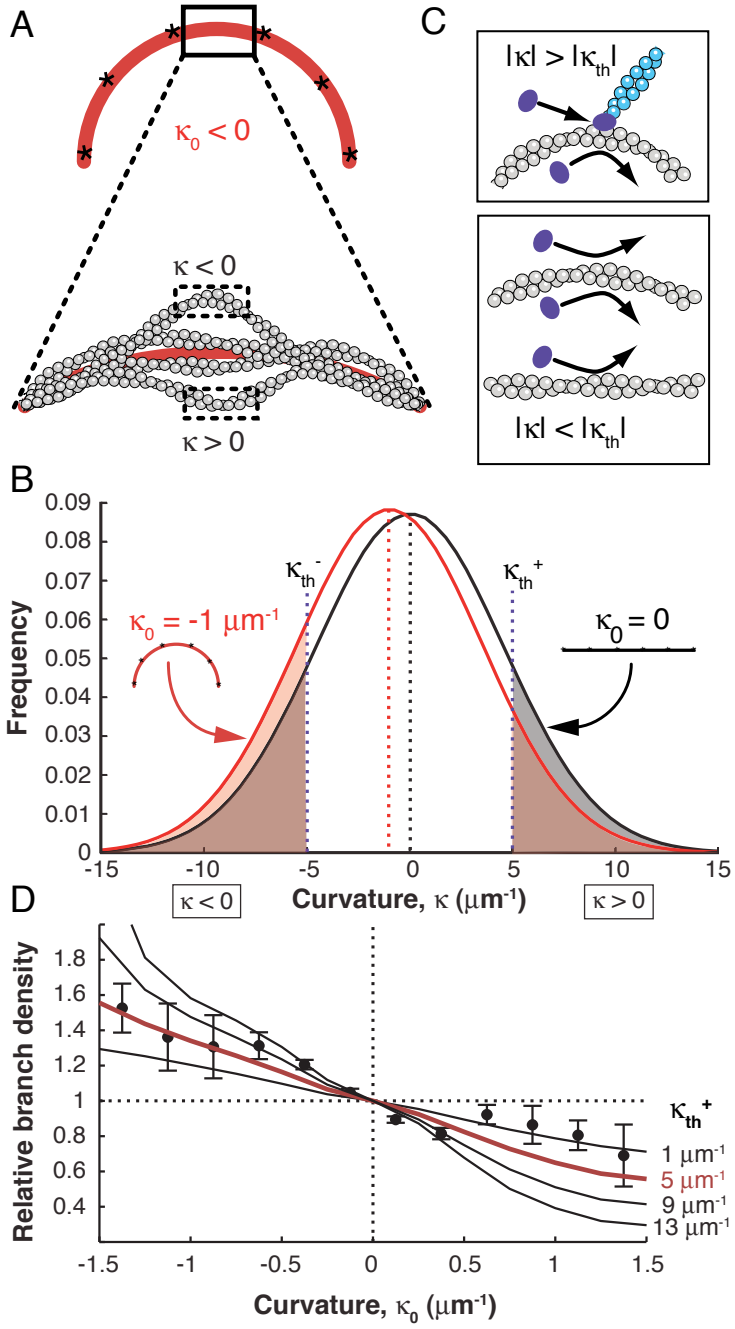

Figure 36. The branching bias can be explained by a shift in the curvature fluctuations of a WLC filament tethered to a curved path. (A) Schematic of the WLC polymer tethered at six points (asterisks) to a curve with imposed curvature $\kappa_0 < 0$. Fluctuations with local curvature $\kappa < 0$ and $\kappa > 0$ are possible. Curvature was calculated from the section between the middle two tethered particles, in order to avoid end effects. (B) Distribution of local curvature fluctuations for a filament tethered to a straight (black) or curved (red) path. Shaded areas indicate probability of branching. (C) The fluctuation gating model predicts a threshold convex local curvature beyond which stable binding and branching by the Arp2/3 complex (violet) can occur. (D) Relative branch density calculated from the ratio of the red and black shaded areas in B for several values of κ_{th} plotted with experimental data (also shown in Figure 29D, with the red line corresponding to the same value of κ_{th}). Error bars: SEM.

Despite being constrained to an average curvature of κ_0, the simulated filament exhibits large thermal fluctuations in nanometer-length-scale local curvature about that average (Figure 36A,B and Figure 35E). The breadth of the local curvature distribution is large in comparison to the range of experimentally accessible imposed curvatures. Therefore, for a filament with convex average curvature of -1 μm^{-1}, locally concave fluctuations occur almost as often as locally convex ones (Figure 35C-E). This small, 10% asymmetry is inconsistent with the larger, 99% asymmetry in branch density we observed between the two sides filaments with -1 μm-1 average

curvature (Figure 29D and Figure 30A). Strong differences between the sides of the filament with convex and concave average curvature only occur in the extreme tails of the corresponding curvature distributions. Therefore, we conclude that branching must be sensitive to local curvature fluctuations that are far from the average. In addition, because such extreme local curvature fluctuations occur rarely, making the system slow to reach chemical equilibrium, we discuss the effect of curvature on branch nucleation by Arp2/3 in kinetic terms.

A fluctuation gating model for branching by the Arp2/3 complex is consistent with the experimental data

Two lines of evidence support the hypothesis that curvature regulates branch nucleation kinetics. First, the Arp2/3 complex binds F-actin in solution with a slow on-rate, perhaps because it must wait for a favorable structural fluctuation of the filament (Beltzner & Pollard, 2008). Second, a structural model of the Arp2/3-actin branch shows a local distortion involving subdomain 2 of an actin monomer at the Arp2/3 binding site (Rouiller et al., 2008). Extensional strain could weaken longitudinal inter-monomer contacts in F-actin, helping to stabilize a transition state with high local curvature and increasing the kinetic rate of either Arp2/3 binding or branch nucleation.

Based on this evidence, we developed a filament fluctuation gating model, conceptually similar to fluctuation-gated binding of ligands to proteins (McCammon & Northrup, 1981). In our model, stable Arp2/3 ternary complex binding and branch nucleation occur only when the local curvature of the filament fluctuates beyond a threshold value κ_{th} (Figure 36C). A sharp threshold is chosen because in the extreme wings of the local curvature distribution, probability attenuates so rapidly that the only pertinent model parameter is the lowest curvature value where branching is greatly enhanced, in effect, κ_{th}. Thus, the probability that a branch forms on either side of the curved filament under our model is the net probability of respective curvature values in excess of $+\kappa_{th}$ or $-\kappa_{th}$ (Figure 36B,C). Our calculations assess how extreme this curvature threshold needs to be in order to account for the curvature preference we observe experimentally.

With these simple assumptions, the fluctuation gating model captures the shape of the curvature-dependent branching bias and agrees quantitatively with our data over the entire experimental range for a value of $\kappa_{th} = 5\mu m^{-1}$ (red curve, Figures 29D and 36D). These results are consistent with a mechanism in which F-actin bending fluctuations play a role in regulating branch formation by the Arp2/3 complex, suggesting that branching can be regulated by alterations of bending fluctuations of filaments due to constraints on actin network architecture or by binding of other ABPs. However, because of its coarse-grained resolution, this model cannot make predictions about conformational changes of the actin monomer caused by bending in the Arp2/3 binding site on the scale of individual amino acid residues. This model is presented in the simplest form that is consistent with our data and experimental parameters, but could be extended to include details about the dependence of branch direction on curvature based on future findings. For example, we currently have little data in the very high convex curvature regime, where the branch density may decrease as the curvature distorts the mother filament to an extent at which it can no longer accommodate branch nucleation.

Autocatalytic branching amplifies the branching bias

Directionally biased branching has important implications for branched actin assembly in vivo, where autocatalytic nucleation amplifies small effects (Carlsson, 2003; Pollard, 2007). A large fraction of filaments in a branched actin network adopt an approximately ± 35˚ orientation (Verkhovsky et al., 2003), and the side of a bent filament experiencing extensional strain is the same side that typically faces the bending force. Excess growth on the convex side of the curved filament would therefore create more branches oriented toward the bending force, reinforcing the branched network (Figure 37A). The excess of branches on the most convex side of the mother filament may also define a preferred plane for branching that coincides with the plane of filament curvature, possibly contributing to the flat and thin shape of lamellipodia. It would also lead to more filaments growing into membrane-adjacent zone where new branches can be nucleated, increasing total branch density. We studied this effect with a different, stochastic simulation of branching in two dimensions (Figure 37B), and found that for a 15% bias toward the membrane, the total number of filaments is double that of the zero bias case after only 10 branch generations (Figure 37B). Based on our experimental data (Figure 29D), a 15% curvature bias corresponds to a radius of curvature of 2.3 µm and a bending energy of 0.6 k_BT per µm of ATP-bound filament (Isambert et al., 1995). This amount of curvature could result from a lateral force of 1 pN applied perpendicularly to the end of a 0.05 µm long filament fixed at the other end (Belendez et al., 2002), which reflects the average force per filament due to membrane tension and rigidity (Abraham et al., 1999; Mogilner & Edelstein-Keshet, 2002) and the approximate length of free F-actin (Svitkina & Borisy, 1999) at the leading edge of the cell. If the length of free F-actin is longer at the leading edge (Small et al., 2011; Urban et al., 2010), the filaments require even less force to bend. Therefore, even modest filament curvature that is caused by the normal force balance of branched actin growth against a membrane can generate a significant bias in the direction of actin branch nucleation.

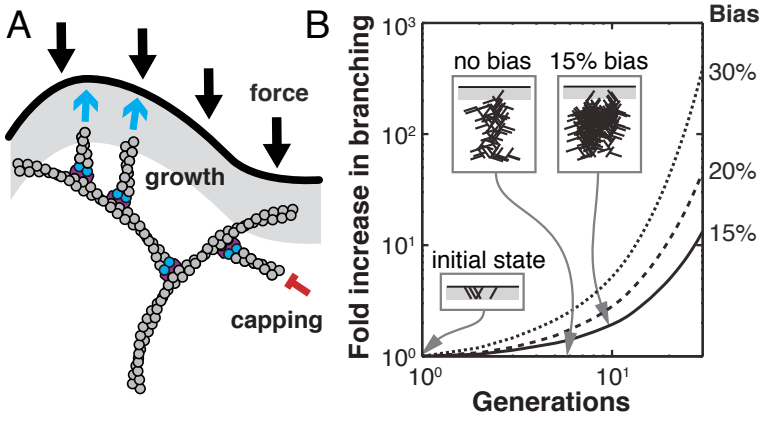

Figure 37. A bias in the direction of branching can increase the total amount of actin in a branched network. (A) In a branched network, compressive forces bend filaments away from the membrane (black). Excess branching on the convex side of a bent filament creates more branches pointing toward the membrane, increasing the number of filaments pushing against the membrane (cyan blue arrows). Capping (red) can occur anywhere, but filaments can only branch in the branching zone (gray). (B) Results of a stochastic branching simulation (Materials and Methods) in which rigid branches with angles of ± 36˚ and ± 108˚ grow with a given bias (right column) toward the membrane. Insets: schematic snapshots of branching with 0% and 15% bias (gray: branching zone).

Materials and methods

Proteins

Actin was purified from rabbit skeletal muscle (Spudich & Watt, 1971) and labeled on thiol groups with Alexa Fluor 546-C5-maleimide (AF546; Invitrogen, Carlsbad, CA), Alexa Fluor 488-C5-maleimide (AF488; Invitrogen), or maleimide-PEO2-biotin (Pierce, Thermo Fisher Scientific, Inc., Rockford, IL). It was labeled on primary amines using Alexa Fluor 488 SDP ester (Invitrogen) and Cy3 NHS (GE Healthcare, Little Chalfont, UK). Rabbit skeletal muscle actin biotinylated on random lysines was purchased (Cytoskeleton, Inc., Denver, CO). Arp2/3 complex was purified from bovine brain as described (Egile et al., 1999) or purchased (Cytoskeleton). Rat N-WASP $(His)_6$-WCA, a kind gift from D. Wong and J. Taunton, was expressed in E. coli BL21 DE3 R2L and purified by affinity chromatography as described previously (Egile et al., 1999).

Branching assays

A flow channel was assembled with a plasma-cleaned (~300 mTorr oxygen; Plasmod, March Instruments, Concord, CA) cover slip and incubated with 10 mg/mL biotinylated BSA (A6043, Sigma-Aldrich Co., St. Louis, MO) in 80 mM PIPES pH 6.9, 1 mM EGTA, and 4 mM $MgCl_2$ for 180 min at 4°C, and 0.2 mg/mL streptavidin (S4762, Sigma-Aldrich) in 1x calcium and magnesium free PBS (Cellgro, Mediatech, Inc., Manassas, VA) for 30-60 minutes at 23°C. The channel was washed with buffer composed of 9 parts G-buffer (5 mM Tris, 0.2 mM ATP, 0.1 mM CaCl2, 0.5 mM DTT, 1 mM NaN_3, pH 8.0 at 4˚C) 1 part either 10x KMEI buffer (500 mM KCl, 10 mM $MgCl_2$, 10 mM EGTA, 100 mM imidazole, pH 7.0) or 10x PKMEI buffer (92 mM KH_2PO_4, 158 mM K_2HPO_4, 92 mM KCl, 10 mM $MgCl_2$, 10 mM EGTA, 100 mM imidazole, pH 7.0). In both cases, the final pH was 7.0 at 23˚C. We refer to the compound buffers as KMEI and PKMEI, respectively.

F-actin (10-20% biotinylated and 30% AF546-labeled) was polymerized 1 hour at 23°C in KMEI or PKMEI and 0.5 mM ATP (Roche, F. Hoffman-La Roche AG, Basel). 50 nM F-actin and 1 μM of G-actin containing similar ratios of unlabeled, biotinylated, and AF546- or Cy3- labeled monomers was incubated in the channel for 5 min. We estimated that ~10% of biotin moieties on a filament bind streptavidin and thus the spacing between surface attachment points was 140-270 nm. The channel was washed with KMEI or PKMEI and incubated with branching mix containing 0.5 mM ATP, 100 nM N-WASP WCA, 100 nM Arp2/3 complex, 2 mg/mL BSA (A0281, Sigma-Aldrich), and 0.6-1 μM actin (50% AF488 labeled), for 70-120 s at 23°C. The concentrations and incubation times were chosen such that individual branches were sparse enough to be individually identified. Finally, the channel was washed with KMEI or PKMEI containing 1 μM phalloidin (Sigma-Aldrich) and in the case of cysteine-labeled mother filaments, an oxygen scavenger system consisting of 250 μg/mL glucose oxidase (Sigma-Aldrich), 4.5 mg/mL glucose, and 30 μg/mL catalase (Roche).

For branching assays with phalloidin-stabilized mother filaments, 5 μM G-actin (10% biotinylated) and 5 μM rhodamine-phalloidin (Sigma-Aldrich), were co-polymerized in KMEI buffer with 1 mM ATP at 23°C in the dark for 1 hr. and the resulting phalloidin-F-actin was stored at 23°C in the dark for 3-16 hrs. This stock was diluted to 50 nM in KMEI and incubated

in the flow channel 6-8 min. The branch nucleation mix in this case contained unlabeled G-actin and was washed out with KMEI containing 1 μM AF488-phalloidin (Invitrogen), then KMEI containing oxygen scavenger.

For branch stability experiments, the branching mix was replaced with debranching buffer containing KMEI, unlabeled and unstabilized F-actin to prevent de-polymerization, and 2 mg/mL BSA to prevent branches from adsorbing to the surface. Each surface was then incubated for 33 min. to allow debranching to take place and imaged during the incubation. To obtain curvature distributions, identical samples were prepared and incubated with debranching buffer for 50 sec. (the minimum time possible, due to washes) or 15 min. before stabilization with phalloidin and imaging.

Imaging and image processing

Filaments were imaged using a spinning disk confocal microscope (Axiovert, Carl Zeiss AG, Jena; Solamere Technology Group, Salt Lake City, UT; 491 nm and 561 nm lasers) with an EMCCD camera (Cascade II, Photometrics, Tucson, AZ), a 63x, 1.4 NA oil-immersion objective (Carl Zeiss), and MetaMorph software (Molecular Devices, Inc., Sunnyvale, CA). Red channel images were thresholded, median-filtered with a filter radius of one pixel, and skeletonized to 8-connected digital curves using ImageJ. Curves that intersected were split by removing one pixel at the intersection point.

Curvature estimation, tangent angle method

We estimated filament curvature from skeletonized digital filament images (Fig. 1E-H) by implementing the tangent angle-based method (Method II) described previously (Worring & Smeulders, 1993) with MATLAB (The Mathworks, Natick, MA) using a Gaussian differentiating kernel with $\sigma = 3$ pixels and a filter size of $m = 9$ pixels, chosen empirically by estimating the curvature of digital circles of known radius. The accuracy of this and similar local methods, compared to other curvature estimation strategies such as the global spline fit method, has been previously demonstrated (Bicek et al., 2007; Worring & Smeulders, 1993). Curvature error as evaluated using the tangent angle method was 0.08 μm^{-1}, which is less than the bin width we used for histograms. End effects made curvature unreliable m points in from each end, so these end segments and any branches growing on them were excluded from further analysis. The resulting curves were sampled in two ways. First, to maximize the number of data points collected, curvature was measured every 1.1 pixels (182 nm), accepting the fact that curvature is correlated between nearby points on the same filament. Secondly, to remove any potential correlations between the curvature values sampled and thus satisfy the assumptions of the Kolmogorov-Smirnov test and weighted linear regression procedures, one point was randomly chosen on each filament, in a region away from the ends, and its curvature was measured in an identical way. Both curvature samples were used to create histograms of the curvature distribution of mother filaments for each experiment, which were normalized to sum to one.

Curvature estimation, spline method

We re-analyzed the unstabilized, maleimide-labeled actin data with a cubic spline-based method of curvature estimation, which is prone to more systematic error than the tangent angle method

but provides an independent check on systematic errors inherent to the tangent angle-based method (Bicek et al., 2007; Worring & Smeulders, 1993). All automated curvature analysis was done using custom-written routines in MATLAB. The 8-connected digital curves were then traced and re-parameterized in terms of the chord length t, an approximation for the arc length s. Cubic splines ($x(t)$,$y(t)$) were then fit to the digital curves using a least-squares algorithm weighted by the intensity of the digital curve's corresponding pixels in the original gray-scale image. The distance (in pixels) between knots (polynomial join sites in the splines) was 10 pixels. Digital curves with less than 11 pixels were ignored in the analysis. Curvature was measured at points 1.1 pixels apart along the filament curve by applying the definition of curvature

$$\kappa = \frac{x'y'' - y'x''}{\left(x'^2 + y'^2\right)^{3/2}}, \qquad \text{Equation 12}$$

where all derivatives are with respect to t. The first and last two pixels of each digital curve were ignored to avoid end effects.

Branch analysis

Branches were manually identified using two criteria: (1) overlap between one end of the green branch and the red mother filament, and (2) lack of collinearity with the end of any other filament. Long branches that had one blurred end due to thermal fluctuations over the 1-1.5 s exposure were counted if their blurred end pointed away from the mother filament. Branch points were assigned the average curvature of the three closest pixels on the nearest mother filament skeleton; any branch point more than three pixels away from a skeleton was ignored. Branch orientation was determined by taking the cross product of the branch vector and the tangent vector to the mother filament curve, which was calculated by smoothing the digitized tangent vectors to the same curve with a Gaussian filter (Worring & Smeulders, 1993) in the tangent angle based analysis, or from the cubic spline in the spline based analysis. Branches with indeterminate direction were assigned the absolute value of curvature and only used in the analysis of total linear branch density. Histogram bins with zero branches or curvature measurements were ignored.

Calculation of relative branch density

Controls with randomly located and oriented simulated branches were created for each image to quantify the artifacts of digital curvature estimation. They were analyzed in parallel with real data to create control histograms for each data set. The linear branch density as a function of curvature was calculated by taking a ratio of the branch curvature histogram to the mother filament curvature histogram. The control density was subtracted from the real density to remove digitization artifacts (Figure 30C,D). We quantified the trend with a least squares linear fit to the relative branch density (Figure 30A,B) weighted by the number of samples of mother filament curvature in each curvature bin.

The branching bias we observe is most likely an underestimate of the true directional bias because our experiment averages over branches growing horizontally along the plane of the surface, where bending strain is highest ($\theta = 0°$ or 180° in Fig. 28B) and those growing at other angles, because the fluorescence images are 2-D projections of 3-D branches (Figure 28B,C). Large-amplitude bending of mother filaments in three dimensions was not observed except at untethered ends, due to the stiffness of F-actin (Isambert et al., 1995), but small-amplitude, out-of-plane local curvature fluctuations over length scales of nanometers were underestimated by construction in simulations because curvature in experiments was also measured in projection.

Stochastic model of bias propagation during branching

To quantify how the directional branching bias is amplified by branched actin growth, we created a simple 2-D model in which actin filaments are represented as rigid rods of constant length, corresponding to the average filament length that can grow before capping occurs, and growing at ± 36° and ± 108° relative to the direction of network growth. Starting with 30 filaments at each of the four angles, the filaments were allowed to grow two branches, each pointing either away from or toward the direction of network growth, for 30 generations. The "branching zone" was defined such that only filaments at ± 36°, grown in the last generation could give rise to new branches. Each branch had a $0.5 + b$ probability of growing into the branching zone (and toward the direction of growth) and a $0.5 - b$ probability of growing out of the branching zone (and away from the direction of growth), where $2b$ is the directional branching bias.

Statistics

Each independent experiment consisted of at least 30 (usually, 60) fields of view, and only experiments with 500 or more branches for which local curvature could be assigned were used (with about 2000 branches and 12 mm of filaments each, on average). To strictly satisfy the assumptions of linear regression and the Kolmogorov-Smirnov test, relative linear branch density was calculated from a subset of mother filament curvature points randomly chosen, one per filament. These data were fit in two ways: they were either pooled, or fit individually for each experiment, such that the extracted slope and intercept from each independent experiment could be then pooled and analyzed using a one-sample t-test or a one-sample Wilcoxon signed-rank test (Table 8). In all cases, linear regression was performed using weighted least squares, with the number of mother filament samples in each bin serving as the weight for each point, in order to compensate for unequal variance between low and high curvature data. The slope of the trend line from experiments performed under different conditions was compared using ANCOVA for the least-squared fits to pooled data, or a two-sample Welch's t-test or a non-parametric two-sample Wilcoxon signed-rank test (also known as a Mann-Whitney test) for the slopes calculated from individual experiment line fits (Table 9). A two-sample Kolmogorov-Smirnov test was used to ask whether mother filament curvature samples and branch curvatures are drawn from the same distribution (Table 7). In all cases, $\alpha = 0.05$ and all p-values reported are for two-tailed hypothesis tests. Statistical calculations were performed using R.

Monte Carlo sampling of WLC filament conformations

F-actin was coarse-grained as a discretized WLC polymer composed of 5.4 nm long bonds between particles, approximately the size of an actin monomer (Rouiller et al., 2008) (Fig. S6), with a persistence length of 9 μm (Isambert et al., 1995). In order to mimic the tethering of actin filaments to a plane surface in experiments, we restrict Monte Carlo moves to certain sections of the 1.25-μm-long filament, effectively pinning down the filament at six equally spaced points. The Monte Carlo moves consist of attempts to perform a crankshaft move. A crankshaft move involves rotating two randomly selected particles *i* and *j* and all the particles in between by a random angle around the line segment that connects particles *i* and *j* (Ullner et al., 1998). Conformations are sampled with the Metropolis acceptance criterion,

$$P_{acc} = \min\left[1, e^{-\beta \Delta E}\right] \qquad \text{Equation 13}$$

for $\beta = 1/k_B T$ and worm-like chain (WLC) bending energy

$$E = E_{bending} = k_B T \frac{L_p}{2} \int_0^L \left| \frac{d^2 \vec{r}(s)}{ds^2} \right|^2 ds \,, \qquad \text{Equation 14}$$

where L is the contour length of the polymer, L_p is its persistence length, and $\vec{r}(s)$ is the position of the polymer at arc length coordinate s. Robustness analysis was performed to examine the effect of changing various simulation parameters on the distribution of local curvatures. The parameters considered were (1) length between adjacent particles, (2) contour length of filament between tether points, (3) "looseness," the ratio of end-to-end length to contour length between tether points, (4) number of tethers, and (5) curvature resolution and the possible need to average curvature over neighboring angles. These test simulations revealed that only averaging over neighboring angles has a significant effect on curvature distributions. The final set of parameters employed for the simulations is 5.4 nm between adjacent particles, a contour length of 250 nm between tether points, the end-to-end length between tether points for a given contour length equal to the average end-to-end distance $\langle R \rangle$ for a free WLC polymer of the same persistence length and contour length, as given by

$$\langle R \rangle = \sqrt{2 L_p L \left[1 - \frac{L_p}{L} \left(1 - e^{-L/L_p} \right) \right]}, \qquad \text{Equation 15}$$

and no averaging of the local curvature. Curvature of the WLC polymer, κ, was calculated from the angle between successive bonds, θ, and the length of the bonds, Δs (Fig. S6):

$$\kappa = \sqrt{\frac{2}{(\Delta s)^2} (1 - \cos\theta)}. \qquad \text{Equation 16}$$

This definition of curvature is equivalent to a discretization of Equation 12. The key difference between continuous and discrete measures of curvature is that in the discrete case, the increment of arc length, Δs, must have a non-zero value, which has a strong effect on the value of the

curvature measured. Counter-intuitively, even though a discretized WLC polymer is stiff on short length scales, it can have large curvature fluctuations on those scales because the polymer's small fluctuations in θ, the bending angle, are divided by a small Δs. These scale effects motivated our use of MC simulations to make a connection between the length scale observable by light microscopy and the length scale of the Arp2/3 complex.

Projection of 3-D curvature onto 2-D

Imposed curvatures were largely in a two-dimensional (2-D) plane because filaments were tethered to the cover slip surface and their stiffness limited out-of-plane bending of large amplitude. Filament ends and large loops that were not tethered were blurred during the 1 s exposures used, and were eliminated during image thresholding. To approximate the experimental conditions, the WLC filament was simulated in three dimensions, but tethered to a 2-D plane and curvature was measured in 2-D from the projection of the filaments' shape onto that plane, neglecting out-of-plane bending. For consistency, 2-D projection was used for all curvature analysis of filament shape in experiments and simulations, as well as for determination of branch direction. The reported relative linear branch density also contained an internal control, as branching from curved filament sections can be compared directly to branching from straight filament sections.

Conclusions

We have shown that F-actin curvature regulates Arp2/3 complex activity, providing the cell with a distributed, filament-dependent mechanism for sensing and responding to the compressive stress on branched actin networks. Our results suggest the possibility that mechanical stress on cytoskeletal filaments can modulate how they interact with their binding partners. The actin filament takes on a diversity of structural states as it grows, interacts with binding proteins, encounters physical constraints, and fluctuates due to thermal motion (Kueh & Mitchison, 2009; Reisler & Egelman, 2007). It is likely that other side-binding ABPs besides the Arp2/3 complex exhibit similar sensitivity to local actin curvature, providing a direct mechanism for altering organization of the actin cytoskeleton in response to force. For example, filament severing by the ADF/cofilin homolog actophorin occurs more readily at points of high curvature (Maciver et al., 1991), consistent with a recently elucidated mechanism for severing by cofilin that depends on a mechanism that takes advantage of the mechanical instability at the border between two structural states of F-actin (McCullough et al., 2011). However, it is not yet known whether cofilin binding or the cooperativity of cofilin binding is affected by local filament curvature, although it has been shown that its binding lowers the persistence length of actin (McCullough et al., 2008). Nor have other proteins that modify the persistence length of actin, such as drebrin (Sharma et al., 2011) or tropomyosin (Isambert et al., 1995), been tested for sensitivity to F-actin curvature. The methods we have developed can be used as a platform to investigate the curvature dependence of other ABP-filament interactions and the role of actin filament bending in mechanotransduction and cytoskeletal reorganization.

References

Abraham VC, Krishnamurthi V, Taylor DL, Lanni F (1999) The actin-based nanomachine at the leading edge of migrating cells. *Biophys J* 77, 1721-1732.

Arai Y, Yasuda R, Akashi K, Harada Y, Miyata H, Kinosita K Jr, Itoh H (1999) Tying a molecular knot with optical tweezers. *Nature* 399, 446-448.

Belendez T, Neipp C, Belendez A (2002) Large and small deflections of a cantilever beam. *Eur J Phys* 23, 371.

Beltzner CC, Pollard TD (2008) Pathway of actin filament branch formation by Arp2/3 complex. *J Biol Chem* 283, 7135-7144.

Bicek AD, Tüzel E, Kroll DM, Odde DJ (2007) Analysis of microtubule curvature. *Methods Cell Biol* 83, 237-268.

Blanchoin L, Amann KJ, Higgs HN, Marchand JB, Kaiser DA, Pollard TD (2000) Direct observation of dendritic actin filament networks nucleated by Arp2/3 complex and WASP/Scar proteins. *Nature* 404, 1007-1011.

Carlsson AE (2003) Growth velocities of branched actin networks. *Biophys J* 84, 2907-2918.

Chaudhuri O, Parekh SH, Fletcher DA (2007) Reversible stress softening of actin networks. *Nature* 445, 295-298.

De La Cruz EM (2005) Cofilin binding to muscle and non-muscle actin filaments: isoform-dependent cooperative interactions. *J Mol Biol* 346, 557-64.

Egile C, Loisel TP, Laurent V, Li R, Pantaloni D, Sansonetti PJ, Carlier MF (1999) Activation of the CDC42 effector N-WASP by the *Shigella flexneri* IcsA protein promotes actin nucleation by Arp2/3 complex and bacterial actin-based motility. *J Cell Biol* 146, 1319-1332.

Farge E (2011) Mechanotransduction in development. *Curr Top Dev Biol* 95, 243-265.

Firat-Karalar EN, Welch MD (2011) New mechanisms and functions of actin nucleation. *Curr Opin Cell Biol* 23, 4-13.

Fletcher DA, Mullins RD (2010) Cell mechanics and the cytoskeleton. *Nature* 463, 485-492.

Galkin VE, Orlova A, Lukoyanova N, Wriggers W, Egelman EH (2001) Actin depolymerizing factor stabilizes an existing state of F-actin and can change the tilt of F-actin subunits. *J Cell Biol* 153, 75-86.

Gardel ML, Shin JH, MacKintosh FC, Mahadevan L, Matsudaira P, Weitz DA (2004) Elastic behavior of cross-linked and bundled actin networks. *Science* 304, 1301-1305.

Giardini PA, Fletcher DA, Theriot JA (2003) Compression forces generated by actin comet tails on lipid vesicles. *Proc Natl Acad Sci U S A* 100, 6493-6498.

Goley ED, Rodenbusch SE, Martin AC, Welch MD (2004) Critical conformational changes in the Arp2/3 complex are induced by nucleotide and nucleation promoting factor. *Mol Cell* 16, 269-279.

Goley ED, Welch MD (2006) The ARP2/3 complex: an actin nucleator comes of age. *Nat Rev Mol Cell Biol* 7, 713-726.

Gouin E, Welch MD, Cossart P (2005) Actin-based motility of intracellular pathogens. *Curr Opin Microbiol* 8, 35-45.

Hoffman BD, Grashoff C, Schwartz MA (2011) Dynamic molecular processes mediate cellular mechanotransduction. *Nature* 475, 316-323.

Ichetovkin I, Grant W, Condeelis J (2002) Cofilin produces newly polymerized actin filaments that are preferred for dendritic nucleation by the Arp2/3 complex. *Curr Biol*, 79-84.

Isambert H, Venier P, Maggs AC, Fattoum A, Kassab R, Pantaloni D, Carlier MF (1995) Flexibility of actin filaments derived from thermal fluctuations. Effect of bound nucleotide, phalloidin, and muscle regulatory proteins. *J Biol Chem* 270, 11437-11444.

Janmey PA, McCulloch CA (2007) Cell mechanics: integrating cell responses to mechanical stimuli. *Annu Rev Biomed Eng* 9, 1-34.

Kim T, Hwang W, Lee H, Kamm RD (2009) Computational analysis of viscoelastic properties of crosslinked actin networks. *PLoS Comput Biol* 5, e1000439.

Kueh HY, Mitchison TJ (2009) Structural plasticity in actin and tubulin polymer dynamics. *Science* 325, 960-963.

Lieleg O, Kayser J, Brambilla G, Cipelletti L, Bausch AR (2011) Slow dynamics and internal stress relaxation in bundled cytoskeletal networks. *Nat Mater* 10, 236-242.

Maciver SK, Zot HG, Pollard TD (1991) Characterization of actin filament severing by actophorin from *Acanthamoeba castellanii*. *J Cell Biol* 115, 1611-1620.

Mahaffy RE, Pollard TD (2006) Kinetics of the formation and dissociation of actin filament branches mediated by Arp2/3 complex. *Biophys J* 91, 3519-3528.

Mahaffy RE, Pollard TD (2008) Influence of phalloidin on the formation of actin filament branches by Arp2/3 complex. *Biochemistry* 47, 6460-6467.

Marcy Y, Prost J, Carlier M, Sykes C (2004) Forces generated during actin-based propulsion: a direct measurement by micromanipulation. *Proc Natl Acad Sci U S A* 101, 5992-5997.

McCammon JA, Northrup SH (1981) Gated binding of ligands to proteins. *Nature* 293, 316-317.

McCullough BR, Blanchoin L, Martiel J, De la Cruz EM (2008) Cofilin increases the bending flexibility of actin filaments: implications for severing and cell mechanics. *J Mol Biol* 381, 550-558.

McCullough BR, Grintsevich EE, Chen CK, Kang H, Hutchison AL, Henn A, Cao W, Suarez C, Martiel J, Blanchoin L, Reisler E, De La Cruz EM (2011) Cofilin-linked changes in actin filament flexibility promote severing. *Biophys J* 101, 151-159.

McGough A (1998) F-actin-binding proteins. *Curr Opin Struct Biol* 8, 166-176.

Mogilner A, Edelstein-Keshet L (2002) Regulation of actin dynamics in rapidly moving cells: a quantitative analysis. *Biophys J* 83, 1237-1258.

Okreglak V, Drubin DG (2007) Cofilin recruitment and function during actin-mediated endocytosis dictated by actin nucleotide state. *J Cell Biol* 178, 1251-1264.

Padrick SB, Doolittle LK, Brautigam CA, King DS, Rosen MK (2011) Arp2/3 complex is bound and activated by two WASP proteins. *Proc Natl Acad Sci U S A* 108, E472-E479.

Parekh SH, Chaudhuri O, Theriot JA, Fletcher DA (2005) Loading history determines the velocity of actin-network growth. *Nat Cell Biol* 7, 1219-1223.

Pollard TD (2007) Regulation of actin filament assembly by Arp2/3 complex and formins. *Annu Rev Biophys Biomol Struct* 36, 451-477.

Pollard TD, Borisy GG (2003) Cellular motility driven by assembly and disassembly of actin filaments. *Cell* 112, 453-465.

Prass M, Jacobson K, Mogilner A, Radmacher M (2006) Direct measurement of the lamellipodial protrusive force in a migrating cell. *J Cell Biol* 174, 767-772.

Reisler E, Egelman EH (2007) Actin structure and function: what we still do not understand. *J Biol Chem* 282, 36133-36137.

Rouiller I, Xu X, Amann KJ, Egile C, Nickell S, Nicastro D, Li R, Pollard TD, Volkmann N, Hanein D (2008) The structural basis of actin filament branching by the Arp2/3 complex. *J Cell Biol* 180, 887-895.

Sharma S, Grintsevich EE, Phillips ML, Reisler E, Gimzewski JK (2011) Atomic force microscopy reveals drebrin induced remodeling of f-actin with subnanometer resolution. *Nano Lett* 11, 825-827.

Small JV, Winkler C, Vinzenz M, Schmeiser C (2011) Reply: Visualizing branched actin filaments in lamellipodia by electron tomography. *Nat Cell Biol* 13, 1013-1014.

Soo FS, Theriot JA (2005) Large-scale quantitative analysis of sources of variation in the actin polymerization-based movement of Listeria monocytogenes. *Biophys J* 89, 703-723.

Spudich JA, Watt S (1971) The regulation of rabbit skeletal muscle contraction. I. Biochemical studies of the interaction of the tropomyosin-troponin complex with actin and the proteolytic fragments of myosin. *J Biol Chem* 246, 4866-4871.

Svitkina TM, Borisy GG (1999) Arp2/3 complex and actin depolymerizing factor/cofilin in dendritic organization and treadmilling of actin filament array in lamellipodia. *J Cell Biol* 145, 1009-1026.

Ti S, Jurgenson CT, Nolen BJ, Pollard TD (2011) Structural and biochemical characterization of two binding sites for nucleation-promoting factor WASp-VCA on Arp2/3 complex. *Proc Natl Acad Sci U S A* 108, E463-E471.

Ullner M, Staikos G, Theodorou DN (1998) Monte Carlo Simulations of a Single Polyelectrolyte in Solution:Activity Coefficients of the Simple Ions and Application to Viscosity Measurements. *Macromolecules* 31, 7921-7933.

Urban E, Jacob S, Nemethova M, Resch GP, Small JV (2010) Electron tomography reveals unbranched networks of actin filaments in lamellipodia. *Nat Cell Biol* 12, 429-435.

Verkhovsky AB, Chaga OY, Schaub S, Svitkina TM, Meister J, Borisy GG (2003) Orientational order of the lamellipodial actin network as demonstrated in living motile cells. *Mol Biol Cell* 14, 4667-4675.

Vogel V, Sheetz M (2006) Local force and geometry sensing regulate cell functions. *Nat Rev Mol Cell Biol* 7, 265-275.

Welch MD, Mullins RD (2002) Cellular control of actin nucleation. *Annu Rev Cell Dev Biol* 18, 247-288.

Worring M, Smeulders AWM (1993) Digital curvature estimation. *CVGIP: Image Underst* 58, 366-382.

Xu X, Rouiller I, Slaughter BD, Egile C, Kim E, Unruh JR, Fan X, Pollard TD, Li R, Hanein D, Volkmann N (2011) Three-dimensional reconstructions of Arp2/3 complex with bound nucleation promoting factors. *EMBO J* 31, 236-247.

Tables

Table 7. Two-sample, two-sided Kolmogorov-Smirnov tests to compare distribution of overall mother filament curvature and curvature at branch points for maleimide-labeled unstabilized actin in KMEI buffer. The data used to compare distributions is drawn from the same data sets as Figure 29, but only one mother filament curvature sample was randomly chosen from every filament to eliminate correlations between mother filament curvature samples and satisfy the assumptions underlying the Kolmogorov-Smirnov test.

Signed curvature				
Experiment	$N_{branches}$	$N_{MF\ points}$	D	*p*
1	829	2782	0.052	0.065
2	840	5930	0.10	2.9×10^{-7}
3	3064	8720	0.079	1.1×10^{-12}
4	4506	7206	0.081	7.2×10^{-9}
5	1204	3226	0.081	2.0×10^{-5}
Pooled 1-5	10443	27864	0.068	$< 2.2 \times 10^{-16}$
Unsigned curvature				
Experiment	$N_{branches}$	$N_{MF\ points}$	D	*p*
1	896	1391	0.024	0.91
2	917	2965	0.025	0.78
3	3316	4360	0.019	0.47
4	4840	3603	0.049	9.2×10^{-5}
5	1310	1613	0.020	0.94
Pooled 1-5	11279	13932	0.039	1.1×10^{-8}

Table 8. The trend of branch density change with curvature was quantified with weighted least-squares linear regression for each condition. Fitting was done one pooled data and used directly for hypothesis testing (LRPD, linear regression on pooled data; DF, degrees of freedom), or data from each experiment was individually fit, and the slopes and intercepts of the resulting best-fit lines were compared with zero using either a one-sample t-test (OSTT), or the non-parametric Wilcoxon signed-rank test (WSRT). R^2 values for t-test and Wilcoxon test results are averages of the R^2 values for each line fitted to data from individual experiments.

Signed curvature										
				Slope			***Intercept***			
Condition	*Item for each condition*	*N*	***Stat. test method***	*Estimate (% per μm^{-1})*	*95% conf. interval*	*p-value (H_0: slope = 0)*	*Estimate (%)*	*95% conf. interval*	*p-value (H_0: int. = 100)*	R^2
Maleimide-labeled, unstabilized actin; many κ_0 samples per mother filament; 165 nm/pixel; tangent angle-based κ analysis	Indep. expts.	5	*LRPD*	-37	(-44, -30)	8.3×10^{-16}	100	(97.3, 103)	0.97	0.60
	Branches	10,443	*OSTT*	-35	(-47, -22)	0.0016	100.06	(100.03, 100.09)	0.0056	0.55
	M.F. samples	151,012	*WSRT*	-37	(-44, -17)	0.063	100.06	(100.03, 100.09)	0.063	0.55
	Regression DF	72								
Maleimide-labeled, unstabilized actin; one κ_0 sample per mother filament; 165 nm/pixel; tangent angle-based κ analysis	Indep. expts.	5	*LRPD*	-33	(-40, -26)	1.7×10^{-14}	100	(97.1, 103)	0.98	0.56
	Branches	10,443	*OSTT*	-31	(-45, -17)	0.0033	100.06	(100.01, 100.11)	0.038	0.55
	M.F. samples	13,932	*WSRT*	-31	(-43, -15)	0.063	100.05	(99.998, 100.10)	0.13	0.55
	Regression DF	72								
Maleimide-labeled, unstabilized actin; one κ_0 sample per mother filament; 165 nm/pixel; spline-based κ analysis	Indep. expts.	5	*LRPD*	-14	(-17, -10)	3.3×10^{-12}	100	(98.1, 102)	0.99	0.40
	Branches	22,580	*OSTT*	-12	(-22, -2.0)	0.029	100.0	(99.99, 100.0)	0.37	0.39
	M.F. samples	30,420	*WSRT*	-14	(-19, 1.8)	0.125	100.00	(100.00, 100.04)	0.44	0.39
	Regression DF	97								
Maleimide-labeled actin stabilized with phalloidin; one κ_0 sample per mother filament; 165 nm/pixel; tangent angle-based κ analysis	Indep. expts.	7	*LRPD*	-23	(-31, -16)	3.8×10^{-8}	100	(97.6, 102)	0.97	0.26
	Branches	18,676	*OSTT*	-26	(-36, -16)	0.00066	100.04	(99.990, 100.09)	0.10	0.36
	M.F. samples	30,420	*WSRT*	-24	(-37, -17)	0.016	100.03	99.997, 100.09)	0.08	0.36
	Regression DF	102								

Condition	*Item for each condition*	*N*	***Stat. test method***	*Estimate (% per μm^{-1})*	*95% conf. interval*	*p-value (H_0: slope = 0)*	*Estimate (%)*	*95% conf. interval*	*p-value (H_0: int. =100)*	R^2
NHS-labeled, unstabilized actin; one κ_0 sample per mother filament; 165 nm/pixel; tangent angle-based κ analysis	Indep. expts.	5	*LRPD*	-35	(-46, -24)	7.5×10^{-9}	100.0	(96.21, 103.9)	0.98	0.37
	Branches	6,042	*OSTT*	-37	(-47, -27)	5.7×10^{-4}	100.04	(99.982, 100.10)	0.13	0.39
	M.F. samples	21,468	*WSRT*	-38	(-48, -28)	0.063	100.04	(99.996, 100.10)	0.063	0.39
	Regression DF	74								
NHS-labeled actin stabilized with 25 mM phosphate; one κ_0 sample per mother filament; 165 nm/pixel; tangent angle-based κ analysis	Indep. expts.	6	*LRPD*	-35	(-44, -27)	1.6×10^{-12}	100.0	(97.30, 102.8)	0.98	0.47
	Branches	9,207	*OSTT*	-35	(-40, -30)	1.0×10^{-5}	100.04	(99.989, 100.08)	0.11	0.53
	M.F. samples	16,929	*WSRT*	-35	(-42, -29)	0.03	100.03	(100.00, 100.11)	0.03	0.53
	Regression DF	80								
NHS-labeled actin stabilized with 25 mM phosphate; one κ_0 sample per mother filament; 103 nm/pixel; tangent angle-based κ analysis	Indep. expts.	5	*LRPD*	-26	(-31, -20)	2.9×10^{-14}	100.1	(98.02, 102.1)	0.94	0.54
	Branches	7,473	*OSTT*	-26	(-32, -20)	2.8×10^{-4}	100.05	(99.961, 100.14)	0.19	0.56
	M.F. samples	9,085	*WSRT*	-26	(-32, -21)	0.063	100.05	(99.967, 100.15)	0.19	0.56
	Regression DF	75								
NHS-labeled, unstabilized actin; one κ_0 sample per mother filament; 165 nm/pixel; tangent angle-based κ analysis; 0.83 min. debranching	Indep. expts.	4	*LRPD*	-33	(-42, -25)	2.6×10^{-10}	100.0	(97.47, 102.6)	0.98	0.54
	Branches	8,552	*OSTT*	-37	(-58, -15)	0.012	100.01	(99.958, 100.06)	0.66	0.57
	M.F. samples	8,329	*WSRT*	-36	(-55, -23)*	0.13	100.01	(99.971, 100.05)*	0.63	0.57
	Regression DF	52								
NHS-labeled, unstabilized actin; one κ_0 sample per mother filament; 165 nm/pixel; tangent angle-based κ analysis; 15 min. debranching	Indep. expts.	4	*LRPD*	-31	(-40, -22)	1.1×10^{-8}	100.1	(97.22, 100.3)	0.93	0.46
	Branches	5,636	*OSTT*	-31	(-44, -18)	0.0048	100.1	(99.93, 100.3)	0.13	0.58
	M.F. samples	8,581	*WSRT*	-36	(-42, -24)*	0.13	100.1	(99.98, 100.3)*	0.13	0.58
	Regression DF	53								

* Only an 88% confidence interval could be calculated in these cases.

Unsigned curvature										
				Slope			***Intercept***			
Condition	*Item for each condition*	*N*	***Stat. test method***	*Estimate (% per μm^{-1})*	*95% conf. interval*	*p-value (H_0: slope = 0)*	*Estimate (%)*	*95% conf. interval*	*p-value (H_0: int. = 100)*	R^2
Maleimide-labeled, unstabilized actin; many κ_0 samples per mother filament; 165 nm/pixel; tangent angle-based κ analysis	Indep. expts.	5	*LRPD*	17	(6.1, 27)	0.0029	95.2	(91.0, 99.4)	0.026	0.22
	Branches	11,279	*OSTT*	16	(-3.0, 35)	0.080	95.3	(89.6, 101)	0.089	0.25
	M.F. samples	151,012	*WSRT*	16	(-3.6, 35)	0.13	95.2	(89.2, 101)	0.13	0.25
	Regression DF	37								
Maleimide-labeled, unstabilized actin; one κ_0 sample per mother filament; 165 nm/pixel; tangent angle-based κ analysis	Indep. expts.	5	*LRPD*	13	(3.3, 23)	0.010	95.9	(91.8, 100)	0.053	0.17
	Branches	11,279	*OSTT*	13	(-4.2, 30)	0.10	95.7	(90.0, 101)	0.11	0.26
	M.F. samples	13,932	*WSRT*	12	(-4.6, 29)	0.13	95.6	(89.6, 102)	0.13	0.26
	Regression DF	37								
Maleimide-labeled, unstabilized actin; one κ_0 sample per mother filament; 165 nm/pixel; spline-based κ analysis	Indep. expts.	7	*LRPD*	5.5	(0.92, 10)	0.020	97.7	(95.1, 100)	0.073	0.11
	Branches	24,980	*OSTT*	8.1	(-7.0, 23)	0.21	96.4	(89.5, 103)	0.21	0.44
	M.F. samples	30,420	*WSRT*	6.1	(-9.5, 20)	0.19	96.1	(90.6, 104)	0.19	0.44
	Regression DF	48								
NHS-labeled, unstabilized actin; one κ_0 sample per mother filament; 165 nm/pixel; tangent angle-based κ analysis	Indep. expts.	5	*LRPD*	36	(23, 49)	2.6×10^{-6}	90.6	(85.8, 95.3)	0.00025	0.44
	Branches	7,014	*OSTT*	40	(16, 64)	0.0098	89.5	(83.6, 95.4)	0.0077	0.52
	M.F. samples	21,468	*WSRT*	34	(26, 74)	0.063	90.6	(81.5, 93.4)	0.063	0.52
	Regression DF	38								

Table 9. Comparisons and hypothesis testing for the effects of analysis method, actin labeling method, actin stabilization, magnification, and debranching on the relative branch density trend as a function of curvature. Signed curvature data was used for all comparisons.

Base condition	Change	Statistical method	Change in slope (% per μm^{-1})	95% Conf. interval	p-value
Maleimide-labeled, unstabilized actin; one κ_0 sample per mother filament; 165 nm/pixel; tangent angle-based curvature analysis	Many κ_0 samples per mother filament	ANCOVA	-3.9	(-21, 13)	0.64
		Wilcoxon signed-rank test	-3.9	(-23, 13)	0.55
		Welch's t-test	-3.7	(-19, 12)	0.60
Maleimide-labeled, unstabilized actin; one κ_0 sample per mother filament; 165 nm/pixel; tangent angle-based curvature analysis	Spline-based curvature analysis	ANCOVA	19	(11, 26)	2.1×10^{-6}
		Wilcoxon signed-rank test	18	(1.2, 32)	0.031
		Welch's t-test	19	(4.5, 33)	0.017
Maleimide-labeled, unstabilized actin; one κ_0 sample per mother filament; 165 nm/pixel; tangent angle-based curvature analysis	Stabilization of actin with phalloidin	ANCOVA	9.3	(-1.9, 20)	0.10
		Wilcoxon signed-rank test	6.7	(-8.4, 20)	0.53
		Welch's t-test	4.8	(-9.7, 19)	0.47
Maleimide-labeled, unstabilized actin; one κ_0 sample per mother filament; 165 nm/pixel; tangent angle-based curvature analysis	Labeling of actin with NHS reactive esters	ANCOVA	-2.5	(-15, 10)	0.69
		Wilcoxon signed-rank test	-5.1	(-23, 11)	0.55
		Welch's t-test	-5.9	(-20, 8.4)	0.37
NHS-labeled, unstabilized actin; one κ_0 sample per mother filament; 165 nm/pixel; tangent angle-based κ analysis	Stabilization of actin with 25 mM phosphate	ANCOVA	-0.022	(-14, 14)	0.998
		Wilcoxon signed-rank test	2.2	(-7.1, 13)	0.79
		Welch's t-test	2.1	(-8.1, 12)	0.64
NHS-labeled actin stabilized with 25 mM phosphate; one κ_0 sample per mother filament; 165 nm/pixel; tangent angle-based κ analysis	Imaging at higher magnification with 103 nm/pixel	ANCOVA	9.5	(-1.0, 20)	0.076
		Wilcoxon signed-rank test	9.0	(-1.6, 23)	0.095
		Welch's t-test	11	(-0.048, 0.21)	0.043
NHS-labeled, unstabilized actin; one κ_0 sample per mother filament; 165 nm/pixel; tangent angle-based κ analysis; 0.83 min. debranching	Extended unstabilized debranching incubation for 15 min.	ANCOVA	2.8	(-9.6, 15)	0.66
		Wilcoxon signed-rank test	-5.4	(-31, 20)	0.86
		Welch's t-test	-5.5	(-26, 15)	0.52

Chapter 4. The curvature Fluctuations of Constrained Semiflexible Filaments

The work described in this section was performed in collaboration with Mr. Evan B. Wang, Dr. David L. Richmond, and Prof. Phillip L. Geissler, with help from Ms. Anna Schneider. It has not been previously published.

Introduction

In Chapter 3, we showed how constraints on the average shape of an actin filament affect the fluctuations of the filament and in turn modulate the nucleation of new branches. In this chapter, we describe how other geometries of constraints, inspired by actin networks in vivo, affect the nanometer-scale curvature fluctuations of filaments. Three geometries are considered: (1) a filament with a free end at different distances from a fixed barrier, simulating the ends of filaments at the leading edge of the lamellipodium, (2) tightly bundled filaments similar to those in a filopodium, and (3) a filament under tension, similar to those in a stress fiber.

The purpose of this work is to investigate which types of constraints on actin filaments have the strongest effects on the nanometer-scale curvature fluctuations of the filaments. We believe that the fluctuation-gating model can serve as a useful framework for studying the binding and action of other actin-binding proteins. Currently, we have only been able to estimate a threshold curvature for branching by the Arp2/3 complex, and this curvature was measured in two dimensions because of the limitations of fluorescence imaging of surface-immobilized actin filaments. To apply the fluctuation gating model to other actin-binding proteins in quantitative terms, threshold curvature values will have to be calculated by directly measuring the effect of curvature on the binding or action (such as severing) of other actin-binding proteins. An analogous fluctuation-gating model for twist fluctuations of the filament may also be applicable for changes in F-actin conformation induced by torsional strain that affect the binding of proteins such as cofilin (McGough et al., 1997; Prochniewicz et al., 2005), but is beyond the scope of this work. In addition, estimations of the distribution of actin curvature fluctuations will also be applicable to any model that presupposes a role of local filament bending in the association of ABPs with the side of F-actin. The fluctuation gating model is only the simplest of a family of such models.

This work aims to identify, in relative terms, which types of spatial constraints on actin lead to the largest changes in bending fluctuations. The results can help to guide future experiments that measure ABP/F-actin interactions in the presence of biologically relevant mechanical constraints.

Unconstrained filament

Implementation

The actin filament was simulated as a discretized worm-like chain (WLC), as in Chapter 3 of this work (Risca et al., 2012). The implementation of the filament is identical to that in Chapter 3 with the exception that it was not pinned to a plane, and it described in additional detail in this section. In subsequent sections, we describe how we expanded on this model by adding constraints that reproduce the architectural features of three types of actin network.

Individual particles were connected by rigid linkers measuring 5.4 nm, and representing a fundamental unit of two actin monomers (Fujii et al., 2010; Holmes et al., 1990; Oda & Maeda, 2010). The bending energy between adjacent links was obtained from the WLC bending energy (Equation 14, which is another way to express Equation 1) as a function of the difference

between the two vectors joining any three consecutive particles in the chain. The same three-particle unit was used to calculate curvature along the simulated filament, using Equation 16.

Besides filament contour length, which was varied between simulations, the only other relevant parameter for the WLC model is the persistence length. It was varied, but the values most often used were 9 μm, which corresponds to Mg^{2+}-ADP-bound F-actin, and 13.5 μm, which corresponds to Mg^{2+}-ADP-BeF_3—bound F-actin, a mimic for freshly polymerized actin containing mostly monomers that have yet to release phosphate, and perhaps some which are still bound to ATP (Isambert et al., 1995). Although many studies have obtained larger values for the persistence length of actin (Brangwynne et al., 2007; Gittes et al., 1993; Ott et al., 1993; Mameren et al., 2009), those experiments were performed on F-actin stabilized with phalloidin, which, under consistent experimental conditions, was shown to increase the persistence length (Isambert et al., 1995).

Interactions between different filaments or between filaments and other barriers were mediated by a spherical hard-shell excluded volume potential around every filament particle. This excluded volume interaction only applied to particles from different filaments, and therefore did not affect the WLC potential governing the interaction between adjacent particles in the same filament. Although distant particles on the same filament could theoretically interact without excluded volume in these simulations, this did not occur in practice because all contour lengths in our simulations were kept an order of magnitude below the persistence length, putting the simulated filaments in between the semiflexible and rigid rod regimes.

The diameter of the excluded volume sphere was chosen to be 8 nm. This value was chosen because it was measured as the excluded volume of F-actin at 90 mM NaCl in liquid crystalline sols, (Oda et al., 1998). In another experiment that used electron microscopy to image 2D filament arrays, the closest-packed inter-filament spacings were 7.5-8 nm and the apparent diameter of the filament in projection was found to be 9 nm (Volkmann et al., 2001). For comparison, the Holmes model of F-actin, based on fiber diffraction, has a maximum diameter of 9-9.5 nm (Holmes et al., 1990), a more recent fiber diffraction structure of F-actin found a smaller (but not precisely specified) radius of gyration than the Holmes model (Oda et al., 2009), and the most recent, high resolution structure of F-actin obtained by cryoelectron microscopy showed a maximum diameter of 10 nm (Fujii et al., 2010). Because F-actin is a double helix, the maximum diameter is not the same as the closest-packing diameter of the filament.

The Monte Carlo simulation was implemented using the Metropolis algorithm, with an acceptance criterion described in Equation 13. The Monte Carlo moves applied to the filament's conformation were a combination of crankshaft moves, in which a section of the filament between randomly selected particles *i* and *j* is rotated around the axis connecting the two particles (Ullner et al., 1998), and free-rotation moves, in which the section of filament from a randomly selected particle *i* to the end of the filament is rotated around the tangent vector at particle *i* by a random angle. The ratio of crankshaft moves to free-rotation moves was set to 50/50, but changing it to 90/10 had no effect on the final results of the simulation, indicating that sampling is ergodic. In some cases (for bundled actin simulations), the maximum rotation angle for crankshaft moves was adjusted as a function of the distance between *i* and *j* to create a move acceptance rate that was approximately independent of the distance between *i* and *j*, and decrease

the total number of Monte Carlo steps that are required to equilibrate the filament conformation at both long and short length scales. Preliminary simulations indicated that this adjustment of the rotation angle had no effect on the final result (not shown). All simulations were pre-equilibrated until the total potential energy stabilized, usually for several million Monte Carlo sweeps, before making curvature measurements. Curvature was sampled every 100 Monte Carlo sweeps, for 10 million Monte Carlo sweeps. The number of moves in each Monte Carlo sweep corresponds to the number of filament particles in the simulation. Simulations were written in C++, using the Mersenne Twister algorithm to generate random numbers.

The methodology described in this section was carried through to all other WLC simulations, with additional details corresponding to various architectures or applied forces added in addition to the WLC parameters.

Filament model validation

To verify that the discretized WLC filaments behaved as expected, the curvature distributions obtained from Monte Carlo simulations of 1 μm long filaments were compared with the theoretical WLC curvature distribution in three dimensions, at several persistence lengths. The theoretical distribution of the curvature κ of an unconstrained WLC polymer in three dimensions with persistence length L_p that is discretized in length increments of Δs, is derived in (Rappaport et al., 2008):

$$p(\kappa)d\kappa = L_p \Delta s e^{-\frac{1}{2}L_p \Delta s \kappa^2} \kappa d\kappa . \qquad \text{Equation 17}$$

The simulation results agreed very well with the theoretical calculation (Figure 38). The discretization length was kept constant for all simulations, so the only parameter that changes the curvature distribution for a fully unconstrained filament is the persistence length. The three-dimensional curvature distribution for several persistence lengths is shown in Figure 39.

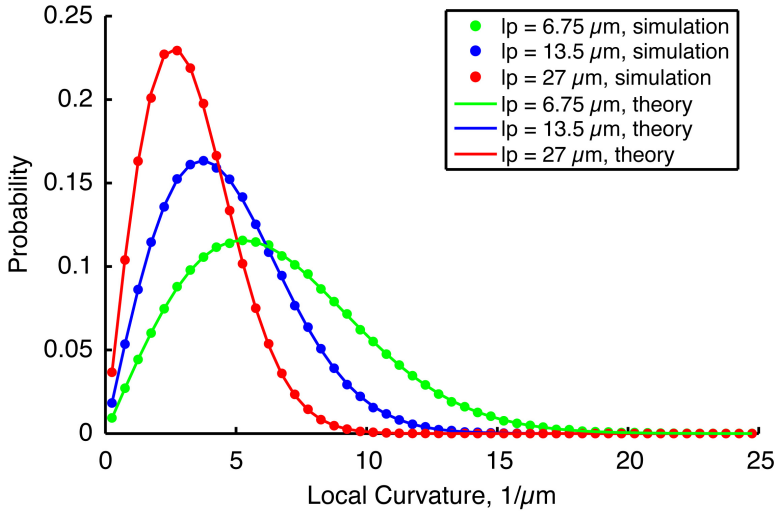

Figure 38. Validation of discretized WLC simulation. The curvature distribution in three dimensions of an unconstrained 1μm filament with a discretization length of 5.4 nm was simulated and calculated from Equation 17. Because the curvature distribution is a function of only the persistence length and discretization length of the polymer, the contour length does not affect the results.

The persistence length of actin has been well characterized under many biochemical conditions and has been correlated with changes in the detailed structure of the filament (Chapter 1, Tables 3 and 4), so it provides a useful way to make biologically meaningful comparisons between the results of our simulations and filament properties in vivo or in vitro. For this reason, we refer to the effective persistence length of a constrained filament, which is simply the persistence length of the pure WLC polymer whose curvature distribution (Figure 39) most closely fits the curvature distribution of the constrained filament. We apply this analogy even when the curvature distribution of the constrained filament does not exactly follow WLC statistics, because it is so useful for interpretation. Figure 39 serves as a visual guide to the magnitude of changes in the curvature distribution expected for the range of persistence lengths observed in F-actin in vitro.

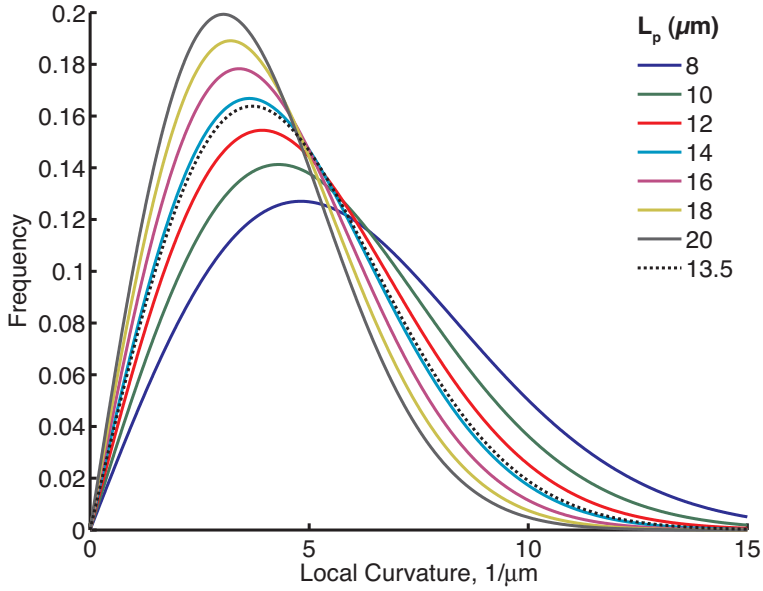

Figure 39. Calculated curvature distribution for filaments of several different persistence lengths. These results were obtained from Equation 17. The dotted line shows the persistence length of undecorated Mg-ATP-F-actin (Isambert et al., 1995).

The curvature in two dimensions can be calculated from the Boltzmann distribution using Equation 1, with $\kappa = d\hat{t}(s)/ds$, where $\hat{t}(s)$ is the tangent vector of the curve,

$$p(\kappa)d\kappa = L_p \Delta s e^{-\frac{1}{2}L_p \Delta s \kappa^2} d\kappa \qquad \text{Equation 18}$$

Unlike in the three-dimensional case, the curvature in two dimensions has a sign that depends on the coordinate system (Figure 40). In a few cases where a clear plane of interest could be defined, we obtained both the three-dimensional and two-dimensional curvature from the simulations. In all cases, simulations were done in three dimensions and the two-dimensional curvature was obtained by projecting the shape of the filament onto the plane of interest.

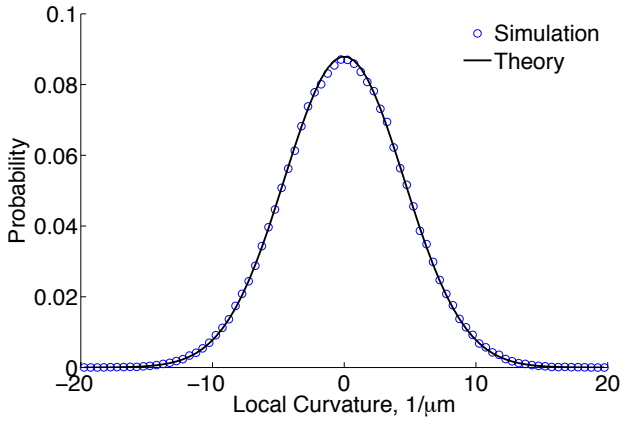

Figure 40. Curvature distribution projected onto two dimensions of an unconstrained WLC filament with a persistence length of 9 μm.

Discussion

The nanometer-scale curvature distribution calculated using Monte Carlo simulations of a discretized WLC polymer matches the expected distribution calculated from WLC theory. We proceeded to use these simulations to study how biologically relevant constraints on actin filaments modify the very small-scale curvature fluctuations that we believe may be relevant to the activity of actin-binding proteins (ABPs) that regulate F-actin dynamics and organize filaments into subcellular structures.

Nanometer-scale curvature has not been experimentally measured on actin filaments, which is one reason why simulations are needed to bridge the micron scales on which fluorescence imaging and low-resolution electron microscopy can yield useful information with the molecular scale of several nanometers. However, one experiment that used optical traps to tie a knot in single actin filaments revealed that a local radius of curvature of ~180 nm, corresponding to a curvature of 5.6 μm^{-1}, led to filament breaking at low forces ~ 1 pN (Arai et al., 1999). This suggests that curvatures of ~6 μm^{-1}, may weaken inter-monomer contacts. In freely fluctuating actin filaments, fluctuations with wave vectors of ~6 μm^{-1} should decay in ~100 μs, while fluctuations over smaller length scales are even more transient, because the correlation time of fluctuation amplitudes scales with the inverse fourth power of the wave number (Brangwynne et al., 2007). Therefore, even though such curvatures can distort the local filament structure, they are too transient to lead to fragmentation in the absence of external influences. The average curvature for a given mode of the Fourier decomposition of the tangent angle is $\kappa = \left(\sqrt{2/L}\right) q a_q$, with $q = (n + ½)\pi/L$, and the mode amplitude a_q is proportional to the inverse square of the mode number. High-curvature fluctuations are heavily disfavored in thermal fluctuations because the WLC's bending energy is a simple quadratic function of the local curvature (Equation 1).

Filament against a barrier

The lamellipodium is a narrow, sheet-like region at the leading edge of a motile or spreading cell (Nicholson-Dykstra & Higgs, 2008) that coordinates with the formation of adhesions to the extracellular matrix (Wu et al., 2012), in which the Arp2/3 complex is enriched and nucleates a network of branched filaments (Iwasa & Mullins, 2007). Actin in the lamellipodium is fast-growing (Ponti et al., 2004) and branched (Small et al., 2011; Yang & Svitkina, 2011), although the density of branches has been the subject of heated debate (Higgs, 2011; Insall, 2011; Small, 2010; Small, 2011; Svitkina & Borisy, 1999). Filaments are nucleated by the Arp2/3 complex and grow toward the membrane at the leading edge. The force generated by this polymer growth is distributed between pushing the leading edge forward and retrograde flow of the actin network (Ponti et al., 2004). It is difficult to know to what degree filaments bend while pushing against the membrane at the leading edge in most preparations because the precise shape of filaments and the transient nature of strain on filaments in a dynamic network are very sensitive to preparation conditions, but cryoelectron tomograms of fibroblast lamellipodia in which the membrane is clearly visible do show filaments at the leading edge that are slightly or moderately curved (Urban et al., 2010). Additional evidence of biologically relevant filament bending near the leading edge comes from comparisons of negative stained electron tomograms of actively protruding and paused or retracting regions of the same cell, showing dramatic changes in the angular orientation and curvature of filaments (Koestler et al., 2008).

Most importantly, because we have shown that mother filament curvature biases branch nucleation by the Arp2/3 complex (Risca et al., 2012), we sought to test how the nanometer-scale curvature distribution of a filament oriented at a 35˚ angle to a resisting barrier is affected by the degree of bending imposed by that barrier. It is very likely that actin filaments growing against the leading edge of the cell do feel at least transient bending forces. Because the largest concentration of activated Arp2/3 complex lies at or very near to the very edge of the cell (Goley & Welch, 2006; Pollitt & Insall, 2009; Sukumvanich et al., 2004), this filament geometry speaks to the biological relevance of the curvature-induced branching bias we described in Chapter 3.

Parameters and implementation

A single WLC filament composed of 27 particles, with a total contour length of 140.4 nm, and a persistence length of 13.5 μm, was placed near a hard wall constraint (Figure 41). The length was chosen to represent the approximate length of filament ends emerging from the dendritic network to impinge on the plasma membrane, as observed by electron microscopy (Svitkina & Borisy, 1999; Urban et al., 2010; Vinzenz et al., 2012). Its persistence length was chosen to reflect freshly polymerized actin (Isambert et al., 1995). The filament was constrained by pinning the first and 14th particles in space such that the filament could rotate freely around them, but they could not translate. The contour length of the filament between the last pinned particle and its free end was 70 nm. This length was chosen based on electron micrographs of the leading edge of motile cells (Svitkina & Borisy, 1999; Svitkina et al., 1997; Urban et al., 2010; Vinzenz et al., 2012). The locations of the pinned particles were on a line forming a 35˚ angle with the normal to the hard wall. This angle was chosen to reflect the average orientation of filaments in a lamellipodial dendritic network with respect to the leading edge membrane of a crawling cell (Verkhovsky et al., 2003). The pinned particles represent the constraints that actin filaments feel

in the dense dendritic network, with the two pins restricting overall filament rotation as is the case with filaments that are rooted in a large network. The pinned particle closer to the membrane stands in for any of several types of constraints that exist in dendritic networks: Arp2/3 crosslink points, crosslinks induced by other actin-binding proteins, such as fascin, and entanglements between adjacent filaments.

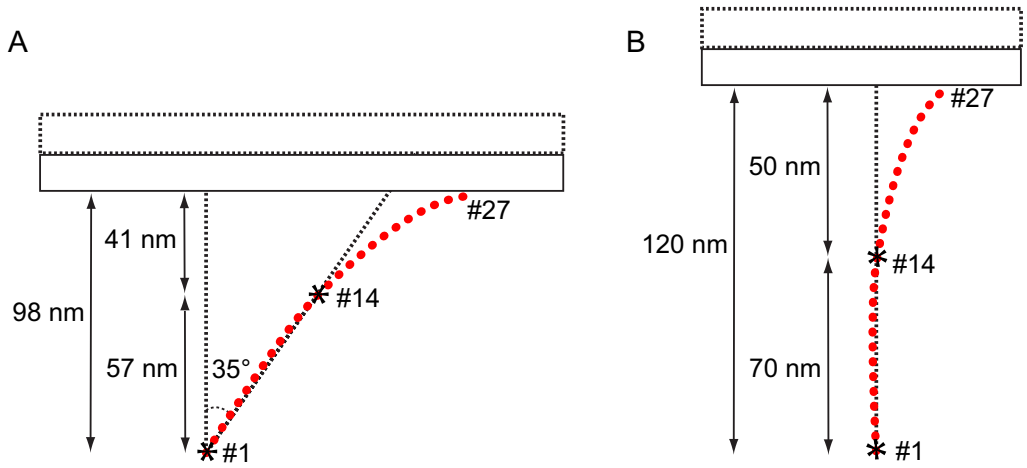

Figure 41. Geometry of filament simulation against a hard wall. (A) This representation shows the simulation setup for a height of 98 nm between the base of the filament and the hard wall barrier. Particle number is indicated along the discretized WLC filament (red dots), and asterisks mark the pinned particles that can rotate but not translate. The angle made by the base of the filament to the normal to the barrier was 35˚. In a series of simulations, geometry was kept constant while the barrier was lowered. (B) Another set of simulations was also carried out with the same filament oriented normal to the barrier, which was progressively lowered.

Results

The length of the free section between the second pinned monomer and the end of the filament was varied as a control. In the absence of a hard wall constraint, this had no effect on the filament's nanometer-scale curvature distribution, as expected (not shown).

As the barrier was lowered, the filament was bent and its curvature distribution broadened and shifted to higher and higher curvatures (Figure 42). At very low barrier heights, a large shoulder in the curvature distribution emerges, corresponding to a filament conformation in which the point that first encountered the barrier is locked at an elevated local curvature, and a free tail of filament from that point to the end is free to fluctuate.

One peak came from the filament under the constraint imposed by the hard barrier, while the other came from the curvature fluctuations in the relatively unconstrained filament tail. Analysis of the curvature as a function of the position along the filament showed that the peak in curvature occurred at the location of the last tether point, as would be expected (Figure 43). Similar results

were obtained from a simulation in which the filament was initially oriented normal to the barrier (Figure 44).

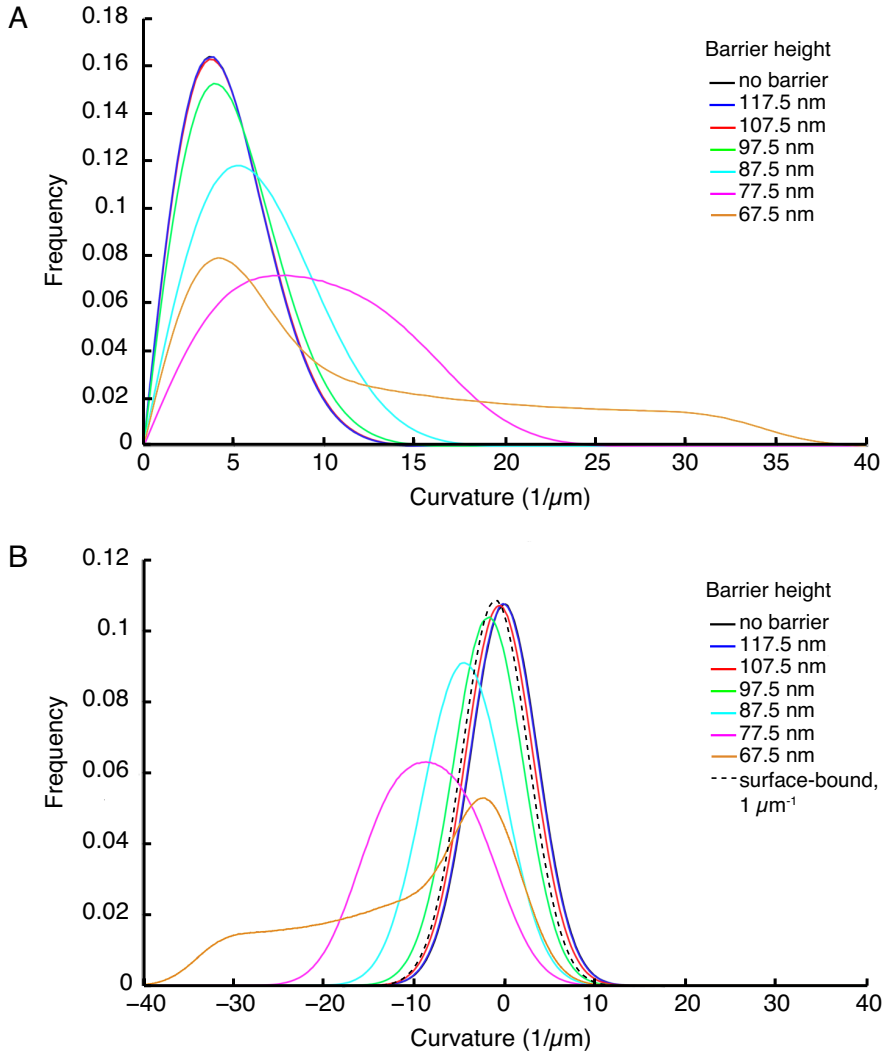

Figure 42. Curvature distribution for a filament at a 35° angle to a hard barrier. The geometry of the simulation is as shown in Figure 41. In the absence of thermal fluctuations, the barrier would first touch the filament's end at a height of 115 nm. (A) Three-dimensional curvature. (B) Two-dimensional curvature measured from a projected shape of the filament containing the two pinned monomers and the filament's end. The dashed line represents the curvature distribution of a filament bound to a plane with tethered particles 250 nm apart, with an imposed radius of curvature of 1 μm.

Discussion

The curvature distribution of a WLC filament bent or buckled by a barrier exhibited largely expected behavior, with the small-scale curvature distribution shifting to higher curvature values as an overall bend was imposed by increasing compression against the barrier (Figure 42). Comparing the results of these simulations, which had a more biologically relevant filament and constraint geometry, to those in Chapter 3, we see that large changes in the distribution of curvature fluctuations can occur easily in a three-dimensional geometry with a free filament end. Although cellular membranes are not infinitely stiff, as this barrier was, they do have significant rigidity, and should produce similar results to what we observed in these simulations. In addition, this simulation has direct bearing on dendritic networks growing in vitro against artificial, rigid

loads (Akin & Mullins, 2008; Chaudhuri et al., 2007; Parekh et al., 2005). Crosslinker compliance may also reduce these curvature effects somewhat in a similar geometry, but the overall trends apply. The results suggest that the small length scale curvature distribution of a filament under infinitely rigid constraints, such as the pinned particles and the hard barrier, largely follows the curvature suggested by the large-scale bending of the filament. For example, in the case of a barrier height of 77.5 nm at a filament angle of 35˚ to the barrier, we can approximate the shape of the filament as following part of a circle. By simple geometric arguments, we obtain a radius of curvature of 47 nm, or a curvature of 21 μm^{-1}, which is similar to the upper limit of the curvature fluctuation distribution for that configuration. Considering the curvature distribution at the various particles along the filament, the shift to high curvature was concentrated at the last constrained particle before the barrier (Figure 43). This may be functionally important if the protein responsible for the crosslink is sensitive the curvature of the filament.

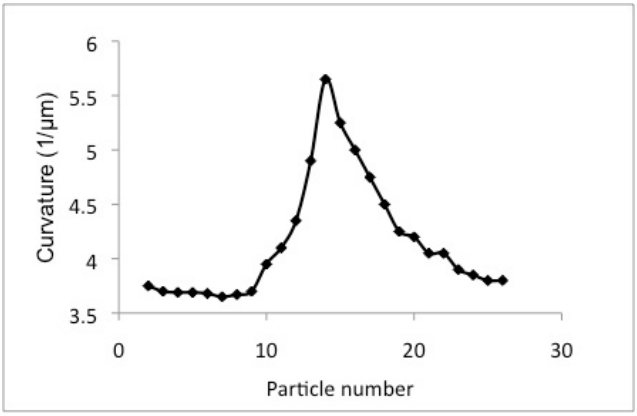

Figure 43. Peak of the curvature distribution as a function of particle along the filament bent by a barrier. In this case, the height of the barrier was 107.5 nm, and the filament was at a 35˚ angle to the normal to the barrier.

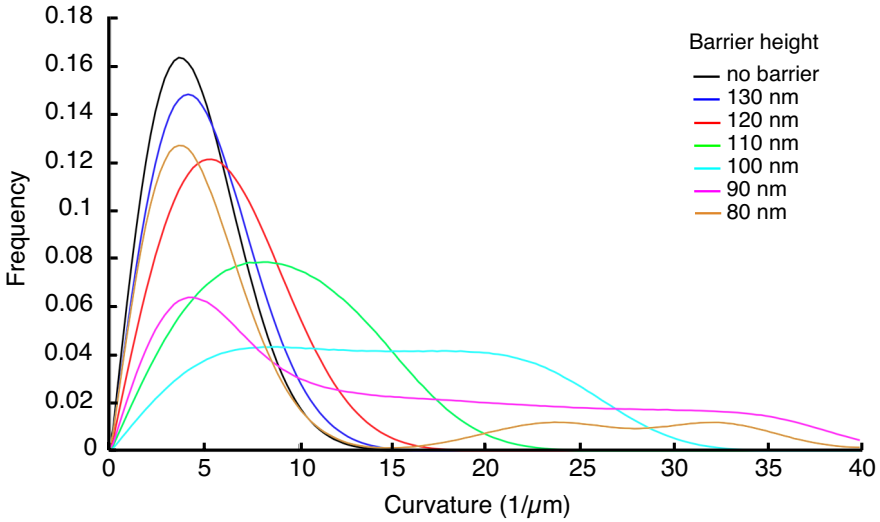

Figure 44. Curvature distribution for a filament normal to a hard barrier. The geometry of the simulation is as shown in Figure 41, except that the angle has been changed from 35˚ to 0˚ and the barrier height has been adjusted accordingly, while keeping the contour length of the filament the same. The three-dimensional curvature distribution is shown as a function of barrier height. The barrier would first touch the filament's end at a height of 140.4 nm.

Bundled filaments

Filopodia are actin-based protrusions that consist of long, parallel, tightly bundled actin filaments enveloped by a membrane tube (Breitsprecher et al., 2011; Svitkina et al., 2003; Urban et al., 2010). One exception to this description is found in the filopodia of Dictyostelium, which contain a network of short filaments that are not necessarily parallel (Medalia et al., 2007). Filopodia play important roles in many cellular processes and are often involved in a cell's exploration of its environment (Gallo & Letourneau, 2004). For example, filopodia in neurons have been shown to respond to substrate stiffness (Chan & Odde, 2008) and to be involved in the guidance of neural growth cones by chemical cues (Davenport et al., 1996; Davenport et al., 1993; Dent et al., 2003; Zheng et al., 1996). Filopodia make the initial contacts that lead to the establishment of adherens junctions (Gallo & Letourneau, 2004; Raich et al., 1999). Filopodia also serve as precursors for contractile actin bundles, which share an architecture based on long, parallel and unbranched actin filaments (Nemethova et al., 2008). Lastly, filopodia play important roles in the motility of metastatic cancer cells (Machesky & Li, 2010).

Filopodia can form as a result of the nucleation of long, straight filaments by the family of actin nucleators called formins, which remain attached to barbed ends and prevent capping (Block et al., 2008; Chhabra & Higgs, 2007; Mellor, 2010; Yang & Svitkina, 2011). They can also form through convergent elongation from certain filaments in a dendritic network whose barbed ends are protected from capping, perhaps by the barbed end polymerase family Ena/VASP (Applewhite et al., 2007; Haviv et al., 2006; Mejillano et al., 2004; Vignjevic et al., 2003; Yang & Svitkina, 2011). An open question is how filaments from the dendritic network are selected for incorporation into filopodia, and how the differing architectures of actin in filopodia and actin in lamellipodia may modulate the behavior and binding partners of the respective filament populations (Michelot & Drubin, 2011). We sought to explore actin curvature fluctuations in this alternative filament architecture.

Although the bundling of filaments in filopodia during filopodium initiation and the mechanical stabilization of the bundle against buckling due to the compressive force exerted by tension in the membrane has been attributed to the action of crosslinking proteins – fascin, in particular (Adams, 2004; Aratyn et al., 2007; Jansen et al., 2011; Mogilner & Rubinstein, 2005) – more recent work by Liu et al. and Pronk et al. shows that the membrane alone is capable of both bundling filaments to initiate filopodium-like bundles (Liu et al., 2008) and reinforcing uncrosslinked bundles of a few filaments against Euler buckling (Pronk et al., 2008). Individual actin filaments without such reinforcement buckle too easily under the resistance posed by membrane bending rigidity and tension. Equation 5 can be applied to individual filaments in filopodia and filopodial precursors to quantify the buckling force as a function of length.

In this simulation, we focused on the actin bundle itself, rather than on membrane-induced effects. Fascin is heavily enriched in mature filopodia (Adams, 2004), so we sought to simulate a fascin-crosslinked actin bundle. Fascin can crosslink filaments tightly because it is a small globular protein with two F-actin binding sites (Jansen et al., 2011). Its binding to F-actin is highly dynamic, with an off-rate of 0.12 s^{-1}, but it appears to remain localized to bundles through avidity effects (Aratyn et al., 2007).

The gross mechanical properties of a bundle of filaments in the absence of membrane have been well characterized (Claessens et al., 2006; Heussinger & Grason, 2011; Heussinger et al., 2010; Lieleg et al., 2007; Mogilner & Rubinstein, 2005). Mogilner and Rubenstein introduced a useful formalism with the mechanical coupling factor $I(N)$,

$$F_{buckling(bundle)} = \frac{\pi^2}{4}\frac{k_B T L_p}{L^2} \times I(N) \qquad \text{Equation 19}$$

where N is the number of filaments in the bundle and L_p is their persistence length (Mogilner & Rubinstein, 2005). The two limits circumscribing the form of $I(N)$ are the independent filament limit, in which $I(N) = N$, and the strongly coupled filament limit, in which the filaments in the bundle are as tightly crosslinked as possible, the bundle essentially acts as a single rod, and $I(N) \approx 0.5N^2$. For the purposes of buckling, the filopodia can therefore be said to have an effective persistence length $L_{p,effective} = L_p I(N)$. We used this result to validate our bundle simulations.

We aimed to explore the fluctuations of individual filaments within bundles, because our observation that local filament curvature helps to regulate branching by Arp2/3 suggests that other ABPs may be similarly sensitive to filament bending, and also because there is evidence that the details of bundle architecture help to determine the localization of regulatory actin-binding proteins. For example, Myosin X is a motor protein that localizes to the tips of filopodia by exhibiting increased processivity when walking on closely apposed, parallel actin filaments like those in bundles (Nagy et al., 2008; Ricca & Rock, 2010). Furthermore, fascin itself has a very strong preference for binding parallel filaments, and exchanges quickly, suggesting that avidity effects that occur when filaments are already in a bundle-like architecture serve to maintain strong fascin localization at filopodia (Courson & Rock, 2010). Bundling by fascin also surprisingly appears to vastly increase the efficiency of severing by cofilin, possibly because the constrained architecture of filaments in a bundle prevent relaxation of the mechanical stress induced by cooperative cofilin binding to sections of F-actin (Breitsprecher et al., 2011).

We hypothesized that the restriction of fluctuations imposed by tight crosslinking of actin filaments would shift the nanometer scale curvature distribution of the bundled filaments to lower curvature values.

Parameters and implementation

Filopodia were simulated as simplified bundles of WLCs (Figure 45). Parameters were chosen to reflect middling values from the range of values in literature, but it should be noted that there is diversity in the morphology and dynamics of filopodia, both among and between cell types (Breitsprecher et al., 2011; Gupton & Gertler, 2007; Medalia et al., 2007; Urban et al., 2010). In some cases, unrealistic parameters values were chosen to keep the computational time required to run the simulation within feasible limits. Actin filaments were simulated by discretized WLCs as described in the previous sections. The default persistence length was 13.5 μm unless otherwise noted, representing freshly polymerized F-actin we expect to lie near the tips of filopodia.

Filopodium length varies, ranging from a few micrometers (Vignjevic et al., 2006) to tens of micrometers (Wood & Martin, 2002). We chose a length of 0.5 μm for the realistic bundle simulation (Figure 45A), and 0.5 or 1 μm for thin bundle simulations (Figure 45B) because longer lengths would be unfeasible to simulate with the available computational resources. This length of a bundle can be thought of as a section of a filopodium, or perhaps as the tip of a newly formed filopodium precursor. The filaments were fixed at their base, as if they were connected to the base of a larger filopodium, by preventing the first particle of each WLC from translating.

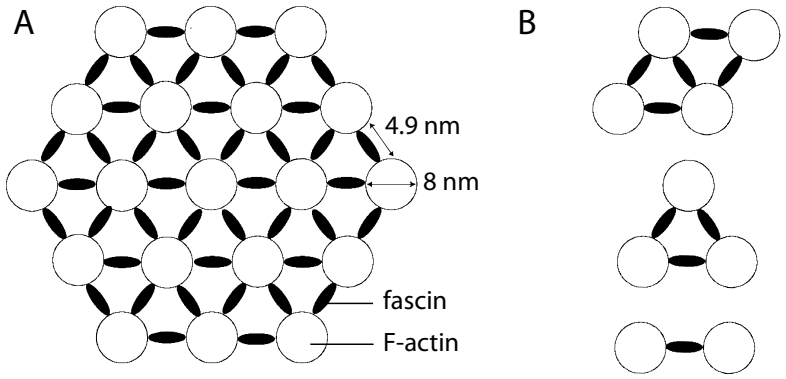

Figure 45. Geometry of simulated actin bundles. (A) A cross-section is shown of the 19-filament bundle chosen to represent a typical filopodium. Fascin cross-links were assigned an unstretched length of 4.9 nm and actin filaments were assigned a diameter of 8 nm, with a hard-shell excluded volume interaction between different filaments. The actin filaments were arranged in a hexagonal close packed lattice. Crosslink density was varied. Filaments in this bundle were 500 nm long, with a default persistence length of 9 μm. (B) Smaller bundles of 500 nm and 1 μm contour lengths were used to test hypotheses about the effects of crosslinkers in control simulations. The cross-link parameters were the same as in A.

The number of actin filaments in filopodia is ~10 – 30 (Breitsprecher et al., 2011; Mogilner & Rubinstein, 2005; Svitkina et al., 2003; Urban et al., 2010; Vignjevic et al., 2006), and at least ~10 are required for filopodium stability under most circumstances (Mogilner & Rubinstein, 2005; Pronk et al., 2008). For the realistic bundle simulation (Figure 45A), we chose 19 filaments because of their symmetry. The smaller bundles used in control simulations contained only 2-4 filaments in order to reduce the time to equilibrate the potential energy and allow us to test more conditions. All filaments were arranged with hexagonal close packed symmetry. Although real filopodia (Aratyn et al., 2007; Svitkina et al., 2003; Urban et al., 2010; Vignjevic et al., 2006) do not exhibit the nearly crystalline order present in, for example, the Limulus acrosomal bundle (Schmid et al., 2004) or stereocilia (Stokes & DeRosier, 1991), there is evidence that freshly extended filopodia in B16-F1 melanoma cells contain parallel, somewhat ordered filaments, and that the order of filament packing decreases in older filaments undergoing disassembly (Atilgan et al., 2006). Fascin has been shown to form hexagonal close packed bundles in vitro, but only after long annealing times (Stokes & DeRosier, 1991). We chose a hexagonal close packed initial configuration to facilitate comparisons between different

simulations, and because any effects due to bundling would probably be more evident in a closely packed bundle than in a more realistic, disordered bundle.

As a model crosslinker, we chose fascin because it is the primary bundling protein in filopodia (Vignjevic et al., 2006). The inter-actin spacing in fascin-actin bundles was found to be 12.9 nm by small angle X-ray scattering (Shin et al., 2009). A similar spacing, was obtained by Claessens et al. (Claessens et al., 2008). Therefore, to match our 8 nm F-actin diameter, we chose a fascin crosslinker length r_0 = 4.9 nm. Fascin was modeled as a simple spring, for which the only energetic penalty is associated with changes in the three-dimensional distance, r, between the two particles being crosslinked:

$$E_{crosslink} = \frac{K_{fascin}}{2}(r - r_0)^2. \qquad \text{Equation 20}$$

The stiffness of this spring, K_{fascin}, was varied, but biologically relevant values are in the range of 0.004 – 10 N/m (Table 10). At the high end of the range are cytoskeletal proteins, which are unusually stiff, and the low end of the range represents myosin, which has a lever arm structure that would make it less stiff than a globular protein like fascin (Howard, 2001). Calculations based on the amount of over-twist observed in fascin-actin bundles, which is in part determined by crosslinker stiffness, suggest that the stiffness of fascin must lie below 0.5 N/m (Shin et al., 2009). Based on these literature values, we chose a default crosslink stiffness of 0.25 N/m. Because the detailed mechanical behavior of fascin-actin crosslinks has not been experimentally tested, we did not include any dependence of the crosslinker energy on rotation of the fascin-actin link, except in one control simulation where shear was considered. In that case, the same stiffness was applied to a second crosslink spring whose extension depended on the axial displacement between crosslink points on neighboring actin filaments.

Table 10. Stiffnesses of representative proteins used to estimate the stiffness of fascin crosslinks.

Protein	***K* (N/m)**	**Reference**
Myosin	0.004	(Howard, 2001)
Fascin, theoretical estimate	0.2	(Howard, 2001)
Tubulin	10	(Howard, 2001)
Lysozyme	2	(Radmacher et al., 1994)
Myoglobin	0.3	(Zaccai, 2000)
Domain 4 of *Dictyostelium* filamin	0.25	(Schlierf & Rief, 2005)
α-Actinin	0.46	(Ferrer et al., 2008)
Filamin	0.82	(Ferrer et al., 2008)

Crosslinks were randomly placed along the WLC polymers, with the restriction that two crosslinkers cannot bind the same particle. The density of crosslinks was varied around the value of 25-60 actin monomers per fascin molecule measured in filopodia (Aratyn et al., 2007). A ratio of 25:1 was used as the default. The saturating ratio of actin to fascin is 4.6:1 measured in bundles assembled in vitro (Stokes & DeRosier, 1991), but such a high density of fascin is

unlikely to occur in the dynamic, somewhat disordered filopodia found in vivo. In a few cases, we exceeded this ratio in two-filament bundles in order to test limiting behavior.

The width of filopodia is ~0.1 – 0.5 µm (Breitsprecher et al., 2011; Sheetz et al., 1992; Urban et al., 2010). Our 19-filament bundle has a diameter of 59.6 nm. In simulations used to test the effect of an enclosing membrane on the curvature distribution of the bundled filaments, we used a hard wall barrier in the shape of a cylinder around the bundle. We chose a barrier radius of 60 nm for tight enclosure by the membrane, and 90 nm for a looser enclosure. The latter number is consistent with a membrane bending modulus of 20 k_BT and membrane tension of 0.01 k_BT/nm^2 (Atilgan et al., 2006).

Results

The curvature distribution of bundled WLC filaments was measured as described above, sampling all the filaments in the bundle, in aggregate. The first parameter we varied was the crosslinker density, because it likely changes during the life of a filopodium, from formation, through maturity, to disassembly, and may play a role in modulating the bending dynamics of F-actin in the filopodial bundle. For crosslinker densities in the physiological range of 26-60 actin monomers per fascin, we observed very little effect on the curvature distribution (Figure 46). Comparing Figure 46 with Figure 39, the ratio at the lowest end of that range (25:1) shifted the curvature distribution curve an amount approximately equal to a change in the filament persistence length of 0.5 µm, or 3.7% of the free filament persistence length. The only large deviations from the free filament curvature distribution were observed for unphysiological and near-saturating actin:fascin ratios of 10 and 5, with the latter value causing a shift in the apparent persistence length of approximately 2.5 µm, or 19%.

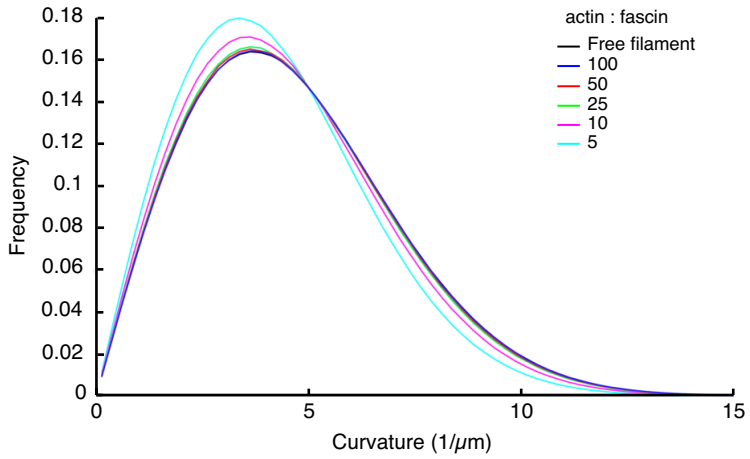

Figure 46: Filament curvature density as a function of crosslinker density in a 0.5 µm long bundle of 19 WLC filaments. The persistence length of each filament is 13.5 µm and the crosslinker stiffness is 0.25 N/m. Each particle in the discretized WLC filament represents two actin monomers, so the actin:fascin ratios are double the ratios of filament particles to crosslinkers.

The second parameter we varied is the stiffness of the crosslinker, because there is currently no direct measurement of this value, and because these results should apply to a variety of similar crosslinking molecules, which primarily differ in their flexibility. We varied the stiffness around 0.25 N/m, and found that values of 0.025-2.5 N/m had indistinguishable effects on the curvature distribution (Figure 47). Although we did observe a dramatic change in the curvature distribution

for crosslinker stiffnesses of 100 and 500 N/m, these inextensible crosslinks are one to several orders of magnitude more rigid than any protein.

Because filopodia are enclosed in a membrane tube, we asked whether enclosing the bundle in a rigid tube would have any effect on the curvature distribution of the enclosed filaments. For a crosslinker stiffness of 0.25 N/m and an actin:fascin ratio of 25, we found that the size of the enclosing membrane tube had no effect on the filament curvature distribution, when varied between 60 nm, only 0.4 nm larger than the diameter of the bundle itself, and 150% that diameter (Figure 48). Using Equation 17, we can derive the average curvature of the discretized filament $\langle \kappa \rangle = \left(L_p \Delta s \right)^{-1/2}$, and from that, by the geometry of three particles, the average lateral deviation $\langle d \rangle = 0.5 \langle \kappa \rangle \left(\Delta s \right)^2 \approx 0.06$ nm, showing that the insensitivity of nanometer length scale curvature to a tube constraint is consistent with discretized WLC statistics.

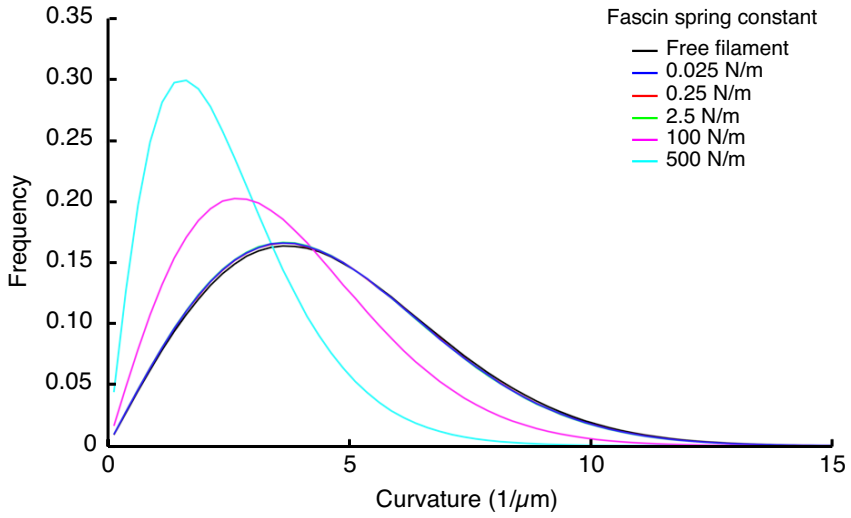

Figure 47: Filament curvature density as a function of crosslinker stiffness in a 0.5 μm long bundle of 19 WLC filaments. The persistence length of each filament is 13.5 μm and the crosslinker density is one crosslinker per 12.5 particles, representing an actin:fascin ratio of 25:1.

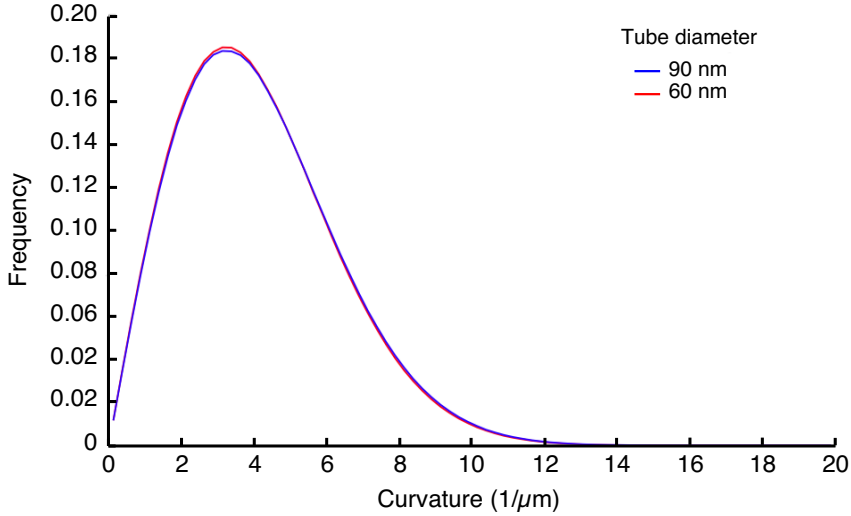

Figure 48: Enclosing the WLC bundle in a rigid tube did not affect the curvature distribution. The tube presents an infinitely rigid barrier. The 60 nm diameter is only 0.4 nm larger than the initial diameter of the bundle itself. All other parameters were kept at default values for the 19-filament bundle.

Because our curvature sampling occurs over the short length scale of 10.8 nm, and at a ratio of actin:fascin of 25:1, the average distance along each filament between crosslinks was 34 nm, we asked whether the curvature distribution of particles near crosslink points was different from that of particles away from crosslink points. The difference in the curvature distribution between the two populations of particles was very small (Figure 49), less than the difference between the curvature distribution of a free filament and that of filaments in the bundle at default parameters (~3.7% change in apparent persistence length). The curvature distribution of filament particles near crosslink points was very slightly shifted toward higher curvatures relative to that of particles away from crosslink points.

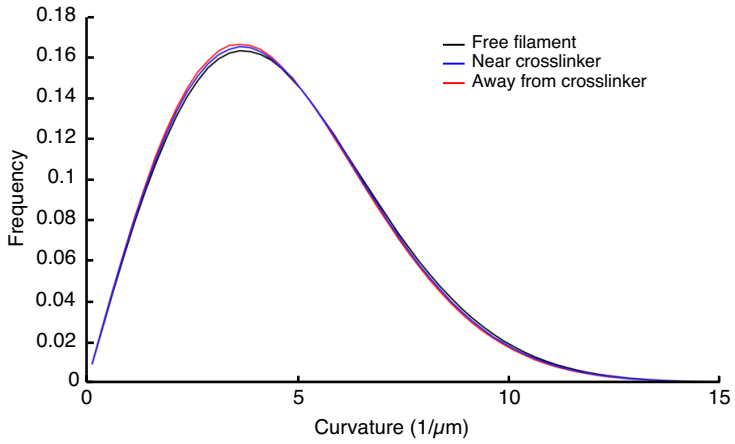

Figure 49: The curvature distribution near crosslinked points is very similar to that away from crosslinked points. A 19-filament bundle was simulated with default parameters. Particles near crosslinkers were defined as the filament particles directly bound to crosslinkers and their first nearest neighbor in either direction along the filament.

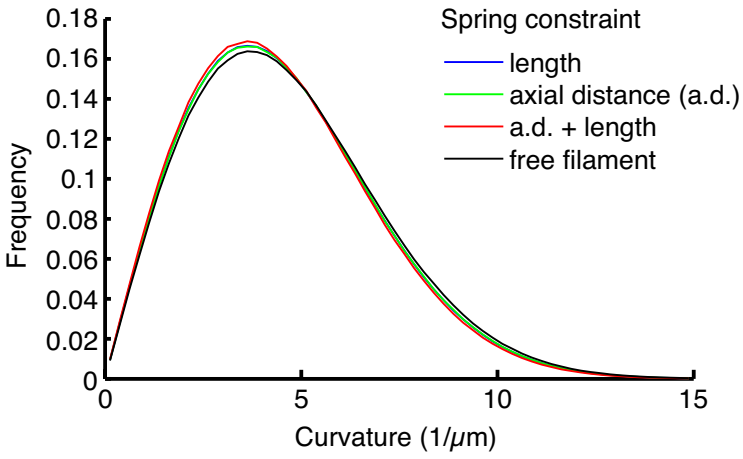

Figure 50: Introducing a constraint on crosslinker shear along the filament axis direction did not significantly shift the curvature distribution of bundled filaments. The constraints shown are a simple spring as used in all other simulations (Equation 20), a similar spring on the axial shear between filaments, for which the energy is of the same form, but the distance in question is measured between the two crosslinked particles only along the bundle axis, and a combination of the two constraints.

The crosslinkers in our simulations were simple springs with no angular dependence of the energy. To test whether this simplification affected our results, we introduced an additional

constraint on the distance between the two ends of a crosslink, projected along the axis of the two filaments being crosslinked. This additional spring had the same spring constant as the normal crosslinker, 0.25 N/m. This effectively created a greater resistance to shear between filaments than is introduced by a simple distance constraint, to mimic the fact fascin may behave differently under shear than under lateral extension. Although the additional constraint did slightly shift the distribution (by a ~3 % shift in the apparent persistence length) toward lower average curvatures (Figure 50), the effect was so small that we did not use the shear constraint in other simulations, because we do not have measurements of fascin elasticity to justify it.

We next asked how crosslinking affected filament bending fluctuations on different length scales. The tangent-tangent correlation function (TTCF) is a measure of how the filament tangent angle behaves over different length scales, and for a pure WLC filament, takes the form

$$\left\langle \hat{t}(0)\cdot \hat{t}(s)\right\rangle = \left\langle \cos\left[\Delta\theta(s)\right]\right\rangle = \exp\left(s/L_p\right), \qquad \text{Equation 21}$$

where $\hat{t}(s)$ is the tangent angle at arc length coordinate s along the filament, and the middle expression is equivalent to Equation 3. To make these measurements, we simplified the realistic 19-filament bundle to smaller bundles of 2-4 filaments (Figure 45B) and reduced the persistence length to 500 nm, in order to reduce the amount of computation time required to equilibrate the simulations. We used a filament length of 1 μm to allow more measurements of the TTCF. Long length scales take the longest to equilibrate, and the equilibration time increases with the number of particles and the stiffness of the bundle, making it unfeasible to perform multiple simulations of realistic bundles. This compromise allowed us to explore general trends in apparent persistence length at different length scales, and ask whether the overall bundle stiffness behaves as expected.

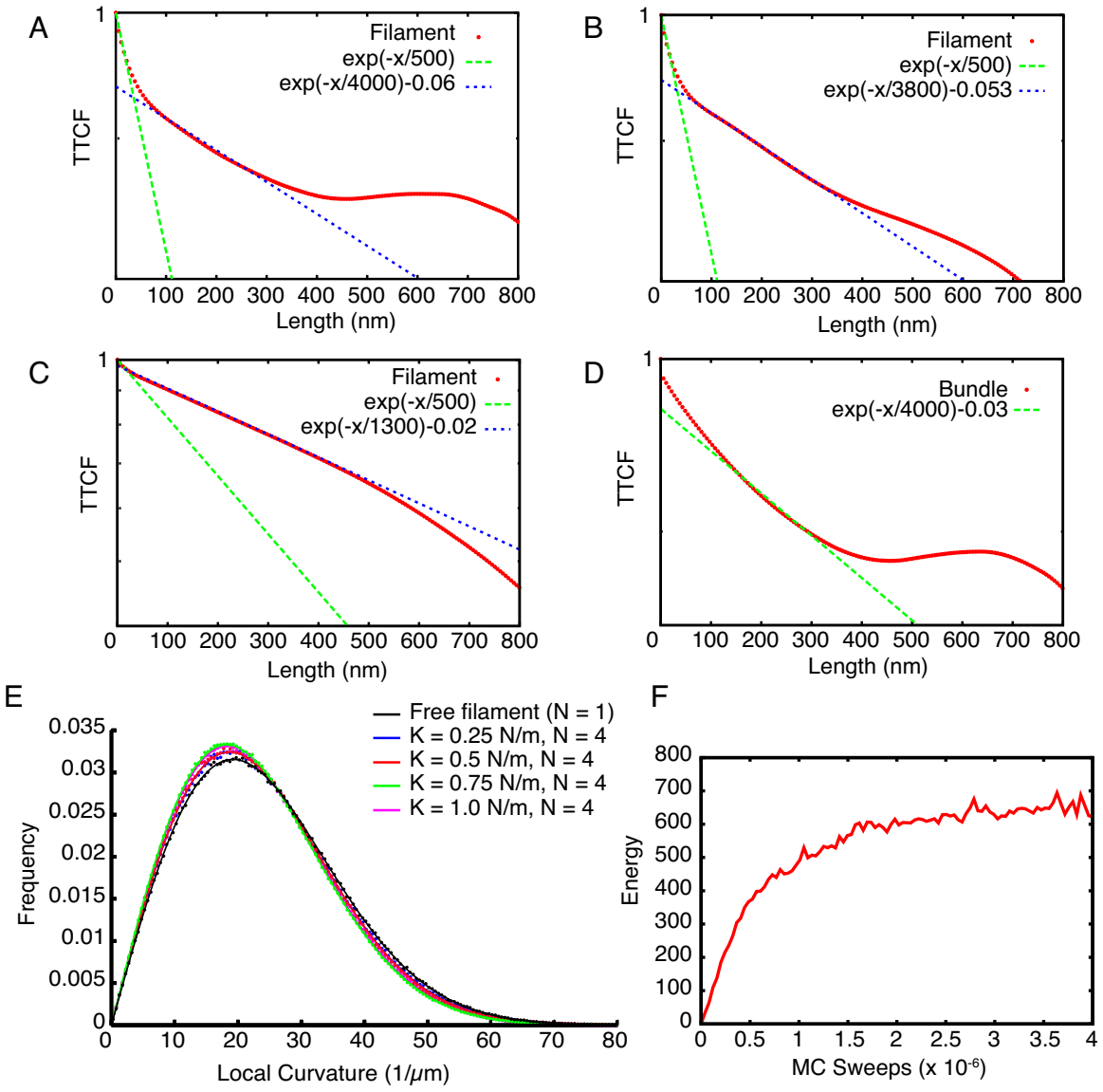

Figure 51. Curvature distribution and TTCF of representative small bundles. (A) TTCF of filaments in a 4 filament bundle with K_{fascin} = 0.75 N/m. (B) TTCF of filaments in a 4 filament bundle with K_{fascin} = 0.25 N/m. (C) TTCF of filaments in a 2 filament bundle with K_{fascin} = 0.75 N/m. (D) TTCF of the medial axis of a 4 filament bundle with K_{fascin} = 0.75 N/m. (A-D) are semi log plots, and the WLC TTCF was fit to the short length scale regime (green in A-C) and the intermediate length scale regime (blue in A-C, green in D). The effective persistence lengths resulting from these plots are shown in Table 11. (E) Curvature distribution of individual filaments in a 4 filament bundle as a function of crosslinker stiffness (here, K = K_{fascin}). Dots are simulation data, lines are fitted distributions. (F) Example of energy equilibration for a 4 filament bundle simulation with K_{fascin} = 0.75 N/m. In all cases, the filaments simulated are 1000 nm long and have a persistence length of 500 nm.

Table 11. Effective persistence lengths of filaments within bundles and whole bundles as a function of crosslinker stiffness and number of filaments, measured using the small-scale curvature distribution and the tangent-tangent correlation function (TTCF).

K_{Fascin} (N/m)	N	Filament L_p from TTCF	Filament L_p from curvature	Bundle L_p from theory: $I(N) = 0.5*N^2$	Bundle L_p from theory: $I(N) = N$	Bundle L_p from TTCF	Bundle L_p from curvature
	2	1250	530	1000	1000	1250	1020
0.25	3	2200	535	2250	1500	1650	1500
	4	3800	530	4000	2000	3550	2000
	2	1000	530	1000	1000	1000	1020
0.5	3	2500	530	2250	1500	1700	1500
	4	4000	530	4000	2000	4200	2000
	2	1300	530	1000	1000	1300	1020
0.75	3	5000	535	2250	1500	5000	1500
	4	4000	560	4000	2000	4000	2000
	2	2200	535	1000	1000	2200	1020
1.0	3	3200	535	2250	1500	3200	1500
	4	15000	550	4000	2000	15000	2000
	2	-	-	1000	1000	-	1020
5.0	3	-	-	2250	1500	-	1500
	4	-	-	4000	2000	-	2000
	2	-	-	1000	1000	-	1100
10.0	3	-	-	2250	1500	-	1800
	4	-	-	4000	2000	-	2500

All persistence lengths in this table are effective persistence lengths obtained from fitting the curvature distribution with Equation 17 and the TTCF with Equation 21 in the intermediate length scale regime (explained in Figure 51 and the text). Persistence lengths are given in units of nm, and N represents the number of filaments in a bundle. Filament persistence lengths refer to the apparent stiffness of filaments within the bundle. Bundle persistence lengths refer to the apparent stiffness of the medial axis of the bundle. Bundle persistence lengths predicted from theory are based on (Mogilner & Rubinstein, 2005). The parameters of the simulation are as in Figure 51, where plots corresponding to a subset of this data are displayed.

Representative results of thin-bundle simulations with the default crosslinker density of 25 actin monomers per 1 fascin are shown in Figure 51, and tabulated in Table 11. The TTCF was measured for filaments within the bundle and for the medial axis of the bundle itself. In the case of individual filaments, the TTCF exhibits three regimes. At short length scales, the TTCF is fit by a decaying exponential with the same persistence length as individual filaments, 500 nm. At intermediate length scales, spanning several crosslinkers, the apparent persistence length is significantly greater, and can be fit by an exponential in some cases to obtain an effective persistence length. At long length scales, the TTCF cannot be adequately interpreted because although the energy of each simulation was allowed to equilibrate before making measurements, these length scales may not have fully equilibrated. In addition, the TTCF is unreliable at length

scales approaching the contour length of the filament because it cannot be adequately sampled there.

Mogilner and Rubinstein have estimated the scaling laws for the relationship between bundle stiffness and the number of filaments in the bundle for uncoupled filaments and tightly coupled filaments, as discussed above in the Parameters and Implementation section (Equation 19) (Mogilner & Rubinstein, 2005). We compared the apparent persistence lengths of the medial axis of simulated thin bundles with the predicted persistence length based on the number of filaments and the two types of coupling, in order to verify that our results are consistent with what is already known about large-scale bundle mechanical properties. This comparison also provided an opportunity to evaluate which values of the crosslinker stiffness correspond to the tightly coupled regime studied by Mogilner and Rubinstein. When measured by fitting the short length scale curvature distribution of bundles, the apparent bundle stiffness scaled with the number of filaments as expected from the scaling relation for an uncoupled bundle (Table 11). Only in the case of K_{fascin} = 10 N/m did the scaling begin to approach the tightly coupled prediction. In an alternative measurement of the apparent bundle stiffness, we fit the WLC prediction to the intermediate length scale regime of the TTCF (distances of ~100-300 nm along the filament), and observed scaling consistent with the tightly coupled bundle prediction for low crosslinker stiffnesses. However, the TTCF measured at a crosslinker stiffness of 1 N/m took on a distorted and non-exponential shape at lower length scales resulting in unreasonably high apparent bundle stiffness values. This result suggests that the stiffest bundles may not have fully equilibrated in these simulations, despite an apparent plateau in the total energy.

Lastly, we investigated whether an extreme amount of crosslinking suppresses filament fluctuations. We simulated bundles of two filaments with a range of crosslinker stiffnesses and a range of crosslinker densities ranging from 8% of filament particles crosslinked to 100% of filament particles crosslinked (8% corresponds to our default of 25 actin : 1 fascin). Crosslinkers were regularly spaced. To make the simulation as realistic as possible, we reverted to a filament persistence length of 13.5 μm and adjusted the filament length to 0.5 μm. We observed that the apparent persistence length of individual filaments did not increase dramatically until every particle was crosslinked, for physiological crosslinker stiffness (Figure 0416A). Bundle stiffness increased linearly for large (unphysiological) crosslinker stiffnesses, and with a lower power scaling law for physiological crosslinker stiffnesses (Figure 52B).

Discussion

Cross-linking of actin filaments had surprisingly little effect on their short length scale curvature distribution fluctuations for crosslinker stiffnesses within an order of magnitude of our best estimates of the physiologically relevant stiffness for fascin and similar ABPs. This may be due to the fact that the average curvature of the WLC is a local quantity, determined (according to the equipartition theorem and Equation 1) only by the persistence length and in the discretized case, the discretization length scale. In the absence of large, nonthermal forces, short length scale curvature is therefore insensitive to filament architecture on larger length scales. We conclude that F-actin network architecture should primarily affect curvature measured over a length scale similar to or larger than the spacing between crosslink points.

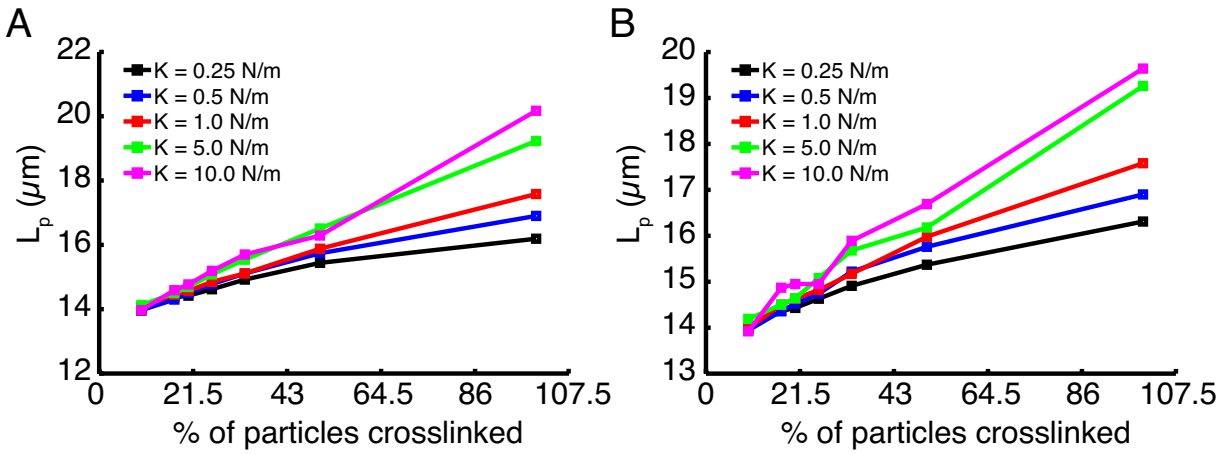

Figure 52. Apparent persistence length of highly crosslinked 2 filament bundles. (A) The apparent persistence length of the individual filaments. (B) The apparent persistence length of the medial axis of the bundle. Crosslinkers were regularly spaced. The bundle persistence length was measured by fitting Equation 17 to the curvature distribution of the bundle's medial axis, while the filament persistence length was obtained by fitting the same equation to the curvature distribution sampled from filaments.

Filament under tension

Actin and myosin cooperate in many biological processes, and the contractility of actomyosin structures is essential in endowing much of the actin cytoskeleton with its shape and mechanical properties (Aratyn-Schaus et al., 2011; Bendix et al., 2008; Cai et al., 2010; Koenderink et al., 2009). In the vast majority of situations, filaments are aligned such that the action of myosin motors applies tension to F-actin (Dasanayake et al., 2011; Miller et al., 2012). Therefore, there are many situations in which the bending fluctuations of actin filaments may be modulated by tension. In fact, it has already been demonstrated that tension on F-actin modulates cofilin binding (Hayakawa et al., 2011) and myosin binding (Galkin et al., 2012; Uyeda et al., 2011).

Parameters and implementation

A single WLC filament with a persistence length of 9 μm or 13.5 μm was simulated, with two ways of introducing tension. In the first alternative, we added the work done by tension T whenever the filament's end-to-end distance R changes by an amount ΔR

$$W_{tension} = \int_0^{\Delta R} T dr = T\Delta R \qquad \text{Equation 22}$$

to the total change in energy used to evaluate the Metropolis Monte Carlo move acceptance criterion (Equation 13). In the second alternative, we introduced a spring potential on the end-to-end distance,

$$E_{tension} = \frac{k}{2}\left(L_c - R\right)^2 \qquad \text{Equation 23}$$

for which the resting length is the contour length of the filament L and the spring constant k is chosen to apply a desired tension when the filament's end to end length is at its mean value for that persistence length, as calculated from Equation 15.

The amount of tension applied to the filament was varied from a physiological low value to higher values that are probably overestimates of the amount of tension per filament in vivo. Individual myosin II motors exert ~3-4 pN (Finer et al., 1994), and because myosin II associates into minifilaments (Vicente-Manzanares et al., 2009), it is reasonable to think that multiple motors would be acting on the same F-actin filament, taking the tension into tens of pN (Sinard et al., 1989; Verkhovsky & Borisy, 1993). Another relevant force value is 30 pN, applied to F-actin to slow down the rate of severing by cofilin by a factor of ~2 (Hayakawa et al., 2011). Lastly, we can also estimate the amount of tension on F-actin in biologically relevant contexts by dividing the average force exerted by a focal adhesion, which we can presume is generated by one stress fiber, by the approximate number of actin filaments in the stress fiber. Studies that measured the tension in stress fibers directly found a typical value of up to 4 nN (Sugita et al., 2011) or ~10 nN (Deguchi et al., 2006), while studies that measured traction forces at focal adhesions obtained tension values of 10-20 nN (Tan et al., 2003) and 10 nN (maximum of 30 nN) (Balaban et al., 2001). The number of actin filaments in stress fibers has not been thoroughly characterized, but it can be estimated because filopodia have been shown to mature into stress fibers (Anderson et al., 2008; Nemethova et al., 2008), so the estimate of 10-30 filaments per stress fiber may be reasonable (Mogilner & Rubinstein, 2005; Svitkina et al., 2003). A similar value was found for graded polarity bundles, a structure similar to stress fibers that may be a precursor to them, in fibroblasts (Cramer et al., 1997). The same study also found contractile mats of ~300 filaments. Taking a typical tension of 10 nN and a stress fiber size of 20 filaments, we estimate that the tension per filament would be 500 pN, which is less than the tensile strength of F-actin, ~600 pN (Tsuda et al., 1996).

Results

We first compared the two methods of applying tension in our simulations (Equations 22 and 23), and found that they gave identical results for the curvature distribution, as expected. We also verified that the contour length of the filament had no effect on the curvature distribution.

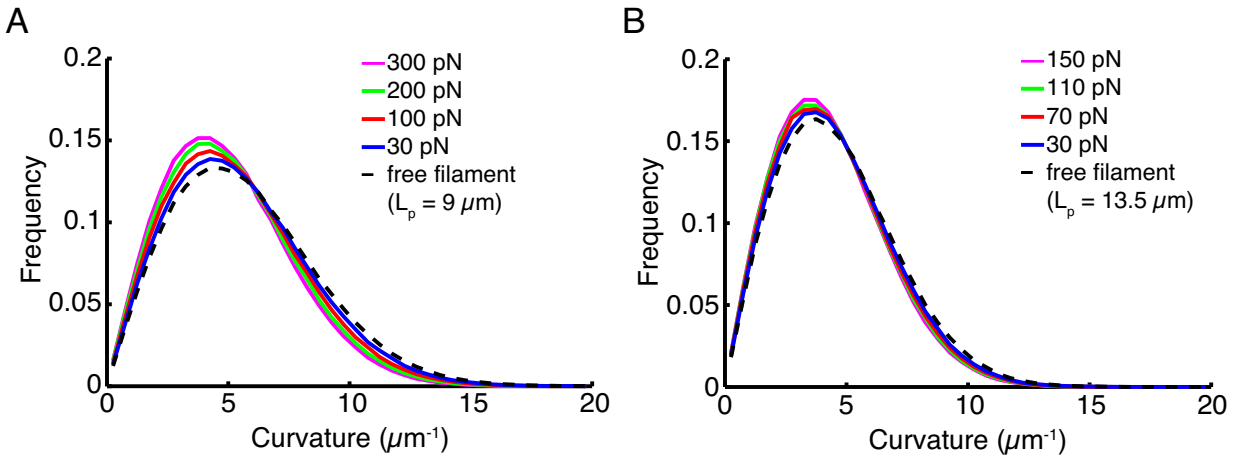

Figure 53. Tension changes the curvature distribution of WLC filaments. The filament simulated was 500 nm in length and had a persistence length of (A) 9 μm and (B) 13.5 μm.

To study the effect of tension on short length scale F-actin curvature fluctuations, we simulated two 500 nm long WLC filaments with persistence lengths of 9 and 13.5 μm, using the method described in Equation 22. The effect of tension on the curvature distribution was significant (Figure 53), with 200 pN of tension applied to a 9 μm persistence length filament changing the effective persistence length to ~11 μm, which is comparable to the change in persistence length that has been measured between ADP-F-actin and ADP-P_i-F-actin (Isambert et al., 1995). 30 pN also had a measurable effect, increasing the effective persistence length by ~0.5 μm. Similar results were obtained for the 13.5 μm persistence length filament.

Discussion

Tension on WLC filaments appeared to have a significant effect on the small-scale curvature distribution. Tension values used in our simulations were within physiologically relevant parameters, and caused changes in the apparent persistence length of several μm, on par with changes due to ATP hydrolysis (but not phosphate release).

Conclusion

Drawing on the observation that the curvature-dependent directional bias of F-actin branch nucleation by the Arp2/3 complex can be explained by small-scale curvature fluctuations of the filament, described in the last chapter (Risca et al., 2012), we sought to understand how the various actin network architectures found in cells modulate the short length scale curvature distribution. We investigated a filament bent by a hard barrier, a bundle of crosslinked filaments, and a filament under tension.

The filament bent by a hard barrier showed that the highest curvature occurs near the last point of constraint before the filament hits the buckling or bending barrier (in vivo, the membrane). Comparing the role of tension with the role of crosslinking constraints in modulating the short length scale curvature distribution (and here, short means shorter than the average spacing between crosslinks), we find that these results are consistent with a model developed for DNA,

which explains how the bending fluctuations of a WLC polymer can be tuned with low-pass filtering induced by tension, and high-pass filtering induced by nano-confinement (Lin et al., 2012). Because we measured curvature over very short length scales, the curvature fluctuation distributions were most sensitive to short-wavelength filament fluctuations, which are suppressed by tension but not by confinement.

References

Adams JC (2004) Roles of fascin in cell adhesion and motility. *Current Opinion in Cell Biology* 16, 590-596.

Akin O, Mullins RD (2008) Capping protein increases the rate of actin-based motility by promoting filament nucleation by the Arp2/3 complex. *Cell* 133, 841-851.

Anderson TW, Vaughan AN, Cramer LP (2008) Retrograde flow and myosin II activity within the leading cell edge deliver F-actin to the lamella to seed the formation of graded polarity actomyosin II filament bundles in migrating fibroblasts. *Mol Biol Cell* 19, 5006-5018.

Applewhite DA, Barzik M, Kojima S, Svitkina TM, Gertler FB, Borisy GG (2007) Ena/VASP proteins have an anti-capping independent function in filopodia formation. *Mol Biol Cell* 18, 2579-2591.

Arai Y, Yasuda R, Akashi K, Harada Y, Miyata H, Kinosita K Jr, Itoh H (1999) Tying a molecular knot with optical tweezers. *Nature* 399, 446-448.

Aratyn YS, Schaus TE, Taylor EW, Borisy GG (2007) Intrinsic dynamic behavior of fascin in filopodia. *Mol Biol Cell* 18, 3928-3940.

Aratyn-Schaus Y, Oakes PW, Gardel ML (2011) Dynamic and structural signatures of lamellar actomyosin force generation. *Mol Biol Cell* 22, 1330-9.

Atilgan E, Wirtz D, Sun SX (2006) Mechanics and dynamics of actin-driven thin membrane protrusions. *Biophys J* 90, 65-76.

Balaban NQ, Schwarz US, Riveline D, Goichberg P, Tzur G, Sabanay I, Mahalu D, Safran S, Bershadsky A, Addadi L, Geiger B (2001) Force and focal adhesion assembly: a close relationship studied using elastic micropatterned substrates. *Nat Cell Biol* 3, 466-472.

Bendix PM, Koenderink GH, Cuvelier D, Dogic Z, Koeleman BN, Brieher WM, Field CM, Mahadevan L, Weitz DA (2008) A Quantitative Analysis of Contractility in Active Cytoskeletal Protein Networks. *Biophysical Journal* 94, 3126-3136.

Block J, Stradal TEB, Hanisch J, Geffers R, Kostler SA, Urban E, Small JV, Rottner K, Faix J (2008) Filopodia formation induced by active mDia2/Drf3. *J Microsc* 231, 506-517.

Brangwynne CP, Koenderink GH, Barry E, Dogic Z, MacKintosh FC, Weitz DA (2007) Bending Dynamics of Fluctuating Biopolymers Probed by Automated High-Resolution Filament Tracking. *Biophys J* 93, 346-359.

Breitsprecher D, Koestler SA, Chizhov I, Nemethova M, Mueller J, Goode BL, Small JV, Rottner K, Faix J (2011) Cofilin cooperates with fascin to disassemble filopodial actin filaments. *J Cell Sci* 124, 3305-3318.

Cai Y, Rossier O, Gauthier NC, Biais N, Fardin M, Zhang X, Miller LW, Ladoux B, Cornish VW, Sheetz MP (2010) Cytoskeletal coherence requires myosin-IIA contractility. *J Cell Sci* 123, 413-423.

Chan CE, Odde DJ (2008) Traction dynamics of filopodia on compliant substrates. *Science* 322, 1687-1691.

Chaudhuri O, Parekh SH, Fletcher DA (2007) Reversible stress softening of actin networks. *Nature* 445, 295-298.

Chhabra ES, Higgs HN (2007) The many faces of actin: matching assembly factors with cellular structures. *Nat Cell Biol* 9, 1110-1121.

Claessens MMAE, Bathe M, Frey E, Bausch AR (2006) Actin-binding proteins sensitively mediate F-actin bundle stiffness. *Nat Mater* 5, 748-753.

Claessens MMAE, Semmrich C, Ramos L, Bausch AR (2008) Helical twist controls the thickness of F-actin bundles. *Proc Natl Acad Sci U S A* 105, 8819-8822.

Courson DS, Rock RS (2010) Actin cross-link assembly and disassembly mechanics for alpha-Actinin and fascin. *J Biol Chem* 285, 26350-26357.

Cramer LP, Siebert M, Mitchison TJ (1997) Identification of novel graded polarity actin filament bundles in locomoting heart fibroblasts: implications for the generation of motile force. *J Cell Biol* 136, 1287-1305.

Dasanayake NL, Michalski PJ, Carlsson AE (2011) General mechanism of actomyosin contractility. *Phys Rev Lett* 107, 118101.

Davenport RW, Dou P, Mills LR, Kater SB (1996) Distinct calcium signaling within neuronal growth cones and filopodia. *J Neurobiol* 31, 1-15.

Davenport RW, Dou P, Rehder V, Kater SB (1993) A sensory role for neuronal growth cone filopodia. *Nature* 361, 721-724.

Deguchi S, Ohashi T, Sato M (2006) Tensile properties of single stress fibers isolated from cultured vascular smooth muscle cells. *J Biomech* 39, 2603-2610.

Dent EW, Tang F, Kalil K (2003) Axon guidance by growth cones and branches: common cytoskeletal and signaling mechanisms. *Neuroscientist* 9, 343-353.

Ferrer JM, Lee H, Chen J, Pelz B, Nakamura F, Kamm RD, Lang MJ (2008) Measuring molecular rupture forces between single actin filaments and actin-binding proteins.. *Proc Natl Acad Sci U S A* 105, 9221-9226.

Finer JT, Simmons RM, Spudich JA (1994) Single myosin molecule mechanics: piconewton forces and nanometre steps. *Nature* 368, 113-119.

Fujii T, Iwane AH, Yanagida T, Namba K (2010) Direct visualization of secondary structures of F-actin by electron cryomicroscopy. *Nature* 467, 724-728.

Galkin VE, Orlova A, Egelman EH (2012) Actin filaments as tension sensors. *Curr Biol* 22, R96-R101.

Gallo G, Letourneau PC (2004) Regulation of growth cone actin filaments by guidance cues. *J Neurobiol* 58, 92-102.

Gittes F, Mickey B, Nettleton J, Howard J (1993) Flexural rigidity of microtubules and actin filaments measured from thermal fluctuations in shape. *J Cell Biol* 120, 923-934.

Goley ED, Welch MD (2006) The ARP2/3 complex: an actin nucleator comes of age. *Nat Rev Mol Cell Biol* 7, 713-726.

Gupton SL, Gertler FB (2007) Filopodia: the fingers that do the walking. *Sci STKE* 2007, re5.

Haviv L, Brill-Karniely Y, Mahaffy R, Backouche F, Ben-Shaul A, Pollard TD, Bernheim-Groswasser A (2006) Reconstitution of the transition from lamellipodium to filopodium in a membrane-free system. *Proc Natl Acad Sci U S A* 103, 4906-4911.

Hayakawa K, Tatsumi H, Sokabe M (2011) Actin filaments function as a tension sensor by tension-dependent binding of cofilin to the filament. *J Cell Biol* 195, 721-727.

Heussinger C, Grason GM (2011) Theory of crosslinked bundles of helical filaments: intrinsic torques in self-limiting biopolymer assemblies. *J Chem Phys* 135, 035104.

Heussinger C, Schuller F, Frey E (2010) Statics and dynamics of the wormlike bundle model. *Phys Rev E Stat Nonlin Soft Matter Phys* 81, 021904.

Higgs HN (2011) Discussing the morphology of actin filaments in lamellipodia. *Trends Cell Biol* 21, 2-4.

Holmes KC, Popp D, Gebhard W, Kabsch W (1990) Atomic model of the actin filament. *Nature* 347, 44-49.

Howard J (2001) Mechanics of motor proteins and the cytoskeleton. Sunderland, Mass.: Sinauer Associates, Inc.

Insall RH (2011) Dogma bites back-the evidence for branched actin. *Trends Cell Biol* 21, 2.

Isambert H, Venier P, Maggs AC, Fattoum A, Kassab R, Pantaloni D, Carlier MF (1995) Flexibility of actin filaments derived from thermal fluctuations. Effect of bound nucleotide, phalloidin, and muscle regulatory proteins. *J Biol Chem* 270, 11437-11444.

Iwasa JH, Mullins RD (2007) Spatial and Temporal Relationships between Actin-Filament Nucleation, Capping, and Disassembly. *Current Biology* 17, 395 - 406.

Jansen S, Collins A, Yang C, Rebowski G, Svitkina T, Dominguez R (2011) Mechanism of actin filament bundling by fascin. *J Biol Chem* 286, 30087-30096.

Koenderink GH, Dogic Z, Nakamura F, Bendix PM, MacKintosh FC, Hartwig JH, Stossel TP, Weitz DA (2009) An active biopolymer network controlled by molecular motors. *Proc Natl Acad Sci U S A* 106, 15192-15197.

Koestler SA, Auinger S, Vinzenz M, Rottner K, Small JV (2008) Differentially oriented populations of actin filaments generated in lamellipodia collaborate in pushing and pausing at the cell front. *Nat Cell Biol* 10, 306-313.

Lieleg O, Claessens MMAE, Heussinger C, Frey E, Bausch AR (2007) Mechanics of bundled semiflexible polymer networks. *Phys Rev Lett* 99, 088102.

Lin J, Persson F, Fritzsche J, Tegenfeldt J, Saleh O (2012) Bandpass Filtering of DNA Elastic Modes Using Confinement and Tension. *Biophysical Journal* 102, 96 - 100.

Liu AP, Richmond DL, Maibaum L, Pronk S, Geissler PL, Fletcher DA (2008) Membrane-induced bundling of actin filaments. *Nat Phys* 4, 789-793.

Machesky LM, Li A (2010) Fascin: Invasive filopodia promoting metastasis. *Commun Integr Biol* 3, 263-270.

McGough A, Pope B, Chiu W, Weeds A (1997) Cofilin changes the twist of F-actin: implications for actin filament dynamics and cellular function. *J Cell Biol* 138, 771-781.

Medalia O, Beck M, Ecke M, Weber I, Neujahr R, Baumeister W, Gerisch G (2007) Organization of actin networks in intact filopodia. *Curr Biol* 17, 79-84.

Mejillano MR, Kojima S, Applewhite DA, Gertler FB, Svitkina TM, Borisy GG (2004) Lamellipodial versus filopodial mode of the actin nanomachinery: pivotal role of the filament barbed end. *Cell* 118, 363-373.

Mellor H (2010) The role of formins in filopodia formation.. *Biochim Biophys Acta* 1803, 191-200.

Michelot A, Drubin DG (2011) Building distinct actin filament networks in a common cytoplasm. *Curr Biol* 21, R560-R569.

Miller CJ, Bard Ermentrout G, Davidson LA (2012) Rotational model for actin filament alignment by myosin. *J Theor Biol* 300, 344-359.

Mogilner A, Rubinstein B (2005) The Physics of Filopodial Protrusion. *Biophys J* 89, 782-795.

Nagy S, Ricca BL, Norstrom MF, Courson DS, Brawley CM, Smithback PA, Rock RS (2008) A myosin motor that selects bundled actin for motility. *Proc Natl Acad Sci U S A* 105, 9616-9620.

Nemethova M, Auinger S, Small JV (2008) Building the actin cytoskeleton: filopodia contribute to the construction of contractile bundles in the lamella.. *J Cell Biol* 180, 1233-1244.

Nicholson-Dykstra SM, Higgs HN (2008) Arp2 depletion inhibits sheet-like protrusions but not linear protrusions of fibroblasts and lymphocytes. *Cell Motil Cytoskeleton* 65, 904-922.

Oda T, Iwasa M, Aihara T, Maeda Y, Narita A (2009) The nature of the globular- to fibrous-actin transition. *Nature* 457, 441-445.

Oda T, Maeda Y (2010) Multiple Conformations of F-actin. *Structure* 18, 761-767.

Oda T, Makino K, Yamashita I, Namba K, Maeda Y (1998) Effect of the length and effective diameter of F-actin on the filament orientation in liquid crystalline sols measured by x-ray fiber diffraction. *Biophys J* 75, 2672-2681.

Ott A, Magnasco M, Simon A, Libchaber A (1993) Measurement of the persistence length of polymerized actin using fluorescence microscopy. *Phys Rev E Stat Phys Plasmas Fluids Relat Interdiscip Topics* 48, R1642-R1645.

Parekh SH, Chaudhuri O, Theriot JA, Fletcher DA (2005) Loading history determines the velocity of actin-network growth. *Nat Cell Biol* 7, 1219-1223.

Pollitt AY, Insall RH (2009) WASP and SCAR/WAVE proteins: the drivers of actin assembly. *J Cell Sci* 122, 2575-2578.

Ponti A, Machacek M, Gupton SL, Waterman-Storer CM, Danuser G (2004) Two distinct actin networks drive the protrusion of migrating cells. *Science* 305, 1782-1786.

Prochniewicz E, Janson N, Thomas DD, De la Cruz EM (2005) Cofilin increases the torsional flexibility and dynamics of actin filaments. *J Mol Biol* 353, 990-1000.

Pronk S, Geissler PL, Fletcher DA (2008) Limits of filopodium stability. *Phys Rev Lett* 100, 258102.

Radmacher M, Fritz M, Cleveland JP, Walters DA, Hansma PK (1994) Imaging adhesion forces and elasticity of lysozyme adsorbed on mica with the atomic force microscope. *Langmuir* 10, 3809-3814.

Raich WB, Agbunag C, Hardin J (1999) Rapid epithelial-sheet sealing in the Caenorhabditis elegans embryo requires cadherin-dependent filopodial priming. *Curr Biol* 9, 1139-1146.

Rappaport SM, Medalion S, Rabin Y (2008) Curvature Distribution of Worm-like Chains in Two and Three Dimensions. *arXiv:0801.3183v1 [cond-mat.soft]* , .

Ricca BL, Rock RS (2010) The stepping pattern of myosin X is adapted for processive motility on bundled actin. *Biophys J* 99, 1818-1826.

Risca VI, Wang EB, Chaudhuri O, Chia JJ, Geissler PL, Fletcher DA (2012) Actin filament curvature biases branching direction. *Proc Natl Acad Sci U S A* 109, 2913-2918.

Schlierf M, Rief M (2005) Temperature softening of a protein in single-molecule experiments. *J Mol Biol* 354, 497-503.

Schmid MF, Sherman MB, Matsudaira P, Chiu W (2004) Structure of the acrosomal bundle. *Nature* 431, 104-107.

Sheetz MP, Wayne DB, Pearlman AL (1992) Extension of filopodia by motor-dependent actin assembly. *Cell Motil Cytoskeleton* 22, 160-169.

Shin H, Purdy Drew KR, Bartles JR, Wong GCL, Grason GM (2009) Cooperativity and frustration in protein-mediated parallel actin bundles. *Phys Rev Lett* 103, 238102.

Sinard JH, Stafford WF, Pollard TD (1989) The mechanism of assembly of Acanthamoeba myosin-II minifilaments: minifilaments assemble by three successive dimerization steps.. *The Journal of Cell Biology* 109, 1537-1547.

Small JV (2010) Dicing with dogma: de-branching the lamellipodium.. *Trends Cell Biol* 20, 628-633.

Small JV (2011) Actin networking in lamellipodia and beyond. *Trends in Cell Biology* 21, 4 - 5.

Small JV, Winkler C, Vinzenz M, Schmeiser C (2011) Reply: Visualizing branched actin filaments in lamellipodia by electron tomography. *Nat Cell Biol* 13, 1013-1014.

Stokes DL, DeRosier DJ (1991) Growth conditions control the size and order of actin bundles in vitro. *Biophys J* 59, 456-465.

Sugita S, Adachi T, Ueki Y, Sato M (2011) A novel method for measuring tension generated in stress fibers by applying external forces. *Biophys J* 101, 53-60.

Sukumvanich P, DesMarais V, Sarmiento CV, Wang Y, Ichetovkin I, Mouneimne G, Almo S, Condeelis J (2004) Cellular localization of activated N-WASP using a conformation-sensitive antibody.. *Cell Motil Cytoskeleton* 59, 141-152.

Svitkina TM, Borisy GG (1999) Arp2/3 complex and actin depolymerizing factor/cofilin in dendritic organization and treadmilling of actin filament array in lamellipodia. *J Cell Biol* 145, 1009-1026.

Svitkina TM, Bulanova EA, Chaga OY, Vignjevic DM, Kojima S, Vasiliev JM, Borisy GG (2003) Mechanism of filopodia initiation by reorganization of a dendritic network. *J Cell Biol* 160, 409-421.

Svitkina TM, Verkhovsky AB, McQuade KM, Borisy GG (1997) Analysis of the actin-myosin II system in fish epidermal keratocytes: mechanism of cell body translocation. *J Cell Biol* 139, 397-415.

Tan JL, Tien J, Pirone DM, Gray DS, Bhadriraju K, Chen CS (2003) Cells lying on a bed of microneedles: an approach to isolate mechanical force. *Proc Natl Acad Sci U S A* 100, 1484-1489.

Tsuda Y, Yasutake H, Ishijima A, Yanagida T (1996) Torsional rigidity of single actin filaments and actin-actin bond breaking force under torsion measured directly by in vitro micromanipulation.. *Proc Natl Acad Sci U S A* 93, 12937-12942.

Ullner M, Staikos G, Theodorou DN (1998) Monte Carlo Simulations of a Single Polyelectrolyte in Solution:Activity Coefficients of the Simple Ions and Application to Viscosity Measurements. *Macromolecules* 31, 7921-7933.

Urban E, Jacob S, Nemethova M, Resch GP, Small JV (2010) Electron tomography reveals unbranched networks of actin filaments in lamellipodia. *Nat Cell Biol* 12, 429-435.

Uyeda TQP, Iwadate Y, Umeki N, Nagasaki A, Yumura S (2011) Stretching actin filaments within cells enhances their affinity for the myosin II motor domain. *PLoS One* 6, e26200.

Verkhovsky AB, Borisy GG (1993) Non-sarcomeric mode of myosin II organization in the fibroblast lamellum. *J Cell Biol* 123, 637-652.

Verkhovsky AB, Chaga OY, Schaub S, Svitkina TM, Meister J, Borisy GG (2003) Orientational order of the lamellipodial actin network as demonstrated in living motile cells. *Mol Biol Cell* 14, 4667-4675.

Vicente-Manzanares M, Ma X, Adelstein RS, Horwitz AR (2009) Non-muscle myosin II takes centre stage in cell adhesion and migration.. *Nat Rev Mol Cell Biol* 10, 778-790.

Vignjevic D, Kojima S, Aratyn Y, Danciu O, Svitkina T, Borisy GG (2006) Role of fascin in filopodial protrusion. *J Cell Biol* 174, 863-875.

Vignjevic D, Yarar D, Welch MD, Peloquin J, Svitkina T, Borisy GG (2003) Formation of filopodia-like bundles in vitro from a dendritic network. *J Cell Biol* 160, 951-962.

Vinzenz M, Nemethova M, Schur F, Mueller J, Narita A, Urban E, Winkler C, Schmeiser C, Koestler SA, Rottner K, Resch GP, Maeda Y, Small JV (2012) Actin branching in the initiation and maintenance of lamellipodia. *J Cell Sci,* Advance Online Publication, March 19, 2012, doi:10.1242/jcs.107623.

Volkmann N, DeRosier D, Matsudaira P, Hanein D (2001) An atomic model of actin filaments cross-linked by fimbrin and its implications for bundle assembly and function.. *J Cell Biol* 153, 947-956.

Wood W, Martin P (2002) Structures in focus--filopodia. *Int J Biochem Cell Biol* 34, 726-730.

Wu C, Asokan S, Berginski M, Haynes E, Sharpless N, Griffith J, Gomez S, Bear J (2012) Arp2/3 Is Critical for Lamellipodia and Response to Extracellular Matrix Cues but Is Dispensable for Chemotaxis. *Cell* 148, 973-987.

Yang C, Svitkina T (2011) Visualizing branched actin filaments in lamellipodia by electron tomography. *Nat Cell Biol* 13, 1012-1013.

Yang C, Svitkina T (2011) Filopodia initiation: focus on the Arp2/3 complex and formins.. *Cell Adh Migr* 5, 402-408.

Zaccai G (2000) How soft is a protein? A protein dynamics force constant measured by neutron scattering. *Science* 288, 1604-1607.

Zheng JQ, Wan JJ, Poo MM (1996) Essential role of filopodia in chemotropic turning of nerve growth cone induced by a glutamate gradient. *J Neurosci* 16, 1140-1149.

van Mameren J, Vermeulen KC, Gittes F, Schmidt CF (2009) Leveraging single protein polymers to measure flexural rigidity. *J Phys Chem B* 113, 3837-3844.

Chapter 5. Conclusions and outlook for studies on mechanical modulation of F-actin structure and function

Implications of curvature sensitivity of the Arp2/3 complex

Using a branching assay in which mother filaments are immobilized and their curvature can be measured at branch points, we have shown that dendritic nucleation by the Arp2/3 complex is biased by filament curvature (Risca et al., 2012). The amount of bias depends on the filament's curvature, and for radii of curvature of 1 μm, approximately doubles the density of branches on the convex side of a filament as compared to the density on the concave side of the filament. In vivo, this mechanism may contribute to the orientation of dendritic network barbed ends toward cellular membranes and the compressive forces that the membranes apply to the actin network. It may also contribute to the set of biochemical reactions that give rise to load-independent network velocities observed under high forces in vivo (Prass et al., 2006) and in vitro (Parekh et al., 2005), and are explained by a rate of barbed end creation that depends on the number of filaments in a narrow branching zone in the autocatalytic model of actin network growth (Carlsson, 2003).

In the context of dendritic networks in vivo, there is an additional implication of the branching bias we observed. The amount of branching to be expected in the membrane plane and out of the membrane plane is approximately equal, but the face of the filament with the highest likelihood of branching is the convex one, which would give rise to branches that lie in the plane of the membrane. This would certainly hold for any branching that may happen in the lamella. However, the membrane association is probably established somewhere in the lamellipodium, so a planar bias in branching there can also work to establish or maintain the planar nature of the membrane-associated actin network. Recent super-resolution images of flat and thin lamellipodia in live BSC-1 epithelial cells show that most of the actin density is closely associated with the dorsal and ventral membranes, to within ~1 μm or less of the leading edge (Xu et al., 2012). COS-7 fibroblast cells also appeared to have similar leading edge actin morphology. This data, while not conclusive because of possible imaging artifacts, strongly suggests that most of the large-scale curvature behind the very front of the leading edge would occur in the plane of the membranes. It supports the idea that the branching bias may help orient dendritic networks into a quasi-two-dimensional geometry.

An important question about the branching bias is the extent to which it exists in vivo, and whether it can be directly observed to play a role. Bending energy considerations discussed in Chapter 3 suggests that it is reasonable to believe that the free barbed ends of actin filaments in the network can be bent by typical forces exerted by the membrane. Several experiments, including recent work on a neutrophil-like cell line, show that membrane tension plays an important role in modulating protrusion (Houk et al., 2012; Raucher & Sheetz, 2000). It may be that the branching bias serves to orient branched networks at low membrane resistance, helps reinforce them as new daughter filaments growing toward the load branch from old mother filaments that have been bent away from the load by intermediate membrane resistance forces, and lastly, can be overcome by large membrane tensions that stall polymerization.

As with many mechanisms isolated in vitro, it is likely difficult to disentangle its effects from those of other biochemical reactions and mechanical or geometric effects acting at the same time in the very complex cellular environment (Svitkina & Borisy, 1999). However, the extent of

bending in very close proximity to the membrane, where branch nucleation occurs, may be possible to discern using cryoelectron tomography in samples with good preservation of the membrane. Cryotomograms of 4.8 nm thick sections of the ~600 nm closest to the leading edge of a vitreously frozen goldfish fibroblast qualitatively show that the ends of some filaments are slightly curved (Urban et al., 2010). Estimation of the projected two-dimensional curvature of these filaments from the published images yields values of ~1 μm^{-1}. Although Urban et al. stated that they found few branch points in lamellipodial actin networks, a subsequent reanalysis and follow-up experiments using negative stain did indicate the presence of branches (Vinzenz et al., 2012). Most high-resolution electron microscopy studies of actin networks of the leading edge have used either a platinum replica method or negative staining. In either case, the cells must be fixed and permeabilized and the membrane is not preserved well, so the curvature of filaments that are normally bent by the membrane cannot be relied on. More cryoelectron tomogram data of vitrified samples, with quantitative analysis of three dimensional filament curvature should be sufficient to at least lead to a prediction of the magnitude of the branching bias expected in vivo.

As the sophistication and molecular and mechanical detail incorporated in models of dendritic nucleation increases (Carlsson, 2010), another way to test whether our results are important in vivo is to build the curvature-mediated branching bias into a model that incorporates the elasticity of F-actin with explicit nucleation of new branches. Although this is not currently feasible due to the vast difference in time scales between small-length-scale bending fluctuations and actin polymerization, it may be possible to approximate the shape of filaments under certain force constraints. Comparing the results of such a simulation with and without the branching bias with the observed behavior of real dendritic networks in vivo or in a reconstituted system in vitro may reveal whether the branching bias plays a significant role in dendritic network regulation.

What other ABPs sense the mechanical state of F-actin?

Recently published work shows that the Arp2/3 complex is not unique in its sensitivity to F-actin curvature. There is strong evidence that the ADF/cofilin family proteins respond to the mechanical state of F-actin. They introduce a large structural transition in F-actin upon binding, overtwisting the two protofilaments by 10° per monomer (Galkin et al., 2011; McGough et al., 1997) and reducing the persistence length of the filament by ~5 fold (McCullough et al., 2008; Orlova & Egelman, 1993). The binding of cofilin to F-actin is slow, and believed to require "breathing" motions of the filament, most likely consisting of torsional fluctuations (Cao et al., 2006). Binding is also cooperative, but cofilins bound to adjacent actin monomers in the filament do not contact each other, indicating that cooperativity is mediated through structural changes in the filament (Cao et al., 2006; Galkin et al., 2011).

It has been observed that the "zippering" into bundles of actin filaments nucleated by formins, which presumably restricts bending and twisting fluctuations, protects the filaments from severing by ADF/cofilin (Michelot et al., 2007; Michelot et al., 2006). Similarly, a plant villin (which does not sever) bundles actin filaments and protects them from ADF/cofilin severing, although this protection may be due to the fact that ADF and the villin compete for actin binding (Huang et al., 2005). In apparent opposition to these observations, actin bundled by the crosslinker fascin permits cofilin binding and is in fact more efficiently severed (Breitsprecher et al., 2011). This enhanced severing is consistent with a demonstration that restriction of F-actin

torsional and bending relaxation by multiple attachment points on a surface reduces the ability of cofilin to sever F-actin (Pavlov et al., 2007). Lastly, in the most direct demonstration of mechanosensing by cofilin, Hayakawa et al. demonstrated that the application of tension to actin reduced both binding and overall severing activity of cofilin (Hayakawa et al., 2011).

Tropomyosins are an interesting example, because they alter the persistence length of F-actin (Isambert et al., 1995) and exhibit strongly cooperative binding, but at the same time, are rather loosely coupled to the actin filament itself. The radius at which tropomyosin density is found in the decorated tropomyosin-F-actin fiber is large, precluding tight binding (Holmes & Lehman, 2008). Muscle tropomyosin also shifts its position azimuthally along the actin fiber, suggesting a weak interaction with the actin surface. A "Gestalt" binding hypothesis has been proposed for the tropomyosin-F-actin interaction, which states that the affinity of tropomyosin for F-actin is largely due to the high degree of shape complementarity between the ~40 nm long tropomyosin molecule and the F-actin helix (Holmes & Lehman, 2008). This affinity, which is nevertheless quite weak, is bolstered by cooperativity based on head-to-tail interactions between tropomyosin molecules (Hitchcock-DeGregori et al., 2007; Holmes & Lehman, 2008). Therefore, tropomyosins could be said to act in parallel with the actin filament, as opposed to cofilins, which act through the actin filament.

From this "Gestalt" hypothesis, the question that arises in the mechanical context is, what degree of distortion of F-actin is necessary to disrupt the shape complementarity with tropomyosin? The answer depends on the flexibility of tropomyosin, a quantity that has been the subject of debate. Singh et al. have used a mutational approach with fluorescence measurements, circular dichroism and differential scanning calorimetry to show that repeating alanine-rich clusters destabilize the tropomyosin coiled-coil, and proposed that these alanine clusters create regions of high flexibility in the coiled coil by creating a local axial staggering of residues, allowing tropomyosin to wrap around F-actin (Singh & Hitchcock-DeGregori, 2003; Singh & Hitchcock-DeGregori, 2006). This would suggest that tropomyosin is flexible enough to rearrange and accommodate mechanically induced distortions in the F-actin helix, and its affinity for actin should be largely insensitive to F-actin bending, especially when multiple interacting tropomyosins are engaged in cooperative binding. The increased persistence length of the tropomyosin-actin filament may simply be due to its larger thickness as compared to that of F-actin alone.

However, more recent studies combining electron microscopy and molecular dynamics simulations of tropomyosin have provided evidence that tropomyosin has an intrinsic curvature that, although modulated along the coiled coil, does not coincide with the alanine-rich clusters, creating a more or less smooth profile that matches the turn of the F-actin helix (Li et al., 2010; Li et al., 2010; Li et al., 2010). The same studies have also indicated that the dynamic persistence length (which corresponds to the fluctuation-based persistence length defined for F-actin in earlier chapters) of tropomyosin is ~500 nm, significantly larger than previously thought. When the same analysis was applied to the alanine mutants used by Singh et al., the average curvature of tropomyosin changed. This data lends support to the Gestalt binding model, because it suggests that tropomyosin's shape, not its flexibility determine how it interacts with actin (Holmes & Lehman, 2008). It also suggests that the interaction between tropomyosin and F-actin may be more brittle than previously suggested, leading mechanical perturbation of the actin

filament to cause a shape mismatch that would lower the affinity of tropomyosin for actin. This effect may be particularly strong for mechanical twisting of F-actin that changes the pitch of the helix.

Myosin II also binds Ca^{2+}-F-actin cooperatively (Orlova & Egelman, 1997) and, as a high-affinity-binding mutant tagged with GFP and expressed in cells, has been shown to bind more strongly to actin filaments tensed by application of force to the cortical actin network of the cell by aspiration (Uyeda et al., 2011).

Lastly, the ABP drebrin, a neuronal protein that localizes to dendritic spines, has been shown to increase the persistence length and increses the helical pitch of F-actin upon binding (Sharma et al., 2011). The details of the drebrin-F-actin interaction remain to be characterized in detail, and it may be that that the increase in persistence length is only due to the increased thickness of the drebrin-actin filament, as may be the case for tropomyosin-actin. However, this evidence, and the change in twist in particular, does suggest that drebrin may induce structural changes upon binding, and therefore bind more readily to filaments that are distorted in the same way by force.

How do mechanical perturbations affect the structure of F-actin?

An important outstanding question that is raised by our findings regarding Arp2/3 branch nucleation and by the diversity of forces present in the cell is: how do mechanical perturbations, such as a constraint on the shape of a filament or the force produced by a myosin motor, affect the structure of F-actin? The structure of F-actin includes its average helical arrangement as well as the variance and nature of fluctuations around that average. This question is not only important for the mechanism underlying the curvature-induced branching bias, but is also relevant to any other biochemical interaction between an ABP and F-actin that depends on the mechanical state of the filament.

The best-characterized effects of force on F-actin occur when actin filaments are constrained by crosslinks. A structure of the scruin-actin bundle has shown large deformations, including asymmetric deformations in the two protofilaments of F-actin, that are required to pack it into a crystalline lattice (Schmid et al., 2004). Packing filaments into counterion-crosslinked paracrystals increases their average twist and lowers the amount of disorder in the azimuthal rotation angle between monomers (Orlova & Egelman, 2000). Fascin and espin crosslinks also over-twist in bundled filaments (Claessens et al., 2008; Shin & Grason, 2010; Shin et al., 2009).

The only experiment in the literature in which torque was imposed actively rather than by locking in fluctuations of the filament was done by Tsuda et al. (Tsuda et al., 1996). Although it does not present direct structural evidence, this experiment showed that the tensile strength of F-actin is decreased with even small amounts of torsional stress, suggesting that torsional stress destabilizes F-actin. Surprisingly, both over-twist and under-twist appeared to have the same effect on the tensile strength.

Several recent studies, reviewed by Galkin et al. (Galkin et al., 2012), give clues about the ways in which F-actin structure changes under tension or lateral compression. Most notably, a recent, high-resolution cryoelectron microscopy structure of F-actin was obtained from filaments

prepared in very thin films and straightened by fluid flow prior to vitrification, potentially subjecting them to very large forces (Fujii et al., 2010). In this structure, filaments were highly ordered, with a very low angular disorder (1˚, as opposed to the ~6˚ found by previous studies (Egelman et al., 1982; Egelman et al., 1983)), and the DNAse I binding loop adopted a well-ordered conformation, which is consistent with data showing that disorder in the DNAse I binding loop of subdomain 2 correlates with reduced F-actin rigidity (Orlova & Egelman, 1993). Similar apparent stiffening was observed by Greene et al., in an experiment that compressed F-actin between two mica surfaces and measured its mechanical response (Greene et al., 2009). These observed changes in F-actin structure in response to tension or compression are corroborated by observed changes in the fluorescence of tetramethylrhodamine-labeled F-actin under tension (Shimozawa & Ishiwata, 2009), and by changes in the binding of cofilin (Hayakawa et al., 2011) and myosin to tensed actin filaments (Uyeda et al., 2011), as well as by our observation that bending F-actin biases branch nucleation (Risca et al., 2012). In muscle, x-ray diffraction has probed the helical symmetry of F-actin under tension and found that large forces stretch F-actin ~0.2%, with commensurate small changes in twist, but otherwise, the F-actin structure remains largely the same (Huxley et al., 1994; Wakabayashi et al., 1994).

A third set of evidence suggests that tension may affect the twist of F-actin. Hayakawa et al. observed a ~50% reduction in the torsional fluctuations of a filament under ~5 pN of tension relative to an untensed filament held with < 1 pN of tension (Hayakawa et al., 2011). To our knowledge, this is the only direct experimental evidence for twist-tension coupling (Gore et al., 2006; Lionnet et al., 2006) in F-actin, although it only points to a change in the torsional stiffness, not to a change in the average twist state. Steered molecular dynamics simulations of F-actin under a tension of 200 pN showed that the filament unwound by ~2˚ per monomer (Matsushita et al., 2011) (to be compared with a 5˚ overwinding upon cofilin binding (Galkin et al., 2011; McGough et al., 1997)). The same authors estimated the extension-torsion coupling coefficient for F-actin to be 7.6 x 10^{-11} N (Matsushita et al., 2012). Two mechanical models based on the shape of F-actin have also been developed (De La Cruz et al., 2010; Yamaoka & Adachi, 2010). Both predict unwinding under tension. Yamanoka et al. model the filament as a polymer with a helical centroid (Yamaoka & Adachi, 2010), while De La Cruz et al. focus on the two-protofilament structure, including explicit links between the two protofilaments, and predict a persistence length of 0.15-0.4 μm for the bend-twist coupling (De La Cruz et al., 2010). These models have not yet been adequately tested. Experiments to measure the tension-torsion coupling in F-actin, as well as its modulation by factors such as the bound divalent cation, nucleotide state, and phalloidin stabilization, are a logical next step in understanding the mechanical regulation of F-actin, especially because tension on F-actin is so common (Gardel et al., 2010), and twist state appears to be regulated by ABP binding (Galkin et al., 2011). Experimental geometries for measuring the coupling between tension and torsion have been worked out for DNA and may be applicable to F-actin with minor modifications, primarily in the mode of attachment of the actin filaments to beads (Bryant et al., 2003; Gore et al., 2006; Lionnet et al., 2006). One experiment already used to determine the torsional rigidity of F-actin could also be modified to measure the effect of tension on torsional fluctuations (Hayakawa et al., 2011; Tsuda et al., 1996).

Can we measure the mechanical state of F-actin in dendritic networks?

Recent advances in mechanobiology have led to the development of Förster resonant energy transfer (FRET) sensors that can be used to measure tension at certain connections among actin filaments and between actin filaments and other intracellular elements. They are based on the motor protein myosin (Iwai & Uyeda, 2008), the actin crosslinkers α-actinin (Meng & Sachs, 2011; Meng et al., 2011; Meng et al., 2008; Rahimzadeh et al., 2011) and filamin (Meng et al., 2011; Meng et al., 2008) and the focal adhesion protein vinculin (Grashoff et al., 2010). Rahimzadeh et al. have also interpreted their results as evidence for detection of network compression using an α-actinin FRET stress sensor (Rahimzadeh et al., 2011). These sensors may be used to detect or approximately measure tension or lack thereof in vivo, but their use is only appropriate for F-actin networks that normally couple to the ABPs that the sensors are composed of. A more direct method for measuring tension in F-actin which shows promise was described by Uyeda et al., using a mutant myosin that remains bound to F-actin and is tagged with GFP. This probe has been shown to preferentially bind to actin filaments under tension (Uyeda et al., 2011).

To measure compressive forces or torques acting on F-actin or even delocalized tension in F-actin networks, new methodologies must be developed. The observation by Shimozawa et al. that the fluorescence of tetramethylrhodamine covalently linked to cysteine 374 of actin increases upon polymerization and decreases under tension (Shimozawa & Ishiwata, 2009), as well as the well-established pyrene assay (Cooper et al., 1983), suggest that it may be possible to find a fluorescent label for F-actin that is sensitive to particular conformational changes induced by force or torque. However, changes in fluorescence intensity do not offer a sufficient signal to noise ratio to be usable in cells, because cellular concentrations of actin are a few μM to hundreds of μM, depending on cell type (Pollard et al., 2000). Following the example used by Grashoff et al. for measurement of the FRET efficiency (Grashoff et al., 2010), it may be possible to use fluorescence lifetime of a covalently linked fluorophore as a force indicator, if force-induced changes in F-actin conformation sufficiently change the chemical environment of the fluorophore (Pereira et al., 2011; Wallrabe & Periasamy, 2005; Wang et al., 2008). This assay would be technically challenging, partly because it would likely require microinjection of labeled actin into cells, but mostly because it is not yet known whether a fluorophore that can be coupled to actin would exhibit the desired fluorescence properties. Genetically encoded fluorescent tags such as GFP would probably not interact closely enough with F-actin to report on its structural state, so chemical fluorescent tags must be used. Measurements of fluorescence lifetime as a function of F-actin bending for candidate covalently linked fluorophores could take advantage of the surface immobilization techniques described in Chapters 2 and 3, and could be calibrated in vitro.

Despite decades of intense study, many fascinating questions remain and new ones emerge about the mechanochemical regulation of the actin cytoskeleton, creating a perpetual need for novel experimental tools.

References

Breitsprecher D, Koestler SA, Chizhov I, Nemethova M, Mueller J, Goode BL, Small JV, Rottner K, Faix J (2011) Cofilin cooperates with fascin to disassemble filopodial actin filaments. *J Cell Sci* 124, 3305-3318.

Bryant Z, Stone MD, Gore J, Smith SB, Cozzarelli NR, Bustamante C (2003) Structural transitions and elasticity from torque measurements on DNA. *Nature* 424, 338-341.

Cao W, Goodarzi JP, De La Cruz EM (2006) Energetics and kinetics of cooperative cofilin-actin filament interactions. *J Mol Biol* 361, 257-267.

Carlsson AE (2003) Growth velocities of branched actin networks. *Biophys J* 84, 2907-2918.

Carlsson AE (2010) Actin dynamics: from nanoscale to microscale. *Annu Rev Biophys* 39, 91-110.

Claessens MMAE, Semmrich C, Ramos L, Bausch AR (2008) Helical twist controls the thickness of F-actin bundles. *Proc Natl Acad Sci U S A* 105, 8819-8822.

Cooper JA, Walker SB, Pollard TD (1983) Pyrene actin: documentation of the validity of a sensitive assay for actin polymerization. *J Muscle Res Cell Motil* 4, 253-262.

De La Cruz EM, Roland J, McCullough BR, Blanchoin L, Martiel J (2010) Origin of twist-bend coupling in actin filaments. *Biophys J* 99, 1852-1860.

Egelman EH, Francis N, DeRosier DJ (1982) F-actin is a helix with a random variable twist. *Nature* 298, 131-135.

Egelman EH, Francis N, DeRosier DJ (1983) Helical disorder and the filament structure of F-actin are elucidated by the angle-layered aggregate. *J Mol Biol* 166, 605-629.

Fujii T, Iwane AH, Yanagida T, Namba K (2010) Direct visualization of secondary structures of F-actin by electron cryomicroscopy. *Nature* 467, 724-728.

Galkin VE, Orlova A, Egelman EH (2012) Actin filaments as tension sensors. *Curr Biol* 22, R96-R101.

Galkin VE, Orlova A, Kudryashov DS, Solodukhin A, Reisler E, Schröder GF, Egelman EH (2011) Remodeling of actin filaments by ADF/cofilin proteins. *Proc Natl Acad Sci U S A* 108, 20568-20572.

Gardel ML, Schneider IC, Aratyn-Schaus Y, Waterman CM (2010) Mechanical integration of actin and adhesion dynamics in cell migration. *Annu Rev Cell Dev Biol* 26, 315-333.

Gore J, Bryant Z, Nöllmann M, Le MU, Cozzarelli NR, Bustamante C (2006) DNA overwinds when stretched. *Nature* 442, 836-839.

Grashoff C, Hoffman BD, Brenner MD, Zhou R, Parsons M, Yang MT, McLean MA, Sligar SG, Chen CS, Ha T, Schwartz MA (2010) Measuring mechanical tension across vinculin reveals regulation of focal adhesion dynamics. *Nature* 466, 263-166.

Greene GW, Anderson TH, Zeng H, Zappone B, Israelachvili JN (2009) Force amplification response of actin filaments under confined compression. *Proc Natl Acad Sci U S A* 106, 445-449.

Hayakawa K, Tatsumi H, Sokabe M (2011) Actin filaments function as a tension sensor by tension-dependent binding of cofilin to the filament. *J Cell Biol* 195, 721-727.

Hitchcock-DeGregori SE, Greenfield NJ, Singh A (2007) Tropomyosin: regulator of actin filaments. *Adv Exp Med Biol* 592, 87-97.

Holmes KC, Lehman W (2008) Gestalt-binding of tropomyosin to actin filaments. *J Muscle Res Cell Motil* 29, 213-219.

Houk AR, Jilkine A, Mejean CO, Boltyanskiy R, Dufresne ER, Angenent SB, Altschuler SJ, Wu LF, Weiner OD (2012) Membrane tension maintains cell polarity by confining signals to the leading edge during neutrophil migration. *Cell* 148, 175-188.

Huang S, Robinson RC, Gao LY, Matsumoto T, Brunet A, Blanchoin L, Staiger CJ (2005) Arabidopsis VILLIN1 Generates Actin Filament Cables That Are Resistant to Depolymerization. *The Plant Cell Online* 17, 486-501.

Huxley HE, Stewart A, Sosa H, Irving T (1994) X-ray diffraction measurements of the extensibility of actin and myosin filaments in contracting muscle. *Biophys J* 67, 2411-2421.

Isambert H, Venier P, Maggs AC, Fattoum A, Kassab R, Pantaloni D, Carlier MF (1995) Flexibility of actin filaments derived from thermal fluctuations. Effect of bound nucleotide, phalloidin, and muscle regulatory proteins. *J Biol Chem* 270, 11437-11444.

Iwai S, Uyeda TQP (2008) Visualizing myosin-actin interaction with a genetically-encoded fluorescent strain sensor. *Proc Natl Acad Sci U S A* 105, 16882-16887.

Li XE, Holmes KC, Lehman W, Jung H, Fischer S (2010) The shape and flexibility of tropomyosin coiled coils: implications for actin filament assembly and regulation. *J Mol Biol* 395, 327-339.

Li XE, Lehman W, Fischer S (2010) The relationship between curvature, flexibility and persistence length in the tropomyosin coiled-coil. *Journal of Structural Biology* 170, 313-318.

Li XE, Lehman W, Fischer S, Holmes KC (2010) Curvature variation along the tropomyosin molecule. *J Struct Biol* 170, 307-312.

Lionnet T, Joubaud S, Lavery R, Bensimon D, Croquette V (2006) Wringing Out DNA. *Phys. Rev. Lett.* 96, 178102.

Matsushita S, Inoue Y, Adachi T (2012) Quantitative analysis of extension-torsion coupling of actin filaments. *Biochem Biophys Res Commun* 420, 710-713.

Matsushita S, Inoue Y, Hojo M, Sokabe M, Adachi T (2011) Effect of tensile force on the mechanical behavior of actin filaments. *J Biomech* 44, 1776-1781.

McCullough BR, Blanchoin L, Martiel J, De la Cruz EM (2008) Cofilin increases the bending flexibility of actin filaments: implications for severing and cell mechanics. *J Mol Biol* 381, 550-558.

McGough A, Pope B, Chiu W, Weeds A (1997) Cofilin changes the twist of F-actin: implications for actin filament dynamics and cellular function. *J Cell Biol* 138, 771-781.

Meng F, Sachs F (2011) Visualizing dynamic cytoplasmic forces with a compliance-matched FRET sensor. *J Cell Sci* 124, 261-169.

Meng F, Suchyna TM, Lazakovitch E, Gronostajski RM, Sachs F (2011) Real Time FRET Based Detection of Mechanical Stress in Cytoskeletal and Extracellular Matrix Proteins. *Cell Mol Bioeng* 4, 148-159.

Meng F, Suchyna TM, Sachs F (2008) A fluorescence energy transfer-based mechanical stress sensor for specific proteins in situ. *FEBS J* 275, 3072-3087.

Michelot A, Berro J, Guérin C, Boujemaa-Paterski R, Staiger CJ, Martiel J, Blanchoin L (2007) Actin-filament stochastic dynamics mediated by ADF/cofilin. *Curr Biol* 17, 825-833.

Michelot A, Derivery E, Paterski-Boujemaa R, Guérin C, Huang S, Parcy F, Staiger CJ, Blanchoin L (2006) A novel mechanism for the formation of actin-filament bundles by a nonprocessive formin. *Curr Biol* 16, 1924-1930.

Orlova A, Egelman EH (1993) A conformational change in the actin subunit can change the flexibility of the actin filament. *J Mol Biol* 232, 334-341.

Orlova A, Egelman EH (1997) Cooperative rigor binding of myosin to actin is a function of F-actin structure. *J Mol Biol* 265, 469-474.

Orlova A, Egelman EH (2000) F-Actin Retains a Memory of Angular Order. *Biophysical Journal* 78, 2180 - 2185.

Parekh SH, Chaudhuri O, Theriot JA, Fletcher DA (2005) Loading history determines the velocity of actin-network growth. *Nat Cell Biol* 7, 1219-1223.

Pavlov D, Muhlrad A, Cooper J, Wear M, Reisler E (2007) Actin filament severing by cofilin. *J Mol Biol* 365, 1350-1358.

Pereira AM, Tudor C, Kanger JS, Subramaniam V, Martin-Blanco E (2011) Integrin-dependent activation of the JNK signaling pathway by mechanical stress. *PLoS One* 6, e26182.

Pollard TD, Blanchoin L, Mullins RD (2000) Molecular mechanisms controlling actin filament dynamics in nonmuscle cells. *Annu Rev Biophys Biomol Struct* 29, 545-576.

Prass M, Jacobson K, Mogilner A, Radmacher M (2006) Direct measurement of the lamellipodial protrusive force in a migrating cell. *J Cell Biol* 174, 767-772.

Rahimzadeh J, Meng F, Sachs F, Wang J, Verma D, Hua SZ (2011) Real-time observation of flow-induced cytoskeletal stress in living cells. *Am J Physiol Cell Physiol* 301, C646-C652.

Raucher D, Sheetz MP (2000) Cell spreading and lamellipodial extension rate is regulated by membrane tension. *J Cell Biol* 148, 127-136.

Risca VI, Wang EB, Chaudhuri O, Chia JJ, Geissler PL, Fletcher DA (2012) Actin filament curvature biases branching direction. *Proc Natl Acad Sci U S A* 109, 2913-2918.

Schmid MF, Sherman MB, Matsudaira P, Chiu W (2004) Structure of the acrosomal bundle. *Nature* 431, 104-107.

Sharma S, Grintsevich EE, Phillips ML, Reisler E, Gimzewski JK (2011) Atomic force microscopy reveals drebrin induced remodeling of f-actin with subnanometer resolution. *Nano Lett* 11, 825-827.

Shimozawa T, Ishiwata S (2009) Mechanical Distortion of Single Actin Filaments Induced by External Force: Detection by Fluorescence Imaging. *Biophysical Journal* 96, 1036-1044.

Shin H, Grason GM (2010) Structural reorganization of parallel actin bundles by crosslinking proteins: incommensurate states of twist. *Phys Rev E Stat Nonlin Soft Matter Phys* 82, 051919.

Shin H, Purdy Drew KR, Bartles JR, Wong GCL, Grason GM (2009) Cooperativity and frustration in protein-mediated parallel actin bundles. *Phys Rev Lett* 103, 238102.

Singh A, Hitchcock-DeGregori SE (2003) Local destabilization of the tropomyosin coiled coil gives the molecular flexibility required for actin binding. *Biochemistry* 42, 14114-14121.

Singh A, Hitchcock-DeGregori SE (2006) Dual requirement for flexibility and specificity for binding of the coiled-coil tropomyosin to its target, actin. *Structure* 14, 43-50.

Svitkina TM, Borisy GG (1999) Progress in protrusion: the tell-tale scar. *Trends Biochem Sci* 24, 432-436.

Tsuda Y, Yasutake H, Ishijima A, Yanagida T (1996) Torsional rigidity of single actin filaments and actin-actin bond breaking force under torsion measured directly by in vitro micromanipulation. *Proc Natl Acad Sci U S A* 93, 12937-12942.

Urban E, Jacob S, Nemethova M, Resch GP, Small JV (2010) Electron tomography reveals unbranched networks of actin filaments in lamellipodia. *Nat Cell Biol* 12, 429-435.

Uyeda TQP, Iwadate Y, Umeki N, Nagasaki A, Yumura S (2011) Stretching actin filaments within cells enhances their affinity for the myosin II motor domain. *PLoS One* 6, e26200.

Vinzenz M, Nemethova M, Schur F, Mueller J, Narita A, Urban E, Winkler C, Schmeiser C, Koestler SA, Rottner K, Resch GP, Maeda Y, Small JV (2012) Actin branching in the initiation and maintenance of lamellipodia. *J Cell Sci,* Advance Online Publication, March 19, 2012, doi:10.1242/jcs.107623.

Wakabayashi K, Sugimoto Y, Tanaka H, Ueno Y, Takezawa Y, Amemiya Y (1994) X-ray diffraction evidence for the extensibility of actin and myosin filaments during muscle contraction. *Biophys J* 67, 2422-2435.

Wallrabe H, Periasamy A (2005) Imaging protein molecules using FRET and FLIM microscopy. *Curr Opin Biotechnol* 16, 19-27.

Wang Y, Shyy JY, Chien S (2008) Fluorescence proteins, live-cell imaging, and mechanobiology: seeing is believing. *Annu Rev Biomed Eng* 10, 1-38.

Xu K, Babcock HP, Zhuang X (2012) Dual-objective STORM reveals three-dimensional filament organization in the actin cytoskeleton. *Nat Methods* 9, 185-188.

Yamaoka H, Adachi T (2010) Coupling between axial stretch and bending/twisting deformation of actin filaments caused by a mismatched centroid from the center axis. *International Journal of Mechanical Sciences* 52, 329-333.